

STATIC BEHAVIOUR OF FUNCTIONALLY GRADED MAGNETO-ELECTRO-ELASTIC PLATES AND BEAMS IN THERMAL AND HYGROTHERMAL ENVIRONMENT

Thesis

Submitted in partial fulfillment of the requirements for the degree of

DOCTOR OF PHILOSOPHY

by

VINYAS M.



**DEPARTMENT OF MECHANICAL ENGINEERING
NATIONAL INSTITUTE OF TECHNOLOGY KARNATAKA
SURATHKAL, MANGALORE-575025
MAY, 2018**

DECLARATION

I hereby declare that the Research Thesis entitled “**STATIC BEHAVIOUR OF FUNCTIONALLY GRADED MAGNETO-ELECTRO-ELASTIC PLATES AND BEAMS IN THERMAL AND HYGROTHERMAL ENVIRONMENT**”

which is being submitted to the **National Institute of Technology Karnataka, Surathkal** in partial fulfillment of the requirements for the award of the degree of **Doctor of Philosophy in Department of Mechanical Engineering** is a *bonafide report of the research work carried out by me*. The material contained in this Research Thesis has not been submitted to any other Universities or Institutes for the award of any degree.

Register Number: **155022 ME15F16**

Name of the Research Scholar: **VINYAS M.**

Signature of the Research Scholar:

Department of Mechanical Engineering

Place: NITK-Surathkal

Date: May 3, 2018

C E R T I F I C A T E

This is to certify that the Research Thesis entitled “**STATIC BEHAVIOUR OF FUNCTIONALLY GRADED MAGNETO-ELECTRO-ELASTIC PLATES AND BEAMS IN THERMAL AND HYGROTHERMAL ENVIRONMENT**” submitted by **Mr. VINYAS M. (Register Number: 155022-ME15F16)** as the record of the research work carried out by him, *is accepted as the Research Thesis submission* in partial fulfillment of the requirements for the award of the degree of **Doctor of Philosophy.**

Dr. Subhaschandra Kattimani

Chairman-DRPC

Research Guide

Date:

Date: May 3, 2018

ACKNOWLEDGEMENT

It provides an immense pleasure to acknowledge all the people who have helped, encouraged and supported throughout my dissertation. It is my humble appreciation towards everyone who has sacrificed their comfort in some form or other on the successful completion of my doctoral studies.

First of all, I would like to express my sincere gratitude and heartiest thanks to my supervisor ***Dr. Subhaschandra Kattimani***, Assistant Professor, Department of Mechanical Engineering, National Institute of Technology Karnataka (N.I.T.K), Surathkal, for considering me worthy of working under his esteemed guidance. This research outcome is a result of his excellent guidance and support throughout the work. This thesis could not have attained its present form, both in content and presentation without his active interest, timely support, direction and valuable guidance. My professional ethics, problem solving skills and knowledge level have received the professional boost through all those days I was able to spend in his proximity. His vast knowledge and insight into the area of the smart composite structures have helped me to overcome the hurdles throughout my dissertation. The words are insufficient to express my deep feeling and heartfelt thanks to my supervisor for his unhesitated guidance throughout my doctoral work. For all this I will remain grateful to him throughout my career.

I take this opportunity to thank ***Dr. Narendranath S.***, Professor and Head, Department of Mechanical Engineering for his continuous and timely support.

I would like to express the deepest appreciation to the members of research progress assessment committee *Dr. S. M. Murigendrappa* and *Dr. Nagendrappa H.*, for their valuable remarks, suggestions and technical advices during the length of my research.

I wish to express my sincere gratitude to all the faculty members of Department of Mechanical Engineering, of N.I.T.K Surathkal for their unbiased appreciation and support all through this research work.

I take this opportunity to thank all my friends and colleagues who have supported directly or indirectly to expedite towards my goal. A special thanks to my friend *Dr. Navya P.N.* for her immense support and co-operation.

I would like to take this opportunity to express my gratitude to my family. Words cannot express how grateful I am to my father *Mr. Mahesh T.G.* and mother *Mrs. Sunita Mahesh* for their blessings, love and for all of the sacrifices that they have made on my behalf. It gives me immense pleasure to thank my brother *Mr. Vishwas M.*, sister-in-law *Mrs. Chandrika Vishwas* and their lovely little child *Viaan.V. Aradhya*, for their constant support.

Above all, I am highly indebted to almighty *Lord Shiva* who always blessed me to overcome every hurdles of my life and accomplish the goals with ease.

VINYAS M.

National Institute of Technology Karnataka, Surathkal

Date: May 3, 2018

ABSTRACT

This dissertation deals with the investigation of coupled multiphysics response of stepped functionally graded magneto-electro-elastic (SFGMEE) and multiphase MEE beams and plates in the thermal and hygrothermal environment. The influence of pyroeffects on the direct and derived quantities of MEE beams and plates has been investigated. An attempt has been made to evaluate the effect of external moisture and temperature on the static parameters of hygrothermo-magneto-electro-elastic (HTMEE) beams and plates made of adaptive wood encapsulated with piezoelectric material (Barium Titanate-BaTiO₃) and magnetostrictive material (Cobalt Ferrite-CoFe₂O₄). To this end, three-dimensional finite element (FE) formulation has been derived with the aid of the total potential energy principle and constitutive equations of MEE material considering the temperature and moisture fields. The condensation technique is employed to obtain the nodal values of degrees of freedom such as displacement components, electric potential and magnetic potential. Further, the FE formulation is extended to study the individual and combined effects of thermal, magnetic and electric fields on the static behaviour of SFGMEE plates. The effect of volume fractions, boundary conditions, aspect ratio, stacking sequence and length-to-width ratio on the static response of SFGMEE and multiphase beams and plates has been studied.

The numerical evaluation reveals that the different thermal loading profiles exhibit unique effect on the static behaviour of MEE beams and plates. In addition, the significant influence of pyroeffects is noticed for all the forms of thermal loads. The volume fractions of BaTiO₃ and CoFe₂O₄ show a considerable influence on the variation of multiphase MEE beam. Furthermore, a novel FE approach presented to deal with the hygrothermal response of MEE beams and plates suggest that the moisture and temperature fields exhibit a predominant effect on the static parameters. The empirical constants associated with the temperature and moisture dependent elastic stiffness alter the hygrothermal response of MEE beams and plates.

The comprehensive investigation on the effects of multi-field loads on the characteristic behaviour of SFGMEE plates is carried out using the first order shear deformation theory (FSDT). The results disclose that the predominant influence of the electric and magnetic loads along with the thermal load exhibit a predominant influence on the behaviour of the plates.

Finally, the influence of BaTiO_3 and CoFe_2O_4 particle arrangement on the static response of magneto-electro-thermo-elastic (METE) plates has been investigated. The significant forms of particles arrangement such as body-centered cubic, face-centered cubic and simple cube are considered for the analysis. The investigation reveals that the direct (displacements, electric potential and magnetic potential) and derived quantities (stresses, electric displacement, magnetic flux densities) of METE plate predominantly vary with respect to the particle arrangement.

KEYWORDS: magneto-electro-elastic; pyroeffects; multiphase; hygrothermo-magneto-electro-elastic; fully coupled analysis.

CONTENTS

Acknowledgements	i
Abstract	iii
List of Tables.....	x
List of Figures.....	xii
Nomenclature.....	xxiii
1. INTRODUCTION AND LITERATURE REVIEW	1
1.1. Smart Composite Materials.....	1
1.1.1. Piezoelectric Materials.....	2
1.1.2. Magnetostrictive Materials.....	3
1.2. Magneto-Electro-Elastic composites.....	4
1.3. Analysis of Magneto-Electro-Elastic (MEE) Material.....	8
1.3.1. Free Vibration Study of MEE structures.....	8
1.3.2. Static Studies of MEE structures.....	9
1.3.3. Transient Response of MEE structures.....	10
1.3.4. Analysis of MEE nano structures.....	11
1.4. Effective properties of MEE materials.....	11
1.5. Analysis of structures in thermal environment.....	12
1.5.1. Piezo-thermo-elastic structures.....	12
1.5.2. Magneto-electro-thermo-elastic structures.....	13
1.6. Analysis of structures in hygrothermal environment.....	14
1.6.1. Hygrothermo-piezoelectric structures.....	14
1.6.2. Hygrothermo-magneto-electro-elastic structures.....	14
1.7. Fully coupled analysis of Magneto-Electro-Thermo-Elastic (METE) Solids.....	15
1.8. Effect of electric and magnetic loads on MEE structures.....	15
1.9. Scope and Objective of the Dissertation.....	16
1.10. Contributions from the Dissertation.....	18
1.11. Overview of the Dissertation by chapter	18

2. STATIC RESPONSE OF STEPPED FUNCTIONALLY GRADED MAGNETO-ELECTRO-ELASTIC BEAM IN THERMAL ENVIRONMENT	
2.1. Introduction.....	21
2.2. Stepped Functionally graded magneto-electro-elastic stacking arrangement...	22
2.3. Problem description.....	23
2.4. Constitutive Equations.....	23
2.5. Finite Element Formulation	24
2.6. Equations of Motion.....	26
2.7. Temperature Profiles.....	30
2.7.1. In-plane temperature profiles.....	31
2.7.2. Through thickness temperature profiles.....	32
2.8. Results and Discussion.....	32
2.8.1. Validation of the FE model.....	33
2.8.2. Influence of Pyroeffects.....	35
2.8.3. Effect of cross-thickness temperature profiles.....	39
2.8.4. Investigation at the different beam region.....	47
2.9. Conclusions.....	51
3. STATIC RESPONSE OF MULTIPHASE MAGNETO-ELECTRO-ELASTIC BEAM IN THERMAL ENVIRONMENT	
3.1. Introduction.....	52
3.2. Problem Description And Governing Equations.....	53
3.3. Constitutive Equations.....	53
3.4. Finite Element Formulation.....	54
3.5. Equations of Motion.....	54
3.6. Results and Discussion.....	55
3.6.1. Static analysis of multiphase MEE beam: Clamped-Free boundary condition.....	55
3.6.2. Static analysis of multiphase MEE beam: Clamped-Clamped boundary condition.....	62
3.6.3. Static Analysis of multiphase MEE beam: Clamped-Simply supported Boundary condition.....	93
3.7. Parametric Study.....	64

3.7.1. Effect of Product properties.....	65
3.7.2. Effect of Volume fraction.....	68
3.7.3. Effect of aspect ratio (a/h) on electric and magnetic potentials.....	68
3.8. Conclusions.....	71
4. MULTIPHYSICS RESPONSE OF STEPPED FUNCTIONALLY GRADED MAGNETO-ELECTRO-ELASTIC PLATES IN THERMAL ENVIRONMENT	
4.1. Introduction.....	72
4.2. Problem Description.....	73
4.3. Finite Element Formulation and Governing Equations of Motion.....	74
4.4. Temperature distribution in SFGMEE plate.....	74
4.5. Results and Discussion.....	74
4.5.1. Effect of Thermal loadings.....	77
4.5.2. Effect of Boundary Conditions.....	81
4.5.3. Effect of aspect ratio.....	85
4.5.4. Effect of Length-to-width ratio.....	86
4.5.5. Influence of Pyroeffects.....	94
4.6. Conclusions.....	98
5. HYGROTHERMAL ANALYSIS OF MAGNETO-ELECTRO-ELASTIC PLATES USING FINITE ELEMENT METHODS	
5.1. Introduction.....	99
5.2. Basic Formulation of the Problem.....	100
5.2.1. Problem Description.....	100
5.2.2. Constitutive Equations.....	101
5.2.3. Finite Element Formulation.....	101
5.2.4. Governing Equations of Motion.....	102
5.3. Results and Discussions.....	105
5.3.1. Validation of the FE formulation.....	106
5.3.2. Effect of hygrothermal load.....	109
5.3.3. Effect of temperature and moisture dependent elastic stiffness coefficients.....	109
5.3.4. Simply supported MEE plate (SSSS).....	111
5.3.5. Clamped MEE plate (CCCC).....	116

5.3.6.	MEE plate with adjacent side clamped (CFFC).....	120
5.3.7.	MEE plate with opposite sides clamped (FCFC).....	122
5.3.8.	Effect of a/h ratio.....	128
5.4.	Conclusions.....	130
6.	HYGROTHERMAL ANALYSIS OF MAGNETO-ELECTRO-ELASTIC BEAMS	
6.1.	Introduction.....	131
6.2.	Basic Formulation of the Problem.....	132
6.2.1.	Problem Description.....	132
6.2.2.	Finite element formulation and governing equations.....	132
6.3.	Results and Discussions.....	133
6.3.1.	Effect of hygrothermal loads.....	134
6.3.2.	Empirical constants effect on HTMEE beam.....	142
6.3.3.	Significant combination of empirical constant.....	151
6.4.	Conclusions.....	154
7.	INFLUENCE OF COUPLED FIELDS ON STATIC AND FREE VIBRATION BEHAVIOUR OF STEPPED FUNCTIONALLY GRADED MAGNETO-ELECTRO-THERMO-ELASTIC PLATE	
7.1.	Introduction.....	155
7.2.	Plate Geometry and Displacement Relation.....	156
7.3.	Constitutive Equations.....	157
7.4.	Finite Element Formulation.....	158
7.5.	Equations of Motion.....	160
7.6.	Results and Discussion.....	163
7.6.1.	Validation of the FE formulation.....	164
7.6.2.	Effect of uniform temperature rise.....	165
7.6.3.	Effect of non-uniform temperature rise.....	168
7.6.4.	Effect of electric field force.....	170
7.6.5.	Effect of magnetic field force.....	172
7.6.6.	Effect of combined loading.....	173
7.6.7.	Influence of pyroeffects.....	176
7.6.8.	Effect of boundary conditions.....	177

7.6.9. Effect of aspect ratio (a/b) and length-to-thickness ratio (a/H).....	179
7.6.10. Free vibration analysis of SFG METE plate: Evaluation of effect of coupling factors.....	180
7.7. Conclusions.....	184
8. EFFECT OF PARTICLE ARRANGEMENT ON COUPLED RESPONSE OF MAGNETO-ELECTRO-THERMO-ELASTIC PLATES	
8.1. Introduction.....	188
8.2. Problem Description And Finite Element Governing Equations.....	189
8.3. Results and Discussions.....	190
8.3.1. Effect of particle arrangement.....	190
8.3.2. Influence of pyroeffects and particle arrangement.....	194
8.3.3. Effect of aspect ratio (a/h).....	201
8.4. Conclusions.....	202
9. CONCLUSIONS AND FUTURE SCOPE	
9.1. Major Findings.....	203
9.2. Scope for Future Research.....	206
APPENDIX-A.....	207
APPENDIX-B.....	210
APPENDIX-C.....	211
APPENDIX-D.....	213
REFERENCES	216
LIST OF PUBLICATIONS	233

LIST OF TABLES

Table No.	Description	Page No.
2.1	Material properties of BaTiO ₃ -CoFe ₂ O ₄ composite w.r.t different volume fraction V_f of BaTiO ₃ -CoFe ₂ O ₄	34
2.2	Effect of different cross-thickness temperature loads on the maximum electric potential (ϕ) of MEE beams.....	41
2.3	Effect of different cross-thickness temperature loads on the maximum magnetic potential (ψ) of MEE beams.....	41
3.1	In-plane temperature profiles varying along the multiphase MEE beam length.....	56
4.1	Material coefficients of #B and #T materials used in Sladek <i>et al.</i> (2013).....	77
4.2	Properties of MEE material used in Sladek <i>et al.</i> (2013).....	78
4.3	Comparison study of the direct quantities of E-FGM MEE plate.....	78
4.4	Effect of aspect ratio (a/h) on the maximum values of transverse deflection, normal stresses and shear stresses for different temperature profiles.....	90
4.5	Effect of aspect ratio (a/h) on the maximum values of electric displacement components and magnetic flux density components for different temperature profiles.....	91
4.6	Effect of length-to-width (a/b) ratio on the maximum values of transverse displacement, electric potential and magnetic potential for different temperature profiles and aspect ratio (a/h).....	95
4.7	Influence of pyroeffects on the maximum electric potential ϕ_{max} for different stacking sequences.....	97
4.8	Effect of aspect ratio (a/h) on the maximum electric potential ϕ_{max} for different temperature profiles.....	97
5.1	Material properties of BaTiO ₃ and CoFe ₂ O ₄ and adaptive wood made of BaTiO ₃ and CoFe ₂ O ₄	108

5.2	Effect of boundary conditions on the direct quantities of MEE plate.....	128
7.1	Natural frequency for BFFB stacked MEE plate.....	166
7.2	Normalized Frequencies ($\omega_n = \omega (a^2/H\sqrt{\rho/C_{11}})$), for simply supported three layered BFB plate; $a = 1$ m; $H = 0.3$ m.....	166
7.3	Convergence of the natural frequency of MEE plate with mesh size.....	166
7.4	Different stiffness matrices.....	181
7.5	Natural frequencies (rad/s) for SSSS SFG METE plate.....	185
7.6	Natural frequencies for CCCC SFG METE plate.....	186
7.7	Effect of boundary conditions on natural Frequencies for SFG METE plate.....	187
8.1	Material properties of BaTiO ₃ /CoFe ₂ O ₄ particles with different spatial distribution (BCC, FCC & SC) (Aboudi 2001; Koutsawa 2015).....	190
8.2	Effect of pyro coupling on electric potential, magnetic potential, electric displacement and magnetic flux density for different boundary conditions and spatial particle arrangement ($a/h = 50$; $a/b = 1$).....	200
8.3	Variation of maximum electric potential for different a/h ratio, particle arrangement and boundary conditions.....	201
8.4.	Variation of maximum magnetic potential for different a/h ratio, particle arrangement and boundary conditions.....	202

LIST OF FIGURES

Figure No	Description	Page No.
1.1	Piezoelectric effect.....	2
1.2	Magnetostrictive effect.....	3
1.3	Magneto-electro-elastic coupling effect.....	5
1.4	Additional coupling effects of MEE materials in (a) thermal (b) hygroscopic environment.....	7
2.1	Stepped functionally graded (SFG) (a) BFB (b) FBF stacking sequence.....	23
2.2	Schematic representation of SFGMEE beam.....	23
2.3	Convergence of transverse displacement component U_w with mesh refinement.....	33
2.4	Validation of (a) longitudinal y-direction U_v (b) electric potential ϕ (c) magnetic potential ψ (d) normal stress - σ_x	35
2.5	Variation of displacement components (a) U_x (b) U_v (c) U_w (d) electric potential ϕ (e) magnetic potential ψ for SFG-BFB and SFG-FBF subjected to uniform temperature load.....	37
2.6	Variation of (a) U_x (b) U_v (c) U_w (d) electric potential ϕ (e) magnetic potential ψ for SFG-BFB and SFG-FBF subjected to linear temperature load.....	38
2.7	Variation of (a) U_x (b) U_v (c) U_w (d) electric potential ϕ (e) magnetic potential ψ for SFG-BFB and SFG-FBF subjected to sinusoidal temperature load.....	39
2.8	Effect of through thickness temperature profiles on longitudinal x- direction displacement component U_x (a) SFG-BFB (b) SFG-FBF.....	40
2.9	Effect of through thickness temperature profiles on longitudinal y- direction displacement component U_v (a) SFG-BFB (b) SFG-FBF.....	40
2.10	Effect of through thickness temperature profiles on transverse displacement component U_w (a) SFG-BFB (b) SFG-FBF.....	41

2.11	Effect of through thickness temperature profiles on electric potential, ϕ (a) SFG-BFB (b) SFG-FBF.....	42
2.12	Effect of through thickness temperature profiles on magnetic potential, ψ (a) SFG-BFB (b) SFG-FBF MEE beam.....	43
2.13	Effect of through thickness temperature profiles on normal stress σ_x (a) SFG-BFB (b) SFG-FBF MEE beam.....	43
2.14	Effect of through thickness temperature profiles on the shear stress τ_{xy} (a) SFG-BFB (b) SFG-FBF MEE beam.....	44
2.15	Effect of through thickness temperature profiles on shear stress τ_{yz} (a) SFG-BFB (b) SFG-FBF MEE beam.....	44
2.16	Effect of through thickness temperature profiles on shear stress τ_{xz} (a) SFG-BFB (b) SFG-FBF MEE beam.....	45
2.17	Effect of through thickness temperature profiles on electric displacement D_x (a) SFG-BFB (b) SFG-FBF MEE beam.....	45
2.18	Effect of through thickness temperature profiles on electric displacement D_y (a) SFG-BFB (b) SFG-FBF MEE beam.....	45
2.19	Effect of through thickness temperature profiles on the variation of electric displacement D_z (a) SFG-BFB (b) SFG-FBF MEE beam.....	46
2.20	Effect of through thickness temperature profiles on magnetic flux density B_x (a) SFG-BFB (b) SFG-FBF MEE beam.....	46
2.21	Effect of through thickness temperature profiles on magnetic flux density B_y (a) SFG-BFB (b) SFG-FBF MEE beam.....	46
2.22	Effect of through thickness temperature profiles on magnetic flux density B_z (a) SFG-BFB (b) SFG-FBF MEE beam.....	47
2.23	Variations of displacement components (a) U_x (b) U_y (c) U_z at different regions of SFG-BFB MEE beam.....	48
2.24	Variations of (a) electric potential and (b) magnetic potential at different regions of SFG-BFB MEE beam.....	48
2.25	Variations of stress components (a) σ_x (b) τ_{xz} (c) τ_{xy} (d) τ_{yz} at different regions of SFG-BFB MEE beam.....	49
2.26	Variations of electric displacements (a) D_x (b) D_y (c) D_z at different regions of SFG-BFB MEE beam.....	50

2.27	Variations of magnetic flux densities (a) B_x (b) B_y (c) B_z at different regions of SFG-BFB MEE beam.....	50
3.1	Multiphase magneto-electro-elastic beam	53
3.2	Variation of electric potential ϕ (a) uniform temperature (b) half-sine temperature (c) linear temperature profile (d) bi-triangular temperature profile for C-F boundary condition.....	57
3.3	Effect of temperature profiles on displacement components (a) U_x (b) U_y (c) U_w (d) magnetic potential (ψ) for C-F boundary condition.....	58
3.4	Effect of temperature profiles stress component (a) σ_x (b) σ_y (c) σ_z (d) τ_{xy} (e) τ_{xz} along the length of the C-F multiphase MEE beam.....	60
3.5	Effect of temperature profiles on electric displacements (a) D_x (b) D_y (c) D_z	61
3.6	Effect of temperature profiles on magnetic flux densities (a) B_x (b) B_y (c) B_z	61
3.7	Variation of displacement components (a) U_x (b) U_y (c) U_w (d) electric potential ϕ (e) magnetic potential ψ for various temperature profiles for C-C boundary condition.....	64
3.8	Variation of displacement components (a) U_x (b) U_y (c) U_w (d) electric potential ϕ (e) magnetic potential ψ for various temperature profiles for C-S boundary condition.....	65
3.9	Effect of product property on U_x (a) C-C boundary condition (b) C-S boundary condition.....	66
3.10	Effect of product property on U_y (a) C-C boundary condition (b) C-S boundary condition.....	66
3.11	Effect of product property on U_w (a) C-C boundary condition (b) C-S boundary condition.....	67
3.12	Effect of product property on electric potential ϕ (a) C-C boundary condition (b) C-S boundary condition.....	67
3.13	Effect of product property on magnetic potential ψ (a) C-C boundary condition (b) C-S boundary condition.....	67
3.14	Effect of volume fraction on U_x (a) C-C boundary condition (b)	

	C-S boundary condition.....	69
3.15	Effect of volume fraction on U_v (a) C-C boundary condition (b) C-S boundary condition.....	69
3.16	Effect of volume fraction on U_w (a) C-C boundary condition (b) C-S boundary condition.....	69
3.17	Effect of volume fraction on electric potential ϕ (a) C-C boundary condition (b) C-S boundary condition.....	70
3.18	Effect of volume fraction on magnetic potential ψ (a) C-C boundary condition (b) C-S boundary condition.....	70
3.19	Effect of aspect ratio on the electric potential (a) C-F (b) C-S boundary condition.....	70
3.20	Effect of aspect ratio on the magnetic potential (a) C-F (b) C-S boundary condition.....	71
4.1	Schematic representation of SFGMEE plate.....	73
4.2	Boundary conditions (a) clamped on all edges (CCCC) (b) simply supported on all edges (SSSS) (c) adjacent edges clamped (CFFC) (d) opposite edge clamped (FCFC) (e) opposite edges simply supported (CSCS).....	74
4.3	Verification plots (a) displacement component in x -direction U_x (b) magnetic potential (c) normal stress σ_x (d) magnetic flux density B_z of MEE plate.....	75
4.4	Validation of transverse displacement component U_w of two layered plate (Sladek <i>et al.</i> , 2013).....	76
4.5	Convergence of electric potential ϕ	76
4.6	Effect of temperature distributions on displacement components (a) U_x (b) U_v (c) U_w (d) electric potential ϕ (e) magnetic potential ψ	79
4.7	Effect of temperature distributions on (a) normal stress σ_x (b) shear stress τ_{xz} (c) shear stress τ_{xy}	80
4.8	Effect of temperature distributions on (a) magnetic flux density B_x (b) magnetic flux density B_z (c) electric displacement D_x (d) electric displacement D_z	82

4.9	Effect of boundary condition on (a) U_x (b) U_y (c) U_w (d) electric potential ϕ (e) magnetic potential ψ	83
4.10	Effect of boundary condition on (a) normal stress σ_x (b) shear stress τ_{xz} (c) shear stress τ_{xy}	83
4.11	Effect of boundary conditions on magnetic flux densities (a) B_x (b) B_y (c) B_z	84
4.12	Effect of boundary conditions on electric displacements (a) D_x (b) D_y (c) D_z	85
4.13	Effect of aspect ratio (a/h) on displacements (a) U_x (b) U_y (c) U_w (d) electric potential ϕ (e) magnetic potential ψ	87
4.14	Effect of aspect ratio (a/h) on (a) normal stress σ_x (b) shear stress τ_{xz} (c) shear stress τ_{xy} (d) shear stress τ_{yz}	88
4.15	Effect of aspect ratio (a/h) on magnetic flux densities (a) B_x (b) B_y (c) B_z	89
4.16	Effect of aspect ratio (a/h) on electric displacements (a) D_x (b) D_y (c) D_z	89
4.17	Effect of length-to-width ratio (a/b) on displacement components (a) U_x (b) U_y (c) U_w (d) electric potential ϕ (e) magnetic potential ψ	92
4.18	Effect of length-to-width ratio (a/b) on (a) normal stress σ_x (b) shear stress τ_{xz}	93
4.19	Effect of length-to-width ratio (a/b) on electric displacements (a) D_x (b) D_y (c) D_z	93
4.20	Effect of length-to-width ratio (a/b) on magnetic flux densities (a) B_x (b) B_y (c) B_z	94
4.21	Pyroeffects on electric potential for (a) uniform (b) parabolic (c) linear (d) bi-triangular temperature distributions.....	55
5.1	HTMEE plate geometry.....	100
5.2	Schematic of MEE plate with different boundary conditions.....	101
5.3	Validation plots (a) U_x (b) magnetic potential (c) normal stress σ_x (d) magnetic flux density B_z (e) U_x (f) electric potential of MEE plate with different boundary conditions.....	107
5.4	Convergence of electric potential ϕ for <i>FCFC</i> MEE plate.....	107

5.5	Effect of hygrothermal load on (a) U_w (b) ϕ (c) ψ (d) σ_x (e) D_x (f) B_x	110
5.6	Effect of empirical constants on displacements (a) U_x (b) U_v (c) U_w of <i>SSSS</i> MEE plate.....	112
5.7	Effect of empirical constants on (a) electric potential ϕ (b) magnetic potential ψ of <i>SSSS</i> MEE plate.....	112
5.8	Effect of empirical constants on stress components (a) σ_x (b) τ_{xy} (c) τ_{xz} (d) τ_{yz} of <i>SSSS</i> MEE plate.....	114
5.9	Effect of empirical constants on electric displacements (a) D_x (b) D_z of <i>SSSS</i> MEE plate.....	114
5.10	Effect of empirical constants on magnetic flux densities (a) B_x (b) B_z of <i>SSSS</i> MEE plate.....	115
5.11	Influence of α^* on (a) U_w (b) ϕ (c) ψ (d) σ_x (e) B_z (f) D_z	117
5.12	Influence of β^* on (a) (a) U_w (b) ϕ (c) ψ (d) σ_x (e) B_z (f) D_z	118
5.13	Effect of empirical constants on displacements (a) U_x (b) U_v (c) U_w of <i>CCCC</i> MEE plate.....	119
5.14	Effect of empirical constants on (a) electric potential ϕ (b) magnetic potential ψ of <i>CCCC</i> MEE plate.....	119
5.15	Effect of empirical constants on (a) normal stress- σ_x (b) electric displacement D_x (c) magnetic flux density B_x of <i>CCCC</i> MEE plate.....	120
5.16	Effect of empirical constants on (a) transverse displacement U_w (b) electric potential ϕ (c) magnetic potential ψ of <i>CFFC</i> MEE plate.....	121
5.17	Effect of empirical constants on (a) normal stress- σ_x (b) shear stress τ_{xz} of <i>CFFC</i> MEE plate.....	122
5.18	Effect of empirical constants on electric displacements (a) D_x (b) D_y (c) D_z of <i>CFFC</i> MEE plate.....	123
5.19	Effect of empirical constants on magnetic flux densities (a) B_x (b) B_y (c) B_z of <i>CFFC</i> MEE plate.....	124
5.20	Effect of empirical constants on displacements (a) U_x (b) U_v (c) U_w of <i>FCFC</i> MEE plate.....	125
5.21	Effect of empirical constants on (a) electric potential ϕ (b)	

	magnetic potential ψ of <i>FCFC</i> MEE plate.....	125
5.22	Effect of empirical constants on (a) normal stress σ_x (b) shear stress τ_{xz} (c) shear stress τ_{xy} (d) shear stress τ_{yz} of <i>FCFC</i> MEE plate.....	126
5.23	Effect of empirical constants on electric displacements (a) D_x (b) D_y (c) D_z of <i>FCFC</i> MEE plate.....	127
5.24	Effect of empirical constants on magnetic flux densities (a) B_x (b) B_y (c) B_z of <i>FCFC</i> MEE plate.....	128
5.25	Effect of aspect ratio a/h on (a) U_w (b) ϕ (c) D_x (d) B_z (e) σ_x (f) τ_{xz}	129
6.1	Schematic representation of HTMEE beam.....	132
6.2	Validation plots (a) U_x (b) σ_x (c) B_z (d) D_y	134
6.3	Convergence of transverse displacement component U_w	134
6.4	Effect of hygrothermal loads on displacement components (a) U_x (b) U_y (c) U_w for C-C HTMEE beam.....	135
6.5	Effect of hygrothermal loads on (a) electric potential ϕ (b) magnetic potential ψ for C-C HTMEE beam.....	136
6.6	Effect of hygrothermal loads on (a) normal stress σ_x (b) shear stress τ_{xz} (c) shear stress τ_{xy} for C-C HTMEE beam.....	136
6.7	Effect of hygrothermal loads on electric displacements (a) D_x (b) D_y (c) D_z for C-C HTMEE beam.....	137
6.8	Effect of hygrothermal loads on magnetic flux densities (a) B_x (b) B_y (c) B_z for C-C HTMEE beam.....	138
6.9	Individual effect of moisture concentration gradient Δm on displacement components (a) U_x (b) U_y (c) U_w for C-C HTMEE beam.....	139
6.10	Individual effect of moisture concentration gradient Δm on (a) electric potential ϕ (b) magnetic potential ψ for C-C HTMEE beam.....	140
6.11	Individual effect of moisture concentration gradient Δm on stress components (a) σ_x (b) σ_y (c) σ_z (d) τ_{xz} (e) τ_{xy} (f) τ_{yz} for C-C HTMEE beam.....	141
6.12	Individual effect of moisture concentration gradient Δm on	

	electric displacements (a) D_x (b) D_y (c) D_z for C-C HTMEE beam.....	141
6.13	Individual effect of moisture concentration gradient Δm on magnetic flux densities (a) B_x (b) B_y (c) B_z for C-C HTMEE beam.....	142
6.14	Effect of empirical constants on displacement components (a) U_x (b) U_y (c) U_w for C-C HTMEE beam.....	144
6.15	Effect of empirical constants on (a) electric potential ϕ (b) magnetic potential ψ for C-C HTMEE beam.....	144
6.16	Effect of empirical constants on stress components (a) σ_x (b) σ_y (c) σ_z (d) τ_{xz} (e) τ_{xy} (f) τ_{yz} for C-C HTMEE beam.....	145
6.17	Effect of empirical constants on electric displacements (a) D_x (b) D_y (c) D_z for C-C HTMEE beam.....	146
6.18	Effect of empirical constants on magnetic flux densities (a) B_x (b) B_y (c) B_z for C-C HTMEE beam.....	146
6.19	Effect of empirical constants on displacements (a) U_x (b) U_y (c) U_w for cantilever HTMEE beam.....	148
6.20	Effect of empirical constants on (a) electric potential ϕ (b) magnetic potential ψ for cantilever HTMEE beam.....	148
6.21	Effect of empirical constants on stress components (a) σ_x (b) σ_y (c) σ_z (d) τ_{xz} (e) τ_{xy} (f) τ_{yz} for cantilever HTMEE beam.....	149
6.22	Effect of empirical constants on electric displacement components (a) D_x (b) D_y (c) D_z for cantilever HTMEE beam.....	150
6.23	Effect of empirical constants on magnetic flux densities (a) B_x (b) B_y (c) B_z for cantilever HTMEE beam.....	150
6.24	Effect of (a) moisture dependency coefficient β^* (b) temperature dependency coefficient α^* on transverse displacement U_w for cantilever HTMEE beam.....	151
6.25	Effect of (a) moisture dependency coefficient β^* (b) temperature dependency coefficient α^* on electric potential ϕ for cantilever HTMEE beam.....	152
6.26	Effect of (a) moisture dependency coefficient β^* (b) temperature dependency coefficient α^* on magnetic potential ψ for cantilever	

	HTMEE beam.....	152
6.27	Effect of (a) moisture dependency coefficient β^* (b) temperature dependency coefficient α^* on normal stress σ_x for cantilever HTMEE beam.....	152
6.28	Effect of (a) moisture dependency coefficient β^* (b) temperature dependency coefficient α^* on shear stress τ_{xz} for cantilever HTMEE beam.....	153
6.29	Effect of (a) moisture dependency coefficient β^* (b) temperature dependency coefficient α^* on electric displacement D_x for cantilever HTMEE beam.....	153
6.30	Effect of (a) moisture dependency coefficient β^* (b) temperature dependency coefficient α^* on magnetic flux density B_x for cantilever HTMEE beam.....	153
7.1	Schematic diagram of METE plate.....	156
7.2	Schematic diagram of functionally graded plate showing (a) SFG-BFB and (b) SFG-FBF stacking sequences.....	157
7.3	Validation plots of (a) shear stress τ_{xz} (b) normal stress σ_x (c) magnetic flux density, B_z	165
7.4	Variation of the (a) normal stress σ_x (b) magnetic flux density B_z and (c) electric displacement D_z , across the plate thickness of METE plate subject to uniform temperature rise.....	167
7.5	Variation of (a) displacement U_x (b) centre deflection U_w (c) magnetic potential, ψ (d) electric potential, ϕ along plate length of the simply supported METE plate subject to uniform temperature rise.....	168
7.6	Variation of the (a) normal stress σ_x (b) magnetic flux density B_z and (c) electric displacement D_z , across the plate thickness for METE plate subject to non-uniform temperature rise.....	169
7.7	Variations of (a) displacement U_x (b) centre deflection U_w (c) magnetic potential, ψ and (d) electric potential, ϕ , along plate length of METE plate subject to non-uniform temperature rise....	170

7.8	Variation of the (a) normal stress σ_x (b) magnetic flux density B_z and (c) electric displacement D_z , across the plate thickness for METE plate subject to electric field force.....	171
7.9	Variations of (a) displacement U_x (b) center deflection U_w (c) magnetic potential, ψ and (d) electric potential, ϕ along plate length of the METE plate subject to electric field force.....	172
7.10	Variation of the (a) normal stress σ_x (b) magnetic flux density B_z (c) electric displacement D_z across the plate thickness for METE plate subject to magnetic field force.....	173
7.11	Variation of (a) displacement U_x (b) centre deflection U_w (c) electric potential, ϕ and (d) magnetic potential, ψ , along plate length of the METE plate subject to magnetic field force.....	174
7.12	Influence of combined loads on (a) normal stress σ_x (b) magnetic flux density B_z (c) electric displacement D_z	175
7.13	Influence of combined loads on (a) displacement component U_x (b) centre deflection U_w (c) electric potential ϕ (c) magnetic potential ψ	176
7.14	Influence of pyroeffects (a) uniform temperature loads (b) sinusoidal temperature loads.....	176
7.15	Effect of boundary condition on (a) magnetic field density (b) normal stress - σ_x (c) electric displacement.....	178
7.16	Effect of boundary condition on (a) centre deflection U_w (b) longitudinal displacement component U_x (c) electric potential (d) magnetic potential.....	179
7.17	Effect of a/b ratio on (a) U_x (b) U_w of METE plate subjected to uniform temperature load.....	179
7.18	Effect of a/h ratio on (a) U_x (b) U_w of METE plate subjected to uniform temperature load.....	180
7.19	Comparison of natural frequency (a) SFG-BFB (b) SFG-FBF SSSS METE plate.....	182
7.20	Comparison of natural frequency (a) SFG-BFB (b) SFG-FBF CCCC METE plate.....	183
8.1	Multiphase METE plate geometry.....	189

8.2	Packing arrangement of particulate BaTiO ₃ /CoFe ₂ O ₄ composites (a) simple cubic (SC) (b) body centered cube (BCC) (c) face centered cube (FCC).....	189
8.3	Effect of particle arrangement on (a) U_x (b) U_y (c) U_z (d) electric potential ϕ (e) magnetic potential ψ of CCCC METE plate.....	192
8.4	Effect of particle arrangement on (a) normal stress σ_x (b) shear stress τ_{xz} of CCCC METE plate.....	192
8.5	Effect of particle arrangement on electric displacements (a) D_x (b) D_y (c) D_z of CCCC METE plate.....	193
8.6	Effect of particle arrangement on magnetic flux densities (a) B_x (b) B_y (c) B_z of CCCC METE plate.....	194
8.7	Influence of pyroeffects on U_y of METE plates.....	196
8.8	Influence of pyroeffects on electric potential of METE plates.....	197
8.9	Influence of pyroeffects on magnetic potential of METE plates..	197
8.10	Influence of pyroeffects on electric displacement D_z of METE plates.....	198
8.11	Influence of pyroeffects on magnetic flux density B_z of METE plates.....	199
8.12	Influence of pyroeffects on normal stress σ_x of METE plates.....	199

NOMENCLATURE

B_x, B_y, B_z	Electric displacement components along x -, y - and z -directions
D_x, D_y, D_z	Magnetic flux density components along x -, y - and z -directions
HTMEE	Hygrothermo-magneto-electro-elastic
K	Kelvin
L_t, L_ϕ, L_ψ	Differential operators
MEE	Magneto-electro-elastic
METE	Magneto-electro-thermo-elastic
N	Total number of layers
k	Layer number under consideration
Q^ϕ	Electric charge density
Q^ψ	Magnetic charge density
SFGMEE	Stepped functionally graded magneto-electro-elastic
T_p	Total potential energy of the overall <i>SFGMEE</i> plate
U_x, U_y, U_z	Displacement components along x -, y - and z - directions
V_f	Volume fraction of Barium Titanate (BaTiO_3) and Cobalt Ferrite (CoFe_2O_4)
z	Position of the point of interest from the bottom layer
ϕ	Electric potential
ψ	Magnetic potential
ΔT	Temperature rise
ΔC	Moisture concentration rise
T_{max}	The maximum temperature
T_0	Stress free temperature
T_i	Initial temperature at the bottom layer of SFGMEE plate/beam

Chapter 1

INTRODUCTION AND LITERATURE REVIEW

This chapter encapsulates the basic information related to the smart composite materials like piezoelectric material, magnetostrictive material and magneto-electro-elastic (MEE) material. The physics behind the unique property of coupling among electro-elastic, electro-magnetic and magneto-elastic fields are unveiled. The major contributions of the research community with respect to MEE material properties and their applications have been discussed. Further, a comprehensive literature review on the free vibration, static analysis, buckling analysis, thermal analysis of MEE structures is presented. The MEE structures with functionally graded material properties in the presence of hygrothermal environment have been discussed. From the extensive literature survey, the prominent research gaps have been identified and incorporated as research objectives of this dissertation. In the end, organization of the thesis chapters has been delineated.

1.1. SMART COMPOSITE MATERIALS

The combination of two or more materials with a predominant property difference is termed as *Composites*. Few of the composite materials naturally exhibit the concept of multifunctionality. These multiple functions include load bearing (structural) along with one or more other forms such as vibration sensing, actuation, energy storage etc. The multifunctionality is achieved through the interaction of mechanical, electric, magnetic and thermal fields. There exists a certain class of materials for which the mechanical properties can change drastically with the application of the external stimuli such as light, temperature, electric and magnetic fields. Further, they have the ability to quickly respond to the change produced. Such materials are often termed as *Smart materials*.

Among the various smart materials, much of the interest of the researchers has been vested on the piezoelectric and magnetostrictive materials due to their unique interactive property. A brief description of these materials is illustrated in the following sections.

1.1.1. Piezoelectric materials

The piezoelectric effect was discovered by Curie brothers in 1880. The word ‘*Piezein*’ in Greek means ‘squeeze’ or ‘press’. This effect is generally observed in the crystal structures such as Tourmaline, Quartz, Topaz and Rochelle salt. The piezoelectric effect is schematically represented in Fig. 1.1. It can be demonstrated from this figure that when an external load is applied to the piezo material, it deforms from initial length L_1 to the final length L_2 , and produces strains. Due to the inherent property of these materials, the strains thus produced develop an electric potential. In 1881, Gabriel Lippmann discovered the converse piezo effect where the application of the electric field deforms the crystal structure. Few of the commonly used piezo-electric materials are Zinc Oxide (ZnO), Aluminium nitride (AlN), Polyvinylidene fluoride (PVDF) and Barium Titanate (BaTiO₃).

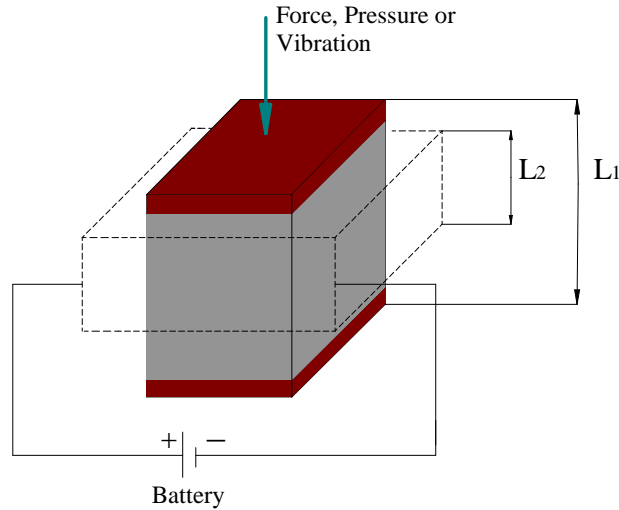


Figure 1.1: Piezoelectric effect

The constitutive equations of piezoelectric materials are given as follows:

$$\{\varepsilon\} = [C]\{\sigma\} + [d]^T \{E\} \quad (1.1)$$

$$\{D\} = [d]\{\sigma\} + [\eta]\{E\} \quad (1.2)$$

where, $\{\varepsilon\}$ and $\{D\}$ are the strain and electric displacement vectors in (C/m²). $[C]$ and $[d]$ are the elastic stiffness matrix in (N/m²) and piezoelectric constant in (C/m²), respectively. $[\eta]$ and $\{E\}$ are the permittivity constant in (C²/Nm²) and electric field, respectively. The piezoelectric and converse piezoelectric effects can be effectively utilised in the applications of sensors and actuators. The actuating and sensing behaviour of piezoelectric materials can be described by Eqs. (1.1) and (1.2),

respectively. The effective sensing and actuating capabilities of piezoelectric material has made them a candidate material for vibration control of many structures (Kundalwal *et al.*, 2013; Kumar and Ray, 2013; Ray and Pradhan, 2008).

1.1.2. Magnetostrictive materials

The concept of magnetostriction was proposed by an English physicist, James Joule in 1842. The term '*Magnetostriction*' refers to the change in the shape of the material under the influence of externally applied magnetic field. It was observed that a sample of magnetostrictive material consists of numerous tiny ferromagnets which possess small magnetic moments as a result of their "3d" shells that are not completely filled with electrons. While, in the presence of the magnetic field, these materials undergo deformation. This is due to the development of the internal strains as a result of rotation and re-orientation of the magnetic domains. Figure 1.2 depicts the schematic representation of the strains developed and magnetic domain re-orientation with the applied magnetic field. Initially, the magnetic domains are randomly arranged with no external magnetic field applied. Once, the magnetic field is applied, the magnetic domains starts to orienting along the direction of the applied magnetic field and there by induces strains. Analogously, when the mechanical force is applied to these materials, it induces a magnetic field. This converse effect is known as *Villari effect*. This phenomenon is usually observed in Iron, Cobalt, and Nickel and also in few rare earth materials like Lanthanum and Terbium. The commercially available well known magnetostrictive material is Terfenol-D which is an alloy of Terbium (Tb), Iron (Fe) and Dysprosium (Dy).

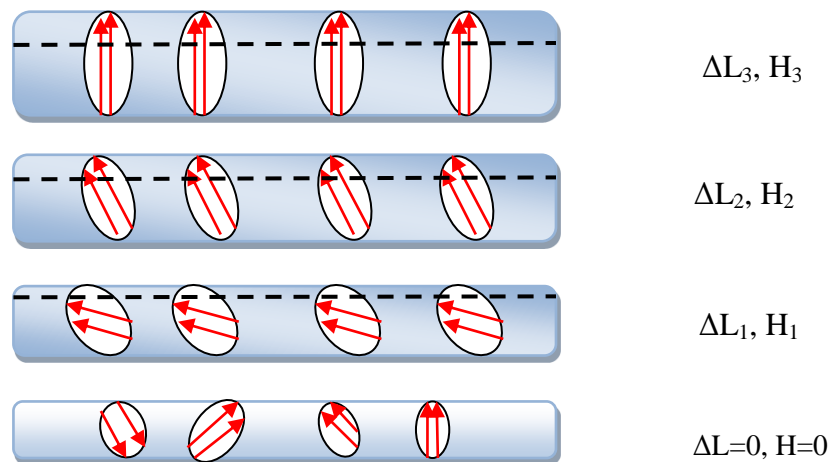


Figure 1.2: Magnetostrictive effect

The linear coupling constitutive equations for the magnetostrictive materials are as follows:

$$\{\varepsilon\} = [C]\{\sigma\} + [q]^T \{H\} \quad (1.3)$$

$$\{B\} = [q]\{\sigma\} + [\mu]\{H\} \quad (1.4)$$

where, $\{\varepsilon\}$ and $\{B\}$ are the strain and magnetic flux density vectors in (N/Am). $[C]$ and $[q]$ are the elastic stiffness matrix in (N/m²) and piezomagnetic constant in (N/Am), respectively. $[\mu]$ and $\{H\}$ are the permeability constant in (Ns²/C²) and magnetic field, respectively.

1.2. MAGNETO-ELECTRO-ELASTIC (MEE) COMPOSITES

The necessity of the man kind to accomplish the tasks with minimum efforts and time paved way for the emergence of the intelligent or smart structures. The advancement in the material science and development in the production technologies of advanced composites supported this vision of the entire research community. As a result, numerous materials with multiphysics characteristics evolved. The phenomenon of inducing magnetic (electric) polarization by applying an external electric (magnetic) field is termed as magneto-electric (ME) effect. In 1894, Curie predicted the existence of ME effect for the first time. Further, ME coupling can be defined as, *the ratio between the magnetic (electric) field output to the electric (magnetic) field input*. The term ME coupling was first coined by Dubey. However, the first experimental observation was made in 1960 when Astrov found the electric field induced magneto-electric effect in Chromia (Cr₂O₃) (Grossinger *et al.*, 2008). Later, Rado noticed the reverse effect in the same system. The ME materials can be divided into two classes namely, single phase compounds and composites. The materials such as Chromia (Cr₂O₃), Bismuth Manganate (BiMnO₃), Bismuth Ferrite (BiFeO₃), Rare earth (Re) ferrobates ReFe₃(BO₃)₄ etc. are the single phase materials which exhibits magneto-electric behaviour, especially at the low temperatures and high external field.

In the early stage of the research, consolidating the ferroelectricity and magnetism together in a single material was found to be a tedious task, as this phenomenon is mutually exclusive. Also, it was witnessed that the simultaneous presence of the electric and magnetic dipoles does not ensure strong coupling between ferroelectricity and magnetism because of the different microscopic mechanism. To

overcome this hurdle, a new class of advanced, high-performance composite material which displays multi-functionality among mechanical, electric and magnetic fields was developed. They are called as *Magneto-electro-elastic* (MEE) materials, which are developed by combining pure piezoelectric and pure piezomagnetic phases. In 1972, Van Suchetelene introduced the concept of “*product properties*” and successfully developed the first MEE composite made of Barium Titanate (BaTiO_3) and Cobalt Ferrite (CoFe_2O_4). Here, the product properties refer to the electro-elastic, magneto-elastic and electro-magnetic coupling displayed by the MEE materials. The MEE material is a prominent smart material with high self sensing and self adaptable capabilities. This unique material exhibits the coexistence of both ferroelectric and ferromagnetic properties. In addition, these materials also display the magneto-electric (ME) coupling such that they produce magnetic and electric field when they are deformed, and conversely they undergo deformation with the application of external electric and magnetic fields as depicted in Fig. 1.3. It is interesting to note that this phenomenon is not exhibited by the individual materials. An applied magnetic field induces polarization via the mechanical coupling between the constituents as follows:

$$\Delta P = \alpha \Delta H \text{ or } \Delta E = \alpha_E \Delta H \quad (\text{Direct ME effect}) \quad (1.5)$$

$$\Delta M = \alpha \Delta E \quad (\text{Converse ME effect}) \quad (1.6)$$

where, α (α_E) is the ME voltage coefficient, P is the electric polarization of a material with applied magnetic field (H). Further, M is the magnetization induced with an external electric field E .

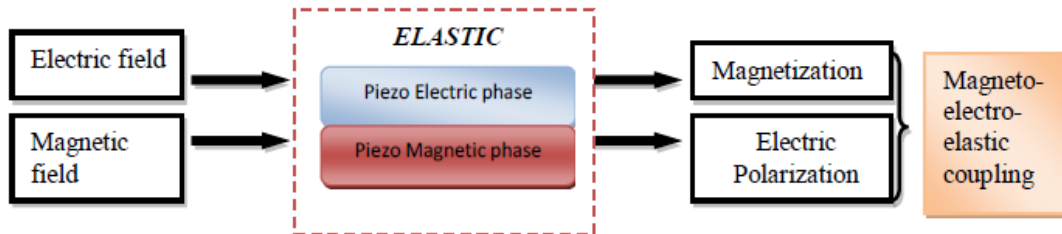


Figure 1.3: Magneto-electro-elastic coupling effect

MEE materials has been considered as a potential candidate in the smart structures due to their efficient capacity to couple between many fields which includes magnetic, electric, elastic, thermal and hygroscopic fields. More importantly, this

feature of MEE materials facilitate energy conversion from one form to another (Nan *et al.*, 1993; Harshe *et al.*, 1993; Lopatin *et al.*, 1994; Nan *et al.*, 1994; Ryu *et al.*, 2002; Hu *et al.*, 2016) which has led their extensive usage in various engineering applications including aerospace, automobiles, nano structures, sensors and actuators etc. Among the various materials exhibiting magneto-electric coupling, the combination of Barium Titanate (BaTiO_3) and Cobalt Ferrite (CoFe_2O_4) has the highest coupling effect (Grossingera *et al.*, 2008).

The numerical results by Dunn (1993) showed that the effective thermal expansion coefficients of MEE composites could significantly exceed those of the constituents themselves. In the thermal environment, this unique class of composites display an additional thermo-electric and thermo-magnetic coupling and are generally termed as pyroelectric and pyromagnetic effects, respectively. These cross products are schematically represented in Fig. 1.4(a), while Fig. 1.4(b) depicts the coupling of hygroscopic field with the elastic, magnetic and electric fields. The application of heat to MEE composite results in thermal expansion of the piezoelectric (piezomagnetic) layups. The mechanical strains developed are transferred to the corresponding layer which leads to the development of electric polarization (magnetization). Even if the individual constituents of the composite do exhibit intrinsic pyroelectricity, the secondary product effect produced due to the coupling of the different phases can make a significant contribution. Among the many MEE composites, *Barium Titanate* (BaTiO_3) and *Cobalt Ferrite* (CoFe_2O_4) is most widely used due to its higher ME coupling. The linear constitutive equations for MEE materials are shown as follows:

$$\{\sigma\} = [C]\{\varepsilon\} - [e]\{E\} - [q]\{H\} \quad (1.7)$$

$$\{D\} = [e]^T \{\varepsilon\} + [\eta]\{E\} + [m]\{H\} \quad (1.8)$$

$$\{B\} = [q]^T \{\varepsilon\} + [m]\{E\} + [\mu]\{H\} \quad (1.9)$$

Where, $[C]$, $[e]$ and $[q]$ are the elastic co-efficient matrix in (N/m^2), piezoelectric coefficient matrix in (C/m^2) and magnetostrictive coefficient matrix in (N/Am), respectively; $[\eta]$, $[m]$ and $[\mu]$ are the dielectric constant matrix in (C^2/Nm^2), electromagnetic coefficient matrix in (Ns/VC) and magnetic permeability constant

matrix in (Ns^2/C^2) , respectively; $\{\sigma\}$, $\{D\}$ and $\{B\}$ represent the stress tensor in (N/m^2) , electric displacement vector (C/m^2) and the magnetic flux vector in (N/Am) , respectively; $\{\mathcal{E}\}$, $\{E\}$, and $\{H\}$ are the linear strain tensor, electric field vector in (V/m) and magnetic field vector in (A/m) , respectively.

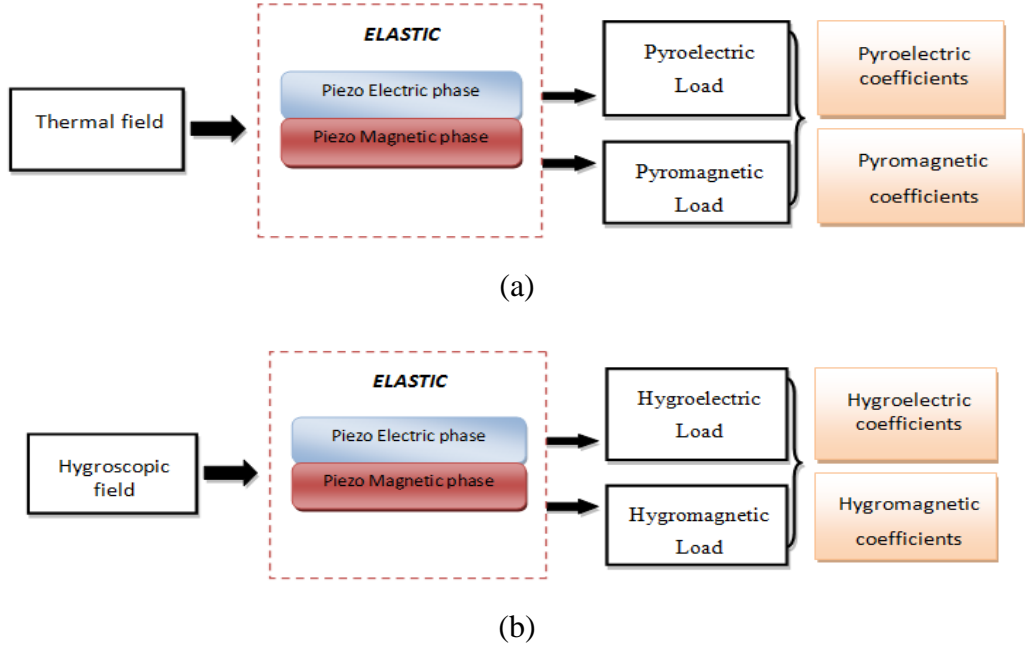


Figure 1.4: Additional coupling effects of MEE materials in (a) thermal (b) hygroscopic environment

Recently, the multiphysics response of MEE materials in hygrothermal environment has been discovered and adopted in the design and analysis of smart structures. In addition to the material coupling effects, the moisture change Δm also exhibits a coupling between the elastic, electric and magnetic fields. Consequently, the coupled constitutive equations of MEE materials in hygrothermal environment i.e., hygrothermo-magneto-electro-elastic (HTMEE) materials can be written as follows:

$$\{\sigma\} = [C]\{\varepsilon\} - [e]\{E\} - [q]\{H\} - [C]\{\alpha\}\Delta T - [C]\{\xi\}\Delta m \quad (1.10)$$

$$\{D\} = [e]^T \{\varepsilon\} + [\eta]\{E\} + [m]\{H\} + \{p\}\Delta T + \{\chi\}\Delta m \quad (1.11)$$

$$\{B\} = [q]^T \{\varepsilon\} + [m]\{E\} + [\mu]\{H\} + \{\tau\}\Delta T + \{\nu\}\Delta m \quad (1.12)$$

where, $\{\xi\}$, $\{\chi\}$ and $\{\nu\}$ are the moisture expansion co-efficient in (m^3/kg) , hygroelectric constants in (Cm/kg) and hygromagnetic constants in $(Nm^2/A \text{ kg})$,

respectively. Further, Δm is the change in moisture concentration from stress free state.

1.3. ANALYSIS OF MAGNETO-ELECTRO-ELASTIC (MEE) STRUCTURES

1.3.1. Free Vibration study of MEE structures

Many researchers have explored the influence of coupling effect on the free vibration, static and buckling characteristics of MEE structures using various computational techniques. Pan and Heyliger (2002) presented an analytical solution to evaluate the natural frequency and mode shapes of a simply supported MEE plate. They also emphasized that few modes are unaffected by the coupling of piezoelectric and piezomagnetic phases. Wang, Qu and Qian (2010) derived three-dimensional exact solutions to evaluate the natural frequencies of MEE cylindrical panels. Milazzo *et al.* (2009) solved the forced vibration problem of MEE bi-morph beam using analytical approach. Davi and Milazzo (2011) carried out dynamic analysis of two-dimensional MEE solids with the aid of regular variational boundary element formulation. The free vibration characteristics of MEE plates were studied using discrete layer approach by Ramirez *et al.* (2006a) and Chen *et al.* (2014). Meanwhile, Ramirez *et al.* (2006b) adopted the same technique and performed modal analysis of functionally graded magneto-electro-elastic plates (FGMEE) plates. Few researchers explored the free vibration behaviour of multilayered and FGMEE structures using state space approach along with discrete singular convolution (DSC) algorithm (Chen *et al.*, 2005; Jiyangi *et al.*, 2006; Huang *et al.*, 2007; Chen *et al.*, 2007; Wang *et al.*, 2010; Xin and Hu, 2015). Using Chebyshev-Ritz method, three-dimensional free vibrations of MEE circular plates was computed by Dong (2008). With the aid of multiple time scales, Tsai and Wu (2008) investigated the modal field variables of FGMEE shells under open circuit condition which was further extended for closed circuit conditions by Wu and Tsai (2010). Analogously, Wu and Lu (2009) carried out the same study for FGMEE plates. Further, considerable study has been reported on the analysis of MEE structures using finite element (FE) methods. Annigeri *et al.* (2006a, b) proposed a semi-analytical method to evaluate the multiphase coupling effect on the natural frequency of MEE cylindrical shells. Bhangale and Ganesan (2005) extended the similar investigation for non-homogeneous FGMEE cylinders. The effect of different coupling phases on the stiffness of the Euler-Bernoulli MEE

beams is investigated by Annigeri *et al.* (2007) and they observed that the piezoelectric phase increases the natural frequency while piezomagnetic phase has an adverse effect on the stiffness of the system. Milazzo *et al.* (2012, 2013); Milazzo and Orlando (2012) performed dynamic analysis of MEE beam by developing a new finite element based upon an elastic equivalent single-layer model. Razavi and Shooshtari (2014) evaluated the effect of elastic foundation on the free vibration behaviour of doubly curved MEE shell. The nonlinear free vibration analysis of MEE plates was carried out by Razavi and Shooshtari (2015) which was later extended for nonlinear forced vibration of MEE thin plates by Shooshtari and Razavi (2015). The active constrained layer damping (ACLD) of geometrically non-linear vibrations of homogenous, functionally graded and multiphase MEE structures were analysed using finite element methods by Kattimani and Ray (2014a, b, 2015, 2017a, b). They made use of Golla-Hughes-McTavish (GHM) method in time domain to model viscoelastic layer of ACLD patch.

Meanwhile, in the application of sensors and actuators, an optimal design of MEE structures becomes prominent. Loja *et al.* (2014) performed the optimization studies to minimize the deformed profile shape of functionally graded MEE beam using differential evolution technique. In order to achieve maximum conversion efficiency from mechanical energy to electric and magnetic energy, Sun and Kim (2010) formulated a systematic design optimization method for the optimal layering of MEE composites. The optimization of the effective magnetoelectric voltage coefficient of fibrous composites made of piezoelectric and piezomagnetic phases was carried out by Kuo and Wang (2012).

1.3.2. Static studies of MEE structures

In many practical cases, the MEE structures may undergo deformation when subjected to various loading forms. Work concerning with the static response of MEE structures can be found in the open literature. Pan (2001) studied the effect of surface and internal loads on the static parameters of multilayered MEE plates by deriving exact solutions. Pan and Han (2005) extended the similar analysis for FGME plates. Pan and Heyliger (2003) found that the magnetic, electric and elastic fields exhibit indifferent responses for different stacking sequence of MEE plates. Lage *et al.* (2004)

adopted Reissner mixed variational principle and developed partial mixed layerwise FE model to investigate the coupled response of MEE plates. The static response of MEE plates under the influence of electric loading was investigated by Wang *et al.* (2003) using state space approach. Jian and Ding (2007) dealt with the MEE beams of density functionally gradient media. Heyliger and Pan (2004) developed discrete layer approximation technique and effectively compared the static behaviour of MEE plates with the exact solutions. Meanwhile, they also emphasized the influence of aspect ratio on the variation of plate fields. Moita *et al.* (2009) performed both static and dynamic analyses of MEE plates using higher order FE model. Li *et al.* (2008) solved the axisymmetric problem of FGMEE circular plate under uniform load by developing three-dimensional analytical solutions. Liu (2011) presented exact solutions and analysed the effect of different volume fraction and loads on the static response of MEE thin plates. Huang *et al.* (2010) presented analytical and semi-analytical solution and examined the static performance of arbitrary loaded FGMEE beam. Haitao *et al.* (2008) exploited the Hamilton's principle in order to evaluate the static and dynamic behaviour of MEE plates and pipes. Bhangale and Ganesan (2006) analysed the effect of material functional gradation on the primary and secondary variables of MEE plates.

1.3.3. Transient response of MEE structures

In addition, extensive research has been carried on the transient response of MEE structures. Hou *et al.* (2006) presented an analytical solution associated with the separation of variable technique to evaluate the transient behaviour of special non-homogeneous MEE cylinder. For fully coupled MEE hollow sphere a similar analysis was performed by Wang and Ding (2006a, b). The same authors extended their study for FGMEE hollow sphere (Wang and Ding, 2006c). The transient behaviour of magneto-electro-thermo-elastic (METE) subjected to thermal shocks was studied in detail by Dai and Wang (2006). Using FE method, the transient response of three phase MEE cylinder (Daga *et al.*, 2008), MEE sensor bonded to mild steel beam (Daga *et al.*, 2009a), multiphase MEE beam (Daga *et al.*, 2009b) and MEE sensor bonded to mild steel cylinder (Biju, Ganesan and Shankar, 2010; Biju, Ganesan *et al.*, 2010) were also studied. More recently, numerous literatures have been reported on a

harmonic analysis of MEE structures (Biju *et al.*, 2009; Biju *et al.*, 2011; Biju *et al.*, 2012; Shooshtari and Razavi, 2017).

1.3.4. Analysis of MEE nano structures

More recently, a motivation occurred among the researchers to examine the characteristic behaviour of nano and micro sized MEE structures. The size effects play an important in accurate analysis of nano structures (Eringen, 1972a, b; 1983). The classical continuum mechanics yields erroneous results as it neglects the size effects. Therefore, the Eringen's non-local theory which considers the size effects is found to be advantageous in this regard. The coupled responses of MEE nano structures exhibit a noticeable difference analogous to macro MEE structures. Many investigators has examined the buckling response (Ansari and Gholami, 2016a, 2017; Ebrahimi and Barati, 2016a, b, c, d, 2017a; Li *et al.*, 2014; Mohammadimehr *et al.*, 2017) and bending response (Arefi and Zenkour, 2017a; Gholami *et al.*, 2017) of MEE structures under various loading condition which includes mechanical loads, thermal loads, hygrothermal loads and electromagnetic loads. The prominent researches can also be seen with respect to free vibration (Ansari and Gholami, 2016b, c; Arefi and Zenkour, 2017b; Ebrahimi and Barati, 2016e, f, g, h; 2017b, c; Jandaghian and Rahmani, 2016; Ke *et al.*, 2014; Ke and Wang, 2014; Farajpour *et al.*, 2016; Ebrahimi *et al.*, 2016) and forced vibration (Ansari *et al.*, 2015a, b) characteristics of MEE nano structures. In addition, Arefi and Zenkour (2016) analysed the transient response of sandwich plates embedded with piezo-magnetic face sheets.

More recently, the effect of porosities on the performance of MEE nanostructures has grasped the attention of the researchers. By considering four variable shear deformation refined plate theory they extended the similar investigation for porous FGMEENanoplates (Ebrahimi and Barati, 2017d). Later, Ebrahimi and Barati (2017e) evaluated the natural frequencies of porous dependent FGMEENanobeams using Eringen's nonlocal theory.

1.4. EFFECTIVE PROPERTIES OF MAGNETO-ELECTRO-ELASTIC (MEE) MATERIAL

Apart from the structural analysis, a plenty of research has been devoted to evaluate the effective coupled properties and constitutive relations of MEE materials.

Considerable amount of work has been carried out to predict the effect of nonlinearity (Carman *et al.*, 1995), volume fractions (Huang *et al.*, 2000; Zhou *et al.* 2017), different reinforcement forms (Espinosa-Almeyda *et al.*, 2017) and inhomogeneities (Hashemi, 2016) on the effective moduli of MEE materials. Among various techniques, asymptotic homogenization micromechanical method is found to be an effective tool in predicting the effective properties of METE composites (Aboudi, 2001; Bravo-Castillero *et al.*, 2009; Challagulla *et al.*, 2011; Hadjiloiiji *et al.*, 2013a, b; Sixto-Camacho *et al.*, 2013). Koutsawa (2015) examined the effect of topological texture on the different properties of METE materials. Recently, Sladek *et al.* (2017) used the meshless local Petrov-Galerkin method to compute the effective MEE material properties. Bakkali *et al.* (2016) numerically evaluated the effective material properties of visco magneto-electro-elastic composites in time and frequency domains.

1.5. ANALYSIS OF STRUCTURES IN THERMAL ENVIRONMENT

1.5.1. Piezo-thermo-elastic structures

The controlled response to the external temperature field made piezoelectric material compatible with many engineering applications. However, analysing the influence of various coupled fields on the response of piezoelectric structures was cumbersome. Numerous computational approaches have been employed by many researchers to evaluate the coupled response of piezoelectric and functionally graded piezoelectric material (FGPM) structures in thermal environment. Among them analytical solution method (Babaei and Chen, 2008; Dai *et al.*, 2010; Alibeigloo, 2011; Hashemi and Kargarnovin, 2016; Jabbari and Barati, 2015; Kulikov and Plotnikova, 2017; Liu *et al.*, 2012; She *et al.*, 2017; Zenkour, 2012), exact method (Kapuria and Achary, 2008; Sharma *et al.*, 2004; Wu *et al.*, 2003; Ying and Zhifie, 2005; Zhong and Shang, 2005; Arani *et al.*, 2010; Khoshgoftar *et al.*, 2009) and finite element methods (Tian *et al.*, 2007; Jiang and Li, 2007; Roy *et al.*, 2010; Boonphennimit *et al.*, 2013; Shegokar and Lal, 2014; Kumar *et al.*, 2016) are prominent. Alashti and Khorsand (2011) carried out the thermo-elastic analysis of FGPM cylinder subjected to asymmetric thermo-electro-mechanical loads. The external thermal field results in the development of undesired vibrations within the piezoelectric structures. Hence, control of these hazardous vibrations is the true challenge for the design engineers (Liew *et*

al., 2001; 2003, Sunar *et al.*, 2012; Zheng *et al.*, 2009; Barati and Jabbari, 2015). The piezoelectric material properties and hence the corresponding multiscale fields are prone to significant variations with the change in temperature. In this regard, few works have been reported on the analysis of piezoelectric structures considering temperature dependent properties (Bacigalupo *et al.*, 2016; Cook and Vel, 2013; Miara and Suarez, 2013; Lv *et al.*, 2014; Barati *et al.*, 2016).

1.5.2. Magneto-Electro-Thermo-Elastic structures

The predominant utilization of MEE structures is usually observed in the harsh environmental conditions like chemical environment, temperature fields, moisture concentration gradients etc. The MEE materials/structures coupled with thermal fields are commonly termed as magneto-electro-thermo-elastic (METE) materials/structures. In the presence of thermal environment, the characteristics behaviour of MEE materials, linear constitutive equations, and thus the equations of motion for METE material (Sunar *et al.*, 2002) alter tremendously. Hence, the investigation of the material properties and the static response of METE structures in the presence of the thermal environment are the prime importance of research for many pioneers. Kumaravel *et al.* (2007) evaluated the steady state response of three layered MEE strip subjected to thermal loads under plane stress condition using FE methods. Neglecting the influence of pyroeffects, Ganesan *et al.* (2007) investigated the thermal coupled response of layered and multiphase MEE cylinder. Badri and Kayiem (2013) adopted the first order shear deformation theory to analyse the static and dynamic analysis of METE plates. Tauchert (1996) developed an exact solution for piezo thermoelastic problem subjected to steady state temperature distribution. Ootao and Tanigawa (2005) studied the effect of non-uniform unsteady heat supply on METE strip using exact solutions.

In thermal environment, the METE materials exhibit an additional coupling through the interaction of thermo-electric and thermo-magnetic fields. These are commonly termed as pyroelectric and pyromagnetic effects, respectively. Kim *et al.* (2011) considered functionally graded METE composites as prime material for investigation and computed the various product properties coupled with pyroelectric and pyromagnetic effects. The analysis of METE structures by considering pyroeffects (pyroelectric and pyromagnetic) and neglecting pyroeffects results in higher

discrepancies of the accuracy (Kondaiah *et al.*, 2013a). Hence, it is recommended to consider the effect of pyro coupling for optimum design of METE structures. Kondaiah *et al.* (2012) studied the static behaviour of MEE beams subjected to uniform temperature loads by considering pyroeffects. They extended their evaluation for MEE plates, cylindrical shells and sensor patch (Kondaiah *et al.*, 2013b, 2014, 2017).

1.6. ANALYSIS OF STRUCTURES IN HYGROTHERMAL ENVIRONMENT

1.6.1. Hygrothermo-piezoelectric structures

The clear understanding of coupled and uncoupled effects of electric, magnetic, moisture and temperature fields on the coupled response of multifield materials is of great significance due to their increased potential applications in the various working environments. Brischetto (2013) adopted Carrera's unified formulation to study the static hygrothermoelastic analysis of multilayered composite and sandwich shells. Smittakorn and Heyliger (2001, 2003) demonstrated a theoretical model to investigate the transient and steady state behaviour of adaptive wood made of piezoelectric material and validated it experimentally. Smittakorn and Heyliger (2000) presented discrete layer model to compute the hygrothermal nature of piezoelectric composites. The bending response of heterogeneous exponentially graded piezoelectric hollow cylinders was investigated by Zenkour (2014a, b; 2016a, b), Allam *et al.* (2014, 2016) and Dini and Abolbashari (2016). Raja *et al.* (2004a, b) demonstrated the active control of bending of hygro thermo piezoelectric flat and curved plates. Altay and Dokmeci (2000, 2007 and 2008) deduced variation principles in hygrothermo piezoelectricity.

1.6.2. Hygrothermo-magneto-electro-elastic (HTMEE) structures

Recently, few pioneers have attempted to analyse the effect of the hygrothermal fields on the structural analysis of MEE structures. Akbarzadeh and Chen (2012) proposed an analytical technique to evaluate the influence of external hygrothermal load on the magnetized hollow and solid MEE cylinders resting on elastic foundation. Later, Akbarzadeh and Pasini (2014) studied the coupled response of multilayered FGME cylinders subjected to hygrothermal loading. Saadatfar and Khafri (2014) carried out a similar analysis for FGME sphere resting on elastic foundation.

Akbarzadeh and Chen (2013) evaluated the hygrothermal stress developed in functionally graded piezoelectric media placed in the constant magnetic field.

1.7. FULLY COUPLED ANALYSIS OF MAGNETO-ELECTRO-THERMO-ELASTIC (METE) SOLIDS

The majority of the analysis of MEE structures in thermal environment considered the partial coupling of thermal field and multiphysics fields. However, an additional constitutive equation related to the entropy of the MEE system exists when full coupling between thermal and other multiphysics fields are considered. This unique characteristic of METE composite has attracted the attention of many researchers to exploit its benefits in engineering applications. Oh and Cho (2004) developed a three noded triangular finite element based on cubic zigzag plate theory to predict fully coupled behaviour of thermo-electro-elastic fields. Ahmad *et al.* (2006) derived a coupled electro-thermo-elastic equations from the fundamental principles of mass, linear momentum, angular momentum, energy and charge conservation. Perez-Fernandez *et al.* (2009) presented different types of constitutive relations of thermo-magneto-electro-elasticity using solid thermodynamics. Soh and Liu (2005) discussed the mathematical properties of the thermodynamic potentials and the relations between the material constants. Further, they also derived various forms of the constitutive equations of MEE solids with the thermodynamic potentials. More recently, Shi *et al.* (2017) exploited the principle of virtual work and Mindlin's plate theory to propose a fully coupled METE plate theory considering non-local and surface effects.

1.8. EFFECT OF ELECTRIC AND MAGNETIC LOADS ON MEE STRUCTURES

The inherent ferroelectric and ferromagnetic property of MEE materials make the structural analysis under the multi-fields loads such as electric and magnetic loads. Many investigators have dealt with analysing the effect of electric and magnetic load on MEE structures. Among them, Wang, Xu *et al.* (2010) analysed a MEE circular plates and demonstrated that the electric and magnetic boundary conditions significantly alter the electric or magnetic field distributions. Wu and Tsai (2007) employed asymptotic approach and computed the influence of electric displacement and magnetic flux on the bending response of doubly curved FGME shells. Wang *et al.* (2003) proposed a theoretical model to predict the instability of ferromagnetic

plates subjected to external thermal and magnetic fields. Vaezi *et al.* (2016) presented a numerical solution to analyse the influence of external electric and magnetic potentials on MEE microbeams. Zhao *et al.* (2017) proposed axisymmetric solutions to analyse multiferroic circular plates under the influence of electric displacement. Ebrahimi and Barati (2017f) used third order shear deformation theory and evaluated the dynamic behaviour of FGMEENANOBEBEAM exposed to external electric and magnetic potential.

1.9. SCOPE AND OBJECTIVE OF THE DISSERTATION

The comprehensive literature review highlights the importance and increasing interest of researchers in the field of design and analysis of MEE structures. However, the studies pertaining to the analysis of MEE structures under the different loading conditions such as thermal, hygrothermal, electric field and magnetic field are limited, even though the prominent applications of MEE structures are found in these harsh environments. Further, due to the pyroelectric and pyromagnetic coupling effects exhibited by the MEE materials in the thermal and hygrothermal environment, the characteristic coupled behaviour displays a deviation from that of the conventional approach (neglecting pyroeffects). Consequently, it is an important and challenging issue to consider the different coupling effects produced by various forms of temperature loads for the accurate design of MEE structures. The finite element method (FEM) has served as a major computational tool in estimating the multiphysics response of various smart structures including MEE structures. Moreover, it is believed that the FE approach reduces the computational efforts and provides accurate results in the analysis of MEE structures. Hence, the FE approach may be utilized to investigate the coupled static response of MEE structures in thermal and hygrothermal environments.

It is evident from the literature survey on the MEE structures that the different volume fractions of Barium Titanate and Cobalt Ferrite yields a different degree of coupling among magnetic, electric and elastic fields. In the thermal environment, the coupling sensitivity still increases due to pyroeffects and the adverse effects of mechanical loads are compensated by thermal stresses developed inherently. Considerable research on the static analysis of MEE structures in a thermal

environment with pyroeffects and without considering pyroeffects has been reported in the literature. However, the research on MEE structures subjected to different thermal loadings has not yet been reported. The static characteristics of stepped functionally graded magneto-electro-elastic (SFGMEE) structures may not be similar to that of multiphase MEE structures because of the different volume fraction of Barium Titanate and Cobalt Ferrite across the thickness of MEE structures. This motivated the present research to explore more on the coupled response of SFGMEE structures (plates and beams). The analytical evaluation of the influence of hygrothermo-magneto-electro-elastic (HTMEE) coupling on the multiphysics response of MEE cylinders and spheres has been reported in the open literature (Akbarzadeh and Chen, 2012, 2013; Akbarzadeh and Pasini, 2014; Saadatfar and Khafri, 2014). However, the quantum of research work related to HTMEE structures is available in scarce. In addition, HTMEE coupling effects for the MEE plates and beams and the FE analysis of the same has not yet been studied. This acts as a driving force to develop a FE formulation and evaluate the effect of hygrothermal loads on the variation of static parameters of MEE plates and beams.

Since, the MEE materials inherently possess the ferroelectric and ferromagnetic properties, it is very much important to evaluate the influence of external electric fields and magnetic fields on the direct (displacements, electric potential and magnetic potential) and derived (stresses, electric displacements and magnetic flux densities) quantities of MEE plate and beams. Also, the combined effects of various external field forces are not available in the literature and this provides further scope to fill the gap in the literature.

The prominent aim of this dissertation is to develop a three-dimensional finite element formulation to investigate the static behaviour of functionally graded and multiphase MEE beams and plates under different thermal environment. Further, to extend the evaluation for hygrothermo-magneto-electro-elastic beams and plates. In addition, the effect of different external loads such as thermal, electric, magnetic fields and the significant combination of loadings on the behaviour of FGMEE beams and plates needs to be analysed. In this regard, the following analyses have been carried out:

1. Static response analysis of stepped functionally graded magneto-electro-elastic beams subjected to various thermal environments.
2. Static behaviour of multiphase MEE beams under the influence of different in-plane temperature loads.
3. Static response analysis of stepped functionally graded magneto-electro-elastic plates under different thermal loads.
4. Hygrothermal analysis of MEE plates.
5. Finite element analysis of HTMEE behaviour of MEE beams.
6. Influence of external electric, magnetic and temperature loads on the multiphysics response of MEE plates.
7. Influence of particle arrangements of MEE material on the static response of magneto-electro-thermo-elastic (METE) plates

1.10. CONTRIBUTIONS FROM THE DISSERTATION

The following contributions have been made in the area of MEE structures in thermal and hygrothermal environment towards the preparation of the dissertation:

- Three-dimensional finite element formulation is derived to investigate the static parameters of stepped functionally graded, multiphase MEE beams and plates.
- Detailed analysis of MEE beams and plates is presented by considering the different in-plane and through thickness temperature profiles representing the various practical heat sources.
- A special emphasis has been placed on the investigation of the influence of pyroeffects and compare it with the conventional approach.
- Effect of hygrothermal loads on the multiphase MEE beams and plates are investigated.
- The influence of external field loads such as electric, magnetic and thermal loads are determined through the FE formulation derived.
- The influence of particle arrangement on the behaviour of MEE plates has been presented.

1.11. OVERVIEW OF THE DISSERTATION BY CHAPTER

The present dissertation is devoted to investigate the coupled behaviour of the MEE beams and plates under the influence of external fields such as thermal and hygrothermal loads using a finite element formulation. In this regard, the total potential energy principle along with linear coupled constitutive equations of MEE material in thermal and hygrothermal environment have been used separately to derive the governing equations of motion. An emphasize has been placed on evaluating the effects of different thermal loads, pyroelectric and pyromagnetic coupling, hygrothermal loads, geometrical parameters (boundary conditions, aspect ratios, length-to-width ratio) etc.

This thesis has been divided into nine chapters. In the first chapter, a brief introduction and a comprehensive literature review on the smart materials, MEE materials, MEE structures, MEE behaviour in thermal environment, HTMEE analysis of MEE structures have been presented. Subsequently, the scope of the present research is identified and the objectives of the present research have been defined.

In Chapter 2, a detailed derivation of FE formulation accounting for the static response of stepped functionally graded magneto-electro-elastic beams under various thermal load profiles has been presented. Each layer of the SFGMEE beam is made of different volume fraction of Barium Titanate and Cobalt Ferrite. The effect of pyroelectric and pyromagnetic coupling associated with different thermal load distribution has been analysed in detail. In addition, the predominant influences of stacking sequences, different beam regions on the static parameters are also evaluated.

Chapter 3 is concerned with the evaluation of the static studies of multiphase MEE beam under the influence of different in-plane thermal loads. The influence of various boundary conditions, different volume fraction of Barium Titanate and Cobalt Ferrite on the displacement components, potentials, stresses, electric displacements and magnetic flux densities are investigated. In addition, the effect of product properties, aspect ratio on the behaviour of multiphase MEE beam has also been computed using FE formulation.

Chapter 4 extends the FE formulation for SFGMEE plates analogous to SFGMEE beams discussed in Chapter 2. A comparative study is presented for SFG-BFB and SFG-FBF stacking sequences with respect to the direct and derived quantities of the SFGMEE plate. Influence of pyroeffects, stacking sequence, geometrical parameters such as boundary conditions, aspect ratio, length-to-width ratio has been studied thoroughly.

Chapter 5 addresses the hygrothermo-magneto-electro-elastic (HTMEE) analysis of MEE plates. The FE formulation derived in chapter 2 has been extended to consider the influence of moisture effect also. The temperature and moisture dependent elastic stiffness coefficients are considered for the analysis and the significant value of the empirical constants are computed.

The effect of moisture and temperature loads on the multiphysics response of HTMEE beams has been studied in Chapter 6. The adaptive wood made of Barium Titanate and Cobalt Ferrite has been used as the material for the analysis. Independent effect of moisture and thermal loads has been studied. Also, the most significant combination of empirical constants is predicted with the aid of FE formulation.

In Chapter 7, the predominant influence of external field forces such as thermal, magnetic, electric and their combined effects on SFGMEE plates have been evaluated. The kinematics of deformation of SFGMEE plate is described by the first order shear deformation theory (FSDT). The effect of geometrical parameters has also been studied in detail.

Chapter 8 encapsulates the effect of different particle arrangement of BaTiO_3 and CoFe_2O_4 such as body centered cubic structure, face centered cubic structure and simple cubic structure on the static characteristics of magneto-electro-thermo-elastic plates. The influence of the pyroelectric and pyromagnetic coupling effects associated with each form of particle arrangement has been assessed in detail.

At last, Chapter 9 encapsulates the major findings of the dissertation and the future possible work for the improvement in the possible application of MEE structures has been outlined. The list of references and appendices are shown at the end of dissertation.

Chapter 2

STATIC RESPONSE OF STEPPED FUNCTIONALLY GRADED MAGNETO-ELECTRO-ELASTIC BEAM IN THERMAL ENVIRONMENT

This chapter deals with analysing the variation of static parameters across the thickness of stepped functionally graded magneto-electro-elastic (SFGMEE) beams under different thermal environments. Each layer of the SFGMEE beam is constituted of the material properties corresponding to a different volume fraction of Barium Titanate and Cobalt Ferrite. Further, a special attention has been devoted to evaluate the effect of product properties (pyroelectric and pyromagnetic coupling), boundary conditions and aspect ratio on the direct (displacements, electric potential and magnetic potential) and derived quantities (stresses, electric displacements, and magnetic flux densities) of the SFGMEE beam. A parametric study is also carried out to evaluate the effect of stacking sequence, pyro coupling and the different SFGMEE beam regions.

Related article: Vinyas, M. and Kattimani, S. C. (2017), “Static studies of stepped functionally graded magneto-electro-elastic beam subjected to different thermal loads”, *Composite Structures*, **163**, 216-237.

2.1. INTRODUCTION

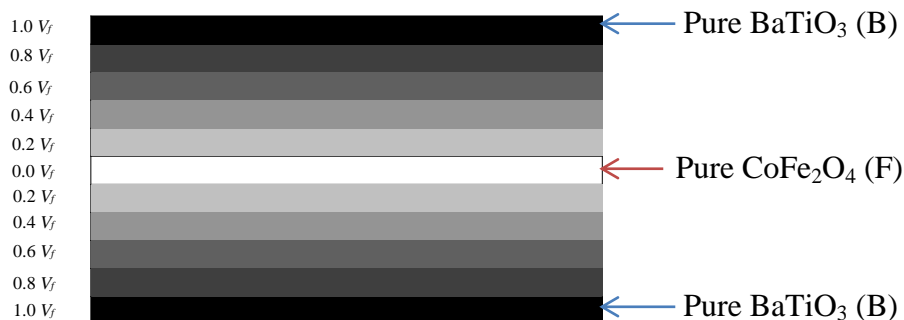
The coupled response of stepped functionally graded magneto-electro-elastic (SFGMEE) structures (beams and plates) stacked with the different volume fraction of Barium Titanate (BaTiO_3) and Cobalt Ferrite (CoFe_2O_4) exhibit a unique behaviour. Hence, it demands special attention while designing smart structures comprised of MEE materials. In the thermal environment, the MEE materials exhibit coupling between thermo-electric and thermo-magnetic fields and are termed as pyroelectric and pyromagnetic effects, respectively. These are commonly called as pyroeffects, whose influence on the MEE structures is observed through the pyroelectric load and

the pyromagnetic load. These product properties influence the potentials directly, and the displacements indirectly (Kondaiah *et al.* 2012).

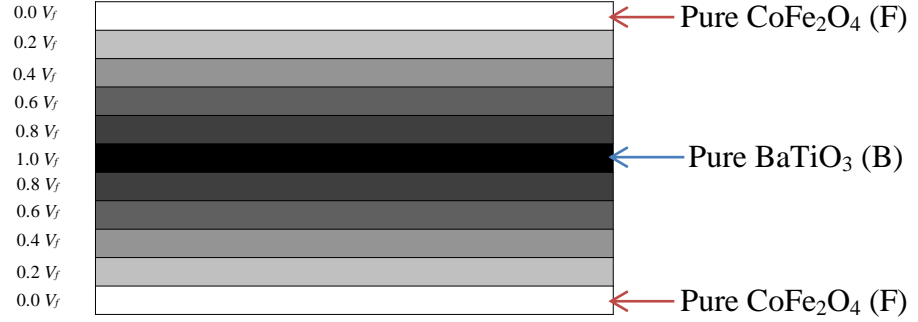
In this chapter, static analysis has been carried out using the three-dimensional finite element formulation derived with the aid of the total potential energy principle and constitutive equations of MEE material, considering the coupling effects. Further, a special attention has been placed to study the influence of pyroeffects on the behaviour of SFGMEE beams. The influence of stacking sequence and different SFGMEE beam regions has also been investigated.

2.2. STEPPED FUNCTIONALLY GRADED MAGNETO-ELECTRO-ELASTIC STACKING ARRANGEMENT

A schematic representation of the SFGMEE stacking arrangement of the beam/plate is shown in Fig. 2.1. Each layer of SFGMEE beam/plate is considered to be made of different volume fraction of BaTiO₃ and CoFe₂O₄ materials. For the convenience, the volume fractions of the materials are varied in steps of 0.2 (20% BaTiO₃). The most commonly used stacking sequences namely, SFG-BFB and SFG-FBF are considered for the analysis. Here, ‘B’ corresponds to pure piezoelectric phase while ‘F’ represents pure piezomagnetic phase. In case of SFG-BFB stacking sequence, the top and bottom layers are made of pure piezoelectric (PE) phase with $V_f = 1.0$ and the volume fraction of the consecutive layers is varied in steps of $V_f = 0.2$ from both the ends to attain pure piezomagnetic (PM) phase at the middle layer as shown in Fig. 2.1(a). On the other hand, by replacing the pure PE phase by the pure PM phase, SFG-FBF stacking sequence is obtained. In which, the top and bottom layers are pure PM phase and the volume fraction of the consecutive layers is increased by 0.2 to attain pure PE phase at the middle layer as depicted in Fig. 2.1(b).



(a)



(b)

Figure 2.1: Stepped functionally graded (SFG) (a) BFB (b) FBF stacking sequence

2.3. PROBLEM DESCRIPTION

The geometrical description of SFGMEE beam with FBF stacking sequence is illustrated in Fig. 2.2. The beam length a is assumed along the x -axis of Cartesian coordinate system. The width w and the thickness h of the SFGMEE beam are considered along the y - and z -coordinates, respectively. The boundary conditions employed for the cantilever SFGMEE beam are given as follows:

$$U_x = U_v = U_w = \phi = \psi = 0 \text{ at } x = 0 \quad (2.1)$$

$$U_x = U_v = U_w = \phi = \psi \neq 0 \text{ at } x = a \quad (2.2)$$

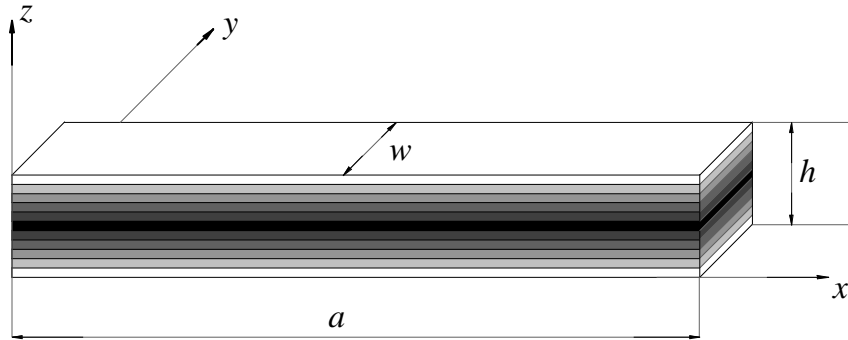


Figure 2.2: Schematic representation of SFGMEE beam

2.4. CONSTITUTIVE EQUATIONS

The linearly coupled constitutive relations for the SFGMEE solid considering thermal effects are given by

$$\{\sigma^k\} = [C_{V_f}^k] \{\varepsilon^k\} - [e_{V_f}^k] \{E^k\} - [q_{V_f}^k] \{H^k\} - [C_{V_f}^k] \{\alpha_{V_f}^k\} \Delta T \quad (2.3)$$

$$\{D^k\} = [e_{V_f}^k]^T \{\varepsilon^k\} + [\eta_{V_f}^k] \{E^k\} + [m_{V_f}^k] \{H^k\} + \{p_{V_f}^k\} \Delta T \quad (2.4)$$

$$\{B^k\} = [q_{V_f}^k]^T \{\varepsilon^k\} + [m_{V_f}^k] \{E^k\} + [\mu_{V_f}^k] \{H^k\} + \{\tau_{V_f}^k\} \Delta T \quad (2.5)$$

where, $[C_{V_f}^k]$, $[e_{V_f}^k]$, $[q_{V_f}^k]$, and $\{\alpha_{V_f}^k\}$ are the elastic co-efficient matrix, the piezoelectric coefficient matrix, the magnetostrictive coefficient matrix and the thermal expansion co-efficient matrix, respectively; $[\eta_{V_f}^k]$, $[m_{V_f}^k]$, $\{p_{V_f}^k\}$, $\{\tau_{V_f}^k\}$ and $[\mu_{V_f}^k]$ are the dielectric constant, electromagnetic coefficient, pyroelectric constant, pyromagnetic constant and the magnetic permeability constant, respectively; $\{\sigma^k\}$, $\{D^k\}$ and $\{B^k\}$, represent the stress tensor, electric displacement and the magnetic flux, respectively; $\{\varepsilon^k\}$, $\{E^k\}$, $\{H^k\}$ and ΔT are the linear strain tensor, electric field, magnetic field and temperature rise from a stress free state, respectively. Meanwhile, the term k represents the layer number and the subscript V_f denotes the volume fraction of Barium Titanate (BaTiO_3) and Cobalt Ferrite (CoFe_2O_4) corresponding to the k^{th} layer of SFGMEE beams /plates.

2.5. FINITE ELEMENT FORMULATION

The finite element model of the SFGMEE beam is generated using eight noded brick element. Each node is assumed to have five degrees of freedom corresponding to the displacement components, electric potential and magnetic potential. Through the shape functions $[N_t]$, $[N_\phi]$ and $[N_\psi]$, the generalized displacement vector $\{d_t\}$, the electric potential vector $\{\phi\}$ and the magnetic potential vector $\{\psi\}$ are expressed in terms of the nodal generalized displacement vector $\{d_t^e\}$, the nodal electric potential vector $\{\phi^e\}$ and the nodal magnetic potential vector $\{\psi^e\}$, respectively, as follows:

$$\{d_t\} = [N_t] \{d_t^e\}, \quad \{\phi\} = [N_\phi] \{\phi^e\}, \quad \{\psi\} = [N_\psi] \{\psi^e\} \quad (2.6)$$

in which,

$$\begin{aligned} \{d_t^e\} &= \left[\{d_{t1}\}^T \{d_{t2}\}^T \dots \{d_{t8}\}^T \right]^T, \quad \{\phi^e\} = [\phi_1 \ \phi_2 \ \dots \ \phi_8]^T, \quad \{\psi^e\} = [\psi_1 \ \psi_2 \ \dots \ \psi_8]^T, \\ [N_t] &= [N_{t1} \ N_{t2} \ \dots \ N_{t8}], \quad N_{ti} = n_i I_t, \quad [N_\phi] = [N_\psi] = [n_1 \ n_2 \ \dots \ n_8] \end{aligned} \quad (2.7)$$

where, n_i is the natural coordinate shape function associated with the i^{th} node of the element; I_t is the identity matrix; The size of the shape functions $[N_t]$, $[N_\phi]$ and $[N_\psi]$ are (3×24) , (1×8) and (1×8) shape function matrices, respectively. Making use of Maxwell's fundamental electrostatic equations, the linear relation between the electric field and the electric potential can be expressed as

$$\{E\} = \left\{ -\frac{\partial\phi}{\partial x}, -\frac{\partial\phi}{\partial y}, -\frac{\partial\phi}{\partial z} \right\} \quad (2.8)$$

Similarly, the magnetic field and the magnetic potential is related as

$$\{H\} = \left\{ -\frac{\partial\psi}{\partial x}, -\frac{\partial\psi}{\partial y}, -\frac{\partial\psi}{\partial z} \right\} \quad (2.9)$$

Using the derivative of shape function matrices, the strain vector, electric field vector and the magnetic field vector of the system are expressed in terms of the nodal displacements, nodal electric potential and nodal magnetic potential, respectively, as follows:

$$\begin{aligned} \{\varepsilon\} &= L_t \{d_t\} = [L_t N_t] \{d_t^e\} = [B_t] \{d_t^e\}, \quad \{H\} = L_\psi \{\psi\} = [L_\psi N_\psi] \{\psi^e\} = [B_\psi] \{\psi^e\}, \\ \{E\} &= L_\phi \{\phi\} = [L_\phi N_\phi] \{\phi^e\} = [B_\phi] \{\phi^e\} \end{aligned} \quad (2.10)$$

where, L_t , L_ψ and L_ϕ are the differential operators, and the sub matrices $[B_t]$, $[B_\psi]$ and $[B_\phi]$ can be expressed as follows:

$$[B_{ti}] = \begin{bmatrix} \frac{\partial n_i}{\partial x} & 0 & 0 \\ 0 & \frac{\partial n_i}{\partial y} & 0 \\ 0 & 0 & \frac{\partial n_i}{\partial z} \\ 0 & \frac{\partial n_i}{\partial z} & \frac{\partial n_i}{\partial y} \\ \frac{\partial n_i}{\partial z} & 0 & \frac{\partial n_i}{\partial x} \\ \frac{\partial n_i}{\partial y} & \frac{\partial n_i}{\partial x} & 0 \end{bmatrix}, \quad [B_{\psi i}] = \begin{bmatrix} -\frac{\partial n_i}{\partial x} \\ -\frac{\partial n_i}{\partial y} \\ -\frac{\partial n_i}{\partial z} \end{bmatrix}, \quad [B_{\phi i}] = \begin{bmatrix} -\frac{\partial n_i}{\partial x} \\ -\frac{\partial n_i}{\partial y} \\ -\frac{\partial n_i}{\partial z} \end{bmatrix} \quad (2.11)$$

where, $i = 1, 2, 3, \dots, 8$ represents the node number

2.6. EQUATIONS OF MOTION

The principle of total potential energy is invoked to derive the governing equations of the SFGMEE beam in the thermal environment as follows:

$$\begin{aligned}
T_p = & \frac{1}{2} \sum_{k=1}^N \int_{\Omega^k} \{\varepsilon^k\}^T \{\sigma^k\} d\Omega^k - \frac{1}{2} \sum_{k=1}^N \int_{\Omega^k} [E^k]^T \{D^k\} d\Omega^k - \frac{1}{2} \sum_{k=1}^N \int_{\Omega^k} [H^k]^T \{B^k\} d\Omega^k \\
& - \int_A \{d_t\}^T \{F_{surface}\} dA - \int_{\Omega^k} \{d_t\}^T \{F_{body}\} d\Omega^k - \{d_t\}^T \{F_{conc}\} \\
& - \int_A \phi Q^\phi dA - \int_A \psi Q^\psi dA
\end{aligned} \tag{2.12}$$

where, $k = 1, 2, 3, \dots, N$ represents the number of layers and Ω^k denotes the volume of the k^{th} layer. $\{F_{surface}\}$ is the surface force acting over the area A of the layer, $\{F_{body}\}$ is the body force and $\{F_{conc}\}$ is the point load acting at any particular point on the plate. Further, Q^ϕ and Q^ψ represent the surface electric charge density and magnetic charge density, respectively.

The total potential energy is minimized by setting the first variation of Eq. (2.12) to zero

$$\begin{aligned}
T_p = & \frac{1}{2} \sum_{k=1}^N \int_{\Omega^k} \delta \{\varepsilon^k\}^T \{\sigma^k\} d\Omega^k - \frac{1}{2} \sum_{k=1}^N \int_{\Omega^k} \delta [E^k]^T \{D^k\} d\Omega^k - \frac{1}{2} \sum_{k=1}^N \int_{\Omega^k} \delta [H^k]^T \{B^k\} d\Omega^k \\
& - \int_A \delta \{d_t\}^T \{F_{surface}\} dA - \int_{\Omega^k} \delta \{d_t\}^T \{F_{body}\} d\Omega^k \\
& - \delta \{d_t\}^T \{F_{conc}\} - \int_A \delta \phi Q^\phi dA - \int_A \delta \psi Q^\psi dA = 0
\end{aligned} \tag{2.13}$$

By substituting Eqs. (2.3), (2.4) and (2.5) into Eq.(2.13), we obtain

$$\begin{aligned}
T_p^e = & \frac{1}{2} \sum_{k=1}^N \int_{\Omega^k} \delta \{\varepsilon^k\}^T [C_{V_f}^k] \{\varepsilon^k\} d\Omega^k - \frac{1}{2} \sum_{k=1}^N \int_{\Omega^k} \delta \{\varepsilon^k\}^T [e_{V_f}^k] \{E^k\} d\Omega^k \\
& - \frac{1}{2} \sum_{k=1}^N \int_{\Omega^k} \delta \{\varepsilon^k\}^T [q_{V_f}^k] \{H^k\} d\Omega^k - \frac{1}{2} \sum_{k=1}^N \int_{\Omega^k} \delta \{\varepsilon^k\}^T [C_{V_f}^k] \{\alpha_{V_f}^k\} \Delta T d\Omega^k \\
& - \frac{1}{2} \sum_{k=1}^N \int_{\Omega^k} \delta \{E^k\}^T [e_{V_f}^k]^T \{\varepsilon^k\} d\Omega^k - \frac{1}{2} \sum_{k=1}^N \int_{\Omega^k} \delta \{E^k\}^T [\eta_{V_f}^k] \{E^k\} d\Omega^k
\end{aligned}$$

$$\begin{aligned}
& -\frac{1}{2} \sum_{k=1}^N \int_{\Omega^k} \delta \{E^k\}^T [m_{V_f}^k] \{H^k\} d\Omega^k - \frac{1}{2} \sum_{k=1}^N \int_{\Omega^k} \delta \{E^k\}^T \{p_{V_f}^k\} \Delta T d\Omega^k \\
& -\frac{1}{2} \sum_{k=1}^N \int_{\Omega^k} \delta \{H^k\}^T [q_{V_f}^k]^T \{\varepsilon^k\} d\Omega^k - \frac{1}{2} \sum_{k=1}^N \int_{\Omega^k} \delta \{H^k\}^T [m_{V_f}^k] \{E^k\} d\Omega^k \\
& -\frac{1}{2} \sum_{k=1}^N \int_{\Omega^k} \delta \{H^k\}^T [\mu_{V_f}^k] \{H^k\} d\Omega^k - \frac{1}{2} \sum_{k=1}^N \int_{\Omega^k} \delta \{H^k\}^T \{\tau_{V_f}^k\} \Delta T d\Omega^k \\
& - \int_A \delta \{d_t\}^T \{F_{surface}\} dA - \int_{\Omega^k} \delta \{d_t\}^T \{F_{body}\} d\Omega^k - \delta \{d_t\}^T \{F_{conc}\} \\
& - \int_A \delta \{\phi\} Q^\phi dA - \int_A \delta \{\psi\} Q^\psi dA \tag{2.14}
\end{aligned}$$

substituting Eq. (2.10) into Eq. (2.14), we get

$$\begin{aligned}
T_p^e &= \frac{1}{2} \sum_{k=1}^N \int_{\Omega^k} \delta \{d_t^e\}^T [B_t]^T [C_{V_f}^k] [B_t] \{d_t^e\} d\Omega^k - \frac{1}{2} \sum_{k=1}^N \int_{\Omega^k} \delta \{d_t^e\}^T [B_t]^T [e_{V_f}^k] [B_\phi] \{\phi^e\} d\Omega^k \\
& - \frac{1}{2} \sum_{k=1}^N \int_{\Omega^k} \delta \{d_t^e\}^T [B_t]^T [q_{V_f}^k] [B_\psi] \{\psi^e\} d\Omega^k - \frac{1}{2} \sum_{k=1}^N \int_{\Omega^k} \delta \{d_t^e\}^T [B_t]^T [C_{V_f}^k] \{\alpha_{V_f}^k\} \Delta T d\Omega^k \\
& - \frac{1}{2} \sum_{k=1}^N \int_{\Omega^k} \delta \{\phi^e\}^T [B_\phi]^T [e_{V_f}^k]^T [B_t] \{d_t^e\} d\Omega^k - \frac{1}{2} \sum_{k=1}^N \int_{\Omega^k} \delta \{\phi^e\}^T [B_\phi]^T [\eta_{V_f}^k] [B_\phi] \{\phi^e\} d\Omega^k \\
& - \frac{1}{2} \sum_{k=1}^N \int_{\Omega^k} \delta \{\phi^e\}^T [B_\phi]^T [m_{V_f}^k] [B_\psi] \{\psi^e\} d\Omega^k - \frac{1}{2} \sum_{k=1}^N \int_{\Omega^k} \delta \{\phi^e\}^T [B_\phi]^T \{p_{V_f}^k\} \Delta T d\Omega^k \\
& - \frac{1}{2} \sum_{k=1}^N \int_{\Omega^k} \delta \{\psi^e\}^T [B_\psi]^T [q_{V_f}^k]^T [B_t] \{d_t^e\} d\Omega^k - \frac{1}{2} \sum_{k=1}^N \int_{\Omega^k} \delta \{\psi^e\}^T [B_\psi]^T [m_{V_f}^k] [B_\phi] \{\phi^e\} d\Omega^k \\
& - \frac{1}{2} \sum_{k=1}^N \int_{\Omega^k} \delta \{\psi^e\}^T [B_\psi]^T [\mu_{V_f}^k] [B_\psi] \{\psi^e\} d\Omega^k - \frac{1}{2} \sum_{k=1}^N \int_{\Omega^k} \delta \{\psi^e\}^T [B_\psi]^T \{\tau_{V_f}^k\} \Delta T d\Omega^k \\
& - \int_A \delta \{d_t^e\}^T [N_t]^T \{F_{surface}\} dA - \frac{1}{2} \sum_{k=1}^N \int_{\Omega^k} \delta \{d_t^e\}^T [N_t]^T \{F_{body}\} d\Omega^k \\
& - \delta \{d_t^e\}^T [N_t]^T \{F_{conc}\} - \int_A \delta \{\phi^e\} [N_\phi] Q^\phi dA - \int_A \delta \{\psi^e\} [N_\psi] Q^\psi dA = 0 \tag{2.15}
\end{aligned}$$

Further, bifurcating the terms based on the coefficients of $\{d_t^e\}^T$, $\{\phi^e\}^T$ and $\{\psi^e\}^T$ and globalizing, we obtain the equations of motion as follows:

$$\left[K_{tt}^g \right] \{d_t\} + \left[K_{t\phi}^g \right] \{\phi\} + \left[K_{t\psi}^g \right] \{\psi\} = \{F_m^g\} + \{F_{th}^g\} \quad (2.16)$$

$$\left[K_{t\phi}^g \right]^T \{d_t\} - \left[K_{\phi\phi}^g \right] \{\phi\} - \left[K_{\phi\psi}^g \right] \{\psi\} = \{F_\phi^g\} - \{F_{p.e}^g\} \quad (2.17)$$

$$\left[K_{t\psi}^g \right]^T \{d_t\} - \left[K_{\phi\psi}^g \right]^T \{\phi\} - \left[K_{\psi\psi}^g \right] \{\psi\} = \{F_\psi^g\} - \{F_{p.m}^g\} \quad (2.18)$$

in which, $[K_{tt}^g]$, $[K_{t\phi}^g]$, $[K_{t\psi}^g]$, $[K_{\phi\phi}^g]$, $[K_{\psi\psi}^g]$, $[K_{\phi\psi}^g]$ are the global elastic stiffness matrix, the electro-elastic coupling stiffness matrix, magneto-elastic coupling stiffness matrix, electric stiffness matrix, magnetic stiffness, electro-magnetic stiffness matrix, respectively. The various global load vectors are the global mechanical load vector $\{F_m^g\}$, the global thermal load vector $\{F_{th}^g\}$, the global electric charge load vector $\{F_\phi^g\}$, the global magnetic current load vector $\{F_\psi^g\}$, the global pyroelectric load vector $\{F_{p.e}^g\}$ and the global pyromagnetic load vector $\{F_{p.m}^g\}$.

The explicit elemental forms of these matrices appearing in Eqs (2.16) – (2.18) are given as follows:

$$\begin{aligned} \left[K_{tt}^e \right] &= \sum_{k=1}^N \left\{ \int_{\Omega^k} [B_t]^T [C_{V_f}^k] [B_t] d\Omega^k \right\}, \quad \left[K_{t\phi}^e \right] = \sum_{k=1}^N \left\{ \int_{\Omega^k} [B_t]^T [e_{V_f}^k] [B_\phi] d\Omega^k \right\}, \\ \left[K_{t\psi}^e \right] &= \sum_{k=1}^N \left\{ \int_{\Omega^k} [B_t]^T [q_{V_f}^k] [B_\psi] d\Omega^k \right\}, \quad \left[K_{\phi\phi}^e \right] = \sum_{k=1}^N \left\{ \int_{\Omega^k} [B_\phi]^T [\eta_{V_f}^k] [B_\phi] d\Omega^k \right\}, \\ \left[K_{\phi\psi}^e \right] &= \sum_{k=1}^N \left\{ \int_{\Omega^k} [B_\phi]^T [m_{V_f}^k] [B_\psi] d\Omega^k \right\}, \quad \left[K_{\psi\psi}^e \right] = \sum_{k=1}^N \left\{ \int_{\Omega^k} [B_\psi]^T [\mu_{V_f}^k] [B_\psi] d\Omega^k \right\} \end{aligned} \quad (2.19)$$

The different load vectors are given by

$$\begin{aligned} \{F_m^e\} &= \int_{\Omega^k} [N_t]^T F_{body} d\Omega^k + \int_A [N_t]^T F_{surface} dA + [N_t]^T F_{conc}, \\ \{F_\phi^e\} &= \int_A [N_\phi]^T Q^\phi dA, \\ \{F_\psi^e\} &= \int_A [N_\psi]^T Q^\Psi dA, \quad \{F_{th}^e\} = \sum_{k=1}^N \left\{ \int_{\Omega^k} [B_t]^T [C_{V_f}^k] \{\alpha_{V_f}^k\} \Delta T d\Omega^k \right\}, \\ \{F_{p.e}^e\} &= \sum_{k=1}^N \left\{ \int_{\Omega^k} [B_\phi]^T \{p_{V_f}^k\} \Delta T d\Omega^k \right\}, \quad \{F_{p.m}^e\} = \sum_{k=1}^N \left\{ \int_{\Omega^k} [B_\psi]^T \{\tau_{V_f}^k\} \Delta T d\Omega^k \right\} \end{aligned} \quad (2.20)$$

In the present chapter, the effect of $\{F_m^g\}$, $\{F_\phi^g\}$ and $\{F_\psi^g\}$ are not considered for the analysis. Consequently, the Eqs. (2.16) – (2.18) can be written as

$$\left[K_{tt}^g \right] \{d_t\} + \left[K_{t\phi}^g \right] \{\phi\} + \left[K_{t\psi}^g \right] \{\psi\} = \{F_{th}^g\} \quad (2.21)$$

$$\left[K_{t\phi}^g \right]^T \{d_t\} - \left[K_{\phi\phi}^g \right] \{\phi\} - \left[K_{\phi\psi}^g \right] \{\psi\} = \{F_{p.e}^g\} \quad (2.22)$$

$$\left[K_{t\psi}^g \right]^T \{d_t\} - \left[K_{\phi\psi}^g \right]^T \{\phi\} - \left[K_{\psi\psi}^g \right] \{\psi\} = \{F_{p.m}^g\} \quad (2.23)$$

Using the standard condensation procedure, the nodal thermal displacements, the electric potentials, and the magnetic potentials are computed from Eqs. (2.21) – (2.23) as follows:

Considering the Eq. (2.23) and solving for $\{\psi\}$, we obtain

$$\{\psi\} = \left[K_{\psi\psi}^g \right]^{-1} \left[K_{t\psi}^g \right]^T \{d_t\} - \left[K_{\psi\psi}^g \right]^{-1} \left[K_{\phi\psi}^g \right]^T \{\phi\} - \left[K_{\psi\psi}^g \right]^{-1} \{F_{p.m}^g\} \quad (2.24)$$

Substituting Eq. (2.24) in Eq. (2.22) and solving for $\{\phi\}$, we get

$$\begin{aligned} & \left[K_{t\phi}^g \right]^T \{d_t\} - \left[K_{\phi\phi}^g \right] \{\phi\} - \left[K_{\phi\psi}^g \right] \left[K_{\psi\psi}^g \right]^{-1} \left[K_{t\psi}^g \right]^T \{d_t\} + \left[K_{\phi\psi}^g \right] \left[K_{\psi\psi}^g \right]^{-1} \left[K_{\phi\psi}^g \right]^T \{\phi\} + \\ & \left[K_{\phi\psi}^g \right] \left[K_{\psi\psi}^g \right]^{-1} \{F_{p.m}^g\} = \{F_{p.e}^g\} \\ & \{d_t\} \left[\left[K_{t\phi}^g \right]^T - \left[K_{\phi\psi}^g \right] \left[K_{\psi\psi}^g \right]^{-1} \left[K_{t\psi}^g \right]^T \right] - \{\phi\} \left[\left[K_{\phi\phi}^g \right] - \left[K_{\phi\psi}^g \right] \left[K_{\psi\psi}^g \right]^{-1} \left[K_{\phi\psi}^g \right]^T \right] + \\ & \left[K_{\phi\psi}^g \right] \left[K_{\psi\psi}^g \right]^{-1} \{F_{p.m}^g\} = \{F_{p.e}^g\} \\ & \left[K_1 \right] \{d_t\} - \left[K_2 \right] \{\phi\} = \{F_{p.e}^g\} - \left[K_{\phi\psi}^g \right] \left[K_{\psi\psi}^g \right]^{-1} \{F_{p.m}^g\} \\ & \left[K_1 \right] \{d_t\} - \left[K_2 \right] \{\phi\} = \{F_{\phi_sol}\} \\ & \{\phi\} = \left[K_2 \right]^{-1} \left[K_1 \right] \{d_t\} - \left[K_2 \right]^{-1} \{F_{\phi_sol}\} \end{aligned} \quad (2.25)$$

Further, on substituting Eqs. (2.24) and (2.25) in Eq. (2.21), we obtain

$$\begin{aligned} & \left[K_{tt}^g \right] \{d_t\} + \left[K_{t\phi}^g \right] \{\phi\} + \left[K_{t\psi}^g \right] \left[K_{\psi\psi}^g \right]^{-1} \left[K_{t\psi}^g \right]^T \{d_t\} - \\ & \left[K_{t\psi}^g \right] \left[K_{\psi\psi}^g \right]^{-1} \left[K_{\phi\psi}^g \right]^T \{\phi\} - \left[K_{t\psi}^g \right] \left[K_{\psi\psi}^g \right]^{-1} \{F_{p.m}^g\} = \{F_{th}^g\} \\ & \{d_t\} \left[\left[K_{tt}^g \right] + \left[K_{t\psi}^g \right] \left[K_{\psi\psi}^g \right]^{-1} \left[K_{t\psi}^g \right]^T \right] + \{\phi\} \left[\left[K_{t\phi}^g \right] - \left[K_{t\psi}^g \right] \left[K_{\psi\psi}^g \right]^{-1} \left[K_{\phi\psi}^g \right]^T \right] - \end{aligned}$$

$$\begin{aligned}
& [K_{t\psi}^g][K_{\psi\psi}^g]^{-1}\{F_{p,m}^g\} = \{F_{th}^g\} \\
& [K_5]\{d_t\} + [K_6]\{\phi\} - [K_{t\psi}^g][K_{\psi\psi}^g]^{-1}\{F_{p,m}^g\} = \{F_{th}^g\} \\
& [K_5]\{d_t\} + [K_6][K_3]\{d_t\} - [K_2]^{-1}\{F_{\phi_sol}\} - [K_{t\psi}^g][K_{\psi\psi}^g]^{-1}\{F_{p,m}^g\} = \{F_{th}^g\} \\
& [K_5] + [K_6][K_3]\{d_t\} - [K_6][K_2]^{-1}\{F_{p,e}^g\} + \\
& [K_6][K_4] - [K_{t\psi}^g][K_{\psi\psi}^g]^{-1}\}\{F_{p,m}^g\} = \{F_{th}^g\} \\
& [K_7]\{d_t\} = [K_6][K_2]^{-1}\{F_{p,e}^g\} + [K_{t\psi}^g][K_{\psi\psi}^g]^{-1} - [K_6][K_4]\}\{F_{p,m}^g\} + \{F_{th}^g\} \\
& [K_7]\{d_t\} = [K_8]\{F_{p,e}^g\} + [K_9]\{F_{p,m}^g\} + \{F_{th}^g\} \\
& [K_{eq}]\{d_t\} = \{F_{eq}\} \tag{2.26}
\end{aligned}$$

The component matrices and the equivalent force vectors constituting the Eqs. (2.25) and (2.26) are as follows:

$$\begin{aligned}
& [K_1] = [K_{\phi t}^g] - [K_{\psi\phi}^g][K_{\psi\psi}^g]^{-1}[K_{\psi t}^g], [K_2] = [K_{\phi\phi}^g] - [K_{\psi\phi}^g][K_{\psi\psi}^g]^{-1}[K_{\phi\psi}^g] \\
& [K_3] = [K_2]^{-1}[K_1], [K_4] = [K_2]^{-1}[K_{\psi\phi}^g][K_{\psi\psi}^g]^{-1}, \\
& [K_5] = [K_{tt}^g] + [K_{t\psi}^g][K_{\psi\psi}^g]^{-1}[K_{\psi t}^g], [K_6] = [K_{t\phi}^g] - [K_{t\psi}^g][K_{\psi\psi}^g]^{-1}[K_{\phi\psi}^g], \\
& [K_7] = [K_5] + [K_6][K_3], [K_8] = [K_6][K_2]^{-1}, [K_9] = [K_{t\psi}^g][K_{\psi\psi}^g]^{-1} - [K_6][K_4], \\
& [K_{eq}] = [K_7], [K_{1-\psi}] = [K_{\psi t}^g] - [K_{\psi\phi}^g][K_3], \\
& [K_{2-\psi}] = [K_{\psi\psi}^g]^{-1}[K_{\psi\phi}^g][K_2]^{-1}, \\
& [K_{3-\psi}] = [K_{\psi\psi}^g]^{-1}[K_{\psi\phi}^g][K_2]^{-1}[K_{\psi\phi}^g]^T[K_{\psi\psi}^g]^{-1} + [K_{\psi\psi}^g]^{-1}, \\
& \{F_{eq}\} = [K_9]\{F_{p,m}^g\} + [K_8]\{F_{p,e}^g\} + \{F_{th}^g\}, \\
& \{F_{eq}\} = [K_9]\{F_{p,m}^g\} + [K_8]\{F_{p,e}^g\} + \{F_{th}^g\}, \\
& \{F_{\phi_sol}\} = \{F_{p,e}^g\} - [K_{\psi\phi}^g]^T[K_{\psi\psi}^g]^{-1}\{F_{p,m}^g\} \tag{2.27}
\end{aligned}$$

2.7. TEMPERATURE PROFILES

The nature of temperature distributions may affect significantly on the static performance of SFGMEE structures. The different forms of temperature distribution

can be treated as an outcome of the presence of heat source at various operating positions. The resulting temperature profiles can be approximated and represented in the form of mathematical expressions. The present analysis considers the different in-plane and through thickness varying temperature profiles which can be encapsulated as follows:

2.7.1. In-plane temperature profiles

The in-plane temperature profiles are assumed to vary along the beam length and can be treated as one dimensional temperature profiles. The general equations for each form of temperature distributions can be shown as follows:

➤ *Uniform temperature profile*

The temperature of the SFGMEE beam is uniformly raised from a stress free temperature T_0 to the final temperature T_{max} . For the ease of calculation, T_0 is assumed to be 0 K. The general temperature variation relation can be written as

$$\Delta T = T_{max} - T_0 \quad (2.28)$$

➤ *Half - Sine temperature profile*

In this case, the variation of the temperature distribution resembles the half sine wave and the general equation may be written in the form of Eq. (2.29). The maximum temperature T_{max} appears at the midspan of the SFGMEE beam.

$$\Delta T = T_{max} \left\{ \sin\left(\frac{\pi x}{a}\right) \right\} \quad 0 \leq x \leq a \quad (2.29)$$

in which, T_{max} is the maximum temperature, a is the beam length, x is the point of interest from the left clamped end.

➤ *Linearly varying temperature profile*

This form of temperature variation corresponds to the case where the temperature is minimum, say initial temperature T_i at the left support and linearly attains the maximum temperature T_{max} at the right end of the beam. The corresponding general equation may be expressed as

$$\Delta T = \{T_{max}\} x + \{T_i\} \quad 0 \leq x \leq a \quad (2.30)$$

2.7.2. Through-thickness temperature distribution

The present analysis considers the different through thickness varying temperature profiles which can be encapsulated as follows:

➤ *Linear Temperature profile*

In this case, the temperature is assumed to vary linearly from T_i to T_{max} through the thickness of the beam. The relation for the linear variation of temperature is represented by

$$\Delta T = T_i + T_{max}(z/h) \quad (2.31)$$

in which, T_i is the temperature at the bottom layer of the beam, z is the distance of the point of interest from the bottom of the beam and h is the beam thickness.

➤ *Bi-triangular temperature profile*

The temperature distribution of this profile follows a general trend of variation given by the equation

$$\begin{aligned} \Delta T &= T_{max}(1 - z) & 0 \leq z \leq h/2 \\ \Delta T &= T_{max}(z) & h/2 \leq z \leq h \end{aligned} \quad (2.32)$$

➤ *Parabolic temperature profile*

Here, the temperature distribution is assumed to vary parabolically across the beam thickness. The distribution profile can be represented by the expression as follows:

$$\Delta T = T_{max} \left\{ 1 - \left(\frac{z}{h} \right)^2 \right\} \quad 0 \leq z \leq h \quad (2.33)$$

2.8. RESULTS AND DISCUSSION

In this section, the coupled thermal response of SFGMEE beam in the different thermal environments is investigated using a numerical method. The material properties of the different volume fraction of BaTiO₃ and CoFe₂O₄ (Table 2.1) are used. The numerical calculations are carried out to evaluate the static parameters variation across the SFGMEE beam thickness. Furthermore, two different stacking arrangements namely, SFG - BFB and SFG - FBF are considered, and its influence on multiphysics response of SFGMEE beam is computed. The numerical investigation is

extended to compare the prominent influence of pyroeffects on the multilayered SFGMEE beam comprehensively. The variations of the direct quantities and derived quantities at different beam regions are also investigated.

2.8.1. Validation of the FE model

The present FE formulation of the multilayered SFGMEE beam is verified for its correctness considering the benchmark research results summarized by Kondaiah *et al.* (2012). To this end, the multilayered FE model is simplified to account for a single layer multiphase MEE beam. All the layers of the SFGMEE beam are assigned with the material properties corresponding to $V_f = 0.5$ BaTiO₃ (Table 2.1). The beam geometry, thermal loading and the boundary conditions are considered identical to those considered by Kondaiah *et al.* (2012). In order to improve the accuracy of the obtained results, and to find out the optimum mesh size, the convergence study has been carried out. It may be observed from Fig. 2.3 that the mesh size of 12×10 in the thickness and length direction exhibits a very good convergence of transverse displacement U_w . Figures 2.4(a)-(d) illustrate the validation of the displacement component U_x , the electric potential ϕ , the magnetic potential ψ , and the normal stress σ_x , respectively. Hence, it is expected that the present FE formulation yields accurate results for the analysis of SFGMEE beam in the different thermal environment.

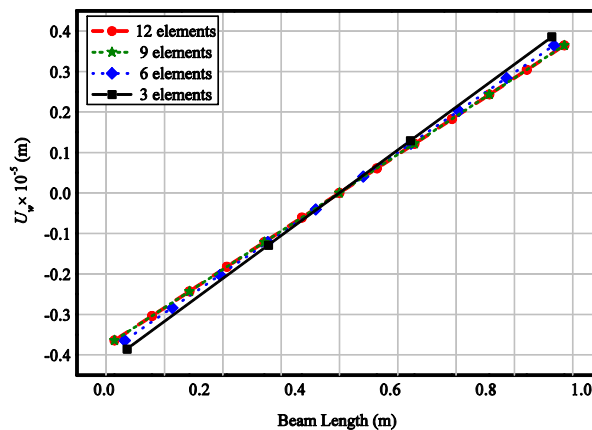


Figure 2.3: Convergence of transverse displacement component U_w with mesh refinement

Table 2.1: Material properties of BaTiO₃-CoFe₂O₄ composite w.r.t different volume fraction V_f of BaTiO₃ – CoFe₂O₄ (Kondaiah *et al.* 2012)

Material property	Material constants	0 V_f	0.2 V_f	0.4 V_f	0.5 V_f	0.6 V_f	0.8 V_f	1 V_f
Elastic constants (GPa)	$C_{11}=C_{22}$	286	250	225	220	200	175	166
	C_{12}	173	146	125	120	110	100	77
	$C_{13}=C_{23}$	170	145	125	120	110	100	78
	C_{33}	269.5	240	220	215	190	170	162
	$C_{44}=C_{55}$	45.3	45	45	45	45	50	43
Piezoelectric constants (C/m ²)	C_{66}	56.5	52	50	50	45	37.5	44.5
	e_{31}	0	-2	-3	-3.5	-3.5	-4	-4.4
	e_{33}	0	4	7	9.0	11	14	18.6
Dielectric constant (10 ⁻⁹ C ² /Nm ²)	e_{15}	0	0	0	0	0	0	11.6
	$\eta_{11}=\eta_{22}$	0.08	0.33	0.8	0.85	0.9	1	11.2
Magnetic permeability (10 ⁻⁴ Ns ² /C ²)	η_{33}	0.093	2.5	5	6.3	7.5	10	12.6
	$\mu_{11}=\mu_{22}$	-5.9	-3.9	-2.5	-2.0	-1.5	-0.8	0.05
Piezomagnetic constants (N/Am)	μ_{33}	1.57	1.33	1	0.9	0.75	0.5	0.1
	q_{31}	580	410	300	350	200	100	0
	q_{33}	700	550	380	320	260	120	0
Magneto-electric constant (10 ⁻¹² Ns/VC)	q_{15}	560	340	220	200	180	80	0
	$m_{11}=m_{22}$	0	2.8	4.8	5.5	6	6.8	0
Pyroelectric-constant (10 ⁻⁷ C/m ² K)	m_{33}	0	2000	2750	2600	2500	1500	0
	p_2	0	-3.5	-6.5	-7.8	-9	-10.8	0
Pyromagnetic constant (10 ⁻⁵ C/m ² K)	τ_2	0	-36	-28	-23	-18	-8.5	0
Thermal expansion coefficient (10 ⁻⁶ K ⁻¹)	$\alpha_1=\alpha_2$	10	10.8	11.8	12.3	12.9	14.1	15.7
	α_3	10	9.3	8.6	8.2	7.8	7.2	6.4
Density (kg/m ³)	ρ	5300	5400	5500	5550	5600	5700	5800

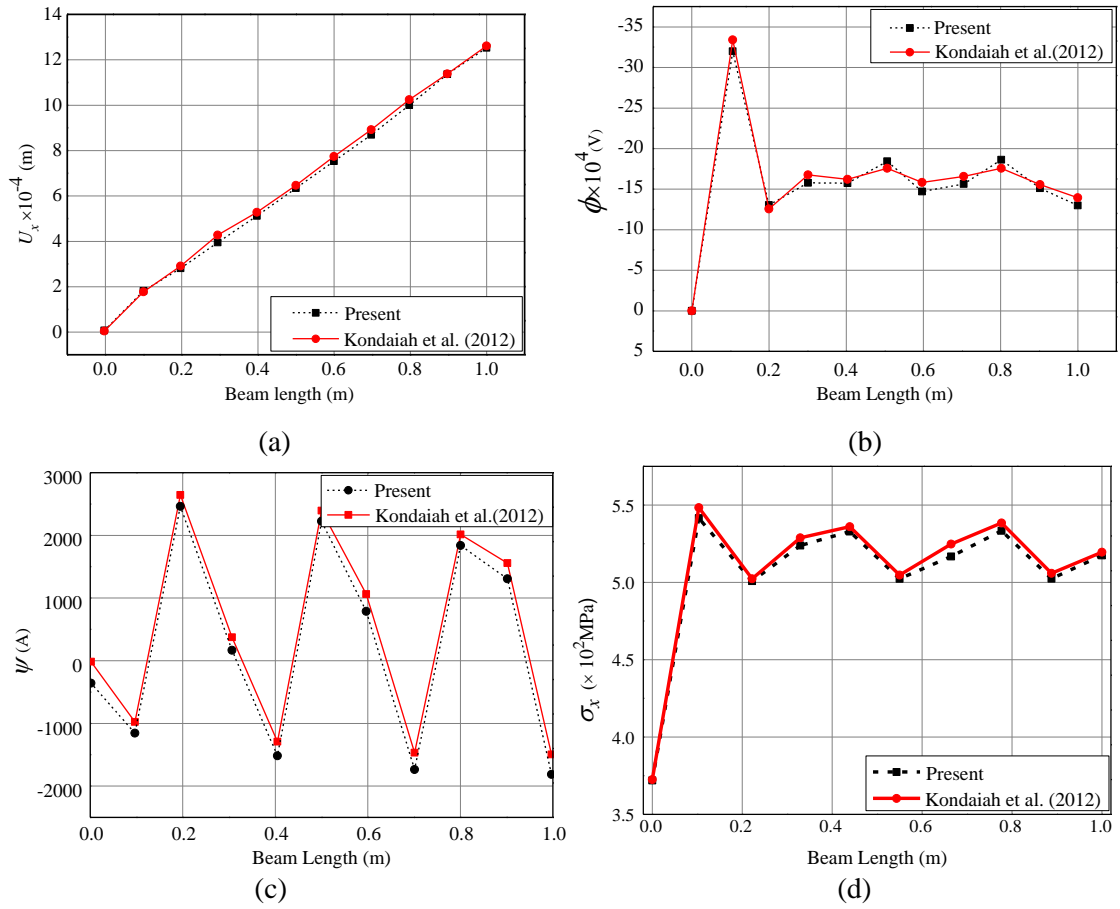


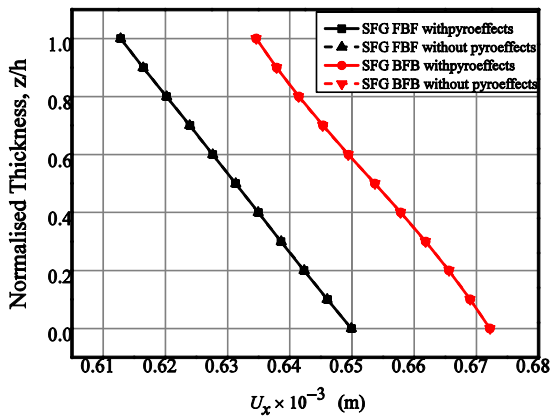
Figure 2.4: Validation of (a) longitudinal x -direction U_x (b) electric potential ϕ (c) magnetic potential ψ (d) normal stress - σ_x

2.8.2. Influence of pyro-effects

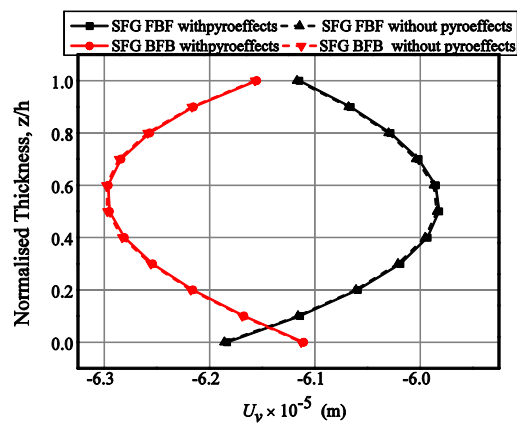
It is familiar that the MEE material displays an additional thermo-electric (pyroelectric effect) and thermo-magnetic (pyromagnetic) coupling in presence of the thermal environment (Kim *et al.* 2012). In this section, the influence of pyroeffects on the direct quantities of SFGMEE beam has been investigated and it is restricted to in-plane temperature distributions (Eqs. (2.28) - (2.30)) only. The values are obtained across the beam thickness at $x = a/2$. Figures 2.5(a) - (e) demonstrate the variation of the direct quantities when the layerwise SFGMEE beam subjected to a uniform temperature rise of 100 K. It may be observed from these figures (Figs. 2.5(a) - (e)) that the pyroeffects show a significant influence only on the electric potential of the SFGMEE beam. In particular, the pyroeffects tend to improve the electric potential of the system, whereas a negligible effect is observed for the displacements and magnetic potential.

Figures 2.5(a) - (c) suggest that the displacements U_x , U_v and U_w are higher for the SFG-BFB MEE beam than SFG-FBF MEE beam. This may be attributed to the lower stiffness of the stacking sequence due to the presence of more pure piezoelectric phase.

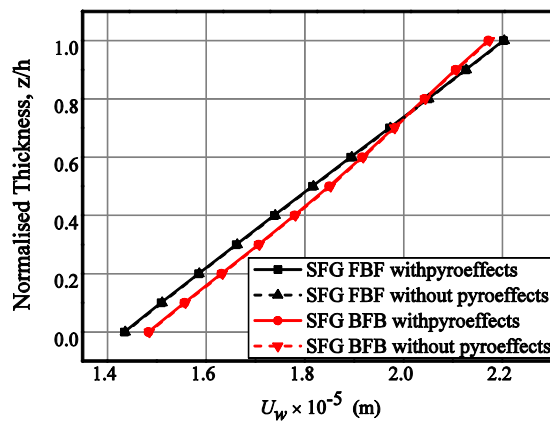
The numerical evaluation is also carried out for the linear and sinusoidal temperature profiles. The variations of the direct quantities of SFGMEE beam subjected to linear temperature profile are illustrated in Figs. 2.6(a) - (e). It is noticed from these figures that the effect of stacking sequence on the displacement component U_w and magnetic potential ψ is negligible.



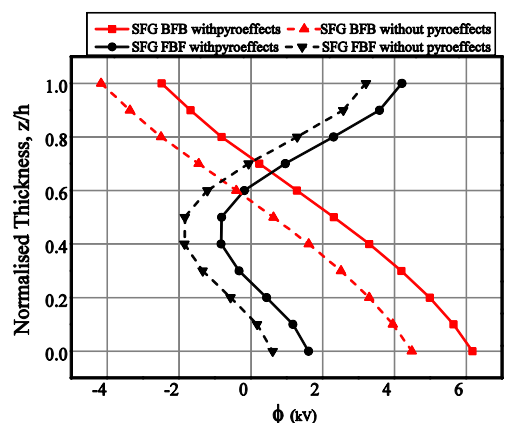
(a)



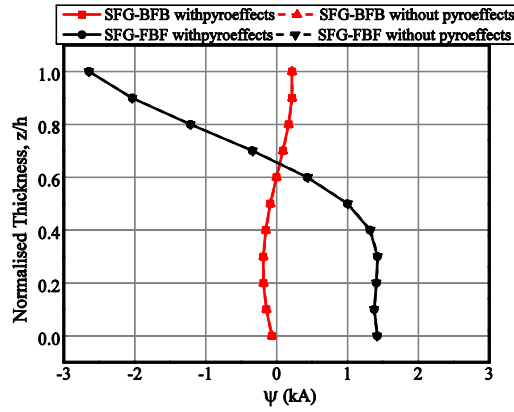
(b)



(c)



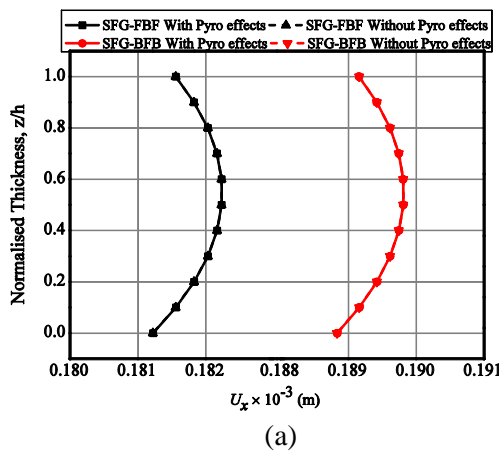
(d)



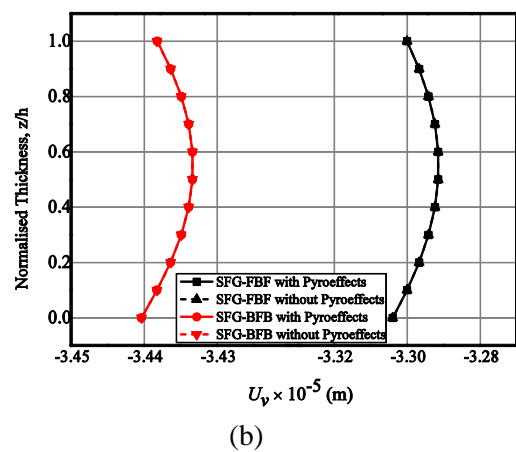
(e)

Figure 2.5: Variation of displacement components (a) U_x (b) U_v (c) U_w (d) electric potential ϕ (e) magnetic potential ψ for SFG-BFB and SFG-FBF subjected to uniform temperature load

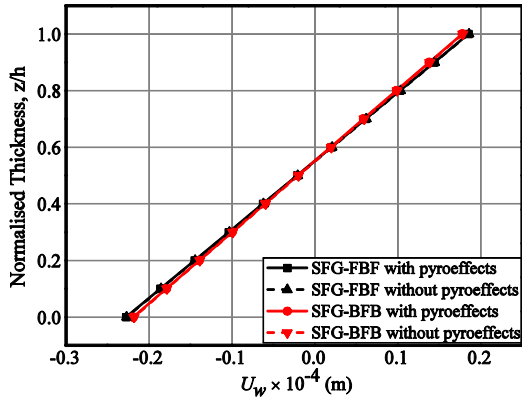
The variation of direct quantities for the SFGMEE beam subjected to sinusoidal temperature profile is shown in Fig. 2.7(a). It can be observed from this figure that the influence of the pyroeffects on the longitudinal x -direction displacement component U_x of the beam is minimal compared to displacement components U_v and U_w as shown in Figs. 2.7(b) and (c), respectively. Figures 2.7(d) and (e) depict the variations of ϕ and ψ , respectively. Further, it can also be seen that the pyroeffects have a noticeable influence on the electric potential as shown in Fig. 2.7(d), whereas the SFG-BFB MEE beam exhibits a higher electric potential.



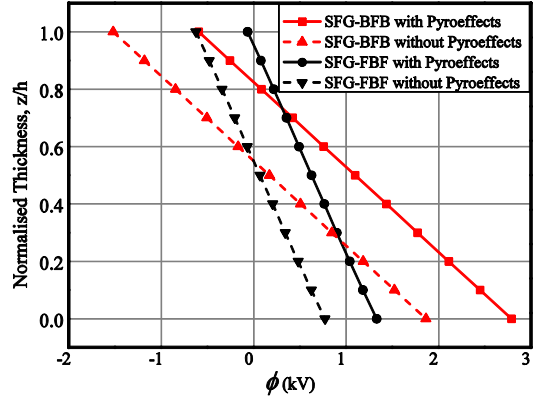
(a)



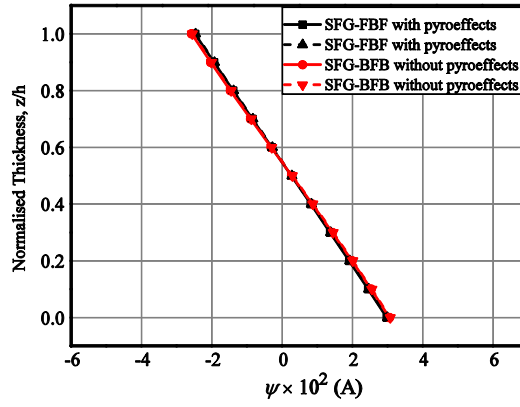
(b)



(c)

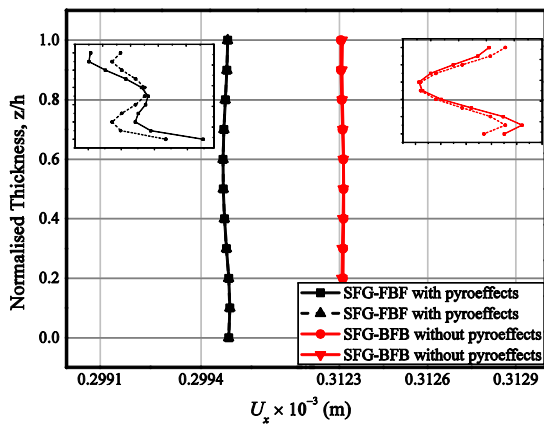


(d)

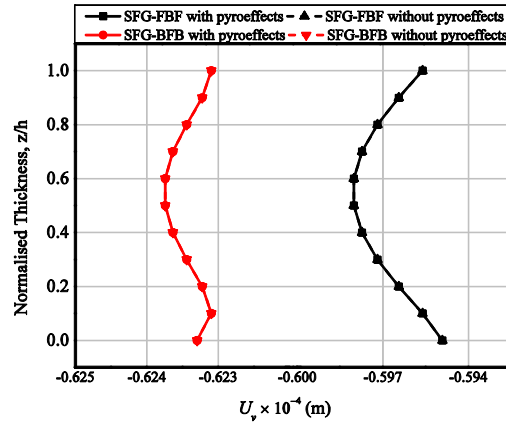


(e)

Figure 2.6: Variation of (a) U_x (b) U_v (c) U_w (d) electric potential ϕ (e) magnetic potential ψ for SFG-BFB and SFG-FBF subjected to linear temperature load



(a)



(b)

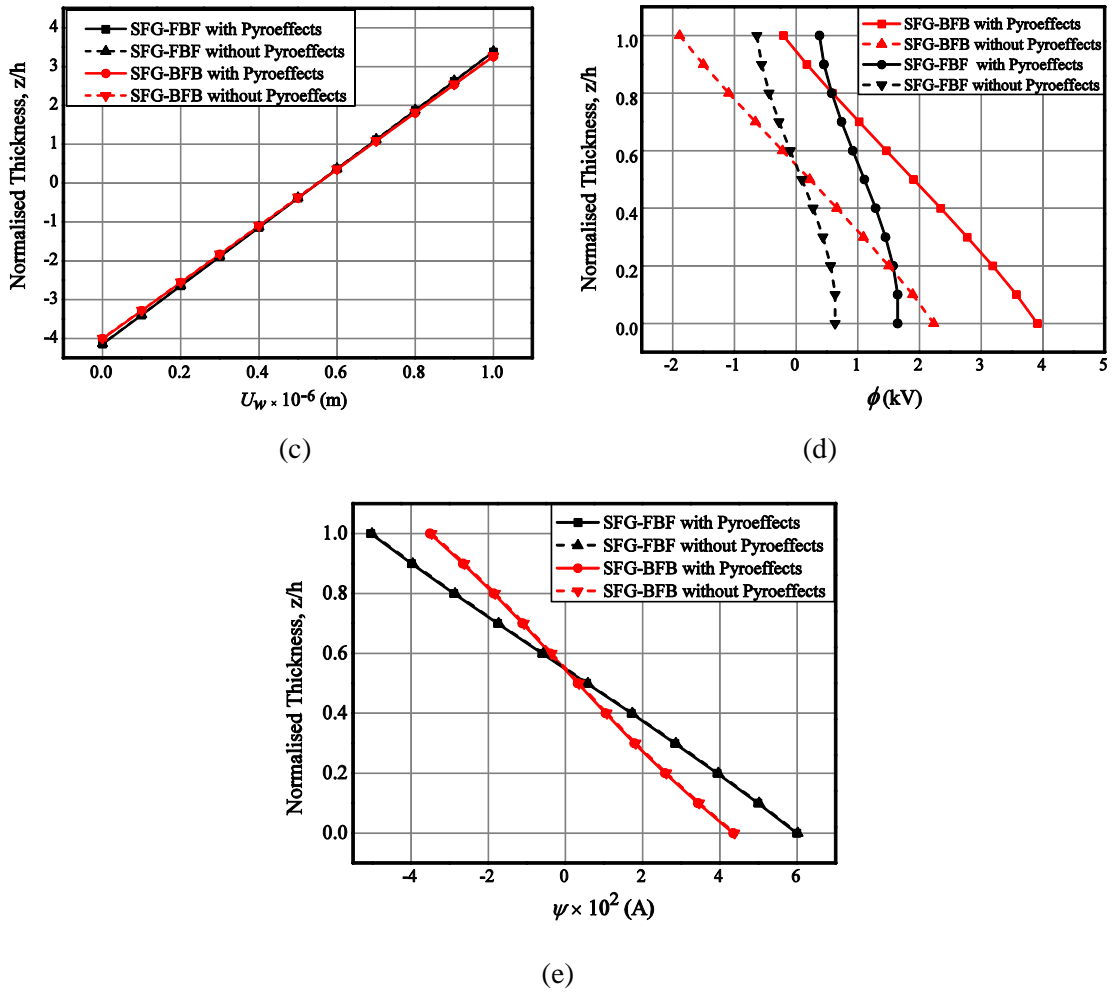


Figure 2.7: Variation of (a) U_x (b) U_v (c) U_w (d) electric potential ϕ (e) magnetic potential ψ for SFG-BFB and SFG-FBF subjected to sinusoidal temperature load

2.8.3. Effect of cross-thickness temperature profiles

The influence of temperature profiles (Eq. (2.28) and Eqs. (2.31) - (2.33)) on the displacement components U_x , U_v and U_w of the SFGMEE beam with SFG-BFB and FBF stacking sequence is illustrated in Figs. (2.8) – (2.10), respectively. It can be seen that the uniform temperature profile exhibit a predominant influence on the U_x and U_v , whereas the variations of these displacement components for the bi-triangular temperature profile is found insignificant. From Figs. 2.10(a) and (b), it can be observed that for both the stacking sequence, U_w is larger for linear temperature profile. Figures 2.11(a) and (b) demonstrate the variation of the electric potential for SFG-BFB and SFG-FBF MEE beam, respectively. It is seen that for all the temperature profiles, SFG-BFB MEE beam has a higher electric potential than the

SFG-FBF MEE beam. This may be attributed to the presence of two pure piezoelectric phase in the stacking sequence. In addition, a significant effect of uniform temperature distribution on the electric potential is observed for SFG-BFB MEE beam, whereas for the SFG-FBF MEE beam, the electric potential is higher for bi-triangular temperature distribution.

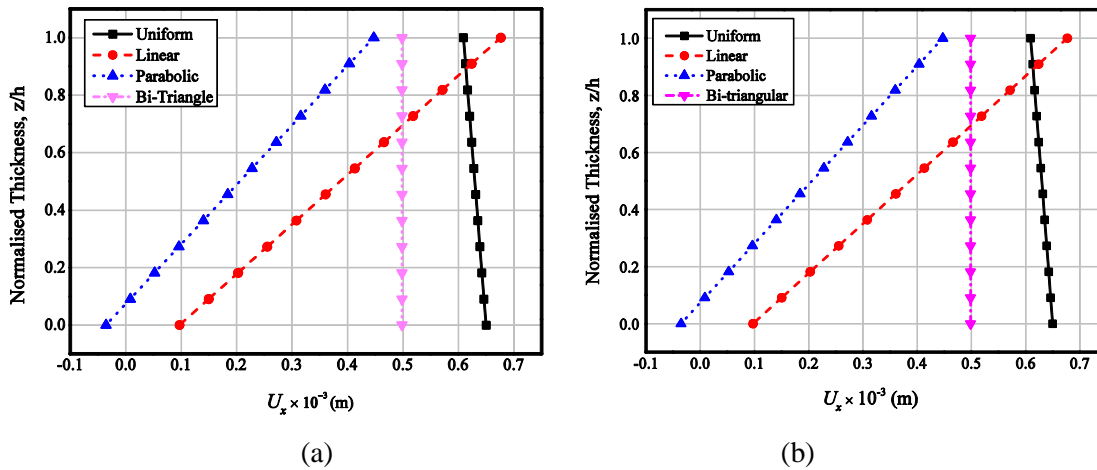


Figure 2.8: Effect of through thickness temperature profiles on longitudinal x -direction displacement U_x (a) SFG-BFB (b) SFG-FBF

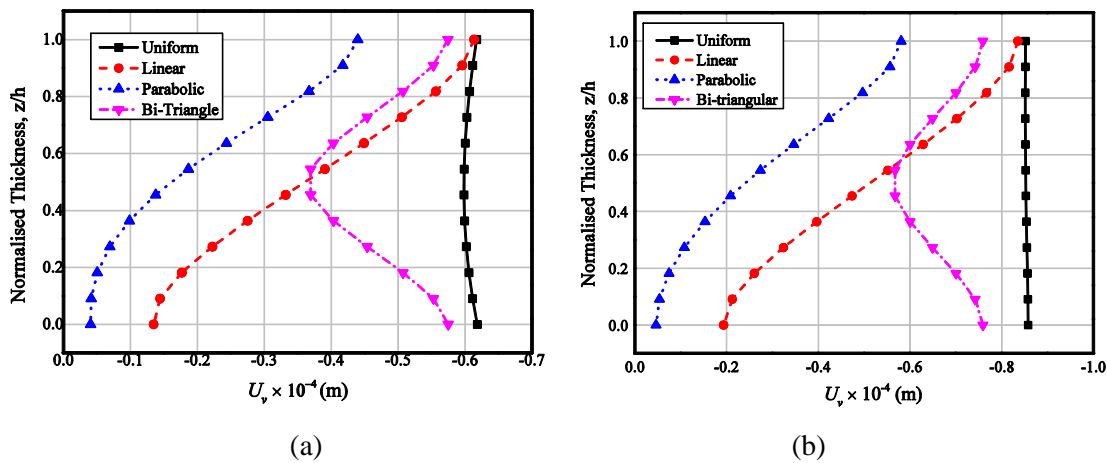


Figure 2.9: Effect of through thickness temperature profiles on longitudinal y - direction displacement U_y (a) SFG-BFB (b) SFG-FBF

Similarly, Figs. 2.12(a) and (b) illustrate the magnetic potential distribution across the thickness of the SFG-BFB and SFG-FBF MEE beam, respectively. Since, the SFG-FBF MEE beam has more pure piezomagnetic phase, it results in a higher magnetic potential than the SFG-BFB MEE beam. For both the stacking sequences, uniform temperature profile shows the maximum magnetic potential. In addition,

Tables 2.2 and 2.3 illustrate the comparison between a normal three-layered MEE and SFGMEE beam for the maximum electric and magnetic potential, respectively. It can be inferred from these tables that the SFGMEE beam has a convincing effect in contrast to the normal three-layered MEE beam.

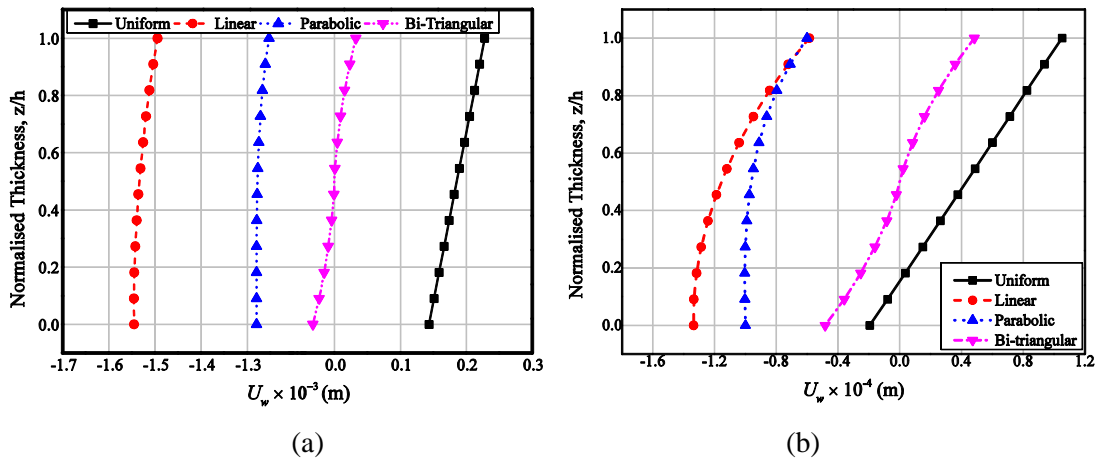


Figure 2.10: Effect of through thickness temperature profiles on transverse displacement U_w
(a) SFG-BFB (b) SFG-FBF

Table 2.2: Effect of different cross-thickness temperature loads on the maximum electric potential (ϕ) of MEE beams

Through-thickness temperature profile	Max. Electric potential ϕ (kV)			
	<i>BFB</i>	<i>SFG-BFB</i>	<i>FBF</i>	<i>SFG-FBF</i>
Uniform	21.4	54.2	-7.7	4.22
Linear	-22.6	-44.1	-10.8	-4.16
Parabolic	-15.7	-27.4	-8.3	5.17
Bi-triangular	-16.4	42.2	5.6	8.53

Table 2.3: Effect of different cross-thickness temperature loads on the maximum magnetic potential (ψ) of MEE beams

Through-thickness temperature profile	Max. Magnetic potential ψ (A)			
	<i>BFB</i>	<i>SFG-BFB</i>	<i>FBF</i>	<i>SFG-FBF</i>
Uniform	656.2	1083.4	723.1	-2924.7
Linear	-498.6	-814.4	-582.3	-1991.3
Parabolic	-333.7	-446.3	-365.8	-1206.4
Bi-triangular	409.7	-882.4	532.3	-1779.2

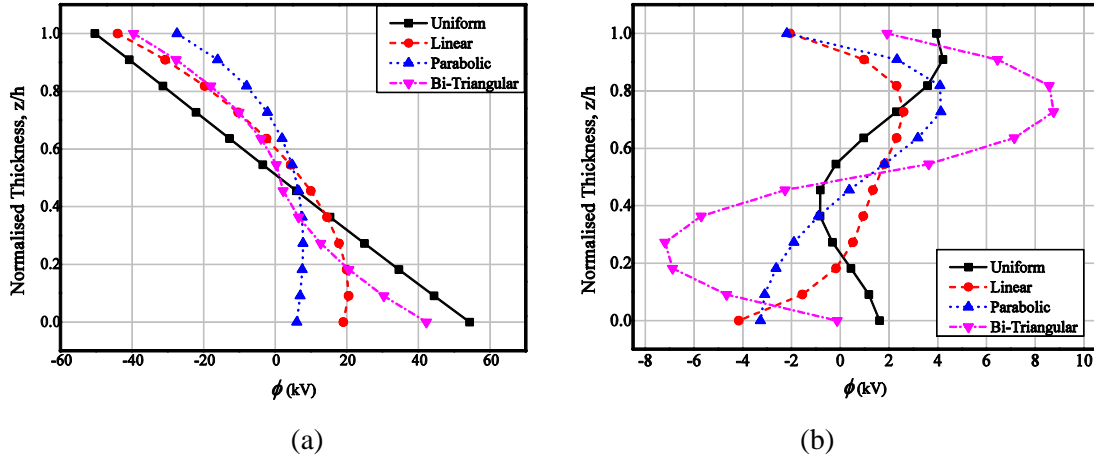


Figure 2.11: Effect of through thickness temperature profiles on electric potential ϕ (a) SFG-BFB (b) SFG-FBF

Furthermore, the numerical calculations are made to investigate the variation of derived quantities such as stresses, electric displacements and magnetic flux densities. It is found that the normal stresses σ_y and σ_z follow a similar variation trend as that of the σ_x . Hence, for the sake of brevity, only the normal stress σ_x distribution is shown in Figs. 2.13(a) and (b) for SFG-BFB and SFG-FBF MEE beam, respectively. For the uniform temperature profile, the variation in the magnitude of the normal stress σ_x is minimal for both the stacking sequence, whereas for the remaining temperature profiles, it is higher for SFG-FBF MEE beam compared to SFG-BFB MEE beam. The shear stress τ_{xy} varies symmetrically across the midplane of the SFG-BFB MEE beam as shown in Fig. 2.14(a), whereas for the SFG-FBF MEE beam, it varies anti-symmetrically as illustrated in Fig. 2.14(b).

It is also be observed that the middle piezomagnetic phase experiences maximum shear stress τ_{xy} in case of the SFG-BFB stacking sequence, whereas for the SFG-FBF sequence, the maximum τ_{xy} is observed at the top or bottom piezomagnetic layers. Further, except for the uniform temperature profile, τ_{yz} varies identically across the beam thickness for both the stacking sequences as shown in Figs. 2.15(a) and (b), respectively. Similarly, Figs. 2.16(a) and (b) illustrate the distribution of shear stress τ_{xz} for the SFG-BFB and SFG-FBF stacking sequence, respectively. The electric displacement component in x -direction D_x with respect to SFG-BFB and SFG-FBF MEE beam is plotted in Figs. 2.17(a) and (b), respectively. According to the constitutive equation (Eq. (2.4)), the magnitude of electric displacements mainly

depends on the piezoelectric co-efficient matrix $[e]$ and the dielectric coefficient matrix $[\eta]$. A higher value of these coefficients can be observed for the pure piezoelectric ($V_f=1.0$) phase (Table 2.1). Hence, it is obvious that the SFG-BFB MEE beam results in higher electric displacement. This holds good for D_y and D_z also, as shown in Figs. 2.18(b) and 2.19(b), respectively. A significant effect of uniform temperature profile with respect to D_x and D_y of the SFG-BFB MEE beam is observed, whereas the bi-triangular temperature profile has a predominant effect on the D_z for both the stacking sequences.

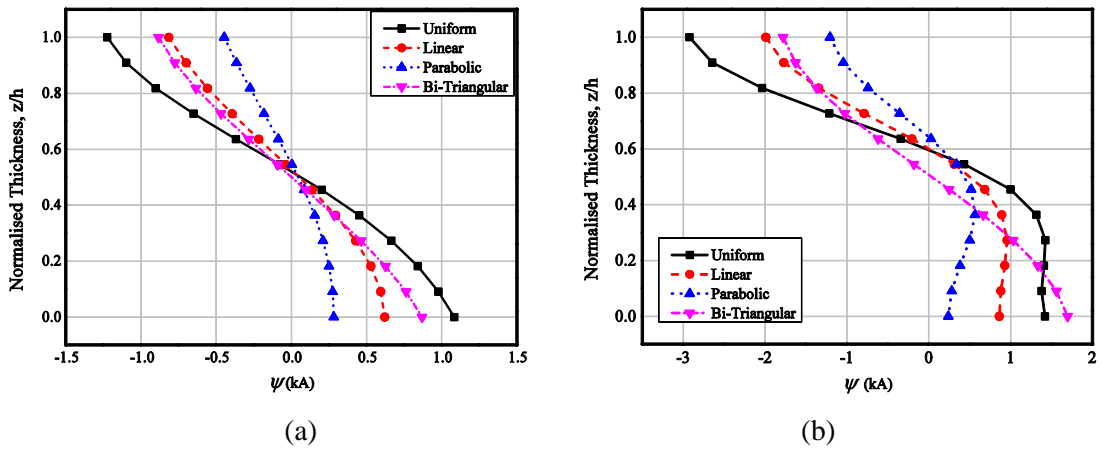


Figure 2.12: Effect of through thickness temperature profiles on magnetic potential ψ (a) SFG-BFB (b) SFG-FBF MEE beam

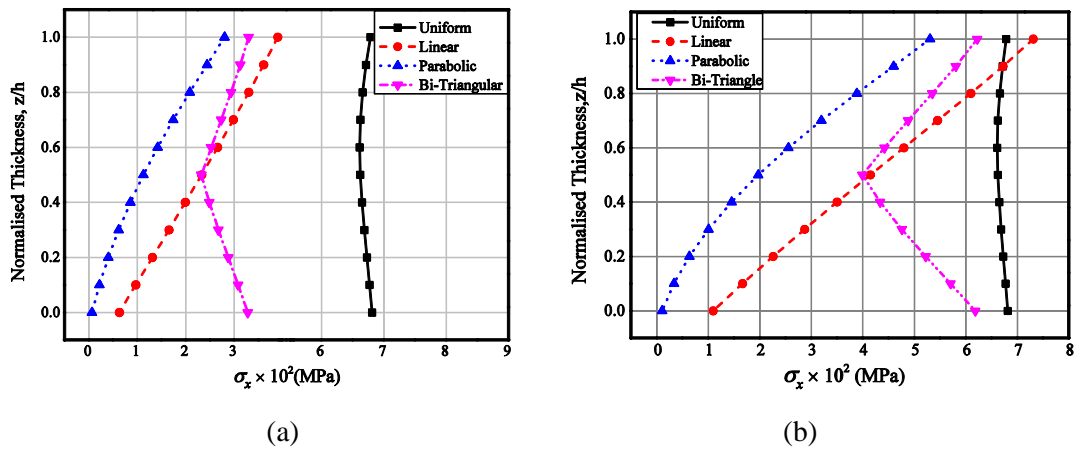


Figure 2.13: Effect of through thickness temperature profiles on normal stress σ_x (a) SFG-BFB (b) SFG-FBF MEE beam

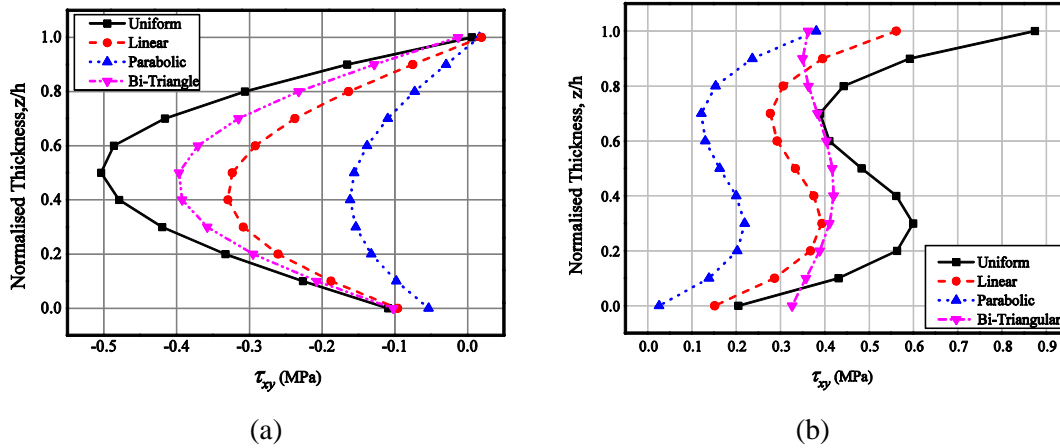


Figure 2.14: Effect of through thickness temperature profiles on the shear stress τ_{xy} (a) SFG-BFB (b) SFG-FBF MEE beam

Figures (2.20) - (2.22) illustrate the variation of magnetic flux densities B_x , B_y and B_z , respectively. The magnetic flux density is higher for SFG-FBF MEE beam because of the higher piezomagnetic constant matrix $[q]$ and magnetic permeability constant matrix $[\mu]$ for the pure piezomagnetic phase. For both the stacking sequences, the magnetic flux densities B_x , B_y and B_z are significantly influenced by the uniform temperature profile as depicted in Figs. (2.20) - (2.22), respectively. However, the maximum value of B_y is observed at the midspan of the beam for all the temperature distributions.

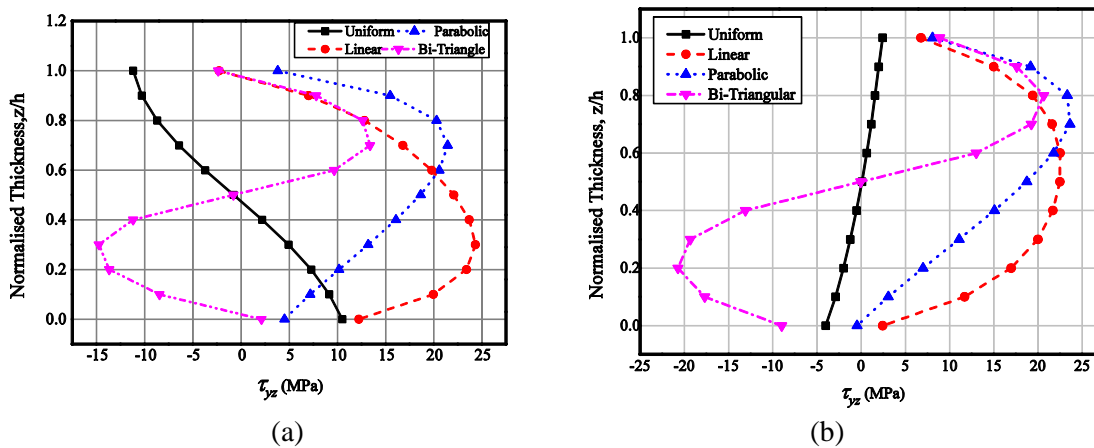
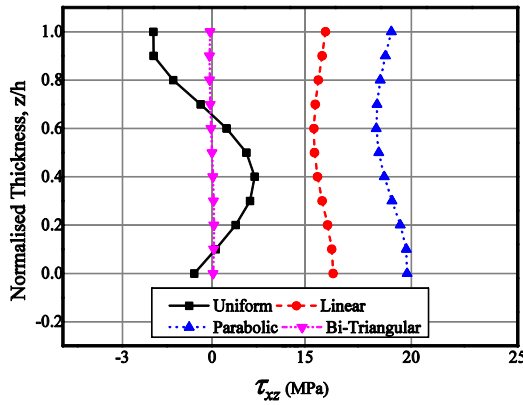
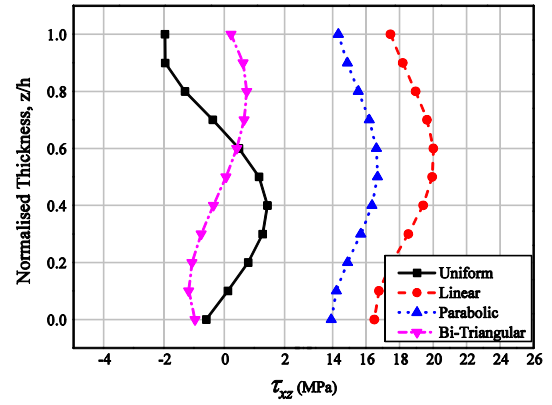


Figure 2.15: Effect of through thickness temperature profiles on shear stress τ_{yz} (a) SFG-BFB (b) SFG-FBF MEE beam

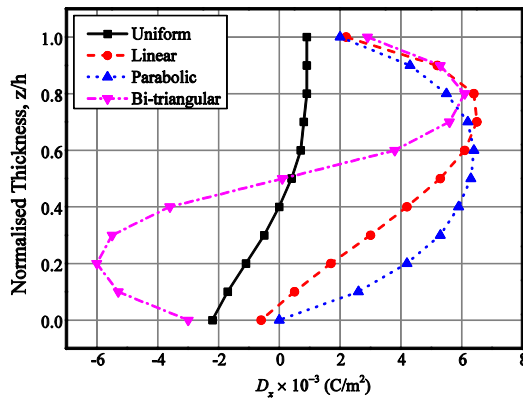


(a)

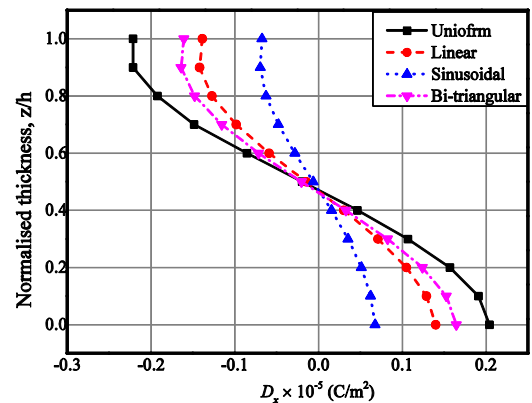


(b)

Figure 2.16: Effect of through thickness temperature profiles on shear stress τ_{xz} (a) SFG-BFB (b) SFG-FBF MEE beam

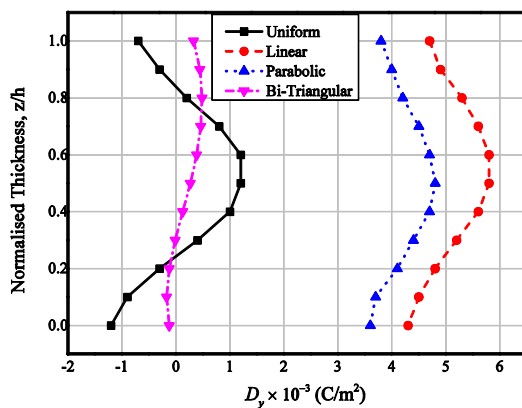


(a)

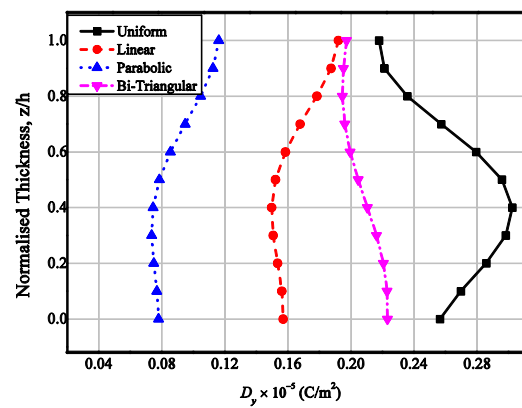


(b)

Figure 2.17: Effect of through thickness temperature profiles on electric displacement D_x (a) SFG-BFB (b) SFG-FBF MEE beam

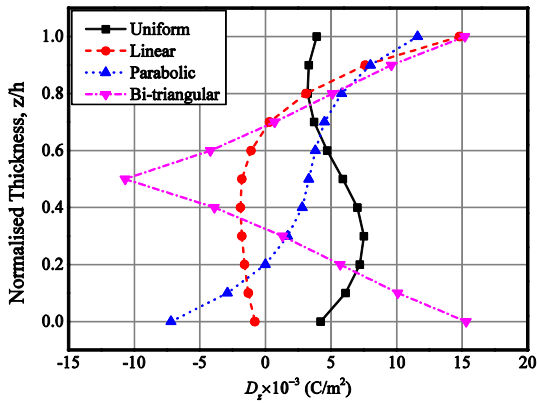


(a)

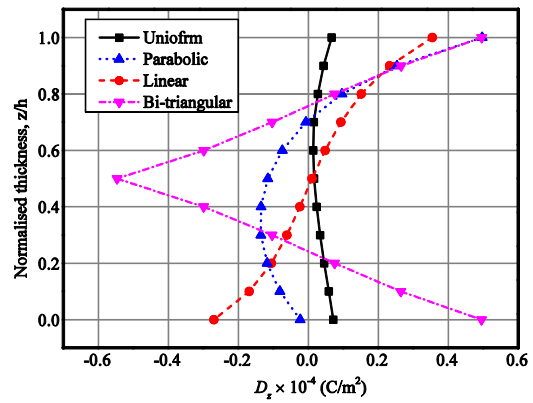


(b)

Figure 2.18: Effect of through thickness temperature profiles on electric displacement D_y (a) SFG-BFB (b) SFG-FBF MEE beam

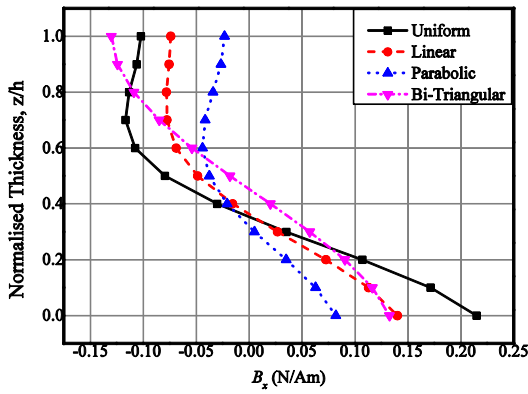


(a)

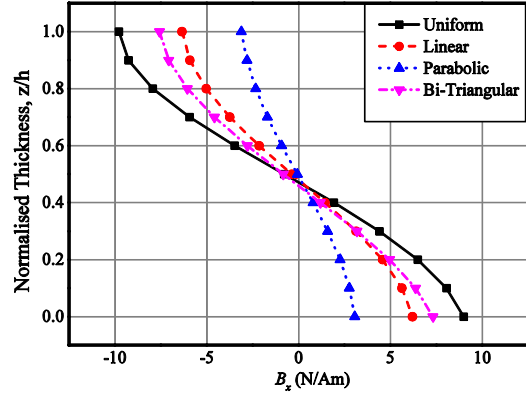


(b)

Figure 2.19: Effect of through thickness temperature profiles on the variation of electric displacement D_z (a) SFG-BFB (b) SFG-FBF MEE beam

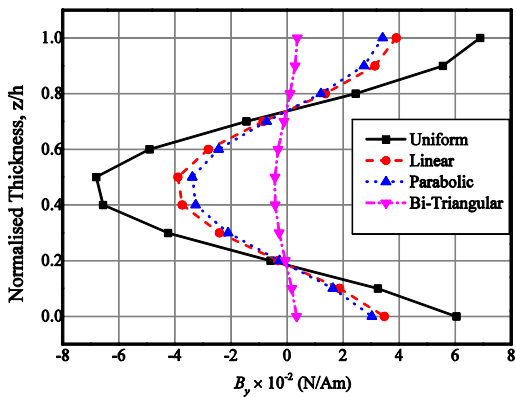


(a)

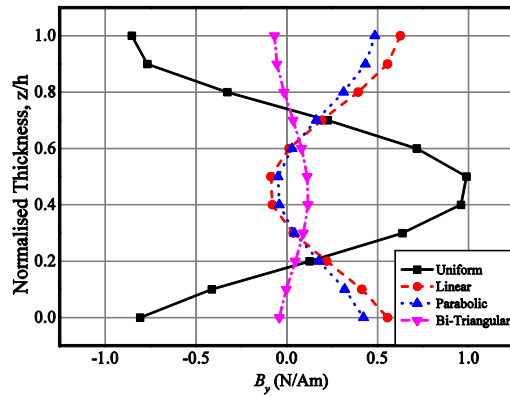


(b)

Figure 2.20: Effect of through thickness temperature profiles on magnetic flux density B_x (a) SFG-BFB (b) SFG-FBF MEE beam



(a)



(b)

Figure 2.21: Effect of through thickness temperature profiles on magnetic flux density B_y (a) SFG-BFB (b) SFG-FBF MEE beam

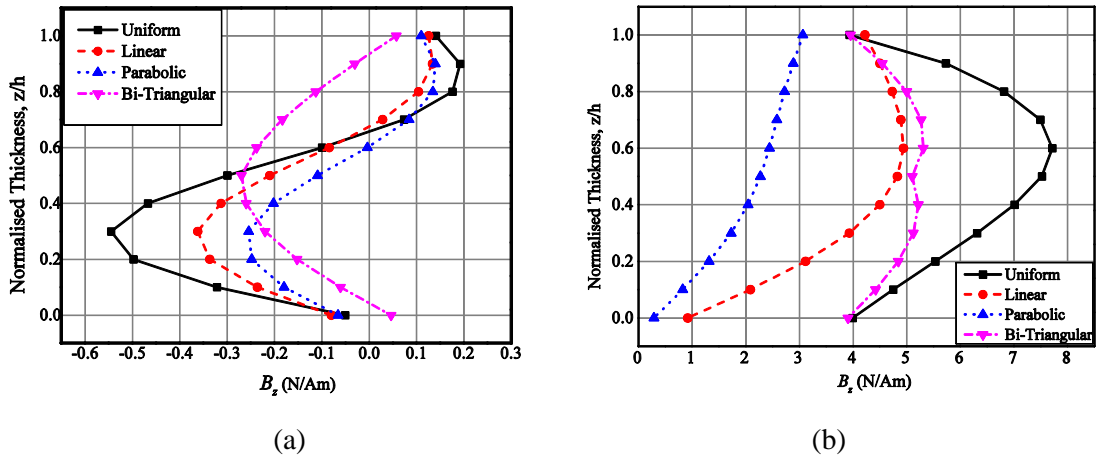


Figure 2.22: Effect of through thickness temperature profiles on magnetic flux density B_z (a) SFG-BFB (b) SFG-FBF MEE beam

2.8.4. Investigation at the different beam region

In this section, the variations of the direct and derived quantities at different beam regions are investigated by considering the parabolically varying temperature distribution. The results are presented only for SFG-BFB MEE beam, for the sake of brevity. The investigation points on the beam are chosen near the clamped end, at the midspan and at the free end. It may be observed from Figs. 2.23(a)-(c) that the displacements U_x and U_w are maximum at the free end. However, negligible discrepancies with respect to U_v is observed in these regions. The electric potential variation is found to be maximum at the free end as depicted in Fig. 2.24(a). The variation in the magnetic potential is illustrated in Fig. 2.24(b). It can be seen from this figure that the variation of magnetic potential is minimal near the clamped end. The comparison plots of stresses at the different beam regions are illustrated in Figs. 2.25(a) – (d). The normal stress σ_x shows an insignificant variation among the beam regions as depicted in Fig. 2.25(a). From Figs. 2.25(b) and (c), a predominant effect of the free end and the clamped end is observed on the shear stresses τ_{xz} , and τ_{xy} , respectively. The free end of the SFG-BFB MEE beam displays a higher magnitude of electric displacements D_x and D_y as shown in Figs. 2.26(a) and (b), respectively. Further, it may be observed from Fig. 2.26(c) that the variation of D_z is almost identical variation over all the regions.

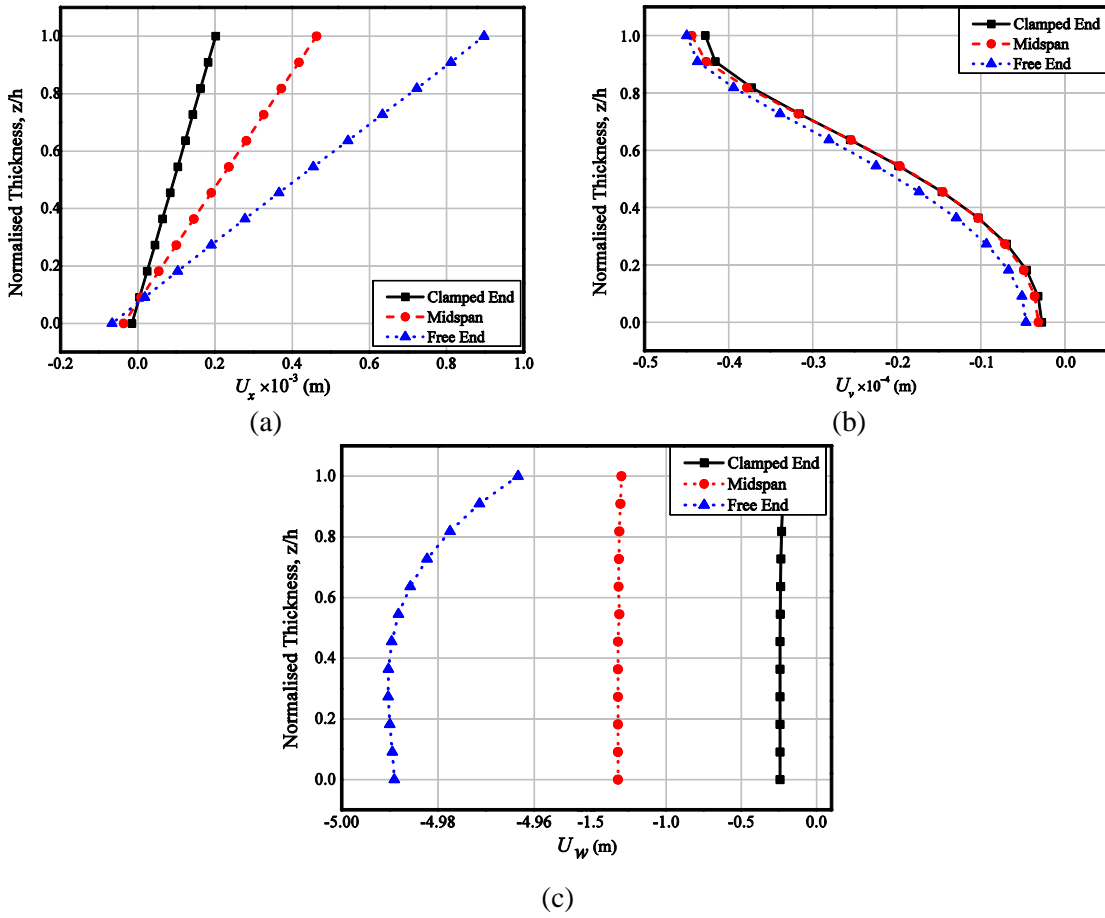


Figure 2.23: Variations of displacement components (a) U_x (b) U_v (c) U_w at different regions of SFG-BFB MEE beam.

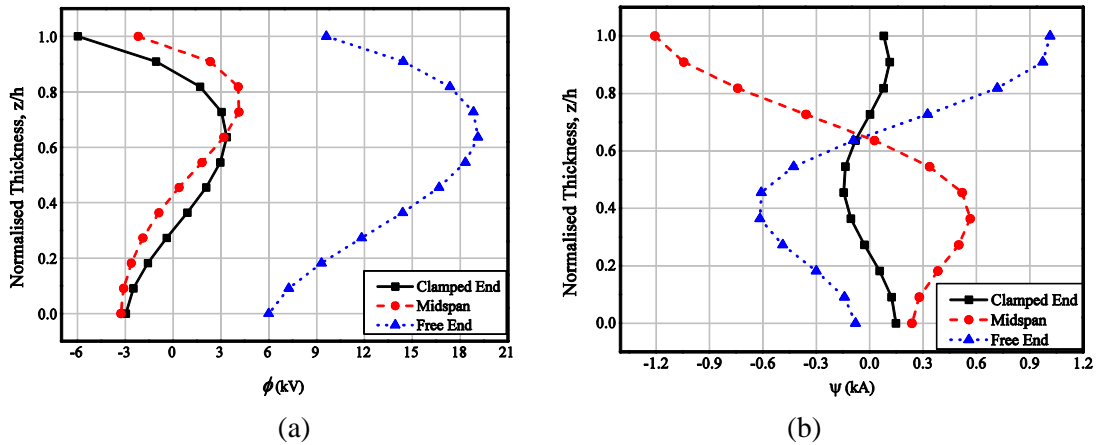


Figure 2.24: Variations of (a) electric potential and (b) magnetic potential at different regions of SFG-BFB MEE beam.

From Fig. 2.27(a), it can be seen that at the midspan of the beam, a slightly higher magnetic flux density B_x is witnessed, whereas the clamped end and the free end exhibit an equal flux distribution. Further, from Figs. 2.27(b) and (c), it can be

witnessed that the variation of B_y and B_z is greater at the free end of the SFG-BFB MEE beam.

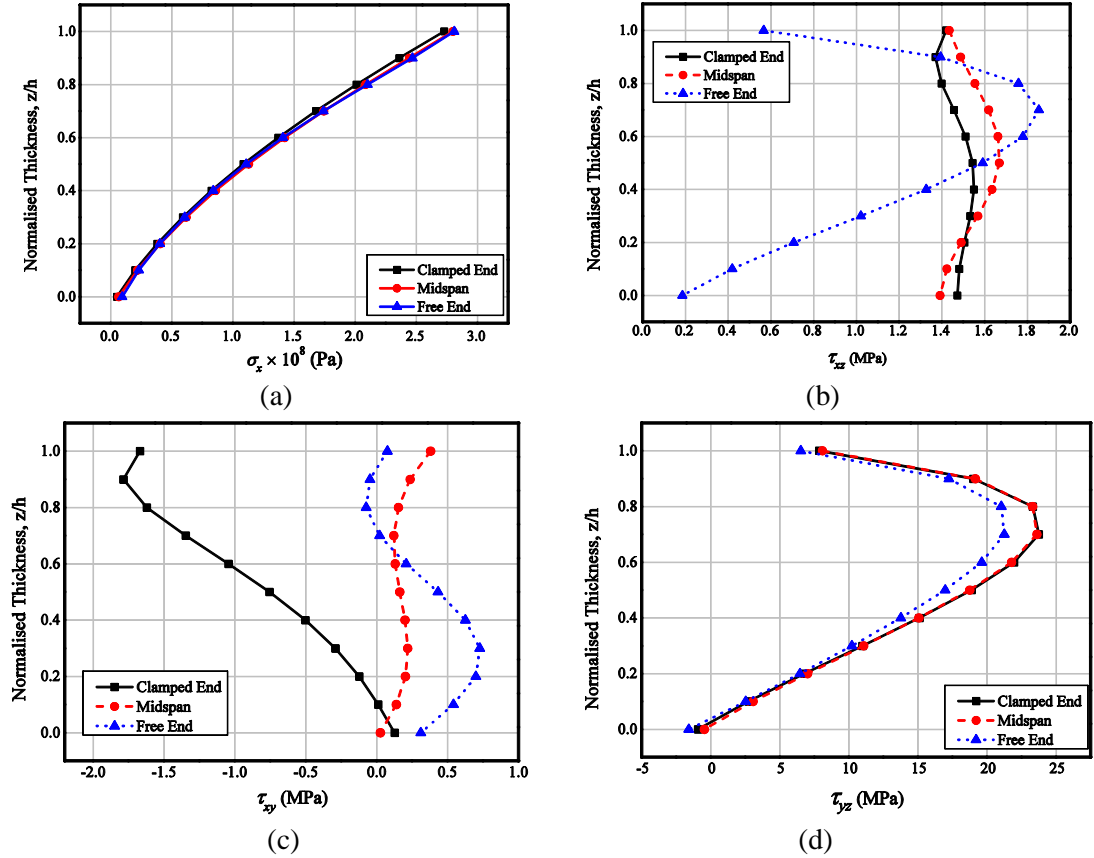
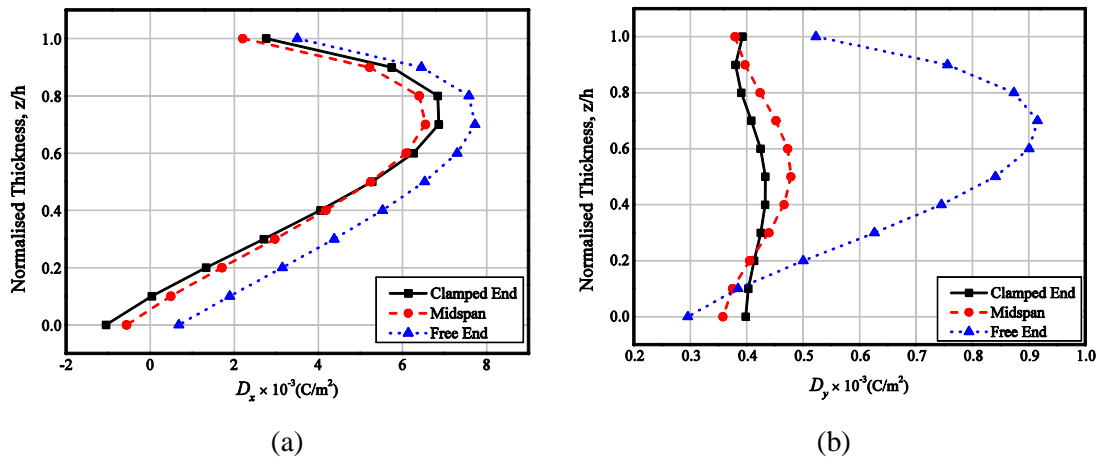
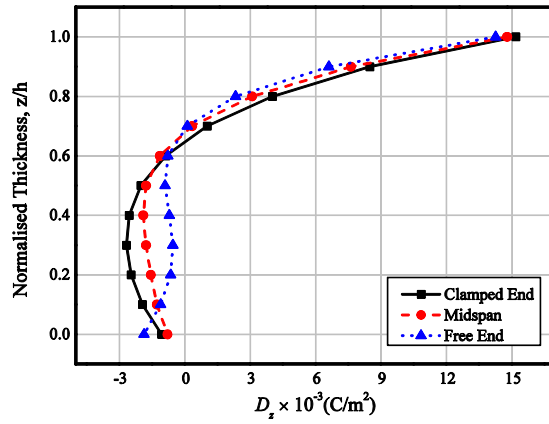


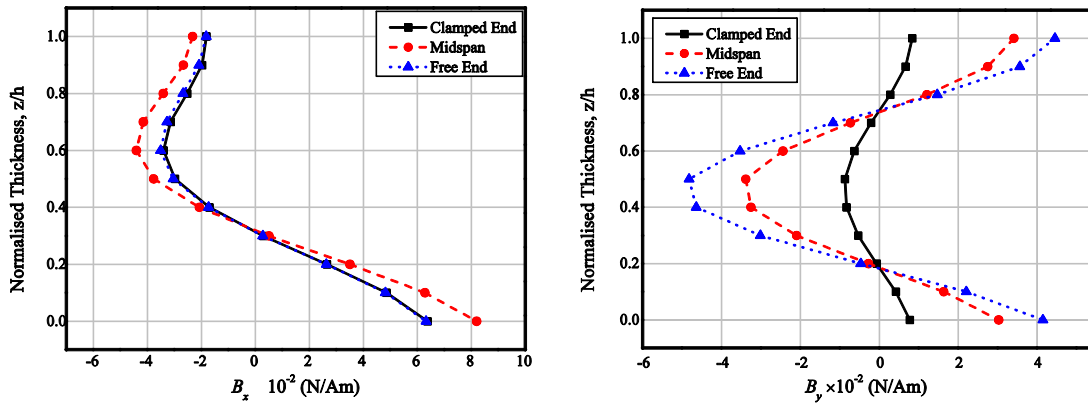
Figure 2.25: Variations of stress components (a) σ_x (b) τ_{xz} (c) τ_{xy} (d) τ_{yz} at different regions of SFG-BFB MEE beam





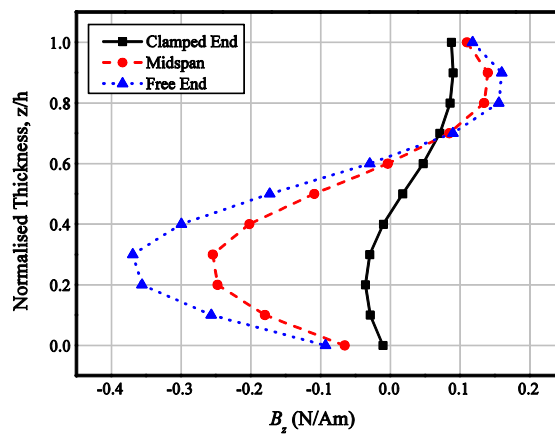
(c)

Figure 2.26: Variations of electric displacements (a) D_x (b) D_y (c) D_z at different regions of SFG-BFB MEE beam



(a)

(b)



(c)

Figure 2.27: Variations of magnetic flux densities (a) B_x (b) B_y (c) B_z at different regions of SFG-BFB MEE beam

2.9.CONCLUSIONS

In this chapter, a three-dimensional finite element analysis has been performed to evaluate the static behaviour of the SFGMEE beam in the different thermal environment by considering the in-plane and through thickness temperature distributions. The cross-thickness variations of the direct and derived quantities of SFGMEE beam are presented. The numerical study reveals that irrespective of the temperature profiles, only the electric potential is influenced by the pyroeffects. The displacement components are higher for SFG-BFB MEE beam, whereas SFG-FBF MEE beams exhibit predominant effect on the in-plane normal stresses. The SFG-BFB MEE beam possesses the maximum electric potential and hence exhibit the maximum electric displacements. Analogously, the maximum magnetic potential and magnetic flux density are noticed for SFG-FBF MEE beam. It is attributed to the fact that the increased number of pure piezoelectric and pure piezomagnetic layers in the corresponding stacking sequences. Among the different temperature profiles considered, the uniform temperature rise exhibit a significant influence on the behaviour of SFGMEE beam. The variation of direct quantities and derived quantities at different regions of the SFGMEE cantilever beam has also been studied.

Chapter 3

STATIC RESPONSE OF MULTIPHASE MAGNETO-ELECTRO-ELASTIC BEAM IN THERMAL ENVIRONMENT

In this chapter, the coupled response of multiphase magneto-electro-elastic beam under various forms of in-plane thermal loading has been discussed. The finite element formulation is derived by considering the influence of pyroeffects. The principle of total potential energy and coupled constitutive equations has been incorporated in modeling of the beam. The effect of volume fraction, forms of thermal loading, length-to-depth ratio and boundary conditions on the static parameters of the MEE beam is investigated.

Related article: Vinyas, M and Kattimani, S.C. (2017). “A finite element based assessment of static behaviour of multiphase magneto-electro-elastic beams under different thermal loading”, *Structural Engineering and Mechanics*, **62**(5), 519 – 535.

3.1. INTRODUCTION

In order to exploit the exceptional characteristics of multiphase magneto-electro-elastic (MEE) structures in thermal environment, a critical evaluation and analysis are very much essential. The term multiphase refers to the homogeneous layers made of different percentage contribution of piezoelectric and piezomagnetic phases. More specifically, the degree of coupling varies with the different volume fraction of Barium Titanate and Cobalt Ferrite. Furthermore, these materials exhibit an additional coupling between the electric, magnetic and thermal fields, which makes them suitable for prominent engineering applications. The main objective of this chapter is to analyse the static behaviour of a multiphase MEE beam subjected to various thermal loading and boundary conditions. In addition, the influence of pyroeffects (pyroelectric and pyromagnetic), and volume fraction on the direct quantities (displacements and the potentials) of the MEE beam under different boundary conditions is studied. The FE formulation of MEE beam is developed by incorporating the total potential energy principle and the constitutive equations of MEE material

taking into account the coupling between elastic, electric, magnetic and thermal properties. Using Maxwell's electrostatic and electromagnetic relations, the variation of stresses, displacements, electric and magnetic potentials along the length of the beam are investigated.

3.2. PROBLEM DESCRIPTION AND GOVERNING EQUATIONS

The schematic diagram of the multiphase MEE beam with Cartesian coordinate system is shown in Fig. 3.1. The beam length a is taken along the x -direction while the width w and the thickness h of the MEE beam are taken along the y - and z -coordinate axes, respectively. The constraints enforced for the simply-supported, clamped-clamped and clamped-free MEE beams are as follows:

$$\text{Simply supported end:} \quad U_x \neq 0, U_v = U_w = \phi = \psi = 0 \quad (3.1)$$

$$\text{Clamped end:} \quad U_x = U_v = U_w = \phi = \psi = 0 \quad (3.2)$$

$$\text{Free end:} \quad U_x = U_v = U_w = \phi = \psi \neq 0 \quad (3.3)$$

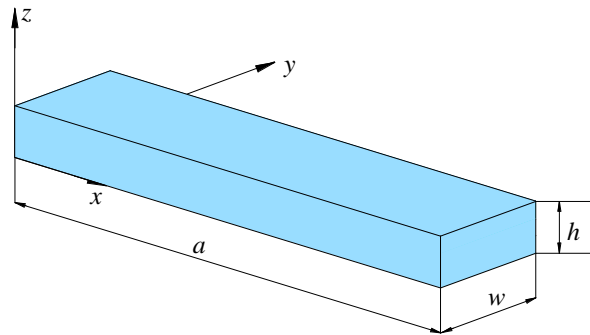


Figure 3.1: Multiphase magneto-electro-elastic beam

3.3. CONSTITUTIVE EQUATIONS

The constitutive equations for the three-dimensional MEE solid considering the linear coupling among electric, magnetic, mechanical and thermal properties in the Cartesian co-ordinates can be written as follows:

$$\{\sigma\} = [C]\{\varepsilon\} - \{e\}E - \{q\}H - \{\alpha\}\Delta T \quad (3.4)$$

$$\{D\} = [e]^T \{\varepsilon\} + [\eta]\{E\} + [m]\{H\} + \{p\}\Delta T \quad (3.5)$$

$$\{B\} = [q]^T \{\varepsilon\} + [m]\{E\} + [\mu]\{H\} + \{\tau\}\Delta T \quad (3.6)$$

The material property matrices and vectors appearing in Eqs. (3.4) - (3.6) are explicitly described in *Appendix A*.

3.4. FINITE ELEMENT FORMULATION

The finite element model of a multiphase MEE beam is developed using an eight noded 3D brick element in a manner similar to that of the SFGMEE beam discussed in Chapter 2. The degrees of freedom associated with each node are three translational displacement components, one electric potential and one magnetic potential. The generalized translational displacement vector can be linked with the i^{th} ($i = 1, 2, 3, \dots, 8$) node of the element as follows:

$$\{d_{ii}\} = [U_x \ U_y \ U_w]^T \quad (3.7)$$

At any point within the element, the generalized degrees of freedom vectors can be represented in terms of the nodal vectors as outlined in Chapter 2 by Eq. (2.6) as follows:

$$\{d_t\} = [N_t] \{d_t^e\}, \ \{\phi\} = [N_\phi] \{\phi^e\}, \ \{\psi\} = [N_\psi] \{\psi^e\} \quad (3.8)$$

The various shape function matrices and nodal vectors represented in Eq. (3.8) can be expressed similar to Eq. (2.7). In the absence of free charge density, the Gauss law can be written as $\nabla D = 0$. Then the relation between the electric field E and the electric potential ϕ can be expressed as $E = -\nabla\phi$. Similarly, in the absence of free current density, the magnetic field can be expressed as $\nabla B = 0$, for which the relation between the magnetic field H and the magnetic potential ψ can be written as $H = -\nabla\psi$. Further, the gradient linear relationship between the electric field and the electric potential as well as magnetic field and the magnetic potential can be explicitly represented as in Eqs. (2.8) and (2.9), respectively. By expressing the strain vector $\{\varepsilon\}$, magnetic field vector $\{H\}$ and electric field vector $\{E\}$ as outlined in the Chapter 2 (Eq. (2.10)) the global equations of motion governing the static behaviour of multiphase MEE beam can be derived.

3.5. EQUATIONS OF MOTION

The equilibrium equations of the multiphase MEE beam subjected to in-plane thermal loading can be obtained in a similar manner to that of the SFGMEE beam

(Chapter 2, section 2.5). In order to obtain multiphase MEE beam, the different layers of the SFGMEE beam is assigned with the material properties of required volume fraction as tabulated in Table 2.1. Subsequently, employing the minimization of total potential energy principle in association with the constitutive equations, the final equations of motion governing the static response of multiphase MEE beam under varying in-plane thermal loads are obtained and are given by Eqs. (2.16) – (2.18).

3.6. RESULTS AND DISCUSSION

In this section, the numerical results are evaluated using the FE model derived in Chapter 2. The static behaviour of the multiphase MEE beam is analysed for different boundary conditions and temperature profiles. The multiphase MEE beam is assumed to be transversely isotropic in both the piezoelectric and piezomagnetic phases (symmetric about the z -axis). The one-dimensional temperature distribution profiles considered in Chapter 2 are considered here also for the analysis and are outlined in Table 3.1. In all cases, the maximum temperature (T_{max}) is considered to be 100 K. The material properties for the different volume fraction of the MEE material are tabulated in Table 2.1. The volume fraction (V_f) of the MEE beam is taken as 0.5 (50% BaTiO₃ and 50% CoFe₂O₄) unless otherwise stated. The dimensions of the beam considered for the analysis are length $a = 1$ m, width $w = 0.1$ m and thickness $h = 0.1$ m. The influences of volume fraction and pyroeffects on the direct quantities are studied for clamped-clamped (C-C) and clamped-simply supported (C-S) boundary conditions, and compared with the conventional approach (neglecting pyroeffects). Further, the effect of ratio of the span length to the thickness of the beam (a/h) on the potentials of the multiphase MEE beam has been investigated.

3.6.1. Static analysis of multiphase MEE beam: Clamped-Free boundary condition.

Influence of various temperature profiles on the structural behaviour of the clamped-free (C-F) multiphase MEE beam has been investigated. The geometrical parameters and the material properties of the multiphase MEE beam remain invariant. The different temperature profiles mentioned in Table 3.1 have been considered for the analysis. It has been observed from the results reported in the literature by Kondaiyah *et*

al. (2012) that for the clamped free multiphase MEE beam subjected to a uniform temperature rise of 100 K, the pyroeffects are dominant only in the variation of the electric potential. The same is verified in the present analysis and extended the analysis for different temperature profiles. It is observed from the numerical simulations that irrespective of the temperature profile, the predominant influence of the pyroelectric and pyromagnetic coupling effects exist only for the electric potential of the beam. Hence, for the sake of brevity, the comparison between the pyroeffects and the conventional approach is presented only for the electric potential as elucidated in Figs. 3.2(a) - (d). It may be observed from these figures that for all the temperature profiles the pyroeffects tend to improve the electric potential of the beam.

Table 3.1: In-plane temperature profiles varying along the multiphase MEE beam length

Notation used	In-plane temperature profiles	General representation	
Temperature profile-1	Uniform	$\Delta T_1 = T_{max} - T_0$	
Temperature profile-2	Half-Sine	$\Delta T_2 = T_{max} \left\{ \sin \left(\frac{\pi x}{a} \right) \right\}$	$0 \leq x \leq a$
Temperature profile-3	Linear	$\Delta T_3 = \{T_{max}\} x + \{T_i\}$	$0 \leq x \leq a$
Temperature profile-4	Bi-Triangular	$\Delta T_4 = \{T_{max}\} \times (1 - x)$ $\Delta T_4 = \{T_{max}\} \times (x)$	$0 \leq x \leq a/2$ $a/2 \leq x \leq a$

Figures 3.3(a) – (c) illustrate the influence of the temperature profiles on the displacement components along x -, y - and z -directions, respectively. It may be noticed from these figures that the longitudinal x -direction displacement component U_x varies almost linearly for all the temperature profiles and it is maximum at the free end of the MEE beam. Among all the temperature profiles, the maximum displacements of U_x , U_y and U_w is observed for the uniform temperature profile (temperature profile-1). The displacement components U_y and U_w are maximum at the region near the clamped end for the uniform and bi-triangular temperature profiles (temperature profile-4) while for

the half-sine (temperature profile-2) and linear temperature profiles (temperature profile-3), the maximum values of these displacement components are witnessed at the midspan and free end of the MEE beam, respectively. This may be due to the maximum temperature value at the respective regions. Figure 3.3(d) depicts the magnetic potential variation along the beam length for different temperature profiles. It may also be observed that the magnetic potential is maximum for the temperature profile-1 and 4 while the temperature profiles 2 and 3 exhibit negligible influence on the variation of magnetic potential.

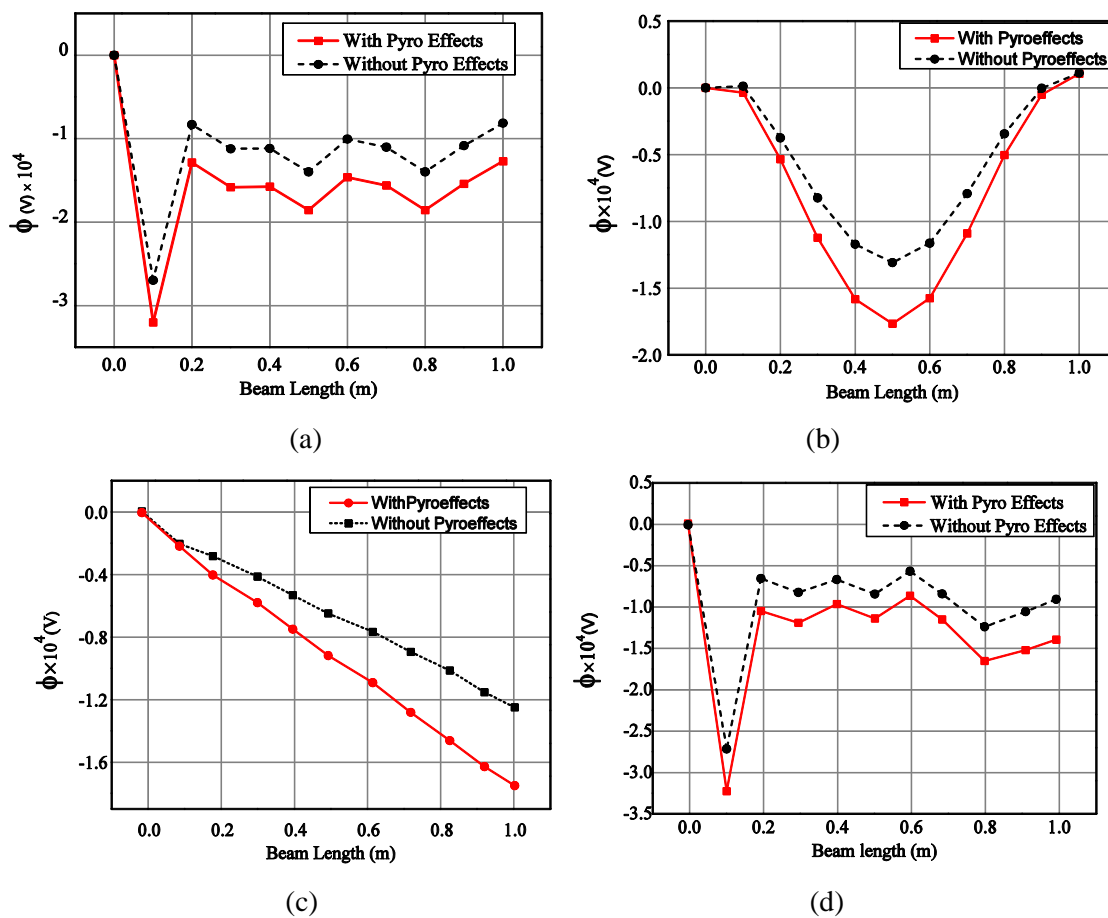


Figure 3.2: Variation of electric potential ϕ (a) uniform temperature (b) half-sine temperature (c) linear temperature profile (d) bi-triangular temperature profile for C-F boundary condition

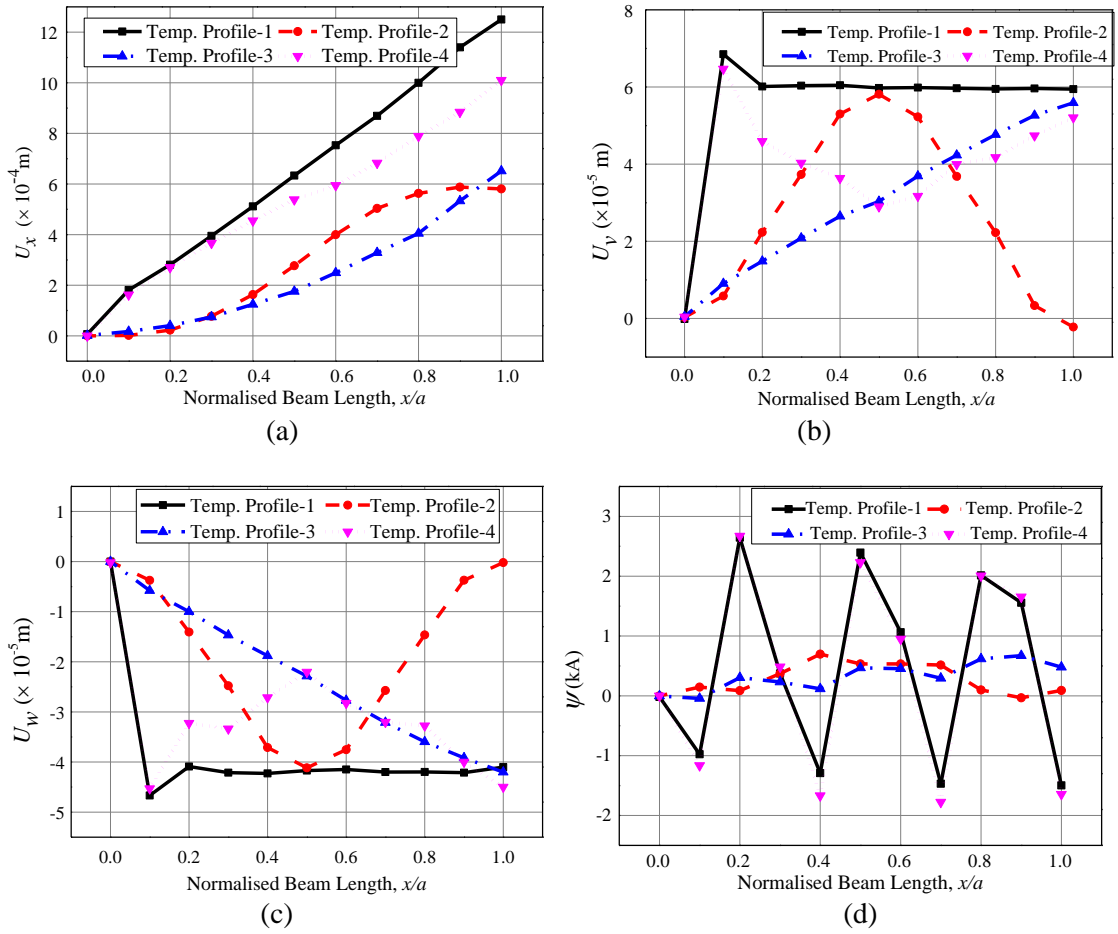
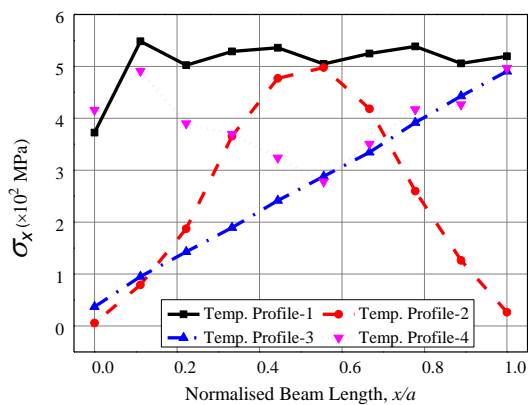


Figure 3.3: Effect of temperature profiles on displacement components (a) U_x (b) U_y (c) U_w (d) magnetic potential (ψ) for C-F boundary condition

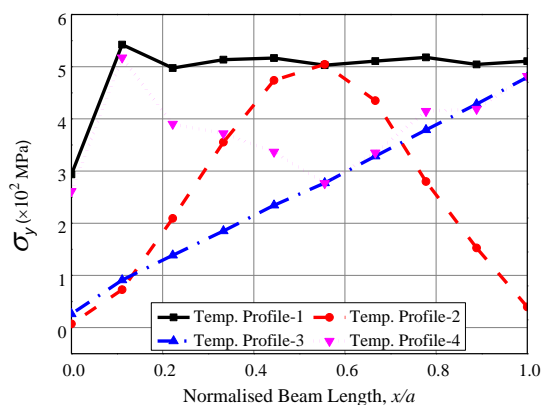
Figures 3.4(a) - (c) demonstrate the variation of normal stresses for clamped-free multiphase MEE beam subjected to different temperature profiles. It may be observed from these figures that for the temperature profile-1 and 4, the maximum normal stresses are observed near the clamped end of the beam. This may be due to the presence of constraints and highest temperature in the corresponding profile. For the temperature profile-2, the normal stresses vary symmetrically along the beam length while a linear variation in the normal stresses is observed for temperature profile-3. At the midspan of the beam, the maximum and the minimum normal stresses are noticed for temperature profile-2 and 4, respectively. This may be due to the fact that the temperature at the midspan is maximum for the temperature profile-2 and minimum for the temperature profile-4. It may also be seen from these figures (Figs. 3.4(a) - (c)) that the temperature profile-1 has a predominant effect on the normal stresses. The

variations of the transverse shear stresses τ_{xy} and τ_{xz} are plotted in Figs. 3.4(d) and (e), respectively. It may be observed that for the temperature profile-2, the shear stresses τ_{xy} and τ_{xz} are zero at the midspan with a symmetrical variation along the beam length. However, for the temperature profile-3, the shear stresses along the beam length are constant. It may also be observed from these figures (Figs. 3.4(d) and (e)) that among all the temperature profiles considered the shear stresses are maximum near the clamped end for temperature profile-4.

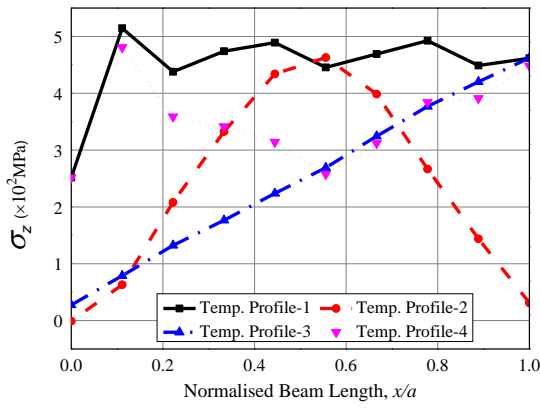
The effect of the temperature profiles on the variation of the electric displacements in x -, y - and z - direction are illustrated in Figs. 3.5(a) - (c), respectively. It may be observed from Fig. 3.5(a) that the similar trend of variation in electric displacement D_x is followed by the temperature profiles 1 and 4. Also, D_x for temperature profile-2 varies symmetrically along the beam length. The electric displacements D_y and D_z for the temperature profile-2 and 3 follows the corresponding temperature distribution as illustrated in Fig. 3.5(b) and (c), respectively. The magnetic flux density variation of the multiphase MEE beam with various temperature profile is shown in Figs. 3.6(a) – (c). It may be observed from these figures that the significant influence of the bi-triangular temperature profile on the magnetic flux densities B_x , B_y and B_z is noticed.



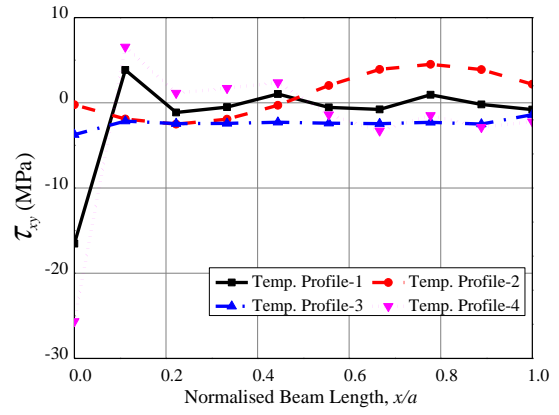
(a)



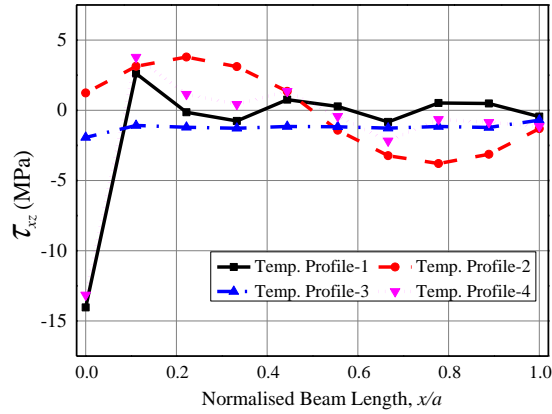
(b)



(c)

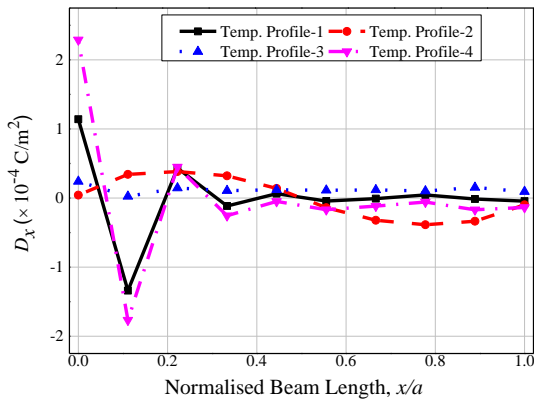


(d)

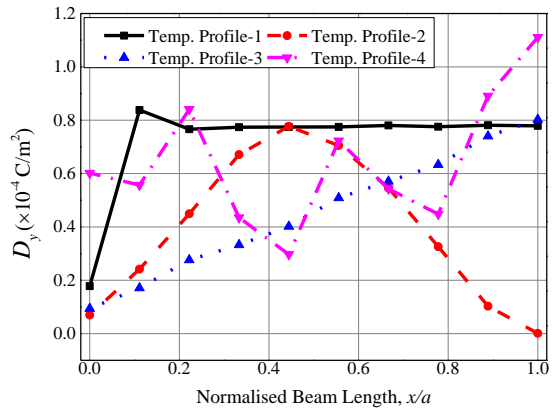


(e)

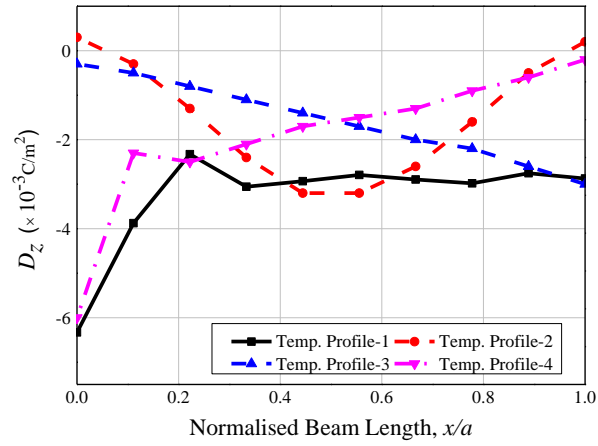
Figure 3.4: Effect of temperature profiles stress component (a) σ_x (b) σ_y (c) σ_z (d) τ_{xy} (e) τ_{xz} along the length of the C-F multiphase MEE beam



(a)

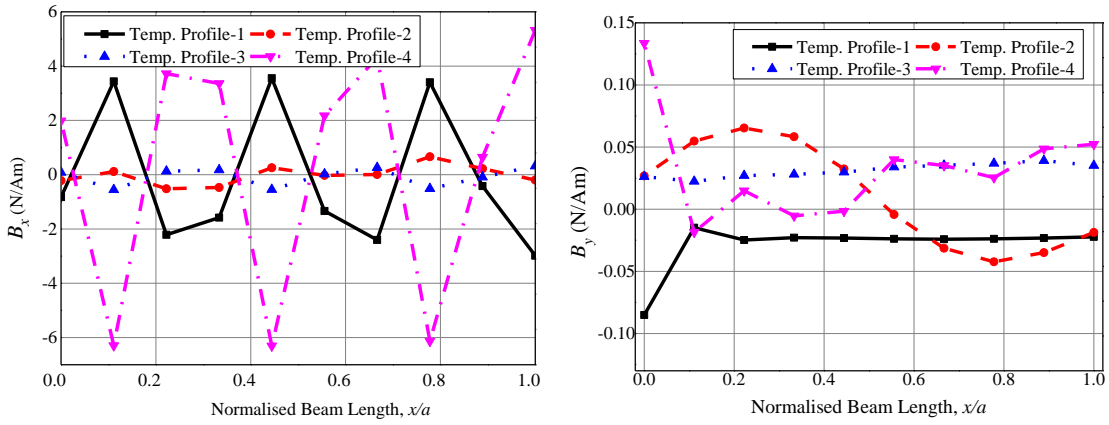


(b)



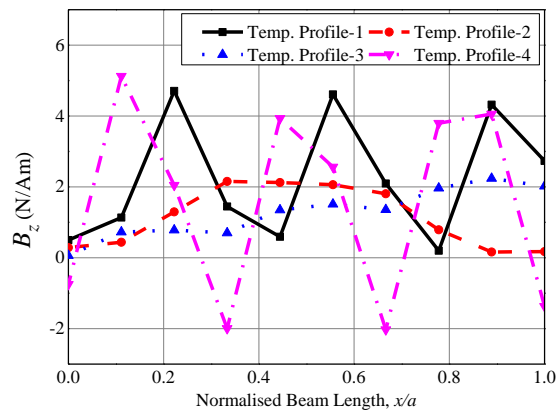
(c)

Figure 3.5: Effect of temperature profiles on electric displacements (a) D_x (b) D_y (c) D_z



(a)

(b)



(c)

Figure 3.6: Effect of temperature profiles on magnetic flux densities (a) B_x (b) B_y (c) B_z

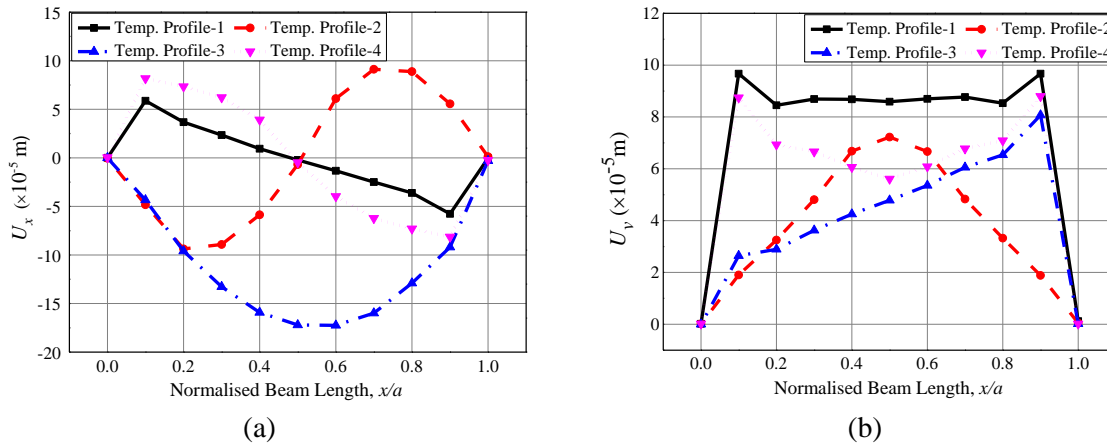
3.6.2. Static analysis of multiphase MEE beam: Clamped-Clamped boundary condition.

The clamped-clamped (C-C) multiphase MEE beam subjected to different temperature loading profiles is considered for the analysis. The effect of different temperature profiles on the direct quantities of the C-C multiphase MEE beam is presented in Figs. 3.7(a) - (e). It may be noticed from Fig. 3.7(a) that when the beam is subjected to temperature profile-1, the U_x displacement is minimum, and this varies accordingly with the temperature profile. At the midspan of the beam, U_x is the maximum for the temperature profile-3 while it is zero for the other temperature profiles. Fig. 3.7(b) depicts the variation of the U_v displacement along the beam length. It may be observed from this figure that the U_v reaches a higher value for the uniform temperature profile. For the temperature profile-3, U_v varies linearly along the beam length exhibiting the maximum value near the right end of the beam. However, U_v is maximum at the midspan for temperature profile-2. It is evident from Fig. 3.7(c) that U_w follows the same characteristics of the U_v .

Figure 3.7(d) depicts the electric potential under different loading conditions. It may be observed that for all the temperature profiles, the maximum value of electric potential is found at the region near the clamped end of the beam. It may also be noticed that at the midspan of the beam, temperature profile-2 exhibit minimum electric potential. Along the beam length, the electric potential varies linearly for temperature profile-3 while for the temperature profile-4 the electric potential follows the same trend as that of the temperature profile-1. Figure 3.7(e) demonstrates the effect of temperature loading on the magnetic potential. The maximum magnetic potential is observed when the multiphase MEE beam is subjected to a uniform temperature profile. For the half-sine temperature profile, the maximum magnetic potential may be observed at the midspan of the beam. It may also be noticed from this figure that among all the temperature loadings, the temperature profile-1 has a significant effect on direct quantities. This may be due to the constant pyro loads (pyroelectric and pyromagnetic) generated along the length of the multiphase MEE beam.

3.6.3. Static analysis of multiphase MEE beam: Clamped-Simply supported boundary condition

The variation of the direct quantities in a clamped-simply supported (C-S) multiphase MEE beam for different temperature profiles are depicted in Figs. 3.8(a)-(e). It may be observed from Fig. 3.8(a) that the temperature profile-1 has more influence on the longitudinal x -direction displacement U_x while temperature profile-3 has the least effect. Further, U_x varies linearly along the length of the beam from the clamped end to the free end. From Figs. 3.8(b) and (c), it is evident that the y -direction displacement U_y and the transverse z -direction displacement U_w follows the same trend as shown in Figs. 3.7(b) and (c), respectively. Figures 3.8(d) and (e) illustrate the effect of temperature loading on the electric potential and magnetic potential, respectively. It may be observed from Fig. 3.8(d) that the variation of the electric potential for the temperature profiles 1 and 4 are almost identical. The unconstrained axial movement at the left support results in significant change of the electric potential as compared to the clamped-clamped condition. However, for the temperature profile-2, the variation of the electric potential in the clamped-simply supported beam is completely reversed to that of the clamped-clamped MEE beam (Fig. 3.7(d)).



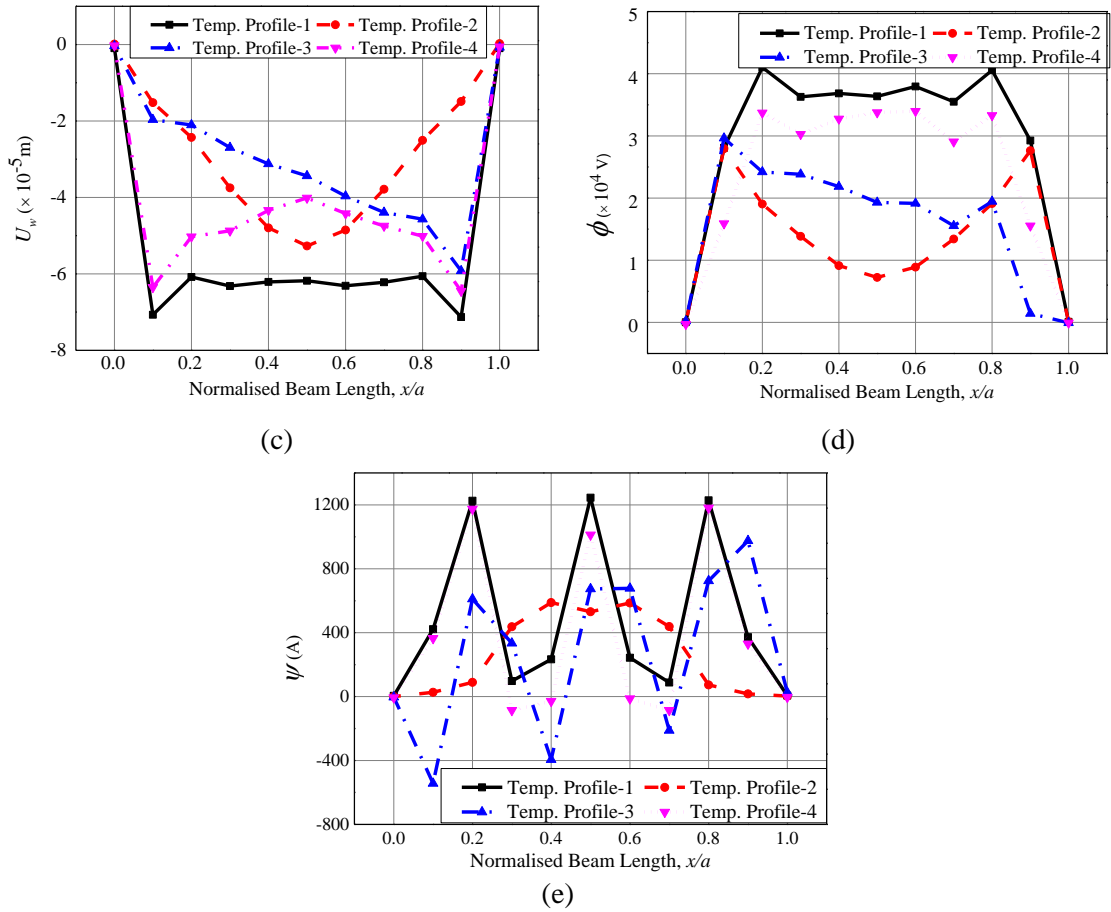


Figure 3.7: Variation of displacement components (a) U_x (b) U_y (c) U_w (d) electric potential ϕ (e) magnetic potential ψ for various temperature profiles for C-C boundary condition

Further, it may be noticed from Fig. 3.8(e) that the variation of magnetic potentials for all the temperature profiles resembles the variation of the magnetic potential of the C-C MEE beam but, with a little higher magnitude. A smooth variation of magnetic potential is observed for temperature profile-2.

3.7. PARAMETRIC STUDY

In this section, a particular attention has been paid to investigate the effect of various parameters such as product properties (pyroeffects), boundary conditions, volume fraction and aspect ratio of the multiphase MEE beam. The value of pyroelectric and pyromagnetic coupling constants depend on the volume fraction of the system. Hence, the parametric analysis of multiphase MEE beam considering different volume fraction becomes prominent.

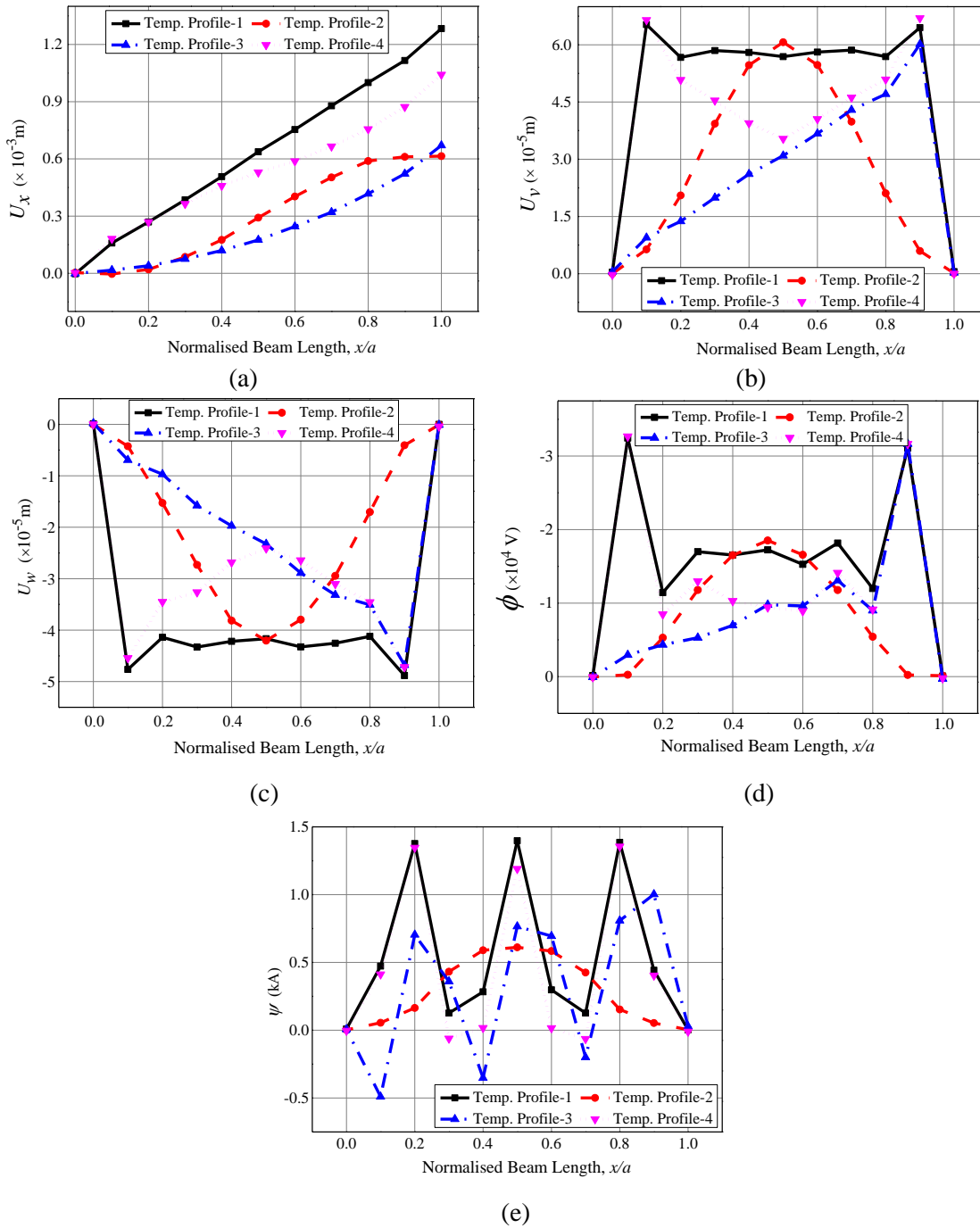


Figure 3.8: Variation of displacement components (a) U_x (b) U_v (c) U_w (d) electric potential ϕ (e) magnetic potential ψ for various temperature profiles for C-S boundary condition.

3.7.1. Effect of product properties

The clamped-clamped and clamped-simply supported multiphase MEE beams subjected to a uniform temperature rise of 100 K is considered for the analysis. The material properties corresponding to the volume fraction $V_f = 0.5$ are tabulated in Table 2.1. Influence of the product properties (pyroeffects) on the direct quantities

(displacements and potentials) of the system is evaluated. Figures 3.9 - 3.13 illustrate the comparison of the displacement components and the potentials for the C-C and the C-S multiphase MEE beams with considering the pyro effects and conventional approach (without pyroeffects). It may be observed from these figures (Figs. 3.9 - 3.11) that the pyroeffects are negligible on the displacement components (U_x, U_v, U_w) of the MEE beam. However, the pyroeffects exhibit a significant variation in the electric potential for both the C-C and C-S beam as depicted in Fig. 3.12. It may be due to the direct effect of the product properties on the electric potentials. For the C-S boundary condition, the pyroeffects tends to increase the electric potential of the beam whereas, for the C-C MEE beam, the pyroeffects reduces the electric potential. Figure 3.13 depicts that the pyroeffects have a negligible influence on the magnetic potentials.

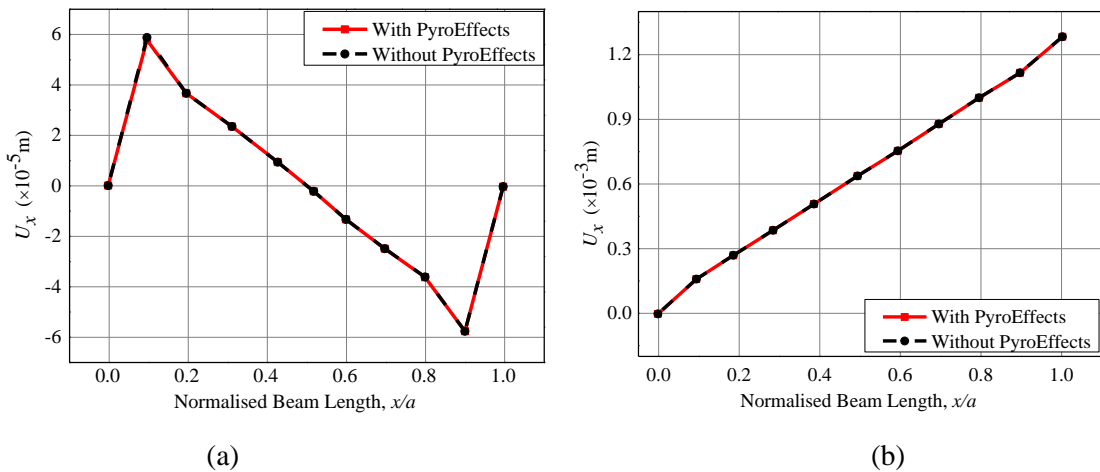


Figure 3.9: Effect of product property on U_x (a) C-C boundary condition (b) C-S boundary condition

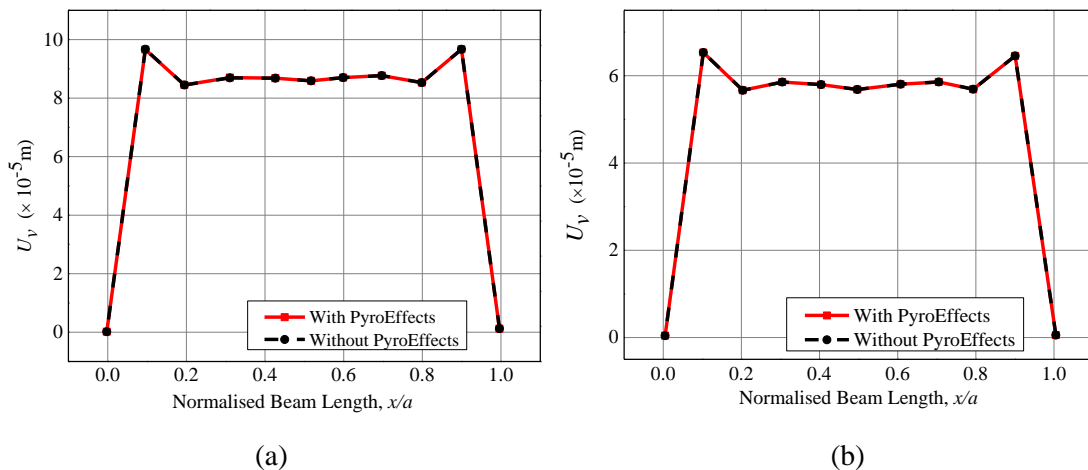


Figure 3.10: Effect of product property U_v (a) C-C boundary condition (b) C-S boundary condition

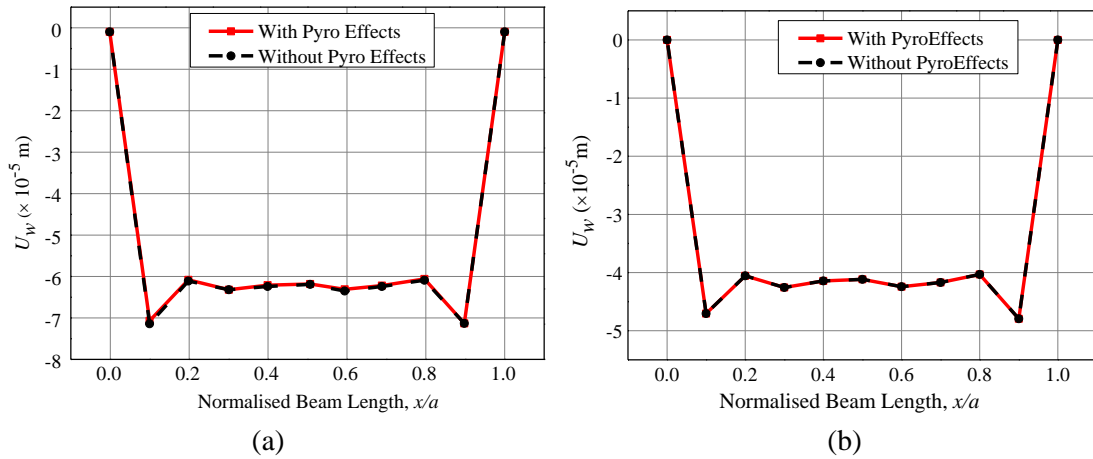


Figure 3.11: Effect of product property on U_w (a) C-C boundary condition (b) C-S boundary condition

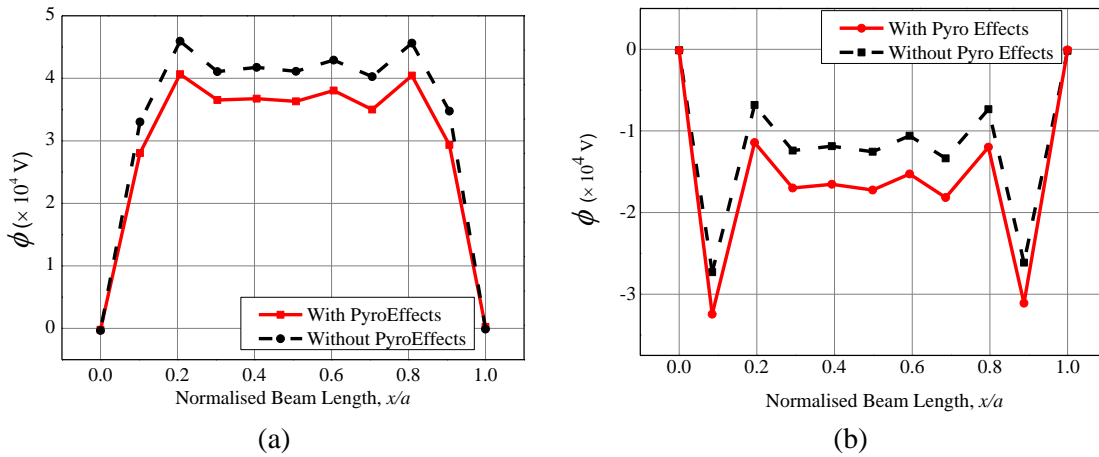


Figure 3.12: Effect of product property on electric potential ϕ (a) C-C boundary condition (b) C-S boundary condition

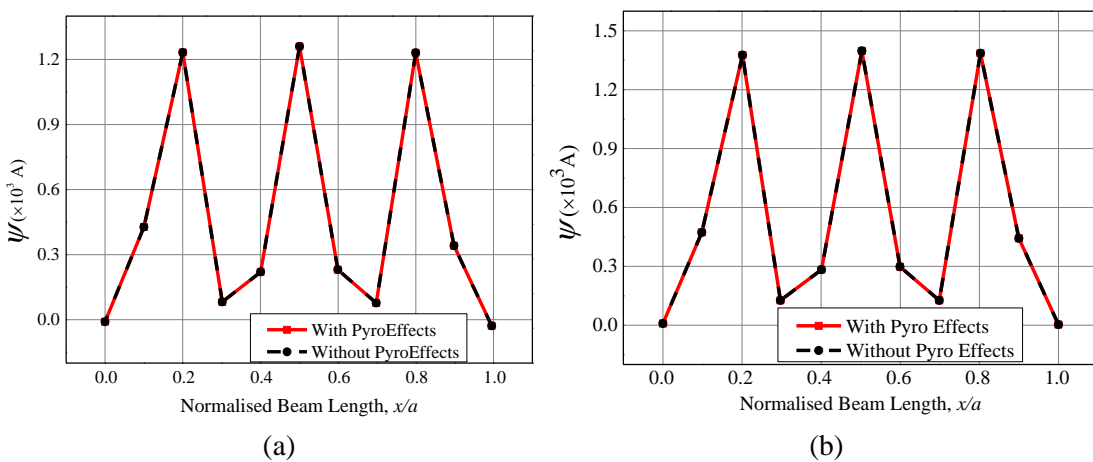


Figure 3.13: Effect of product property on magnetic potential ψ (a) C-C boundary condition (b) C-S boundary condition

3.7.2. Effect of Volume fraction

The effect of volume fraction of the BaTiO₃ and CoFe₂O₄ on the primary variables (displacements and potentials) of the multiphase MEE beam has been investigated by considering the uniform temperature rise of 100 K. The comparison between the primary variables of C-C and C-S MEE beams are shown in Figs. 3.14 - 3.18. It may be observed from Figs. 3.14(a) and (b) that the effect of volume fraction on the U_x is scanty for the C-C MEE beam while noticeable variations may be observed in case of C-S MEE beam. Also, it may be noticed from Figs. 3.14(a) and 3.15(a) that the maximum U_x and U_v occurs for the volume fraction $V_f = 0.0$. However, for the C-S MEE beam, it is observed for the volume fraction $V_f = 1.0$ as shown in Figs. 3.14(b) and 3.15(b). The maximum displacement U_w for the C-C and C-S MEE beam is observed for $V_f = 0.2$ and $V_f = 0.0$, respectively. It may also be seen from Figs. 3.17(a) and (b) that for the volume fraction $V_f = 0.2$, the electric potential is maximum for both the C-C and C-S multiphase MEE beams. Figures 3.18(a) and (b) illustrate that the pure piezomagnetic material ($V_f = 0.0$) exhibit the maximum magnitude of the magnetic potential. As expected, for the volume fraction $V_f = 1.0$, the magnetic potential is the minimum for both the cases.

3.7.3. Effect of aspect ratio (a/h) on the electric and magnetic potentials

The effect of span length to thickness ratio (a/h) on the electric and magnetic potentials has been investigated by considering the C-F and C-S MEE beam. Based on the a/h ratio, the multiphase MEE beams are classified as deep ($0.5 < a/h < 2$), moderate ($2 < a/h < 6$) and shallow beams ($a/h > 6$). In the present study, the uniform temperature rise $\Delta T = 100$ K is assumed and the numerical values of a/h considered for the analysis are 1.25, 3 and 10 for deep, moderate and shallow beams, respectively. Figures 3.19(a) and (b) depict the characteristic behaviour of the electric potential for the C-F and C-S beam, respectively. For both the boundary conditions, the deep MEE beam has a pronounced effect on the electric potential. Figures 3.20(a) and (b) demonstrate the magnetic potential variation for the C-F and C-S MEE beams, respectively. It can be observed from these figures that for the C-F condition, moderate beams ($a/h = 3$) exhibit highest magnetic potential, whereas for the C-S condition, it is witnessed for the deep beam.

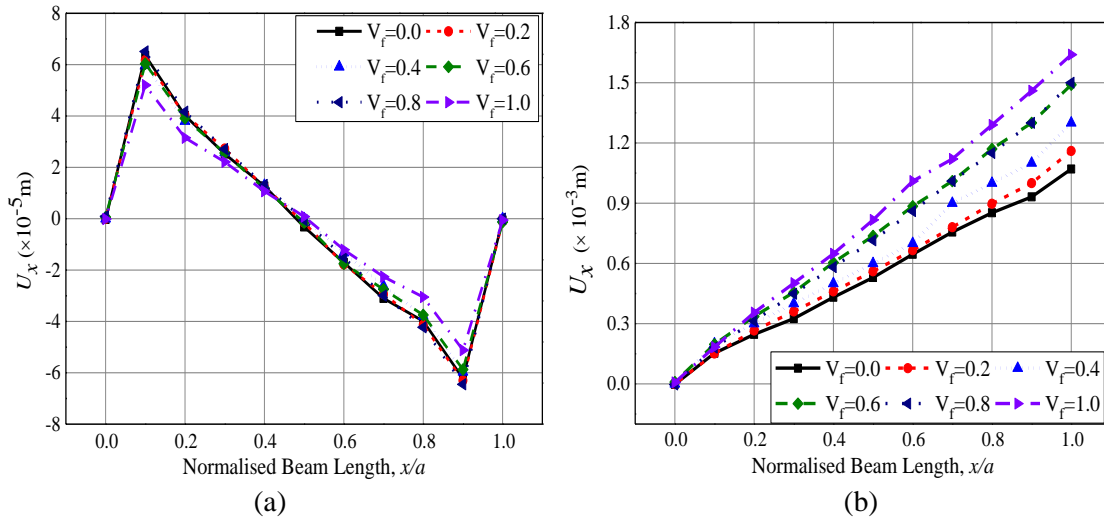


Figure 3.14: Effect of volume fraction on U_x (a) C-C boundary condition (b) C-S boundary condition

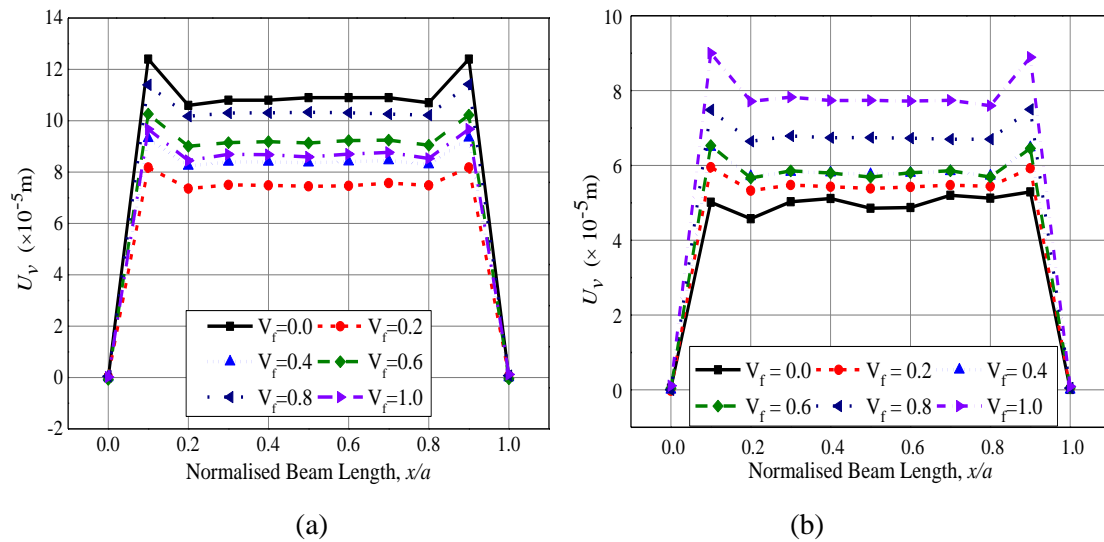


Figure 3.15: Effect of volume fraction on U_v (a) C-C boundary condition (b) C-S boundary condition

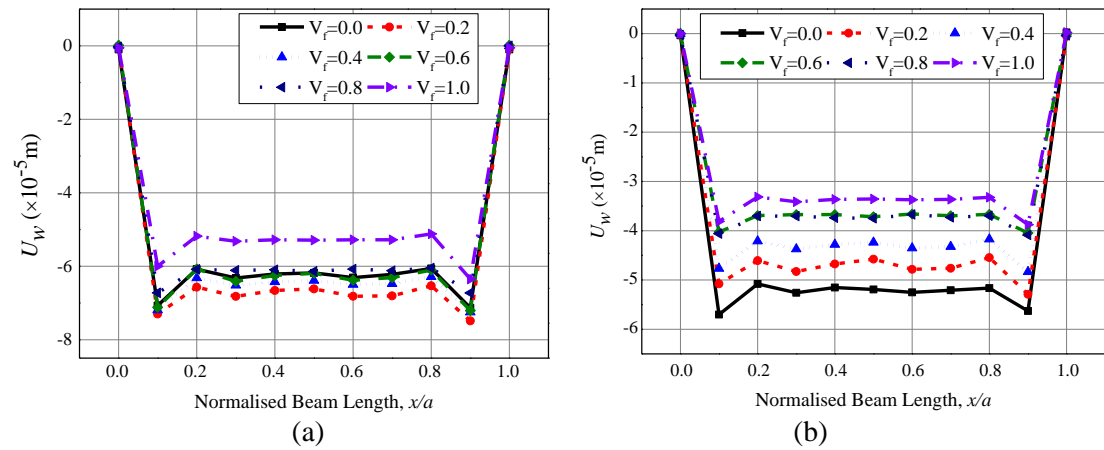


Figure 3.16: Effect of volume fraction on U_w (a) C-C boundary condition (b) C-S boundary condition

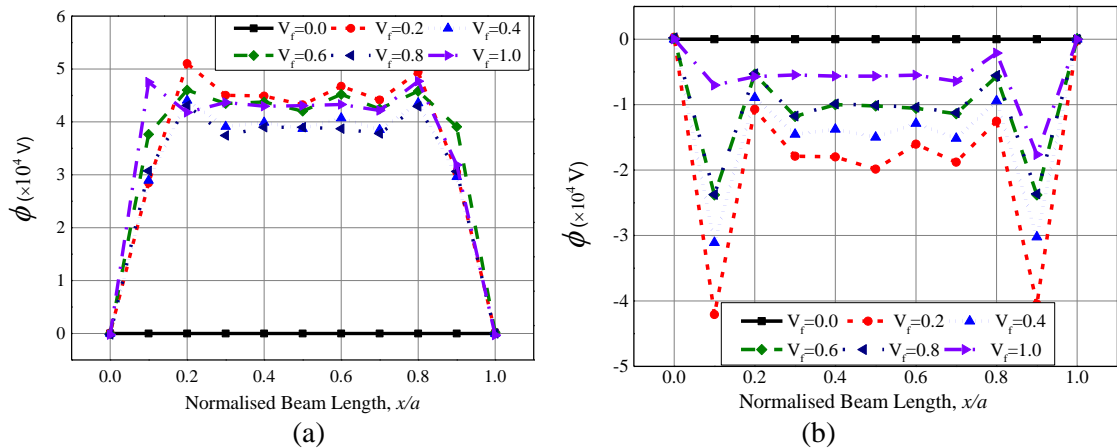


Figure 3.17: Effect of volume fraction on electric potential ϕ (a) C-C boundary condition (b) C-S boundary condition

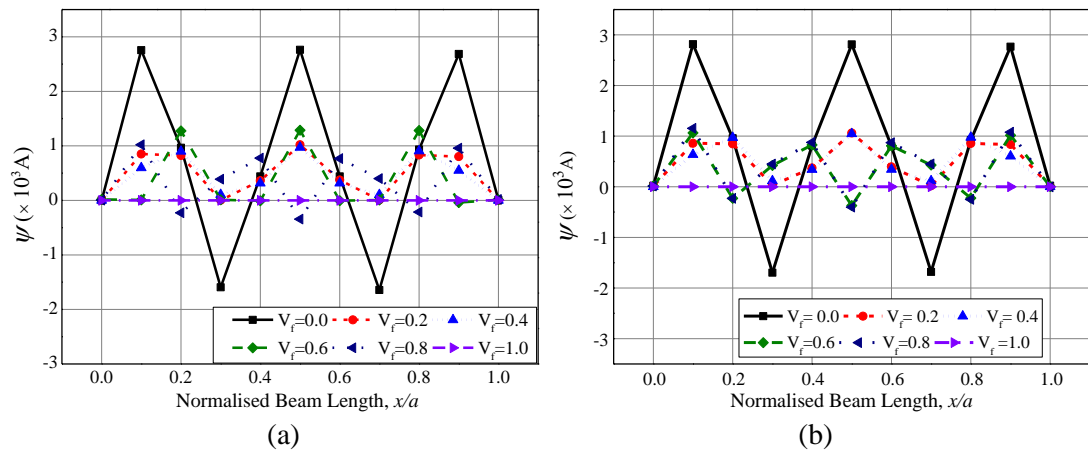


Figure 3.18: Effect of volume fraction on magnetic potential ψ (a) C-C boundary condition (b) C-S boundary condition

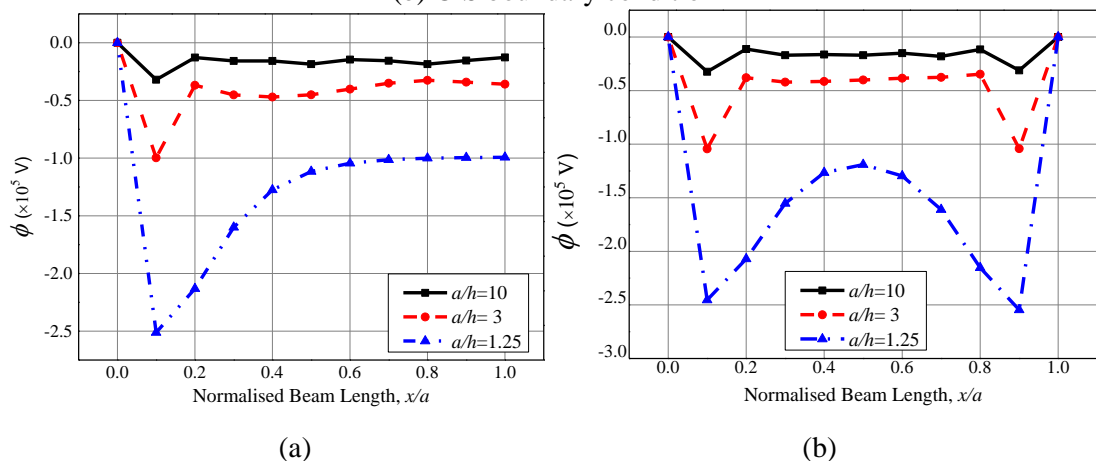


Figure 3.19: Effect of aspect ratio on the electric potential (a) C-F (b) C-S boundary condition

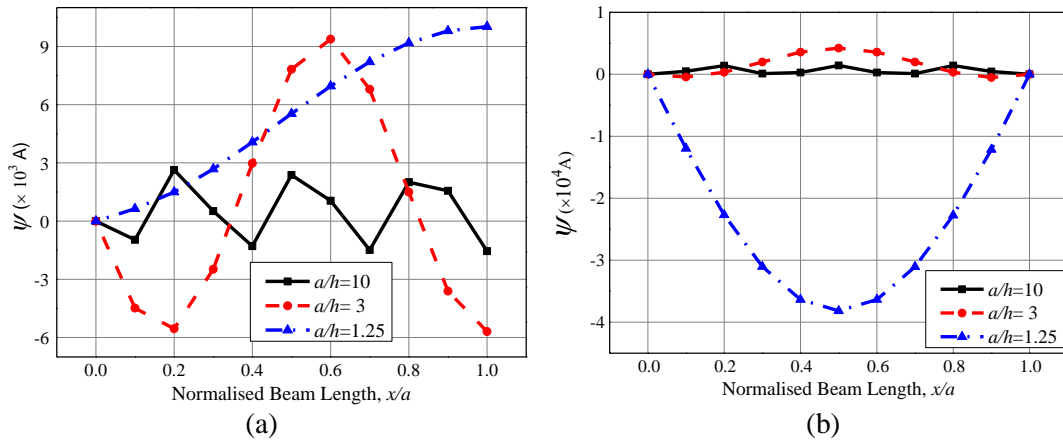


Figure 3.20: Effect of aspect ratio on the magnetic potential (a) C-F (b) C-S boundary condition

3.8. CONCLUSIONS

In this chapter, the static behaviour of the multiphase MEE beam subjected to the various form of thermal loading and boundary conditions is studied using the finite element method. Influence of the pyroelectric and pyromagnetic effects on the direct quantities of the multiphase MEE beam is analysed. Incorporating the Maxwell's electrostatic and electromagnetic equations, the variation of static parameters along the length of the MEE beam has been investigated. The results obtained in the present analysis revealed that irrespective of the boundary conditions and the temperature profiles, the pyroeffects exhibit negligible influence on the displacements and stresses of the MEE beam. It may due to the negligible indirect effects of the pyroeffects. Further, the pyroeffects show a dominant influence only on the electric potential developed in the system. The pyroeffects increase the electric potential for the C-F and C-S MEE beams while deteriorating effect is observed for the C-C condition. Among all the temperature profiles considered, the uniform temperature profile exhibit a significant effect on the direct quantities. The maximum electric potential is observed for clamped-clamped boundary condition at the region near the clamped end of the MEE beam. In addition, for the volume fraction $V_f = 0.2$, the maximum electric potential is noticed. The moderate multiphase MEE beam (aspect ratio $a/h = 3$) with clamped free boundary condition demonstrates the highest magnetic potential at the midspan of the beam, whereas for the clamped simply supported beam, it is observed for the aspect ratio $a/h = 1.25$.

Chapter 4

MULTIPHYSICS RESPONSE OF STEPPED FUNCTIONALLY GRADED MAGNETO-ELECTRO-ELASTIC PLATES IN THERMAL ENVIRONMENT

This chapter deals with evaluating the influence of temperature distributions on the coupled response of stepped functionally graded magneto-electro-elastic (SFGMEE) plates. In this regard, the coupled three-dimensional finite element formulation has been derived. A comparative study has been carried out to analyse the effect of stacking sequence, boundary conditions, length-to-width ratio, and the aspect ratio on the behaviour of the SFGMEE plate. A special attention has been devoted to analyse the pyroeffects (pyroelectric and pyromagnetic) corresponding to the different temperature profiles and aspect ratios. The external thermal field and geometric parameters exhibit significant influence on the static behaviour of SFGMEE plate.

Related article: Vinyas, M. and Kattimani, S.C. (2017), “Static analysis of stepped functionally graded magneto-electro-elastic plates in thermal environment: A finite element study”, *Composite Structures*, **178, 63-86.**

4.1. INTRODUCTION

In Chapter 2, the influence of different thermal fields on the static parameters of the stepped functionally graded magneto-electro-elastic (SFGMEE) beams has been investigated. In this chapter, a similar investigation is extended for SFGMEE plates. The main objective of this chapter is to investigate the influence of different through thickness temperature distributions on the variation of static parameters of SFGMEE plates. Considering the minimization of total potential energy principle and Maxwell's equations, a three-dimensional finite element (FE) formulation has been proposed. The different coupling effects corresponding to various volume fractions of Barium Titanate and Cobalt Ferrite at each layer of SFGMEE plates are accounted. Further, a special attention has been placed to study the influence of pyroeffects on the behaviour

of SFGMEE plates. In addition, the effect of geometrical parameters such as boundary conditions, aspect ratio and length-to-width ratio on the direct and derived quantities has been thoroughly studied. The effect of volume fraction, different loads and geometrical parameters on the influence of pyroeffects has also been evaluated.

4.2. PROBLEM DESCRIPTION

A schematic representation of SFGMEE plate occupying the domain $a \times b \times h$ with respect to a Cartesian coordinate system (x, y, z) is depicted in Fig. 4.1. The various boundary conditions considered for the analysis are illustrated in Figs. 4.2(a) – (e). The constraints corresponding to the different boundary conditions are given as follows:

Clamped edge (C):
$$U_x = U_v = U_w = \phi = \psi = 0 \quad (4.1)$$

Free edge (F):
$$U_x = U_v = U_w = \phi = \psi \neq 0 \quad (4.2)$$

Simply supported edge (S):
$$U_x \neq 0; U_v = U_w = \phi = \psi = 0 \text{ at } x = 0, a$$

$$U_v \neq 0; U_x = U_w = \phi = \psi = 0 \text{ at } y = 0, b \quad (4.3)$$

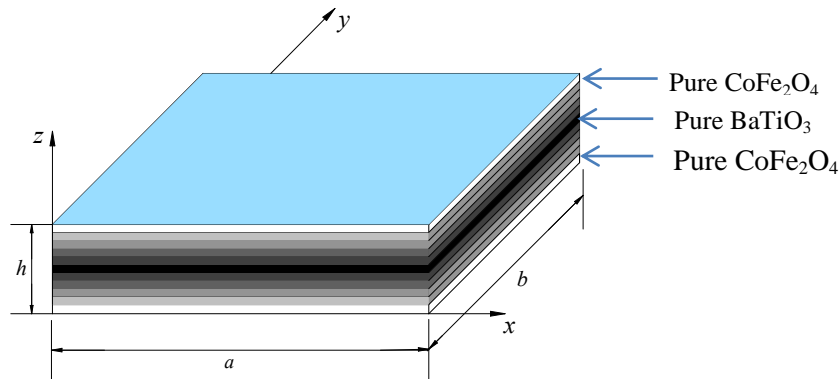
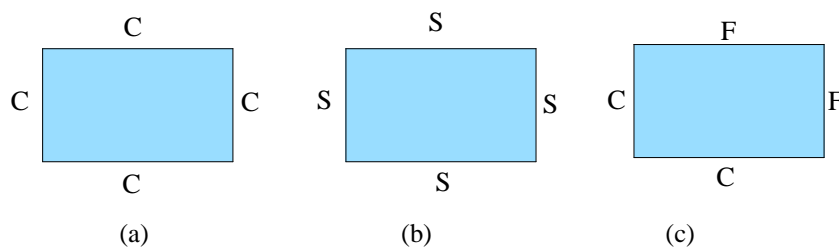


Figure 4.1: Schematic representation of SFGMEE plate



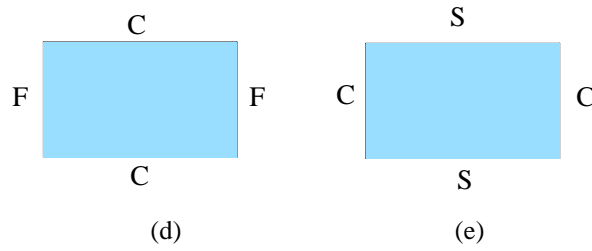


Figure 4.2: Boundary conditions (a) clamped on all edges (CCCC) (b) simply supported on all edges (SSSS) (c) adjacent edges clamped (CFFC) (d) opposite edge clamped (FCFC) (e) opposite edges simply supported (CSCS)

4.3. FINITE ELEMENT FORMULATION AND GOVERNING EQUATIONS OF MOTION

A three-dimensional finite element formulation (Eqs. (2.6) – (2.11)) and the governing equations of motion (Eqs. (2.12) – (2.23)) derived in the Chapter 2 are adopted for the analysis of SFGMEE plate also. The boundary conditions enforced on the plate are modified as per the required plate configuration. In addition, the temperature profiles (in-plane and through thickness) used in the analysis of beams are considered here for the plate also.

4.4. TEMPERATURE DISTRIBUTION IN SFGMEE PLATE

The temperature distributions considered in Chapter 2 (Eq. (2.28) and Eqs. (2.31)-(2.33)) are considered again for the analysis of plate subjected to through thickness temperature distributions.

4.5. RESULTS AND DISCUSSION

The effect of various temperature distributions on the direct and derived parameters of the SFGMEE plate is evaluated using the FE formulation derived in Chapter 2. The SFGMEE plate dimensions considered for the analysis are the length of the plate $a = 0.3$ m, width $b = 0.3$ m and the thickness $h = 0.006$ m. The boundary conditions considered for the SFGMEE plate is illustrated in Figs. 4.2(a) – (e). By reducing the present FE model of multilayered MEE plate to a single layer MEE plate, the results are verified with those established by Kondaiah *et al.* (2013). To this end, the material properties tabulated in Table 2.1 (Kondaiah *et al.* 2012) are considered in the present analysis. It is evident from Figs. 4.3(a) – (d) that an excellent agreement is obtained using the present FE formulation.

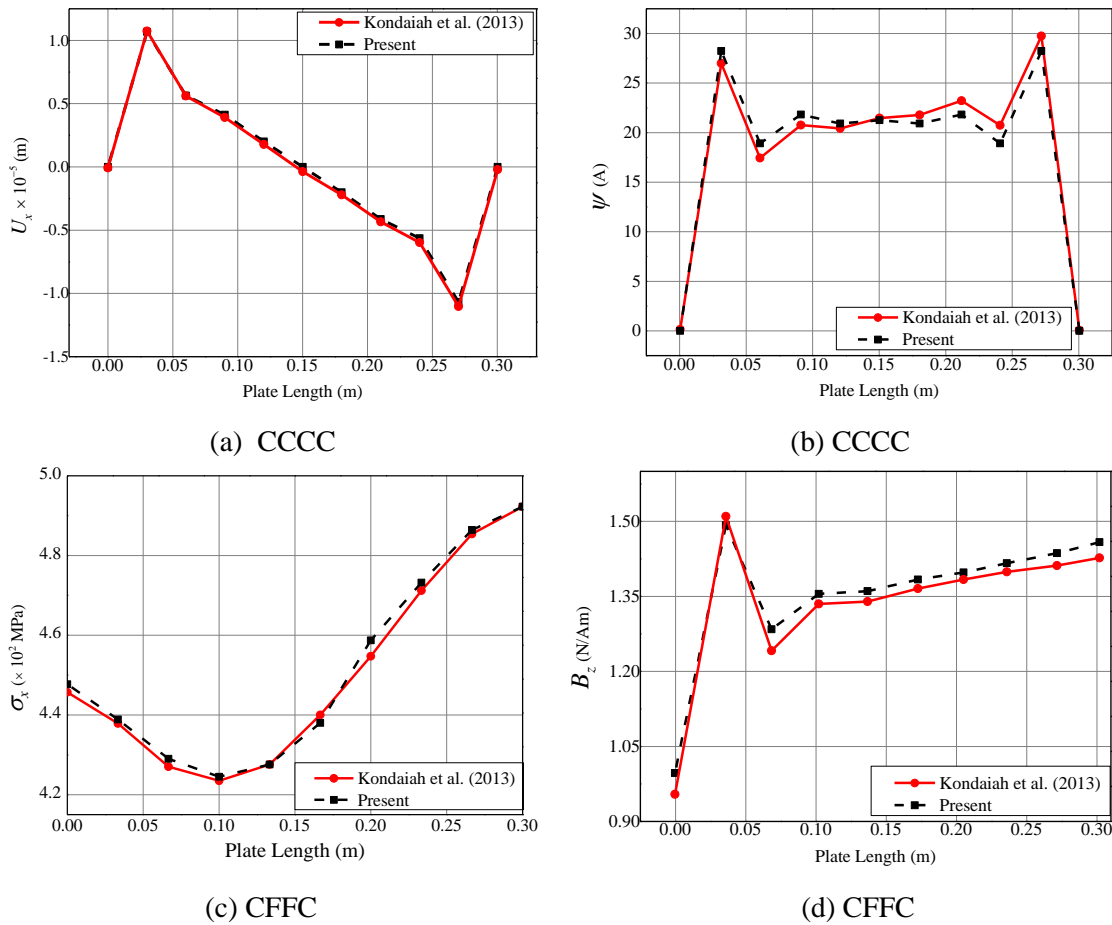


Figure 4.3: Verification plots (a) displacement component in x -direction U_x (b) magnetic potential (c) normal stress σ_x (d) magnetic flux density B_z of MEE plate

Further justification for the correctness of the FE formulation is provided by considering two different examples of FG-MEE plate subjected to mechanical loads. Firstly, a two-layered square plate with identical layer thickness illustrated by Sladek *et al.* (2013) is solved with the help of present FE formulation. The bottom layer is assumed to be made of homogeneous properties, whereas the top layer is comprised of MEE material. In addition, two trials are carried out with different material corresponding to the bottom layer. The first material with a higher value of stiffness coefficients is represented by #B and the material used for the second trial is denoted by #T. The material properties corresponding to these homogeneous layers and MEE material are tabulated in Table 4.1 and Table 4.2, respectively. The boundary conditions and loading parameters of the layered plate are maintained identical to that of Sladek *et al.* (2013). From Figs. 4.4(a) and (b), it can be observed that for both the clamped plate and simply supported plate, the results show an excellent agreement

with Sladek *et al.* (2013). Further, the static problem of FG-MEE plate subjected to a sinusoidal mechanical load (Wang and Pan (2011)) is also considered for the validation. For the purpose of comparison, the MEE plate made of exponentially functionally graded material (E-FGM) with exponential factor $k = 0$ is considered. The boundary conditions and material properties are chosen identical to Wang and Pan (2011). From Table 4.3, it can be observed that the present results agree very well with Wang and Pan (2011). Further, the convergence study of the present FE model is depicted in Fig. 4.5 considering the electric potential ϕ of FCFC MEE plate. It can be observed from this figure that for the mesh size of $10 \times 10 \times 12$ elements, a good convergence of the present FE formulation can be achieved. Moreover, numerical examples are presented to evaluate the effect of various temperature distributions, boundary conditions, pyroeffects and aspect ratio on the behaviour of MEE plate.

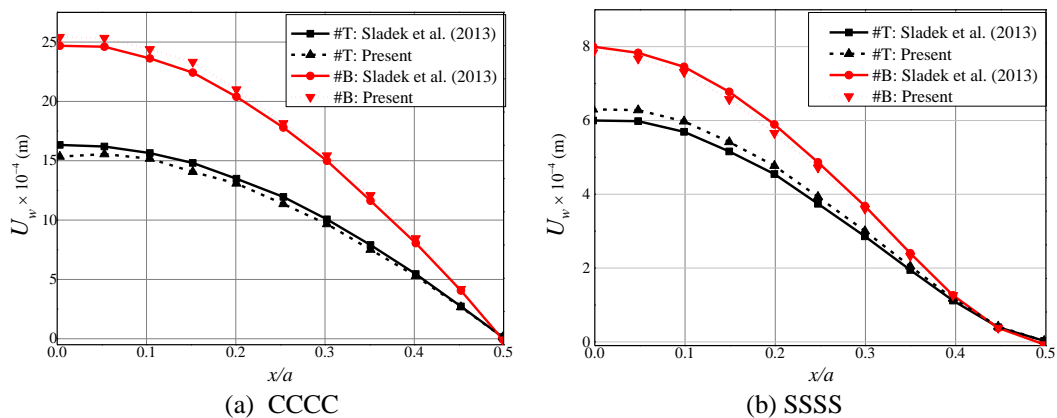


Figure 4.4: Validation of transverse displacement U_w of two layered plate (Sladek *et al.*, 2013).

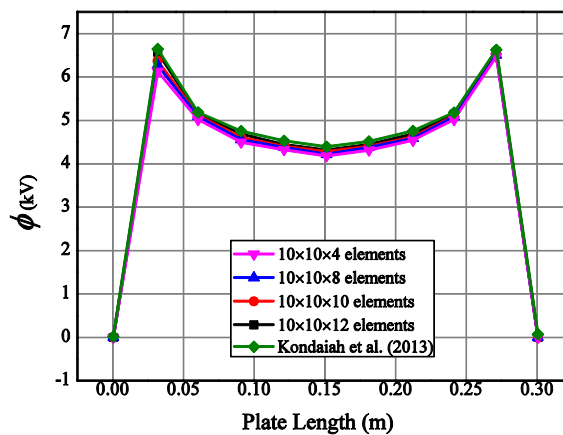


Figure 4.5: Convergence of electric potential ϕ

4.5.1. Effect of thermal loading

In this section, the influence of through thickness temperature distributions (Eq. (2.28) and Eqs. (2.31) – (2.33)) on the static parameters of SFG-BFB MEE plate is analysed. The MEE plate is considered to be clamped on all the edges. Figures 4.6(a) – (c) represent the variation of displacement components U_x , U_v and U_w , respectively. It can be interpreted from these figures that the uniform temperature load has a significant influence on the variations of U_x , U_v and U_w across the plate thickness while the parabolic temperature distribution has a lesser contribution on the displacement components of the plate. The displacement components U_x , U_v and U_w varies symmetrically across the plate thickness for the uniform and bi-triangular temperature distributions. Meanwhile, U_w is zero at the middle layer of SFG-BFB MEE plate. For the linear and parabolic temperature profiles, U_x is maximum at the top layer while U_v and U_w are found to be higher in the bottom layer of the SFG-BFB MEE plate. This may be attributed to the corresponding temperature distribution applied over the plate. The uniform temperature rise results in a linear variation of the electric potential ϕ (Fig. 4.6(d)) across the plate thickness, whereas the symmetric variation is observed for bi-triangular temperature distribution. Also, one can draw the same conclusion with respect to the distribution of magnetic potential ψ as shown in Fig. 4.6(e). It is worth noting that for the uniform and bi-triangular temperature profiles, the electric potential and magnetic potential are zero at the middle layer of the SFGMEE plate.

Table 4.1: Material coefficients of #B and #T materials used in Sladek *et al.* (2013)

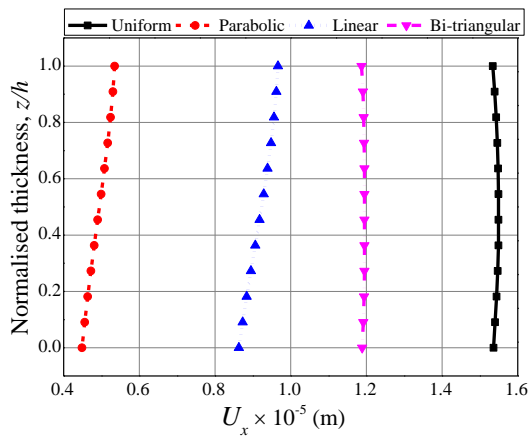
Material 1: #B ($\times 10^{10} \text{ Nm}^{-2}$)		Material 2: #T
$C_{11}^{(1B)}$	10.989	$C_{ij}^{(1T)} = C_{ij}^{(1B)} / 2$
$C_{12}^{(1B)}$	3.297	
$C_{22}^{(1B)}$	10.989	
$C_{66}^{(1B)}$	3.846	
$C_{44}^{(1B)} = C_{55}^{(1B)}$	3.846	

Table 4.2: Properties of MEE material used in Sladek *et al.* (2013)

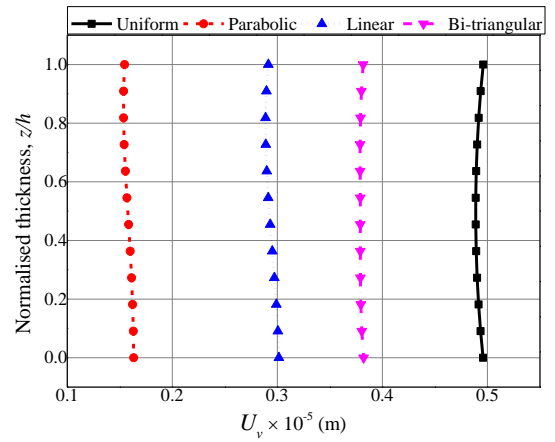
Material constants	Values	Material constants	Values
$c_{11} = c_{22}$	$22.6 \times 10^{10} \text{ Nm}^{-2}$	$d_{31} = d_{32}$	$290.2 \text{ NA}^{-1} \text{ m}^{-1}$
c_{12}	$12.4 \times 10^{10} \text{ Nm}^{-2}$	d_{33}	$350 \text{ NA}^{-1} \text{ m}^{-1}$
c_{33}	$21.6 \times 10^{10} \text{ Nm}^{-2}$	d_{15}	$275 \text{ NA}^{-1} \text{ m}^{-1}$
c_{66}	$5.1 \times 10^{10} \text{ Nm}^{-2}$	α_{11}	$5.367 \times 10^{-12} \text{ Ns (VC)}^{-1}$
$c_{44} = c_{55}$	$4.3 \times 10^{10} \text{ Nm}^{-2}$	α_{33}	$2737.5 \times 10^{-12} \text{ Ns (VC)}^{-1}$
$e_{31} = e_{32}$	-2.2 Cm^{-2}	γ_{11}	297 Wb (Am)^{-1}
e_{15}	5.8 Cm^{-2}	γ_{33}	$83.5 \text{ Wb (Am)}^{-1}$
h_{33}	$6.35 \times 10^{-9} \text{ C(Vm}^{-1})$	ρ	7500 kg m^{-3}
h_{11}	$5.64 \times 10^{-9} \text{ C(Vm}^{-1})$		

Table 4.3: Comparison study of the direct quantities of E-FGM MEE plate

$k = 0$			
	Present FEM	Wang and Pan (2012)	% Error
$U_x (10^{-14} \text{ m})$	26.26	27.13	3.24
$U_v (10^{-14} \text{ m})$	-26.25	-27.13	3.24
$U_w (10^{-14} \text{ m})$	356.2	346.8	-2.71
$\phi (10^{-3} \text{ V})$	1.69	1.65	-2.42
$\psi (10^{-7} \text{ A})$	-14.03	-13.66	-2.64



(a)



(b)

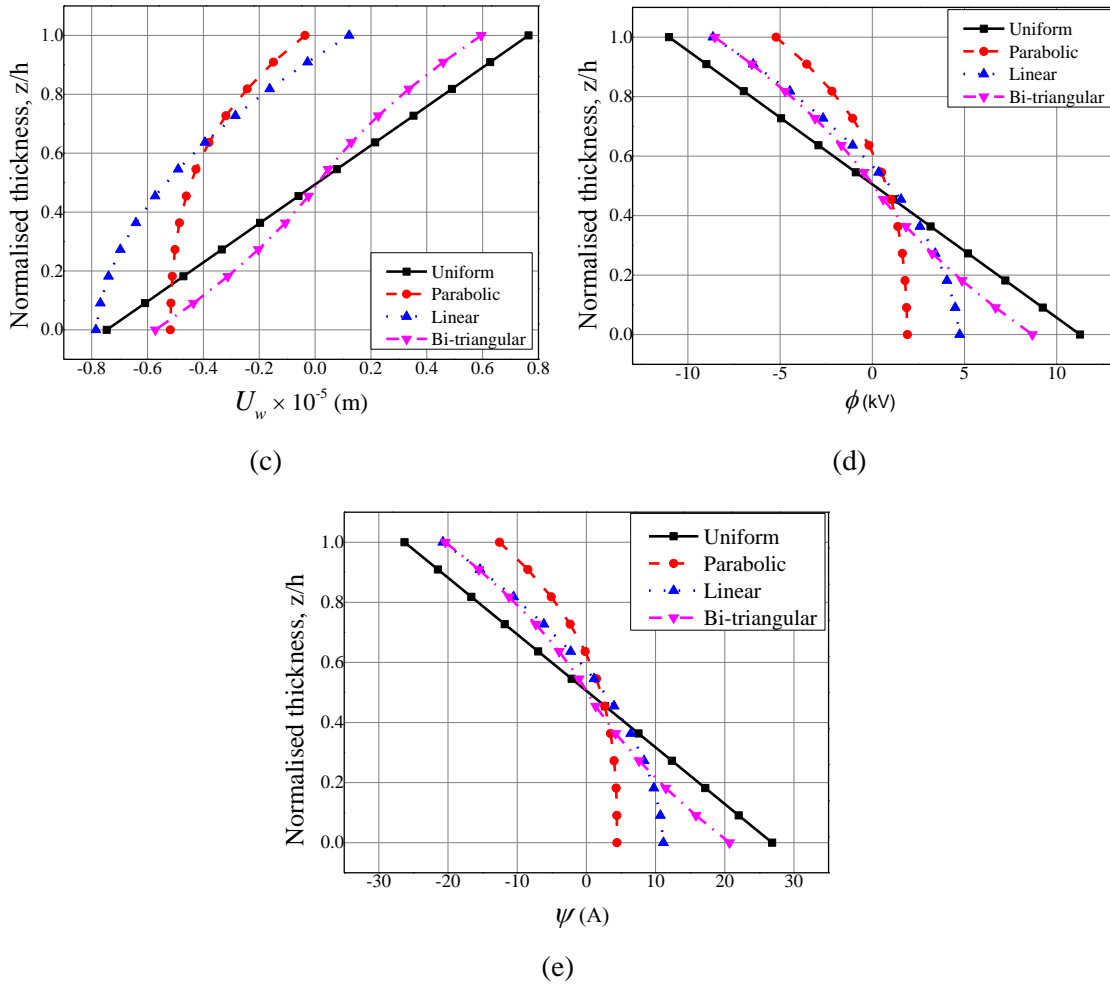


Figure 4.6: Effect of temperature distributions on displacement components (a) U_x (b) U_y (c) U_w (d) electric potential ϕ (e) magnetic potential ψ

Further, the study is extended to evaluate the influence of various through thickness temperature distributions on the derived quantities. It may be noticed from the results plotted in Fig. 4.7(a) that the normal stress σ_x varies accordingly with the temperature distribution. For the uniform temperature rise, the normal stress σ_x remains almost constant across the plate thickness. Likewise, for a bi-triangular temperature distribution, the maximum stress σ_x is witnessed at the midplane of the SFGMEE plate. It is interesting to note that irrespective of the temperature profile, the maximum normal stress σ_x is noticed at the top layer of the SFG-BFB MEE plate. The possible reason may be the appearance of highest temperature at the top layer for the corresponding temperature profile. Also, it can be deduced that among all the through thickness temperature distributions considered, a predominant effect of the uniform

temperature distribution prevails on σ_x . This may be due to the development of constant pyroloads generated through the thickness of the SFG-BFB MEE plate. From Fig. 4.7(b), a significant effect of linear temperature distribution is noticed with respect to the variation of shear stress component τ_{xz} . Moreover, at the midplane of the SFGMEE plate, the maximum value of τ_{xz} is noticed for the linear temperature distribution and parabolic temperature distributions, whereas for the bi-triangular and uniform temperature distribution, it is found to be the minimum. The variation of stress component τ_{xy} across the plate thickness is depicted in Fig. 4.7(c) while Figs. 4.8(a) and (b) display the variation of magnetic flux density components B_x and B_z , respectively. It is clearly seen from Figs. 4.8(c) and (d) that the linear temperature distribution has a significant influence on D_x which is followed by the parabolic, uniform, and bi-triangular temperature profiles. But, the uniform temperature distribution exhibits a predominant effect on D_z .

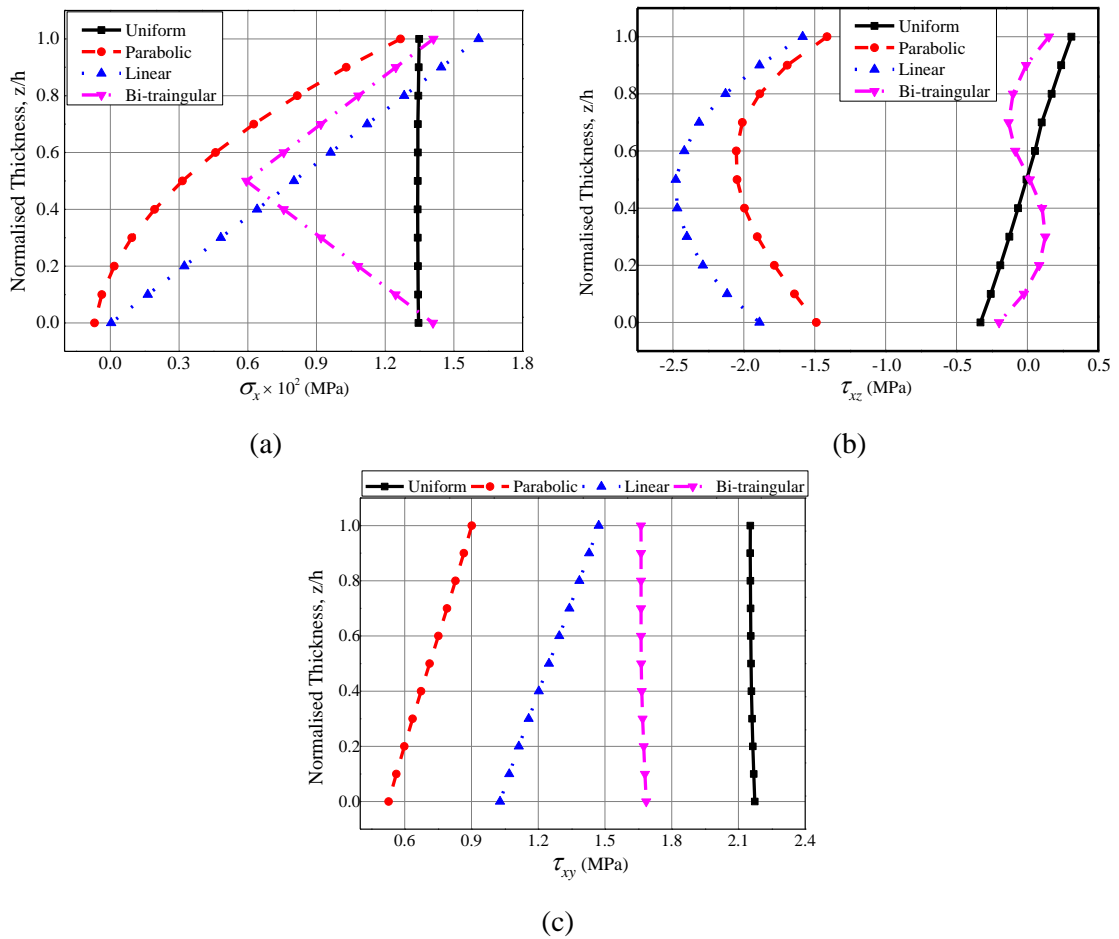
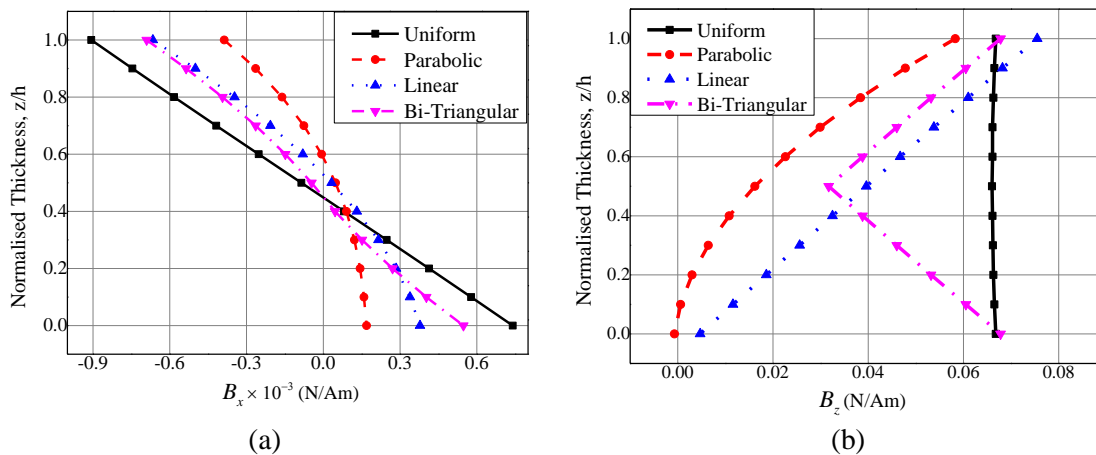
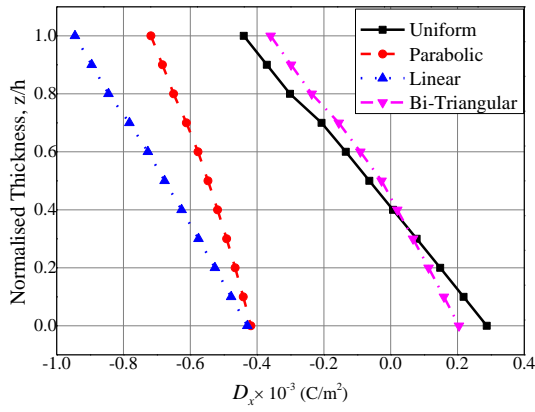


Figure 4.7: Effect of temperature distributions on (a) normal stress σ_x (b) shear stress τ_{xz} (c) shear stress τ_{xy}

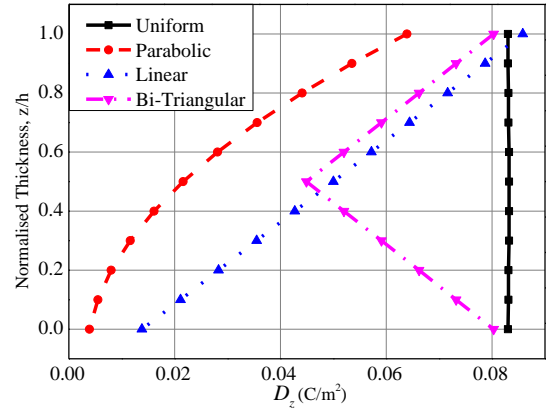
4.5.2. Effect of boundary conditions

The effect of various boundary conditions (see Figs. 4.2(a) – (e)) on the direct and derived quantities of SFG-BFB MEE plate is investigated by considering the bi-triangular temperature distribution. It can be observed from Fig. 4.9(a) that U_x is higher for SSSS MEE plate as compared to other boundary conditions. This may be attributed to the free movement of the plate in x -direction. Further, the displacement component U_v and U_w are higher for CFFC and CCCC MEE plates as shown in Figs. 4.9(b) and 4.9(c), respectively. The distribution of electric potential for the various boundary conditions is represented in Fig. 4.9(d). It can be observed from this figure that CCCC boundary edge has a significant effect on the electric potential while SSSS boundary edge exhibits a minimal effect. In contrast to other boundary edges, a dominant effect of CFCF boundary edge on the magnetic potential is witnessed as indicated in Fig. 4.9(e). Further, a significant influence of CCCC boundary condition is noticed on the variation of normal stress component σ_x as shown in Fig. 4.10(a). For all the boundary conditions, the maximum value of σ_x is witnessed at the midplane of the SFGMEE plate. It may be due to the fact that the temperature is higher at the midspan. It may also be noticed from Fig. 4.10(b) that a substantial effect of SSSS boundary condition exists on the shear stress τ_{xz} while CFFC boundary condition has a significant effect on τ_{xy} as depicted in Fig. 4.10(c). Figures 4.11(a) – (c) illustrate the distribution of B_x , B_y , and B_z , respectively. From these figures (Figs. 4.11(a)-(c)), it may be observed that the SSSS boundary condition has a predominant influence on the variation of B_x and B_z .





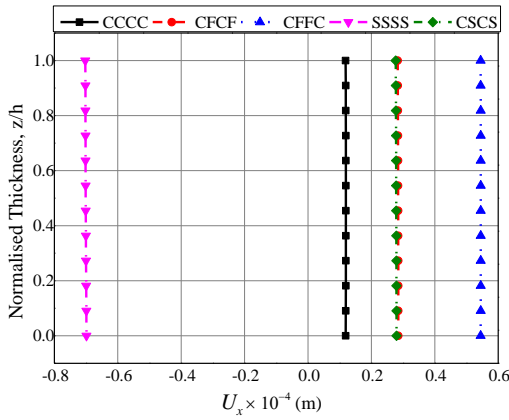
(c)



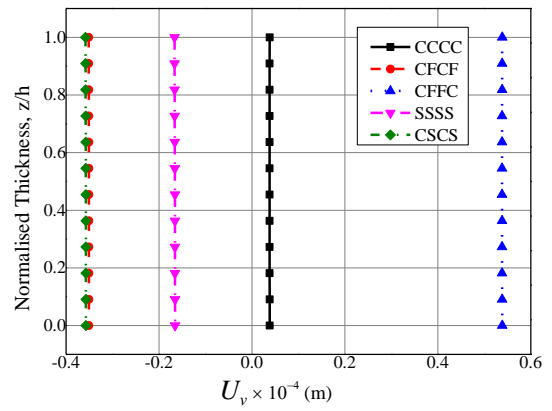
(d)

Figure 4.8: Effect of temperature distributions on (a) magnetic flux density B_x (b) magnetic flux density B_z (c) electric displacement D_x (d) electric displacement D_z

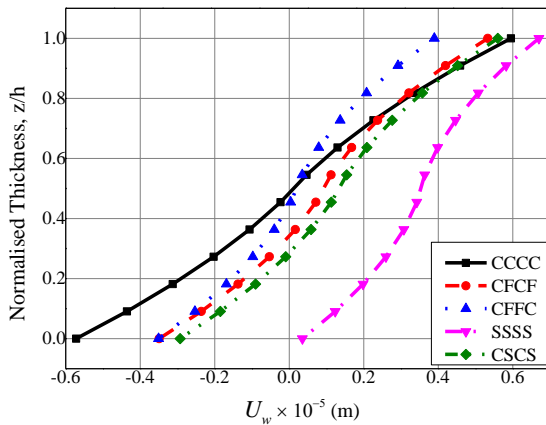
In addition, it is also noticed that the CFCF MEE plate results in a minimum B_y . Further, the numerical evaluation is extended to compute D_x , D_y , and D_z . From Figs. 4.12 (a) – (c), it is observed that in contrast to other boundary conditions, CCCC MEE plate results in a higher electric displacement.



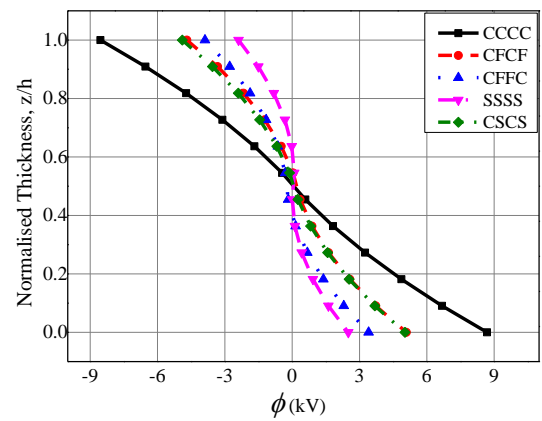
(a)



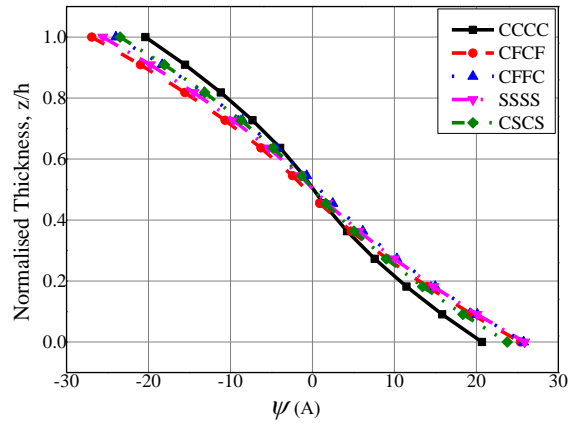
(b)



(c)

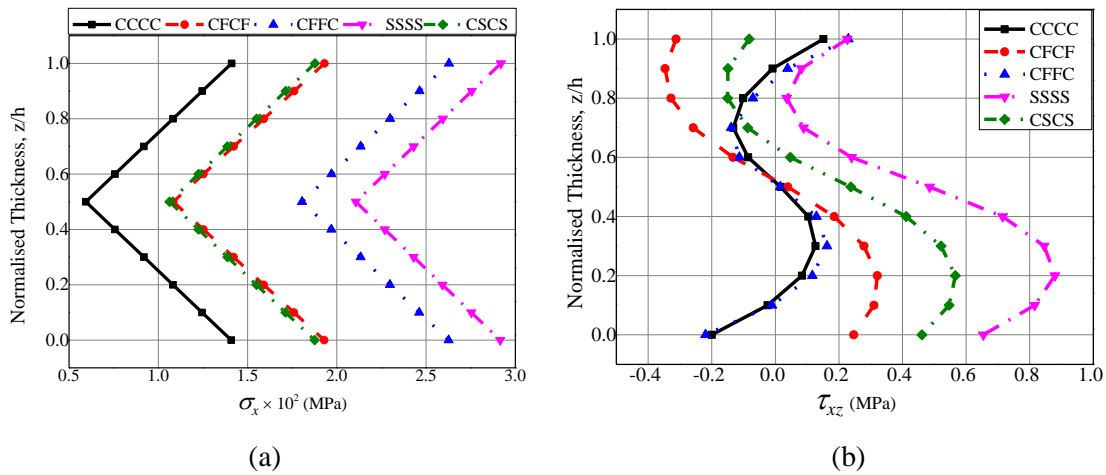


(d)



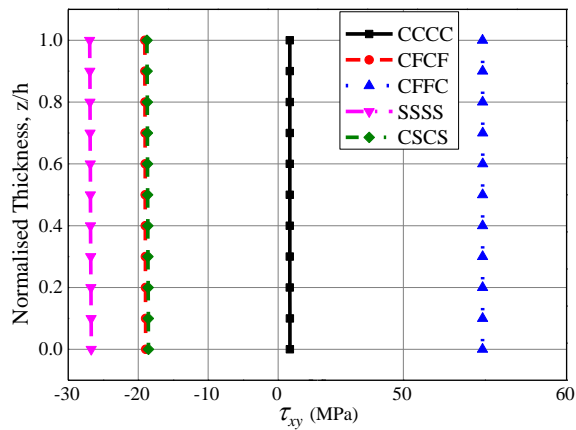
(e)

Figure 4.9: Effect of boundary condition on (a) U_x (b) U_v (c) U_w (d) electric potential ϕ (e) magnetic potential ψ



(a)

(b)



(c)

Figure 4.10: Effect of boundary condition on (a) normal stress σ_x (b) shear stress τ_{xz} (c) shear stress τ_{xy}

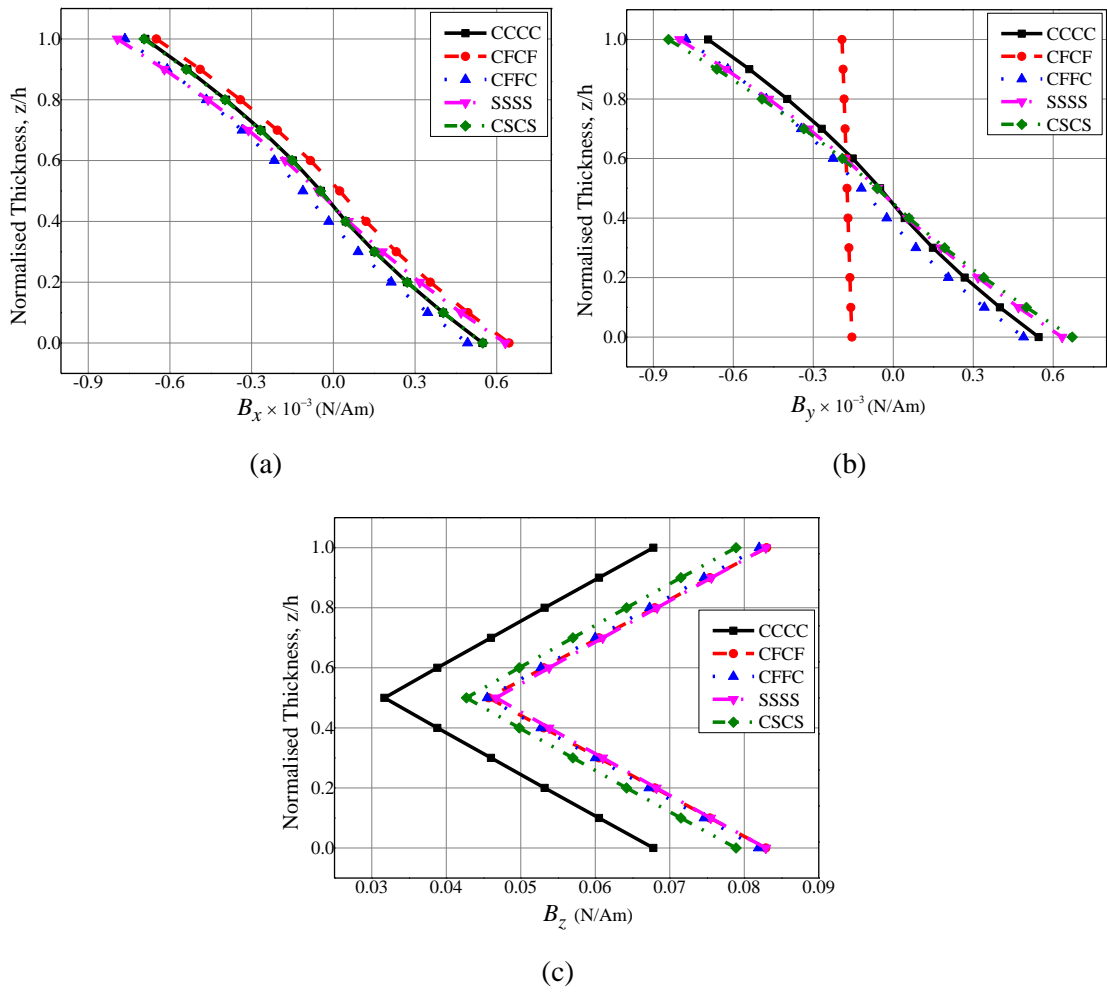
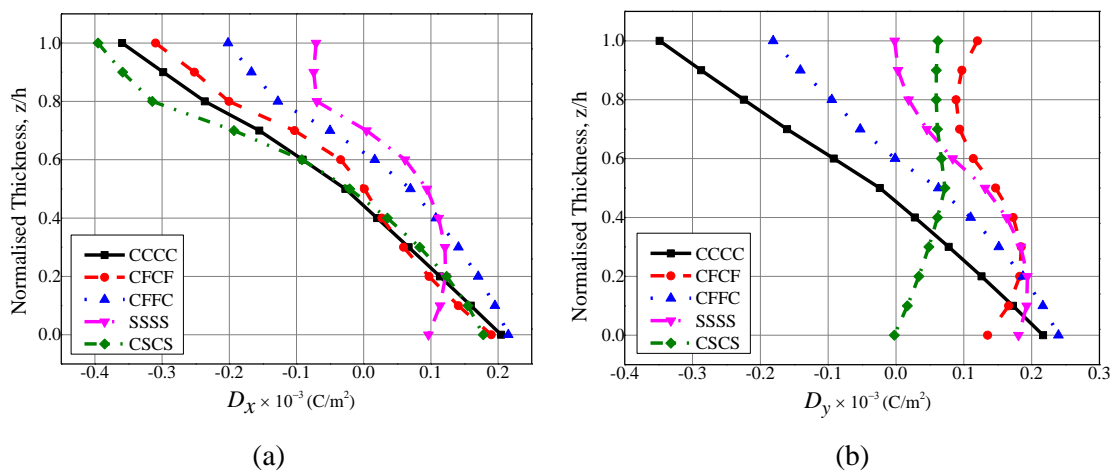
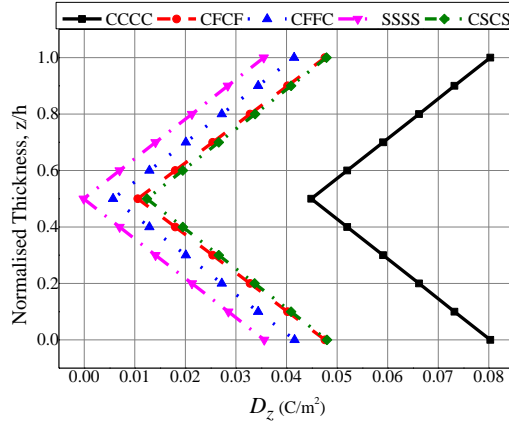


Figure 4.11: Effect of boundary conditions on magnetic flux densities (a) B_x (b) B_y (c) B_z





(c)

Figure 4.12: Effect of boundary conditions on electric displacements (a) D_x (b) D_y (c) D_z

4.5.3. Effect of aspect ratio (a/h)

The effect of aspect ratio (a/h) on SFG-BFB MEE plate subjected to uniform temperature load is evaluated. The clamped boundary condition is enforced on all the edges of the plate. Figures 4.13(a) – (e) illustrate the influence of aspect ratio on the displacement components (U_x , U_y and U_w), electric potential ϕ , and magnetic potential ψ , respectively. It can be inferred from these figures that the SFG-BFB MEE plate with lower aspect ratio exhibit a greater value of U_x , U_y and U_w . However, in contrast to U_x and U_y , a marginal effect of aspect ratio is witnessed on U_w . A further numerical study reveals that the thick plate has a predominant effect on the potentials (ϕ and ψ) of the system. In addition, it is also found that the stresses are greatly affected by the aspect ratios considered. As the aspect ratio (a/h) of SFG-BFB MEE plate increases, the normal stress σ_x drastically reduces across the plate thickness as illustrated in Fig. 4.14(a). Analogously, the shear stress components τ_{xz} , τ_{xy} , and τ_{yz} follow the similar trend of variation as elucidated in Figs. 4.14(b) – (d), respectively. The numerical evaluation is further extended to interpret the influence of different temperature profiles on the SFG-BFB MEE plate for various aspect ratios. It can be noticed from Table 4.4 that irrespective of the temperature distribution considered, the effect of a/h ratios on the displacement U_w and all the stress components remain unchanged. In other words, thick plate ($a/h = 3$) has a significant effect on the direct quantities and stress components as well. Likewise, the results presented in Table 4.5 suggest that for all the forms of temperature loads, a thin plate ($a/h = 100$) yields the lower electric

displacement components (D_x , D_y and D_z) and magnetic flux density components (B_x , B_y and B_z) of the SFGMEE plate (Also shown in Figs. 4.15 and 4.16).

4.5.4. Effect of Length-to-Width ratio (a/b)

The numerical evaluation is carried out to explore the effect of the length-to-width ratio (a/b) on the static parameters of the SFGMEE plate. The present analysis considers the plate is thick ($a/h = 5$) and it is clamped on all the edges (Fig. 4.2a). The variation of direct quantities such as U_x , U_y , U_w , ϕ and ψ with respect to different a/b ratio is plotted in Figs. 4.17(a) – (e), respectively. As elucidated in these figures, the displacement components U_x , U_y and U_w exhibit decreasing trend as a/b ratio increases. However, the electric potential and magnetic potential increases with the increase in the a/b ratio. It is worth stating that for the higher values of a/b ratio, the discrepancy becomes negligible for U_w and ϕ . The variation of normal stress σ_x and the shear stress τ_{xz} along the plate thickness is shown in Figs. 4.18(a) and (b), respectively. The observation from Figs. 4.19 and 4.20 reveal that for $a/b = 2$, a drastic increase in the electric displacement components (D_x , D_y and D_z) and magnetic flux density components (B_x , B_y and B_z) is witnessed. In other words, for the given aspect ratio (a/h), the plate with a higher length-to-width ratio (a/b) tends to increase the electric displacement and magnetic flux density components along the thickness. Further, Table 4.6 depicts the maximum values of direct quantities such as U_w , ϕ and ψ for different combinations of aspect ratio (a/h), the length-to-width ratio (a/b) and the temperature profiles. The results from this table (Table 4.6) suggest that irrespective of the temperature profiles, lower a/h ratio and a/b ratio results in a higher value of U_w , whereas the combination of lower aspect ratio (a/h) and higher the length-to-width ratio (a/b) yields the maximum value of the direct quantities.

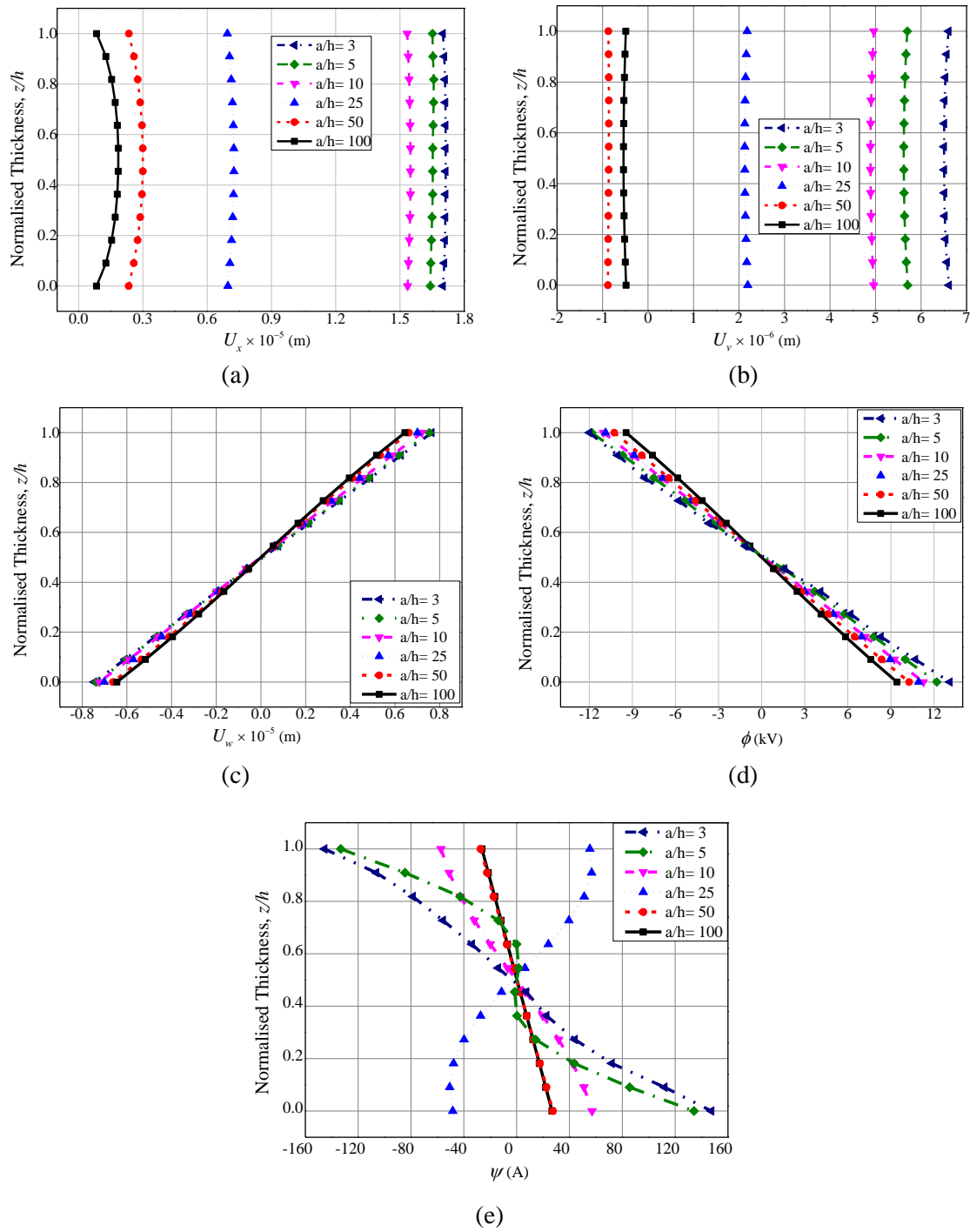
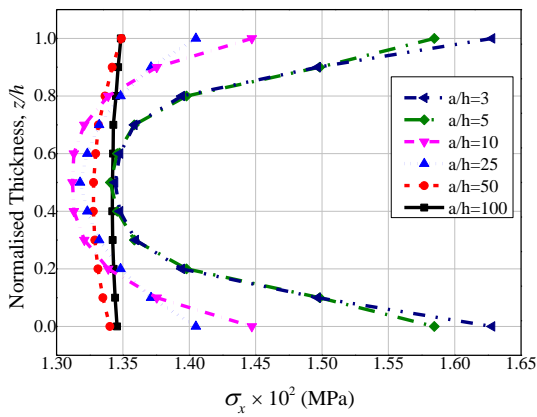
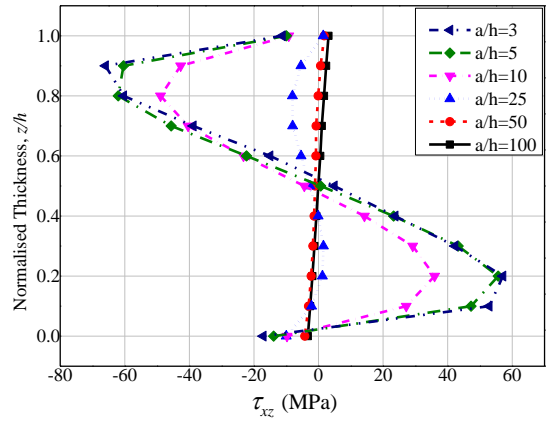


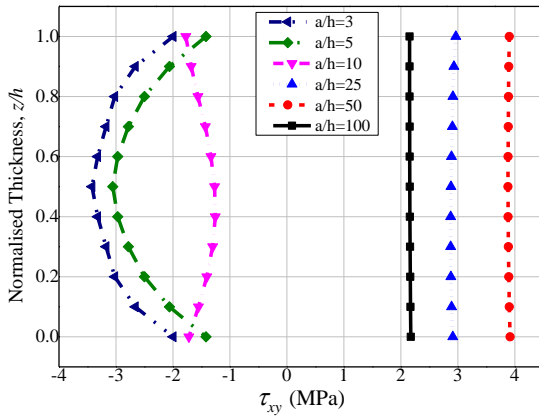
Figure 4.13: Effect of aspect ratio (a/h) on displacement components (a) U_x (b) U_v (c) U_w (d) electric potential ϕ (e) magnetic potential ψ



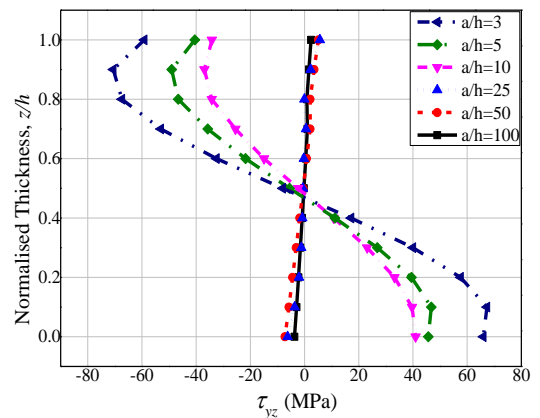
(a)



(b)

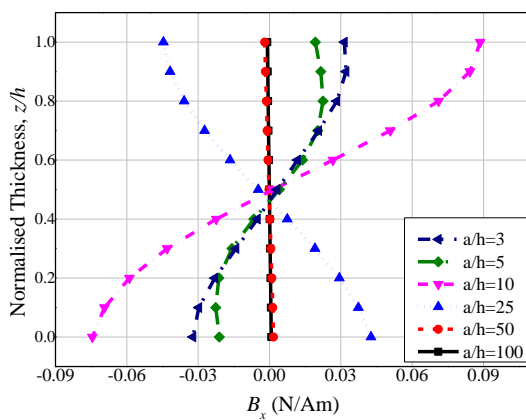


(c)

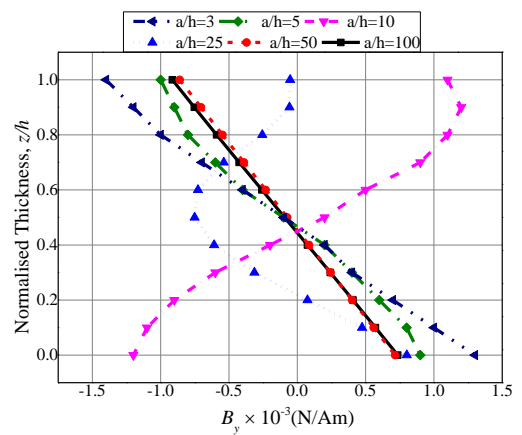


(d)

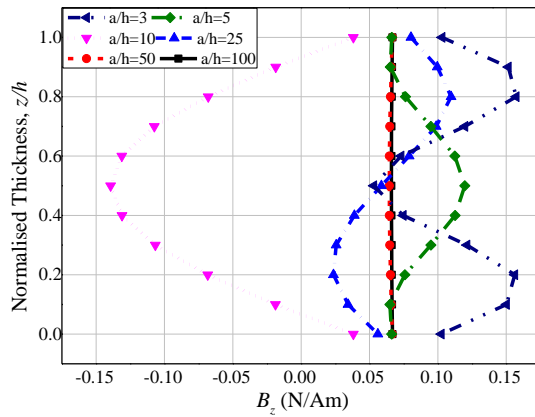
Figure 4.14: Effect of aspect ratio (a/h) on (a) normal stress σ_x (b) shear stress τ_{xz} (c) shear stress τ_{xy} (d) shear stress τ_{yz}



(a)

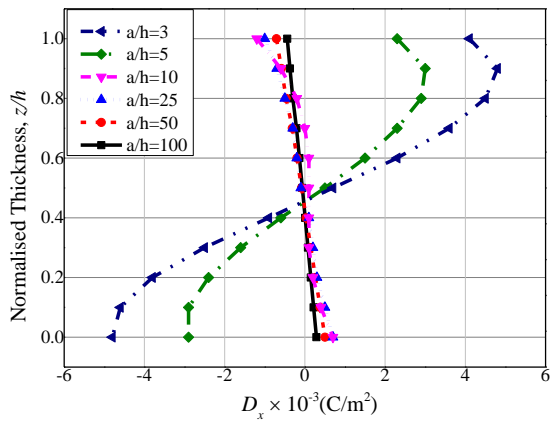


(b)

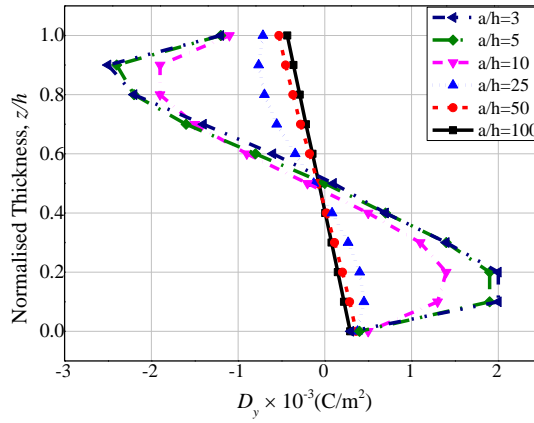


(c)

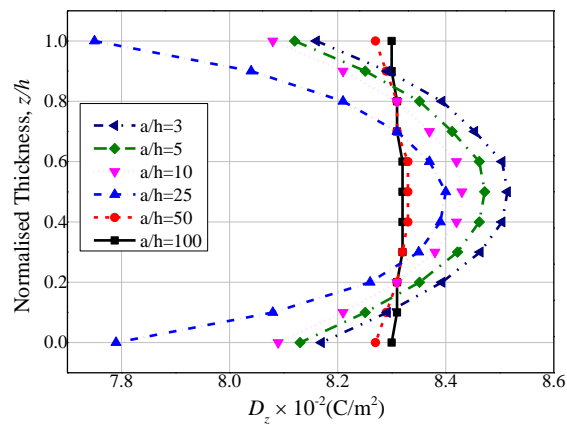
Figure 4.15: Effect of aspect ratio (a/h) on magnetic flux densities (a) B_x (b) B_y (c) B_z



(a)



(b)



(c)

Figure 4.16: Effect of aspect ratio (a/h) on electric displacements (a) D_x (b) D_y (c) D_z

Table 4.4: Effect of aspect ratio (a/h) on the maximum values of transverse deflection, normal stresses and shear stresses for different temperature profiles

a/h	Temperature profiles	U_w	σ_x	σ_y	σ_z	τ_{xz}	τ_{xy}	τ_{yz}
3	Uniform	8.16	1.81	1.68	2.74	6.60	3.92	7.06
	Parabolic	5.88	1.35	1.37	2.23	4.22	1.64	2.69
	Linear	8.34	1.84	1.81	2.96	6.62	2.71	4.71
	Bi-Triangular	6.45	1.70	1.64	2.69	4.73	3.03	5.16
5	Uniform	8.09	1.70	1.64	2.71	6.20	3.22	4.90
	Parabolic	5.62	1.32	1.35	2.22	4.17	1.23	2.26
	Linear	8.12	1.79	1.78	2.94	6.37	2.18	3.49
	Bi-Triangular	6.32	1.66	1.61	2.67	4.42	2.37	3.67
10	Uniform	7.95	1.60	1.53	2.64	4.89	3.06	4.10
	Parabolic	5.49	1.27	1.31	2.20	4.13	1.16	2.21
	Linear	8.01	1.69	1.71	2.89	5.73	1.97	2.93
	Bi-Triangular	6.19	1.56	1.54	2.62	3.70	2.30	3.07
25	Uniform	7.78	1.41	1.37	2.58	1.20	2.96	0.72
	Parabolic	5.32	1.25	1.27	2.17	3.97	1.07	2.10
	Linear	7.94	1.61	1.62	2.84	4.93	1.95	2.76
	Bi-Triangular	6.03	1.44	1.42	2.57	1.24	2.29	0.51
50	Uniform	7.64	1.35	1.36	2.56	0.42	2.17	0.62
	Parabolic	5.18	1.22	1.26	2.16	3.50	0.64	1.89
	Linear	7.85	1.59	1.61	2.83	4.20	1.47	2.66
	Bi-Triangular	5.95	1.41	1.41	2.56	0.41	1.69	0.43
100	Uniform	7.46	1.34	1.34	2.55	0.33	1.77	0.37
	Parabolic	5.04	1.20	1.25	2.15	2.05	0.90	1.63
	Linear	7.65	1.57	1.59	2.82	2.48	1.23	1.95
	Bi-Triangular	5.86	1.40	1.39	2.56	0.21	1.33	0.26

U_w in 10^{-6} m; σ_x , σ_y and σ_z in 10^2 MPa; τ_{xz} , τ_{xy} and τ_{yz} in MPa

Table 4.5: Effect of aspect ratio (a/h) on the maximum values of electric displacements and magnetic flux densities for different temperature profiles

a/h	Temperature profiles	D_x	D_y	D_z	B_x	B_y	B_z
3	Uniform	4.8	2.5	83.1	35.7	1.4	157.3
	Parabolic	1.4	1.4	63.7	15.6	0.59	89.3
	Linear	2.9	2.3	83.1	25.3	0.98	128.6
	Bi-Triangular	3.4	1.8	75.4	30.4	1.1	152.9
5	Uniform	3.1	2.4	83.3	22.6	1.04	119.7
	Parabolic	1.0	1.38	64.2	7.1	0.45	58.2
	Linear	1.9	2.2	83.8	13.9	0.83	83.5
	Bi-Triangular	2.2	1.7	76.4	16.8	0.71	79.2
10	Uniform	1.2	1.9	84.1	88.6	0.80	109.7
	Parabolic	0.9	1.3	64.5	29.2	0.28	49.8
	Linear	1.3	2.01	85.2	53.7	0.56	69.3
	Bi-Triangular	1.1	1.47	77.7	61.1	0.57	81.7
25	Uniform	1.01	0.76	84.3	44.6	1.2	139.4
	Parabolic	0.91	1.27	64.9	13.7	0.45	49.2
	Linear	1.28	1.6	86.4	27.6	0.78	85.1
	Bi-Triangular	0.85	0.71	78.9	31.8	0.85	112.9
50	Uniform	0.44	0.43	83.2	2.03	0.91	66.7
	Parabolic	0.71	0.66	63.9	0.86	0.37	58.1
	Linear	0.95	0.88	85.8	1.5	0.66	75.2
	Bi-Triangular	0.36	0.35	80.3	1.4	0.69	67.6
100	Uniform	0.39	0.37	82.7	0.91	0.92	66.8
	Parabolic	0.65	0.61	63.1	0.39	0.38	58.3
	Linear	0.82	0.76	84.6	0.66	0.67	75.5
	Bi-Triangular	0.32	0.30	79.5	0.69	0.70	67.8

D_x , D_y and D_z in 10^{-3} C/m²; B_x , B_y and B_z in 10^{-3} N/Am

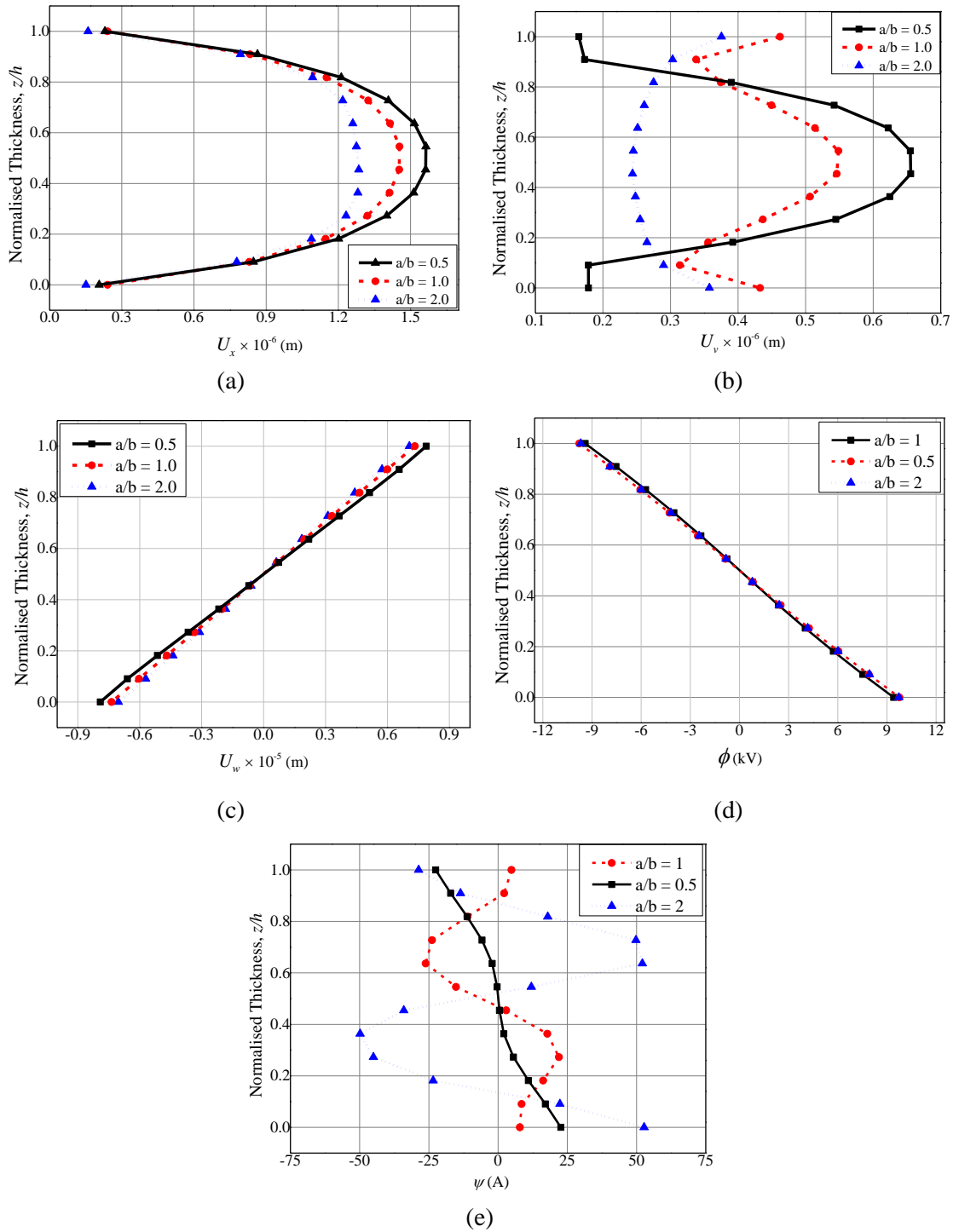


Figure 4.17: Effect of length-to-width ratio (a/b) on displacement components (a) U_x (b) U_v (c) U_w (d) electric potential ϕ (e) magnetic potential ψ

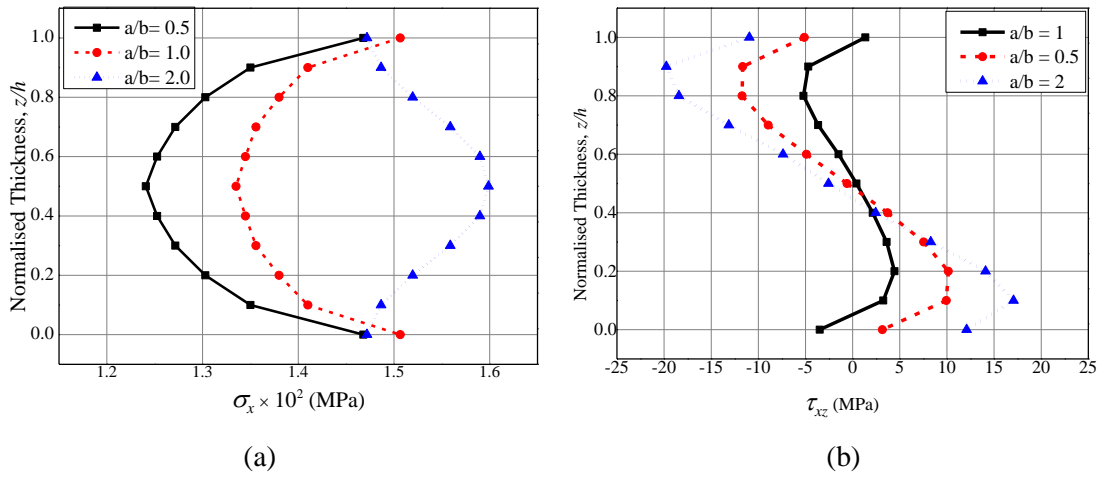


Figure 4.18: Effect of length-to-width ratio (a/b) on (a) normal stress σ_x (b) shear stress τ_{xz}

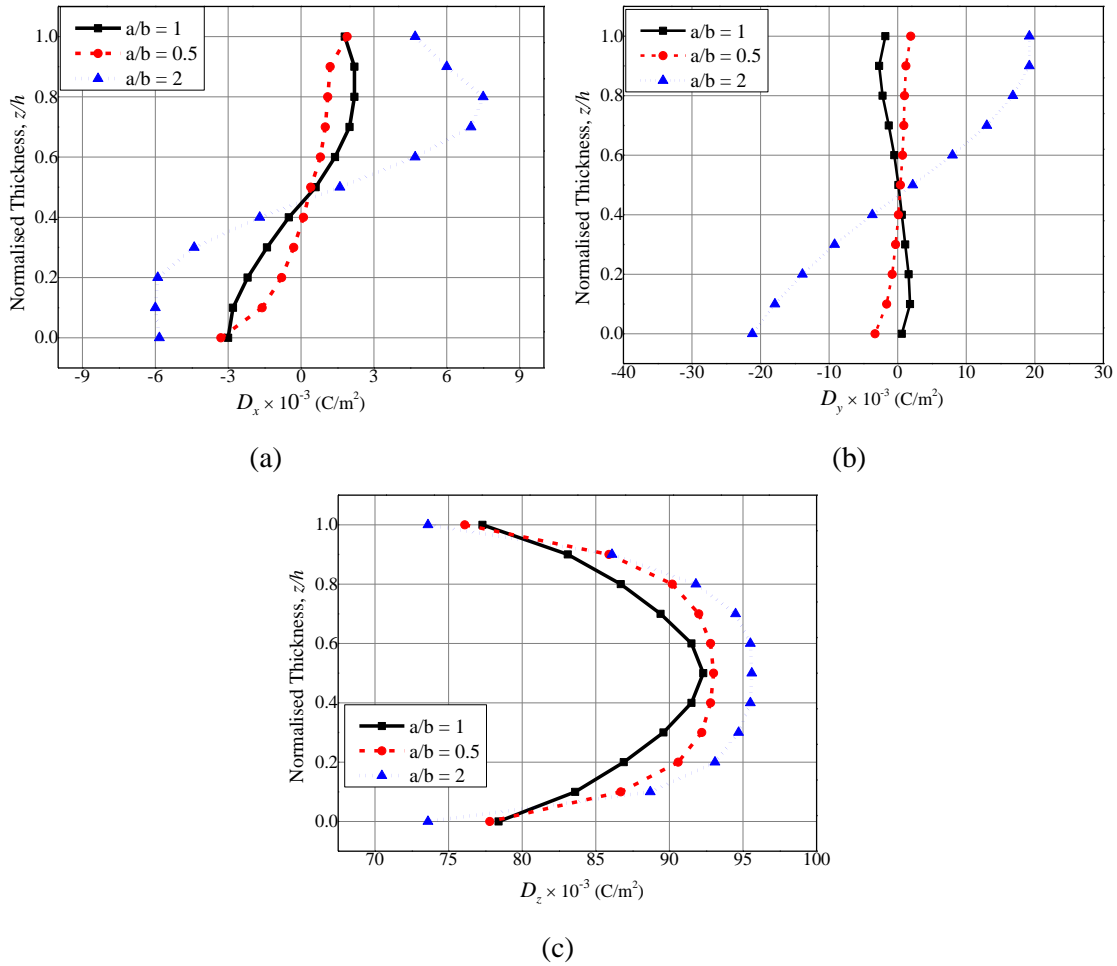


Figure 4.19: Effect of length-to-width ratio (a/b) on electric displacements (a) D_x (b) D_y (c) D_z

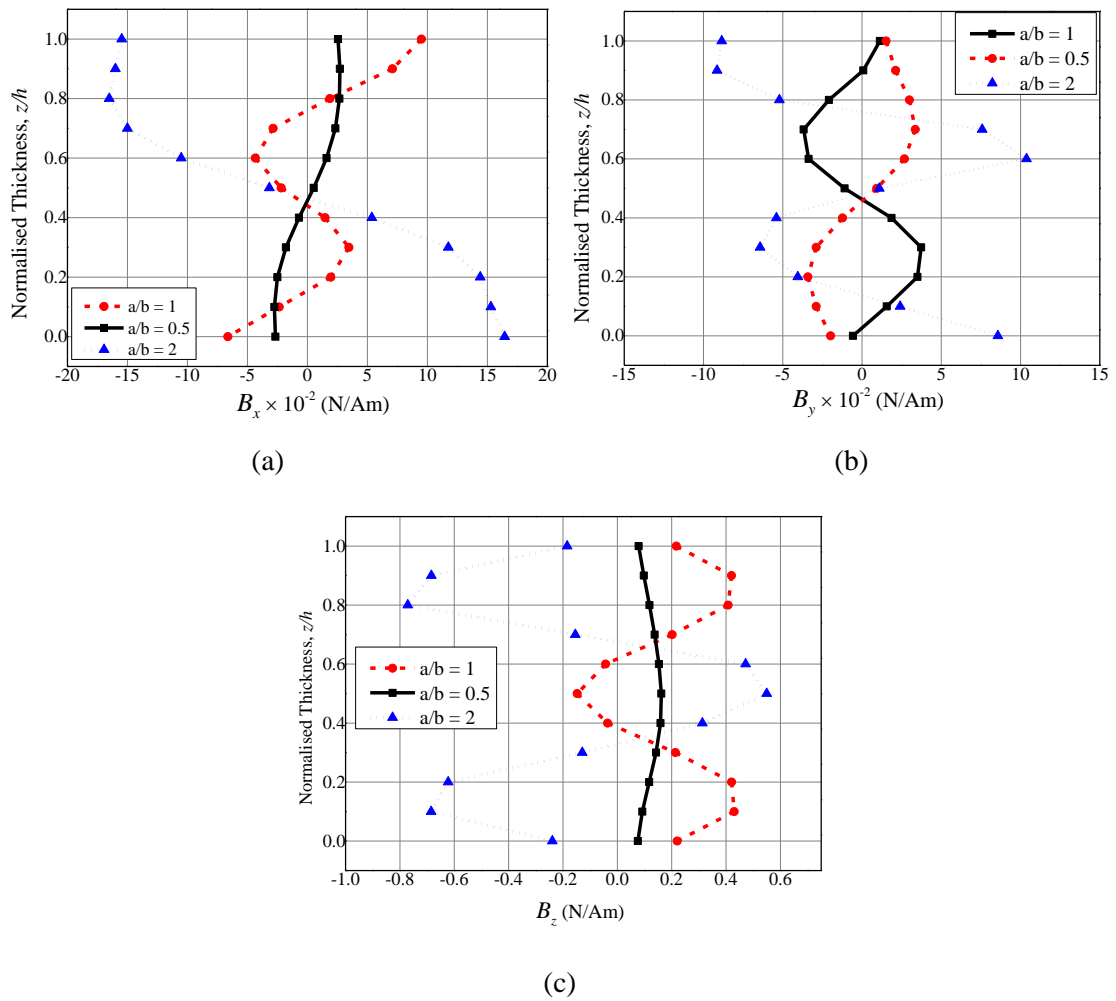


Figure 4.20: Effect of length-to-width ratio (a/b) on magnetic flux densities (a) B_x (b) B_y (c) B_z

4.5.5. Influence of pyroeffects

In this section, considering the different thermal loading profiles, a comparative study is made to analyse the distribution of the electric potential with and without pyroeffects. It can be clearly observed from Figs. 4.21(a) – (d) that for all the temperature distributions, the pyroeffects tend to improve the electric potential across the thickness of the SFG-BFB MEE plate.

Table 4.6: Effect of length-to-width (a/b) ratio on the maximum values of transverse displacement, electric potential and magnetic potential for different temperature profiles and aspect ratio (a/h)

a/h	Temperature Profiles	$U_w (\times 10^{-6} \text{ m})$			ϕ (kV)			ψ (A)		
		$a/b = 0.5$	$a/b = 1.0$	$a/b = 2.0$	$a/b = 0.5$	$a/b = 1.0$	$a/b = 2.0$	$a/b = 0.5$	$a/b = 1.0$	$a/b = 2.0$
5	Uniform	7.84	7.76	7.69	16.14	16.28	16.35	24.04	27.48	52.03
	Parabolic	3.31	3.23	3.17	5.79	5.86	5.94	13.44	15.46	37.56
	Linear	5.54	5.46	5.42	9.21	9.28	9.32	19.30	23.67	40.56
	Bi-Triangular	6.83	6.68	6.52	9.56	9.65	9.77	22.52	24.18	43.53
10	Uniform	7.72	7.69	7.51	13.36	13.48	13.53	22.87	27.12	50.06
	Parabolic	3.17	3.14	2.97	5.37	5.41	5.56	11.56	13.73	33.36
	Linear	5.38	5.28	5.19	8.65	8.74	8.82	18.39	21.11	38.39
	Bi-Triangular	6.49	6.38	6.24	9.20	9.23	9.25	20.59	23.87	41.22
50	Uniform	7.67	7.64	7.49	11.21	11.26	11.28	21.15	26.85	49.71
	Parabolic	3.13	3.03	2.91	5.17	5.21	5.30	10.21	12.55	29.42
	Linear	5.21	5.13	5.04	8.59	8.64	8.67	17.35	20.73	35.72
	Bi-Triangular	6.01	5.95	5.83	8.75	8.82	8.93	17.42	20.67	38.13
100	Uniform	7.64	7.55	7.46	11.08	11.13	11.24	19.53	26.76	47.27
	Parabolic	3.07	2.98	2.88	5.10	5.12	5.16	9.87	12.14	28.98
	Linear	5.16	4.97	4.89	8.51	8.54	8.58	16.83	20.08	34.87
	Bi-Triangular	5.98	5.91	5.81	8.63	8.68	8.75	17.11	19.67	35.41

From Table 4.7, it can be deduced that irrespective of the temperature profiles and stacking sequences, the electric potential are maximum in presence of pyroeffects. In addition, it is also seen that bi-triangular temperature profile has a higher percentage of reduction in the maximum electric potential when the pyroeffects are neglected. Furthermore, the contribution of the pyroeffects towards the maximum electric potential of SFG-BFB MEE plate with different aspect ratios is evaluated. The results tabulated in Table 4.8 reveal that the pyroeffects have a predominant effect on the SFG-BFB MEE plate with higher aspect ratio, whereas it gradually becomes insignificant for thick MEE plates.

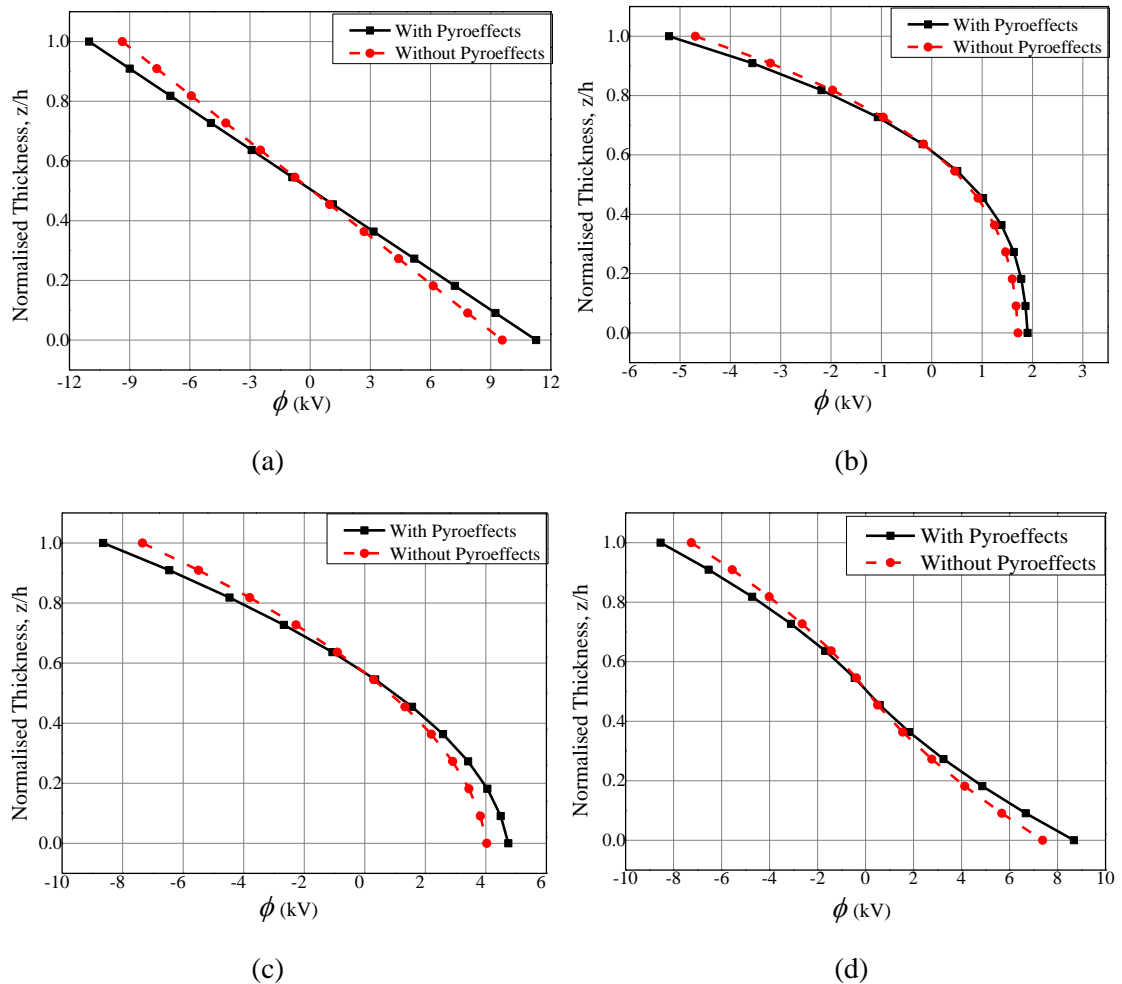


Figure 4.21: Pyroeffects on electric potential for (a) uniform (b) parabolic (c) linear (d) bi-triangular temperature distributions

Table 4.7: Influence of pyroeffects on the maximum electric potential ϕ_{max} for different stacking sequences

Temperature Profile	Max. electric potential ϕ_{max} (kV)					
	SFG-BFB			SFG-FBF		
	With Pyroeffects	Without Pyroeffects	% Reduction	With Pyroeffects	Without Pyroeffects	% Reduction
Uniform	11.26	9.93	11.82	10.69	9.48	12.62
Parabolic	5.21	4.42	15.16	4.28	3.71	13.3
Linear	8.64	7.65	11.45	7.36	6.48	11.9
Bi-Triangular	8.82	7.24	17.91	7.88	6.74	14.38

Table 4.8: Effect of aspect ratio (a/h) on the maximum electric potential ϕ_{max} for different temperature profiles

Temperature profiles	$a/h=100$			$a/h=50$			$a/h=5$			$a/h=3$		
	W.P	Wo. P	% Reduction	W.P	Wo. P	% Reduction	W.P	Wo. P	% Reduction	W.P	Wo. P	% Reduction
Uniform	9.42	7.06	25.05	11.26	9.93	11.82	12.2	11.9	2.46	13.1	12.88	1.68
Parabolic	4.86	3.64	25.10	5.21	4.42	15.16	6.43	6.18	3.93	7.45	7.26	2.48
Linear	7.23	5.42	25.03	8.64	7.65	11.45	9.61	9.40	2.18	10.18	10.05	1.27
Bi-Triangular	7.38	5.47	25.88	8.82	7.24	17.91	10.06	9.63	4.21	10.87	10.51	3.31

where, W.P – with pyroeffects; Wo. P – without pyroeffect

4.6. CONCLUSIONS

In this chapter, the coupled static response of stepped functionally graded magneto-electro-elastic (SFGMEE) plate under different thermal environment is investigated using a FE method. A FE formulation is derived with the aid of the principle of total potential energy and coupled constitutive equations accounting the thermal fields. The variations of direct and derived quantities are evaluated by considering the different temperature distributions. Among the various temperature profiles considered in the present analysis, a significant effect of the uniform temperature distribution is noticed on the static behaviour of SFGMEE plate. Further, a significant effect of SFG-BFB stacking sequence is also observed on the electric potential and electric displacement components while SFG-FBF stacking sequence shows a predominant influence on the magnetic potential and magnetic flux density components. The numerical investigation reveals that the lower aspect ratio (a/h) dominates the variation of static parameters across the thickness of the SFGMEE plate. In addition, for the given aspect ratio, decrease in the length-to-width (a/b) ratio results in a higher value of displacement components. However, the electric potential, magnetic potential and the stress components increase for the higher length-to-width (a/b) ratio. The study on the effect of boundary conditions suggest that the CCCC boundary edge exhibits a significant effect on transverse displacement, electric potential, normal stress and the electric displacement components. A prominent evaluation is carried out to investigate the influence of pyroeffects. It is observed that irrespective of the temperature profiles, the pyroeffects tend to improve the electric potential of the system. In contrast to the other temperature profiles, the bi-triangular temperature profile exhibits a significant reduction in the electric potential of the system when the pyroeffects are neglected. Moreover, the predominant influence of pyro coupling diminishes as the aspect ratio of SFGMEE plate decreases.

Chapter 5

HYGROTHERMAL ANALYSIS OF MAGNETO ELECTRO-ELASTIC PLATES USING FINITE ELEMENT METHODS

This chapter mainly focuses on evaluating the combined effect of moisture and temperature fields on the coupled response of magneto-electro-elastic or hygrothermo-magneto-electro-elastic (HTMEE) plates. The HTMEE plate is considered to be made of adaptive wood with properties of Barium Titanate and Cobalt Ferrite. A three-dimensional finite element (FE) formulation for the HTMEE structures (plates and beams) accounting the moisture and thermal coupling effects has been derived. The influences of temperature and moisture dependent stiffness coefficients on the static parameters have been studied through empirical constants. In addition, the effect of boundary conditions and aspect ratio on the behaviour of HTMEE plates is also studied.

Related article: Vinyas, M. and Kattimani, S. C. (2017), “Hygrothermal analysis of magneto-electro-elastic plate using 3D finite element analysis”, *Composite Structures*, **180, 617-637.**

5.1 INTRODUCTION

The major application of MEE structures can be found in sensors and actuators which are usually prone to fluctuating environmental conditions. Among them, the moisture concentration gradient and temperature gradient are prominent. The external influence of hygrothermal fields (moisture and temperature) propagates the peculiar response of the MEE structures. In this chapter, the static behaviour of MEE plate made of adaptive wood with Barium Titanate and Cobalt Ferrite material is studied in hygrothermal environment. In this regard, finite element formulation derived in Chapter 2 is extended for the hygrothermo-magneto-electro-elastic (HTMEE) plates by considering the influence of moisture gradient. The governing equations of motion

are derived through the minimization of total potential energy of the HTMEE plate. The constitutive equations of HTMEE solid exhibiting coupling between elastic, electric, magnetic, moisture and thermal fields are considered in the present analysis. The nodal displacements are obtained due to the external hygrothermal loads using condensation technique. The effects of different boundary conditions and aspect ratios are thoroughly evaluated in order to understand the behaviour of HTMEE plates.

5.2. BASIC FORMULATION OF THE PROBLEM

5.2.1. Problem description

A schematic representation of an adaptive wood made of BaTiO_3 and CoFe_2O_4 MEE plate spanning its length a , width b and thickness h along the x , y and z coordinates, respectively, is as shown in Fig.5.1. The HTMEE plate is loaded hygrothermally with the uniform temperature rise of ΔT and a moisture concentration change of Δm . The commonly used plate configurations considered for the analysis are illustrated in Fig. 5.2(a) – (d).

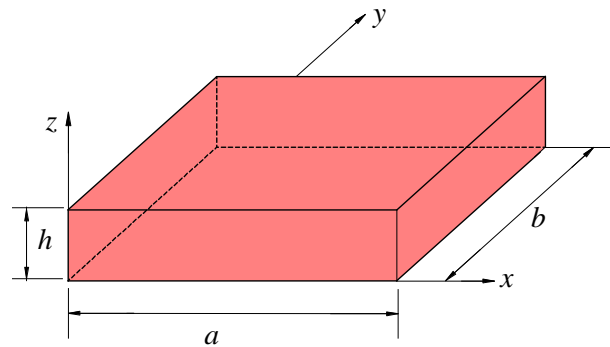
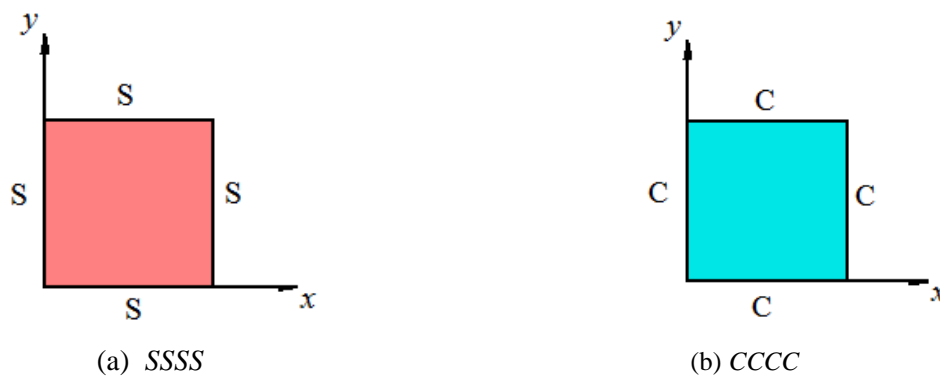


Figure 5.1: HTMEE plate geometry



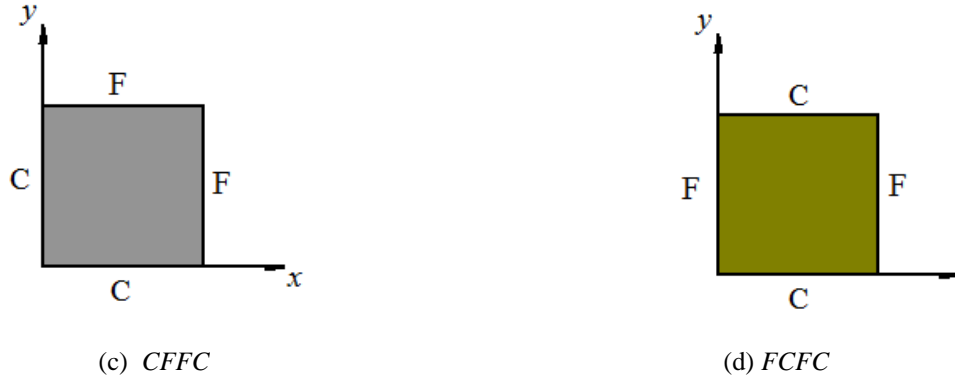


Figure 5.2: Schematic of MEE plate with different boundary conditions

5.2.2. Constitutive equations

The linear coupled constitutive equations of a hygrothermo-magneto-electro-elastic (HTMEE) material can be expressed as follows:

$$\{\sigma^k\} = [C^k] \{\varepsilon^k\} - [e^k] \{E^k\} - [q^k] \{H^k\} - \{\lambda^k\} - \{\gamma^k\} \quad (5.1)$$

$$\{D^k\} = [e^k]^T \{\varepsilon^k\} + [\eta^k] \{E^k\} + [m^k] \{H^k\} + \{p^k\} \Delta T + \{\chi^k\} \Delta m \quad (5.2)$$

$$\{B^k\} = [q^k]^T \{\varepsilon^k\} + [m^k] \{E^k\} + [\mu^k] \{H^k\} + \{\tau^k\} \Delta T + \{v^k\} \Delta m \quad (5.3)$$

$$\{\lambda^k\} = [C^k] \{\alpha^k\} \Delta T \quad (5.4)$$

$$\{\gamma^k\} = [C^k] \{\xi^k\} \Delta m \quad (5.5)$$

where, $\{\gamma^k\}$ corresponds to the hygroscopic stresses developed due to change in moisture concentration; $\{\xi^k\}$ is the moisture expansion coefficient vector. Meanwhile, $\{\chi^k\}$ and $\{v^k\}$ are the hygroelectric coefficient vector and hygromagnetic coefficient vector, respectively; ΔC is the moisture concentration rise from stress free reference concentration.

5.2.3. Finite element formulation

The finite element quantities related to the HTMEE plate such as generalized displacement vector $\{d_t\}$, the electric potential vector $\{\phi\}$, the magnetic potential vector $\{\psi\}$, the strain vector $\{\varepsilon\}$, electric field vector $\{E\}$ and the magnetic field vector $\{H\}$ are similar to that mentioned in Chapter 2 (section 2.4).

5.2.4. Governing equations of motion

The governing equations of MEE plate in the hygrothermal environment is derived by employing the principle of total potential energy as follows:

$$T_p = \frac{1}{2} \left[\int_{\Omega} \delta \{\varepsilon\}^T \{\sigma\} d\Omega - \int_{\Omega} \delta \{E\}^T \{D\} d\Omega - \int_{\Omega} \delta \{H\}^T \{B\} d\Omega \right] - \int_A \delta \{d_t\}^T \{f\} dA - \int_A \delta \{\phi\} Q^\phi dA - \int_A \delta \{\psi\} Q^\psi dA \quad (5.6)$$

where, $\{f\}$ is the traction force vector acting over an area A . The entire volume of the domain is represented by Ω . The surface electric charge density and surface magnetic charge density are represented by Q^ϕ and Q^ψ , respectively. The total potential energy is minimized by setting the first variation of Eq. (5.6) to zero.

$$T_p = \frac{1}{2} \left[\int_{\Omega} \delta \{\varepsilon\}^T \{\sigma\} d\Omega - \int_{\Omega} \delta \{E\}^T \{D\} d\Omega - \int_{\Omega} \delta \{H\}^T \{B\} d\Omega \right] - \int_A \delta \{d_t\}^T \{f\} dA - \int_A \delta \{\phi\} Q^\phi dA - \int_A \delta \{\psi\} Q^\psi dA = 0 \quad (5.7)$$

Substituting Eqs. (5.1) – (5.5) into Eq. (5.7), we get,

$$\begin{aligned} T_p = & \frac{1}{2} \int_{\Omega} \delta \{\varepsilon\}^T [C] \{\varepsilon\} d\Omega - \frac{1}{2} \int_{\Omega} \delta \{\varepsilon\}^T [e] \{E\} d\Omega - \frac{1}{2} \int_{\Omega} \delta \{\varepsilon\}^T [q] \{H\} d\Omega \\ & - \frac{1}{2} \int_{\Omega} \delta \{\varepsilon\}^T [C] \{\alpha\} \Delta T d\Omega - \frac{1}{2} \int_{\Omega} \delta \{\varepsilon\}^T [C] \{\xi\} \Delta m d\Omega - \frac{1}{2} \int_{\Omega} \delta \{E\}^T [e]^T \{\varepsilon\} d\Omega \\ & - \frac{1}{2} \int_{\Omega} \delta \{E\}^T [\eta]^T \{E\} d\Omega - \frac{1}{2} \int_{\Omega} \delta \{E\}^T [m]^T \{H\} d\Omega - \frac{1}{2} \int_{\Omega} \delta \{E\}^T \{p\} \Delta T d\Omega \\ & - \frac{1}{2} \int_{\Omega} \delta \{E\}^T \{\chi\} \Delta m d\Omega - \frac{1}{2} \int_{\Omega} \delta \{H\}^T [q]^T \{\varepsilon\} d\Omega - \frac{1}{2} \int_{\Omega} \delta \{H\}^T [m] \{E\} d\Omega \\ & - \frac{1}{2} \int_{\Omega} \delta \{H\}^T [\mu] \{H\} d\Omega - \frac{1}{2} \int_{\Omega} \delta \{H\}^T \{\tau\} \Delta T d\Omega - \frac{1}{2} \int_{\Omega} \delta \{H\}^T \{v\} \Delta m d\Omega \\ & - \int_A \delta \{d_t\}^T \{f\} dA - \int_A \delta \{\phi\} Q^\phi dA - \int_A \delta \{\psi\} Q^\psi dA = 0 \end{aligned} \quad (5.8)$$

Now, substituting Eq. (2.9) in Eq. (5.8), and assigning the coupled stiffness matrices for the various terms, we obtain Eq. (5.9) as follows:

$$\begin{aligned}
T_p^e = & \frac{1}{2} \left[\int_{\Omega} \delta \{d_t^e\}^T [K_{tt}^e] \{d_t^e\} d\Omega - \int_{\Omega} \delta \{d_t^e\}^T [K_{t\phi}^e] \{\phi^e\} d\Omega - \int_{\Omega} \delta \{d_t^e\}^T [K_{t\psi}^e] \{\psi^e\} d\Omega \right] \\
& - \frac{1}{2} \left[\int_{\Omega} \delta \{d_t^e\}^T \{F_{th}^e\} d\Omega - \int_{\Omega} \delta \{d_t^e\}^T \{F_{hy}^e\} d\Omega - \int_{\Omega} \delta \{\phi^e\}^T [K_{t\phi}^e]^T \{d_t^e\} d\Omega \right] \\
& - \frac{1}{2} \left[\int_{\Omega} \delta \{\phi^e\}^T [K_{\phi\phi}^e] \{\phi^e\} d\Omega - \int_{\Omega} \delta \{\phi^e\}^T [K_{\phi\psi}^e] \{\psi^e\} d\Omega - \int_{\Omega} \delta \{\phi^e\}^T \{F_{p,e}^e\} d\Omega \right] \\
& - \frac{1}{2} \left[\int_{\Omega} \delta \{\phi^e\}^T \{F_{h,e}^e\} d\Omega - \int_{\Omega} \delta \{\psi^e\}^T [K_{t\psi}^e]^T \{d_t^e\} d\Omega - \int_{\Omega} \delta \{\psi^e\}^T [K_{\phi\psi}^e]^T \{\phi^e\} d\Omega \right] \\
& - \frac{1}{2} \left[\int_{\Omega} \delta \{\psi^e\}^T [K_{\psi\psi}^e] \{\psi^e\} d\Omega - \int_{\Omega} \delta \{\psi^e\}^T \{F_{p,m}^e\} d\Omega - \int_{\Omega} \delta \{\psi^e\}^T \{F_{h,m}^e\} d\Omega \right] \\
& - \int_A \delta \{d_t^e\}^T \{F_m^e\} dA - \int_A \delta \{\phi^e\} \{F_{\phi}^e\} dA - \int_A \delta \{\psi^e\} \{F_{\psi}^e\} dA = 0 \tag{5.9}
\end{aligned}$$

Separating the terms corresponding to the coefficients of $\{d_t^e\}^T$, $\{\phi^e\}^T$, $\{\psi^e\}^T$ and Eq. (5.9) can be written as follows:

$$\begin{aligned}
[K_{tt}^e] \{d_t^e\} + [K_{t\phi}^e] \{\phi^e\} + [K_{t\psi}^e] \{\psi^e\} &= \{F_m^e\} + \{F_{th}^e\} + \{F_{hy}^e\} \\
[K_{t\phi}^e]^T \{d_t^e\} - [K_{\phi\phi}^e] \{\phi^e\} - [K_{\phi\psi}^e] \{\psi^e\} &= \{F_{\phi}^e\} - \{F_{p,e}^e\} - \{F_{h,e}^e\} \\
[K_{t\psi}^e]^T \{d_t^e\} - [K_{\phi\psi}^e]^T \{\phi^e\} - [K_{\psi\psi}^e] \{\psi^e\} &= \{F_{\psi}^e\} - \{F_{p,m}^e\} - \{F_{h,m}^e\} \tag{5.10}
\end{aligned}$$

The explicit forms of the matrices and load vectors are given as follows:

$$\begin{aligned}
[K_{tt}^e] &= \int_{\Omega} [B_t]^T [C] [B_t] d\Omega, [K_{t\phi}^e] = \int_{\Omega} [B_t]^T [e] [B_{\phi}] d\Omega, [K_{t\psi}^e] = \int_{\Omega} [B_t]^T [q] [B_{\psi}] d\Omega, \\
[K_{\phi\phi}^e] &= \int_{\Omega} [B_{\phi}]^T [\eta] [B_{\phi}] d\Omega, [K_{\phi\psi}^e] = \int_{\Omega} [B_{\phi}]^T [m] [B_{\psi}] d\Omega, [K_{\psi\psi}^e] = \int_{\Omega} [B_{\psi}]^T [\mu] [B_{\psi}] d\Omega \\
\{F_m^e\} &= \int_A [N_t]^T f dA, \\
\{F_{\phi}^e\} &= \int_A [N_{\phi}]^T Q^{\phi} dA, \{F_{\psi}^e\} = \int_A [N_{\psi}]^T Q^{\psi} dA
\end{aligned}$$

$$\begin{aligned}
\{F_{th}^e\} &= \int_{\Omega} [B_t]^T [C] \{\alpha\} \Delta T d\Omega, \quad \{F_{hy}^e\} = \int_{\Omega} [B_t]^T [C] \{\xi\} \Delta m d\Omega, \\
\{F_{p.e}^e\} &= \int_{\Omega} [B_{\phi}]^T \{p\} \Delta T d\Omega, \quad \{F_{h.e}^e\} = \int_{\Omega} [B_{\phi}]^T \{\chi\} \Delta m d\Omega, \\
\{F_{p.m}^e\} &= \int_{\Omega} [B_{\psi}]^T \{\tau\} \Delta T d\Omega, \quad \{F_{h.m}^e\} = \int_{\Omega} [B_{\psi}]^T \{\nu\} \Delta m d\Omega
\end{aligned} \tag{5.11}$$

In the absence of $\{F_m^e\}$, $\{F_{\phi}^e\}$ and $\{F_{\psi}^e\}$, the elemental equations of motion are globalized in a straightforward manner to obtain the global equations of motion as follows:

$$[K_{tt}^g] \{d_t\} + [K_{t\phi}^g] \{\phi\} + [K_{t\psi}^g] \{\psi\} = \{F_{th}^g\} + \{F_{hy}^g\} \tag{5.12}$$

$$[K_{t\phi}^g]^T \{d_t\} - [K_{\phi\phi}^g] \{\phi\} - [K_{\phi\psi}^g] \{\psi\} = \{F_{p.e}^g\} + \{F_{h.e}^g\} \tag{5.13}$$

$$[K_{t\psi}^g]^T \{d_t\} - [K_{\phi\psi}^g]^T \{\phi\} - [K_{\psi\psi}^g] \{\psi\} = \{F_{p.m}^g\} + \{F_{h.m}^g\} \tag{5.14}$$

where, different global stiffness matrices and load vectors in the governing equations of HTMEE plates (Eqs. (5.12) - (5.14)) are the global elastic stiffness matrix $[K_{tt}^g]$, the global electro-elastic coupling stiffness matrix $[K_{t\phi}^g]$, the global magneto-elastic coupling stiffness matrix $[K_{t\psi}^g]$, the global electric stiffness matrix $[K_{\phi\phi}^g]$, the global magnetic stiffness matrix $[K_{\psi\psi}^g]$, the global electro-magnetic stiffness matrix $[K_{\phi\psi}^g]$. The various global load vectors are the global mechanical load vector $\{F_m^g\}$, the global thermal load vector $\{F_{th}^g\}$, the global hygroscopic load vector $\{F_{hy}^g\}$, the global hygro-electric load vector $\{F_{h.e}^g\}$, the global hygro-magnetic load vector $\{F_{h.m}^g\}$, the global electric charge load vector $\{F_{\phi}^g\}$, the global magnetic current load vector $\{F_{\psi}^g\}$, the global pyroelectric load vector $\{F_{p.e}^g\}$, the global pyromagnetic load vector $\{F_{p.m}^g\}$. Using the condensation approach, Eqs. (5.12) - (5.14) is solved to obtain the nodal displacements generated due to the hygrothermal loading, nodal electric and magnetic potentials. From Eq. (5.14), solving for $\{\psi\}$, we get,

$$\{\psi\} = [K_{\psi\psi}^g]^{-1} \left[[K_{t\psi}^g]^T \{d_t\} - [K_{\phi\psi}^g]^T \{\phi\} - \left\{ \{F_{p.m}^g\} + \{F_{h.m}^g\} \right\} \right] \tag{5.15}$$

Solving Eq. (5.15) in Eq. (5.13) and solving for $\{\phi\}$, we obtain

$$\{\phi\} = [K_2]^{-1} [K_1] \{d_t\} - [K_2]^{-1} \{F_{\phi_sol}\} \quad (5.16)$$

Consequently, on substituting Eq. (5.15) and Eq. (5.16), into Eq. (5.12), we obtain the final global equation as follows:

$$[K_{eq}] \{d_t\} = \{F_{eq}\} \quad (5.17)$$

The explicit form of the global stiffness matrices $[K_{eq}]$ and force vectors appearing in Eqs. (5.16) and (5.17) are given as follows:

$$\begin{aligned} [K_1] &= [K_{\phi t}^g] - [K_{\psi\phi}^g] [K_{\psi\psi}^g]^{-1} [K_{\psi t}^g], [K_2] = [K_{\phi\phi}^g] - [K_{\psi\phi}^g] [K_{\psi\psi}^g]^{-1} [K_{\psi\phi}^g] \\ [K_3] &= [K_2]^{-1} [K_1], [K_4] = [K_2]^{-1} [K_{\psi\phi}^g] [K_{\psi\psi}^g], [K_5] = [K_{tt}^g] + [K_{t\psi}^g] [K_{\psi\psi}^g]^{-1} [K_{\psi t}^g] \\ , [K_6] &= [K_{t\phi}^g] - [K_{t\psi}^g] [K_{\psi\psi}^g]^{-1} [K_{\psi\phi}^g] [K_7] = [K_{eq}] = [K_5] + [K_6] [K_3], \\ [K_8] &= [K_6] [K_2]^{-1}, [K_9] = [K_{t\psi}^g] [K_{\psi\psi}^g]^{-1} - [K_6] [K_4], [K_{1-\psi}] = [K_{\psi t}^g] - [K_{\psi\phi}^g] [K_3] \\ [K_{2-\psi}] &= [K_{\psi\psi}^g]^{-1} [K_{\psi\phi}^g] [K_2]^{-1}, \\ [K_{3-\psi}] &= [K_{\psi\psi}^g]^{-1} [K_{\psi\phi}^g] [K_2]^{-1} [K_{\psi\phi}^g]^T [K_{\psi\psi}^g]^{-1} + [K_{\psi\psi}^g]^{-1} \\ \{F_{eq}\} &= [K_9] [\{F_{p.e}^g\} + \{F_{h.m}^g\}] + [K_8] [\{F_{p.e}^g\} + \{F_{h.e}^g\}] + [\{F_{th}^g\} + \{F_{hy}^g\}], \\ \{F_{\phi_sol}\} &= [\{F_{p.e}^g\} + \{F_{h.e}^g\}] - [K_{\psi\phi}^g]^T [K_{\psi\psi}^g]^{-1} [\{F_{p.m}^g\} + \{F_{h.m}^g\}] \end{aligned} \quad (5.18)$$

5.3. RESULTS AND DISCUSSIONS

The finite element formulation derived in the preceding section is used to demonstrate the static behaviour of MEE plates under hygrothermal loading. The material properties of the adaptive wood made of BaTiO₃ and CoFe₂O₄ (Akbarzadeh and Chen, 2012) tabulated in Table 5.1 are used for the analysis. The geometrical dimensions of the MEE plate considered for the analysis are the length of the plate $a = 0.3$ m, width $b = 0.3$ m and the thickness $h = 0.006$ m. The variation of the direct quantities and derived quantities are evaluated along the plate length. The influence of

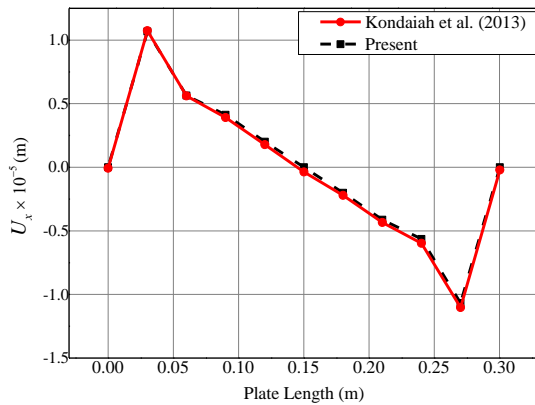
temperature and moisture dependent elastic stiffness coefficients, different boundary conditions and aspect ratios, on the static parameters of the multiphase MEE plate is also analysed through the numerical illustrations. The assumed temperature (T) and moisture (m) constraints can be written as follows:

$$\begin{aligned} T(x,0) &= 0 ; T(x,b) = 0 ; T(0,b) = 0 ; T(L,y) = 0 ; T(x,y,z) = T_{uni} \\ m(x,0) &= 0 ; m(x,b) = 0 ; m(0,b) = 0 ; m(L,y) = 0 ; m(x,y,z) = m_{uni} \end{aligned} \quad (5.19)$$

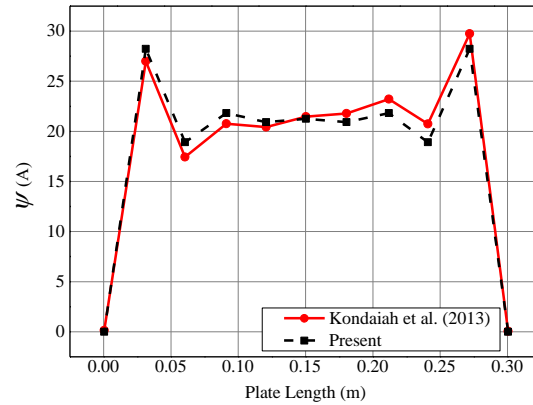
in which, T_{uni} and m_{uni} are the uniform temperature and uniform moisture concentrations, respectively.

5.3.1. Validation of the FE formulation

It is noteworthy to mention that no work has been reported on the static behaviour of MEE plates under hygrothermal environment. Hence, the validation of the present FE formulation is made by neglecting the hygroscopic effect. In this regard, the numerical example considered by Kondaiah *et al.* (2013) is solved by considering the identical plate dimensions and material properties. Figures 5.3(a) – (f) indicate that for the various boundary conditions, the results obtained from the present FE formulation compare very well with Kondaiah *et al.* (2013). Further, Fig. 5.4 depicts the convergence study of the electric potential of *FCFC* MEE plate. It can be observed from this figure that with the mesh size of $10 \times 10 \times 12$ elements, a good convergence is achieved.



(a) CCCC



(b) CCCC

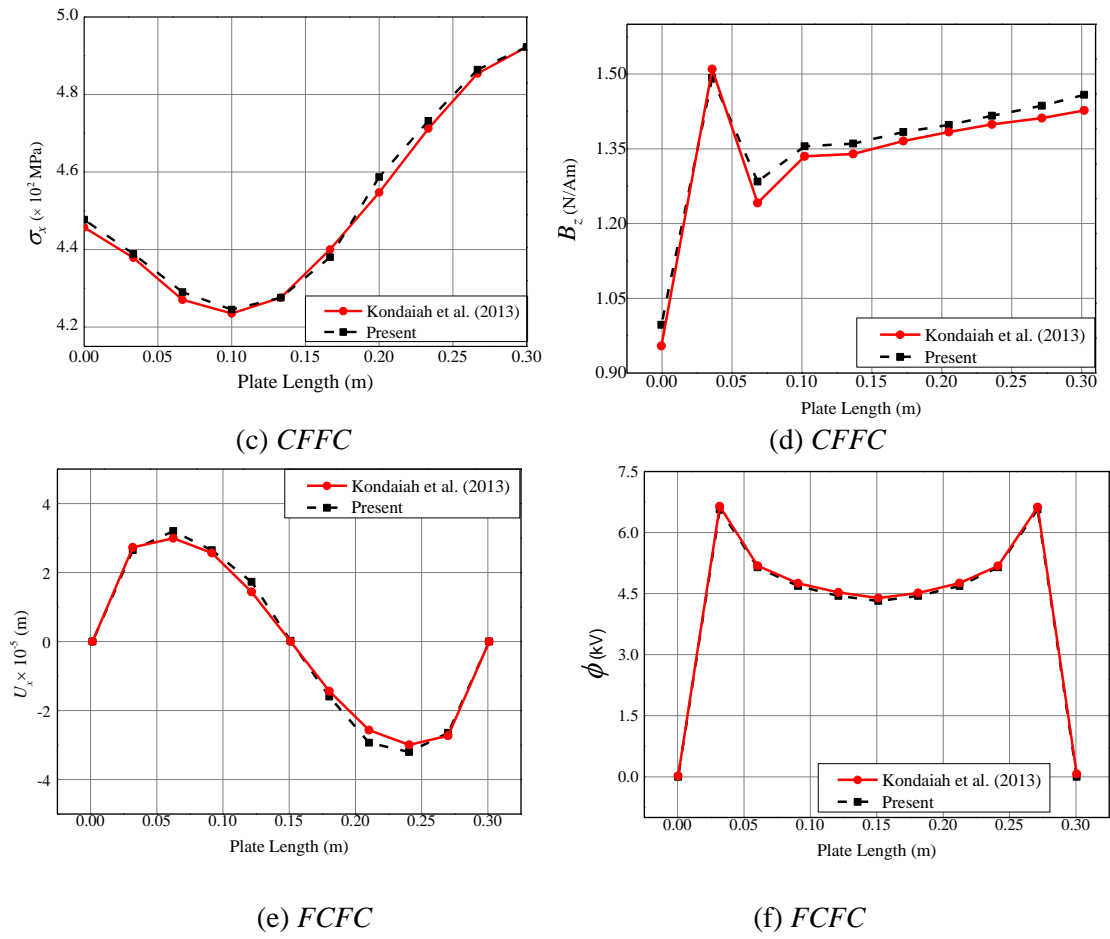


Figure 5.3: Validation plots (a) U_x (b) magnetic potential ψ (c) normal stress σ_x (d) magnetic flux density B_z (e) U_x (f) electric potential ϕ of MEE plate with different boundary conditions

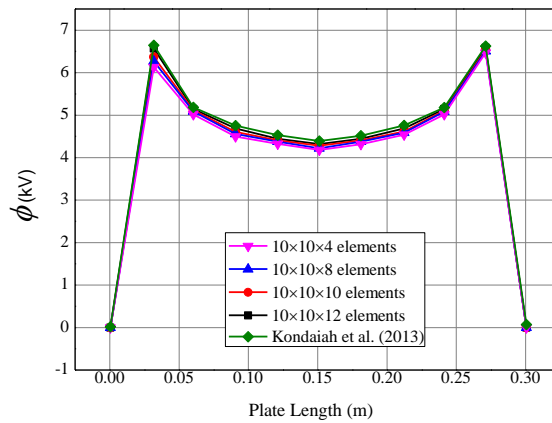


Figure 5.4: Convergence of electric potential ϕ for *FCFC* MEE plate

Table 5.1: Material properties of BaTiO₃ and CoFe₂O₄ and adaptive wood made of BaTiO₃ and CoFe₂O₄.

<i>Material property</i>	Material constants	0.6 V_f (Kondaiah <i>et al.</i> , 2013)	Adaptive wood (Akbarzadeh <i>et al.</i> , 2012)
Elastic constants (GPa)	$C_{11}=C_{22}$	200	286
	C_{12}	110	173
	$C_{13}=C_{23}$	110	170.5
	C_{33}	190	269.5
	$C_{44}=C_{55}$	45	45.3
	C_{66}	45	56.5
Piezoelectric constants (C/m ²)	e_{31}	-3.5	-4.4
	e_{33}	11	18.6
	e_{15}	0	11.6
Dielectric constant (10 ⁻⁹ C ² /Nm ²)	$\epsilon_{11}=\epsilon_{22}$	0.9	0.08
	ϵ_{33}	7.5	0.093
Magnetic permeability (10 ⁻⁴ Ns ² /C ²)	$\mu_{11}=\mu_{22}$	-1.5	-5.9
	μ_{33}	0.75	1.57
Piezomagnetic constants (N/Am)	q_{31}	200	580
	q_{33}	260	700
	q_{15}	180	560
Magneto-electric constant (10 ⁻¹² Ns/VC)	$m_{11}=m_{22}$	6	0
	m_{33}	2500	3
Pyroelectric constant (10 ⁻⁵ C/m ² K)	p_2	-12.4	-13
Pyromagnetic constant (10 ⁻³ C/m ² K)	τ_2	5.92	6
Thermal expansion coefficient (10 ⁻⁶ K ⁻¹)	$\alpha_1=\alpha_2$	12.9	14.1
	α_3	7.8	7.2
Moisture expansion coefficient (m ³ kg ⁻¹)	β_1	-	0
	$\beta_2=\beta_3$	-	1.1×10 ⁻⁴
Density (kg/m ³)	ρ	5600	5300

5.3.2. Effect of hygrothermal load

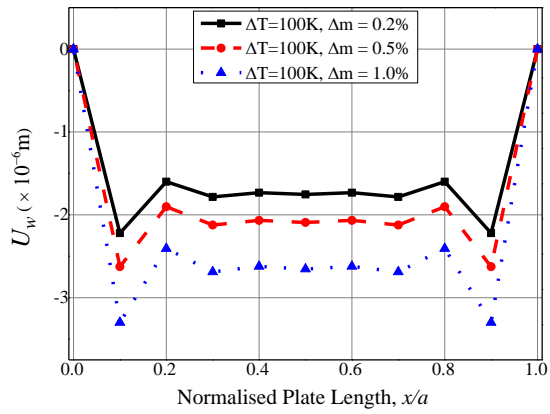
The effect of hygrothermal load on the static behaviour of MEE plate with simply supported boundary conditions (SSSS) is analysed. The temperature rise is kept uniform (100 K) unless otherwise mentioned, whereas the percentage of moisture concentration change Δm is varied. The effect of hygrothermal load on the variations of the transverse displacement U_w , electric potential ϕ , magnetic potential ψ , normal stress σ_x , electric displacement D_x and the magnetic flux density B_x of the SSSS MEE plate is plotted in Figs. 5.5(a) – (f), respectively. It is evident from these figures that with the increase in moisture concentration, the transverse displacement U_w , electric potential ϕ , magnetic potential ψ and normal stress σ_x increases while a negligible influence of hygrothermal load is observed on the electric displacement component D_x and the magnetic flux density component B_x . The MEE plate with *CCCC*, *CFFC* and *FCFC* boundary conditions also exhibit the same variation trend as the *SSSS* boundary condition. Hence, they are not presented here for the sake of brevity.

5.3.3. Effect of temperature and moisture dependent elastic stiffness coefficients

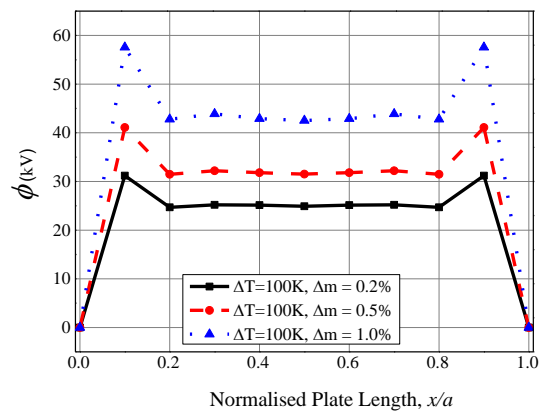
The effect of temperature and moisture dependent elastic stiffness coefficients on the direct and derived quantities of the MEE plate is evaluated. The temperature and moisture dependent elastic stiffness coefficient C is given by (Akbarzadeh and Chen, 2012)

$$C = C_0 (1 + \alpha^* \Delta T + \beta^* \Delta m) \quad (5.20)$$

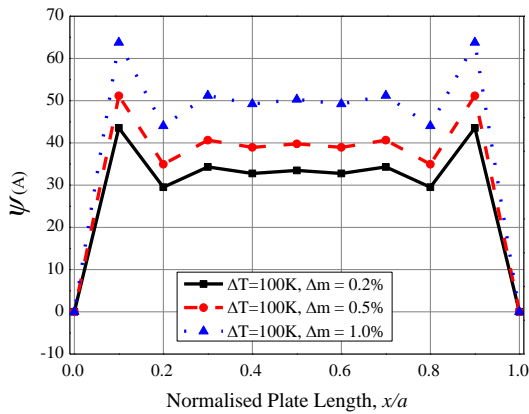
where, α^* and β^* are empirical constants, C_0 corresponds to the temperature and moisture independent elastic coefficient. Further analysis assumes a uniform temperature rise $\Delta T = 100$ K and moisture concentration rise $\Delta m = 1\%$. In addition, emphasis has been placed to investigate the influence of different boundary conditions (*SSSS*, *CCCC*, *CFFC* and *FCFC*) on static behaviour of the MEE plate under hygrothermal loading



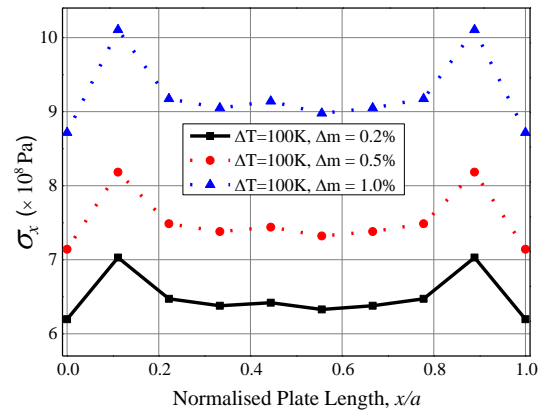
(a)



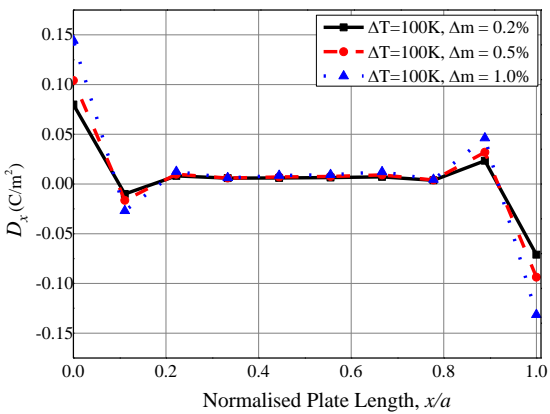
(b)



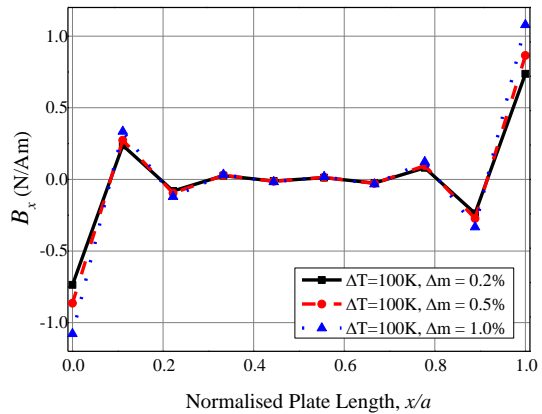
(c)



(d)



(e)



(f)

Figure 5.5: Effect of hygrothermal load on (a) U_w (b) ϕ (c) ψ (d) σ_x (e) D_x (f) B_x

5.3.4. Simply supported MEE plate (SSSS)

Figures 5.6(a) – (c) illustrate the variation of displacement components along the length of the SSSS MEE plate for various temperature and moisture dependent empirical constants (α^* , β^*). It may be noticed from Figs. 5.6(a) – (c) that the MEE plate with empirical constants $\alpha^* = \beta^* = -0.5$ has a substantial influence on the displacement components U_x , U_v and U_w . It may be due to the fact that the elastic stiffness coefficient matrix $[C]$ directly affects the elastic stiffness matrix $[K_{tt}]$, hygroscopic load $\{F_{hy}\}$ and thermal load $\{F_{th}\}$, which in turn influences the $\{F_{eq}\}$ and $[K_{eq}]$. It may also be observed that when the empirical constants ranging from $-0.5 \leq \alpha^*, \beta^* \leq 0$, the influence of temperature and moisture dependent elastic coefficients is more on the load vectors ($\{F_{hy}\}$ and $\{F_{th}\}$) as compared to the elastic stiffness matrix $[K_{tt}]$. In addition, with the increase in negative empirical constants ($\alpha^*, \beta^* \geq -0.5$), the elastic stiffness matrix $[K_{tt}]$ improves in such a way that the value $[K_{eq}]^{-1}\{F_{eq}\}$ decreases. From Fig. 5.6(a), it may be noticed that for a simply supported MEE plate, the maximum U_x is witnessed at the edges of the plate. A symmetric variation of the longitudinal displacement component U_v is noticed along the plate length. In comparison with the MEE plate with negative empirical constants, the hygrothermal loads have a minimal effect on U_v for the different positive empirical constants. Further, at the center of the plate, U_x and U_v are found to be zero. The transverse displacement component U_w remains almost constant along the plate length as illustrated in Fig. 5.6(c). Figures 5.7(a) and (b) demonstrate that $\alpha^* = \beta^* = -0.5$ has a predominant effect on the electric and magnetic potential, respectively, as expected in accordance with Eqs. (5.15) and (5.16). Also, it can be observed that the positive empirical constants increase the coupling effect which in turn increases the electric and magnetic potentials of the MEE plate. Conversely, a reduction in the coupled behaviour of MEE plate with respect to these potentials is observed for the higher negative empirical constants say, ($-2.5 \leq \alpha^*, \beta^* \leq -0.5$).

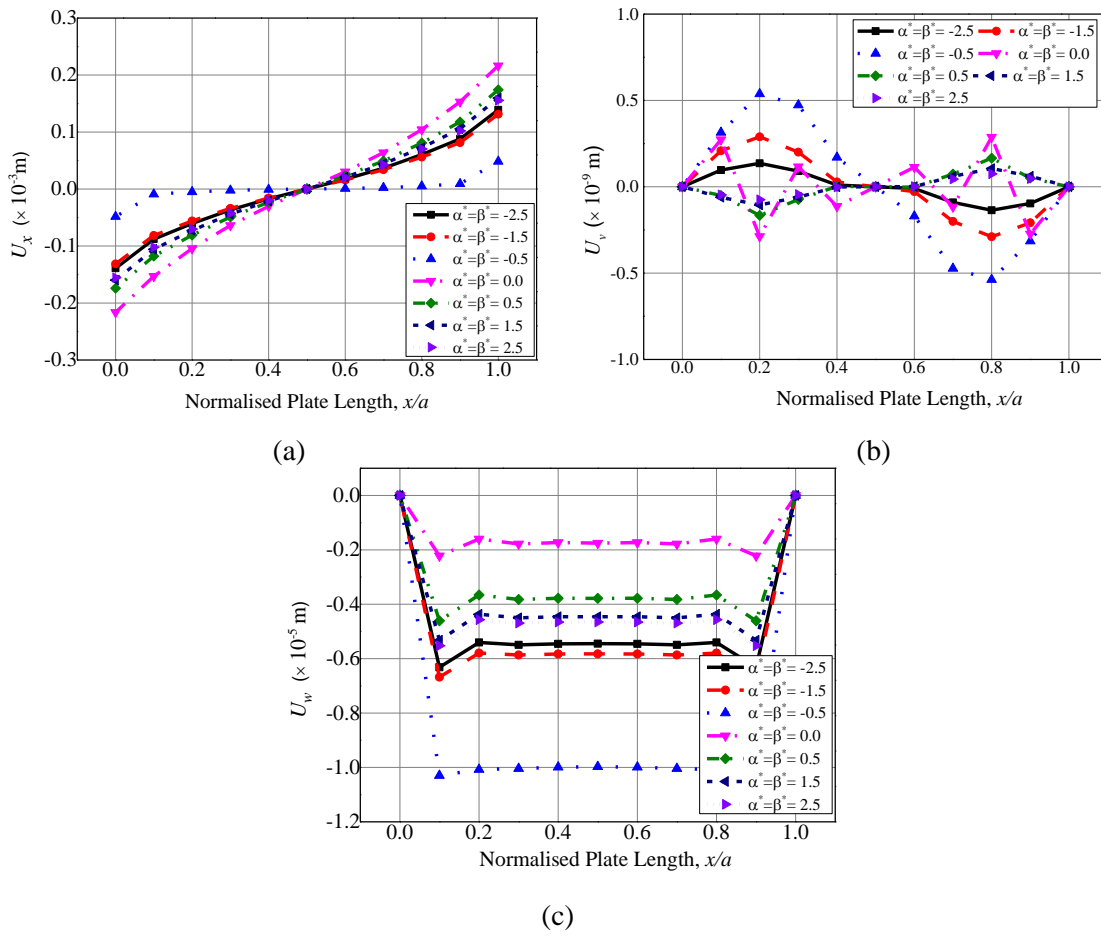


Figure 5.6: Effect of empirical constants on displacement components (a) U_x (b) U_v (c) U_w of SSSS MEE plate

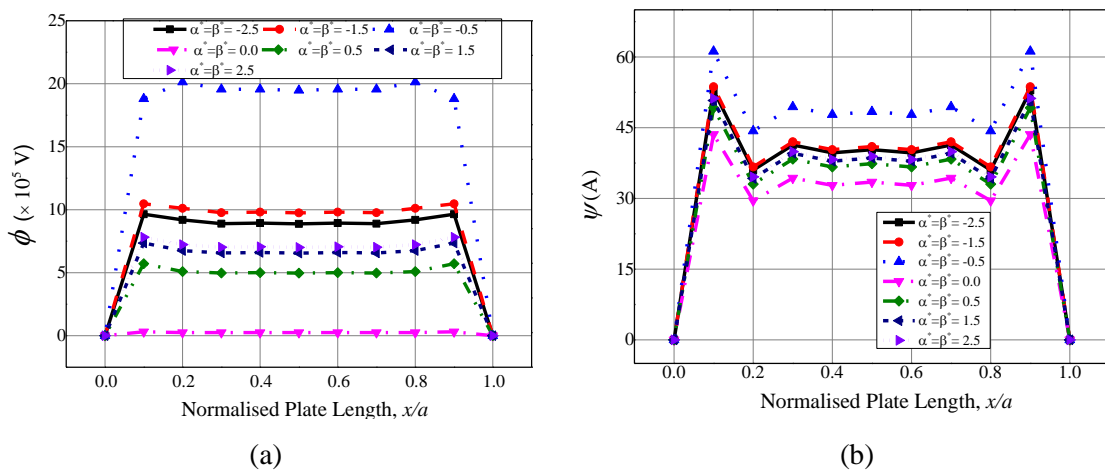


Figure 5.7: Effect of empirical constants on (a) electric potential ϕ (b) magnetic potential ψ of SSSS MEE plate

Figure 5.8(a) demonstrates the distribution of the normal stress σ_x along the length of the MEE plate. It can be seen from this figure that the effect of hygrothermal loads on the normal stress σ_x is minimum when the MEE plate is considered independent of temperature and moisture independent stiffness coefficients ($\alpha^* = \beta^* = 0.0$). Since, the normal stresses σ_y and σ_z follow the similar trend of variation as that of the σ_x , for the sake of brevity, the variation of σ_x alone is represented here. Considering Fig. 5.8(b), at the midlength of the MEE plate the shear stress τ_{xy} is zero regardless of the empirical constants used. However, the negative empirical constants and positive empirical constants of the MEE plate results in the positive and negative value of τ_{xy} , respectively, from one end to the midpoint, while from the midpoint to the other end, the behaviour of shear stress τ_{xy} is reversed. Furthermore, the shear stresses τ_{xz} and τ_{yz} display a negligible variation with respect to empirical constants, whereas significant discrepancies are witnessed at the plate edges as illustrated in Figs. 5.8(c) and (d), respectively.

Figure 5.9(a) depicts that the empirical constants have a negligible effect on the variation of electric displacement component D_x . However, for all the empirical constants, by imposing hygrothermal load, the MEE plate experiences the maximum value of D_x at the plate edges. From Fig. 5.9(b), it can be noticed that D_z varies almost constant along the plate length and reaches the minimum value at the edges. In addition, it is deduced that the coupling effect on D_z is higher when the stiffness coefficients of the MEE plate corresponds to $\alpha^* = \beta^* = -0.5$, whereas the MEE plate with $\alpha^* = \beta^* = 0.0$ yields a minimal value of D_x and D_z when exposed to hygrothermal loads.

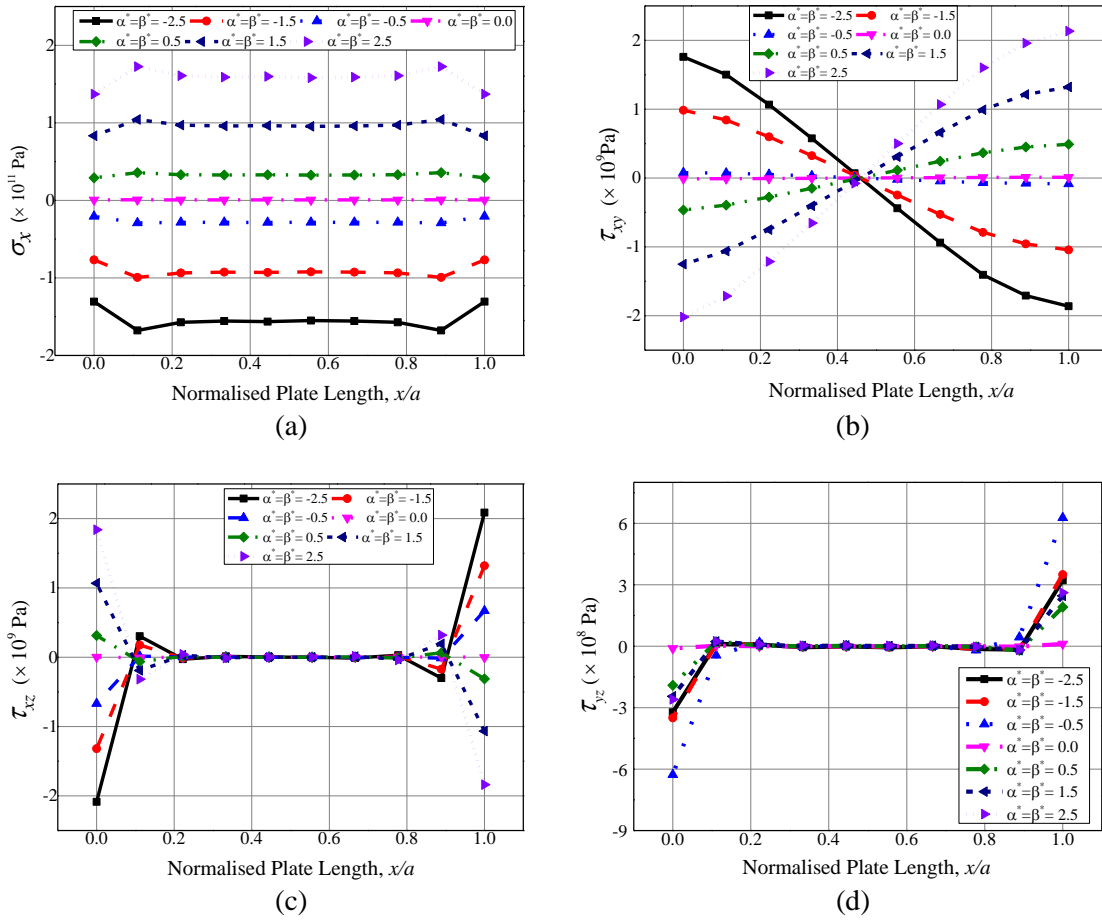


Figure 5.8: Effect of empirical constants on (a) σ_x (b) τ_{xy} (c) τ_{xz} (d) τ_{yz} of SSSS MEE plate

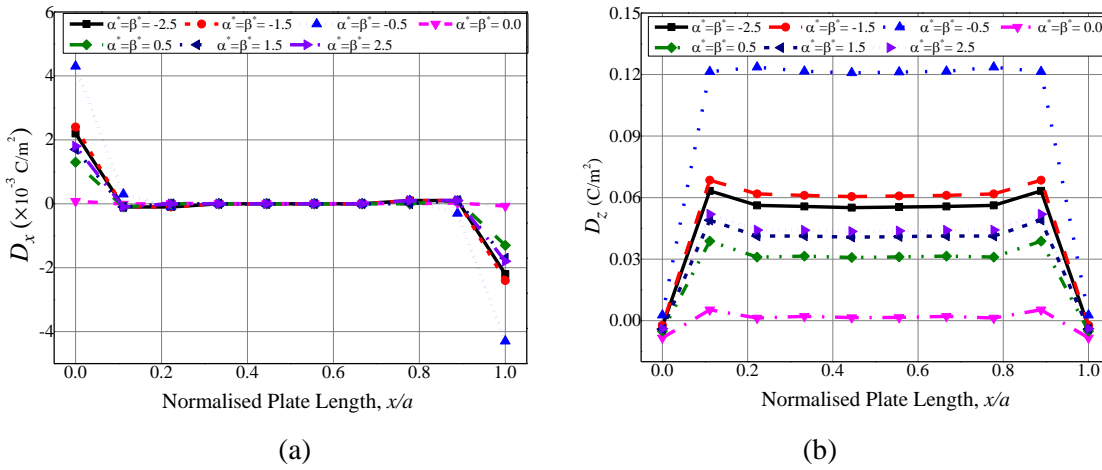


Figure 5.9: Effect of empirical constants on electric displacements (a) D_x (b) D_z of SSSS MEE plate

Figures 5.10(a) and (b) display the variation of magnetic flux density components B_x and B_z , respectively. It can be pointed out from these figures that for the MEE plate with different empirical constants, the influence of hygrothermal loads on the magnetic flux density component B_z is significantly larger than B_x . This may be attributed to the higher value of piezomagnetic constants along z -direction. Moreover, the results suggest that the negative empirical constants have a predominant effect than the positive empirical constants.

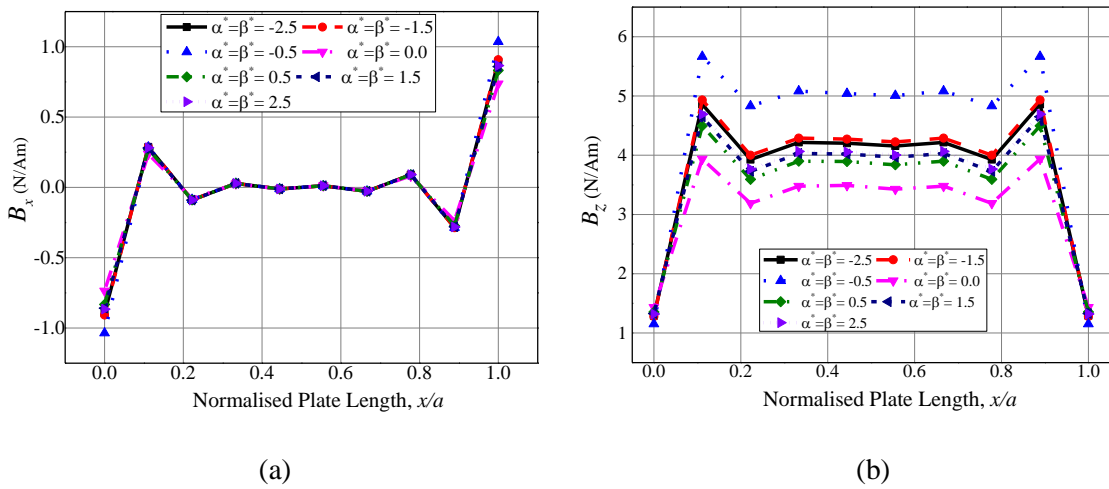


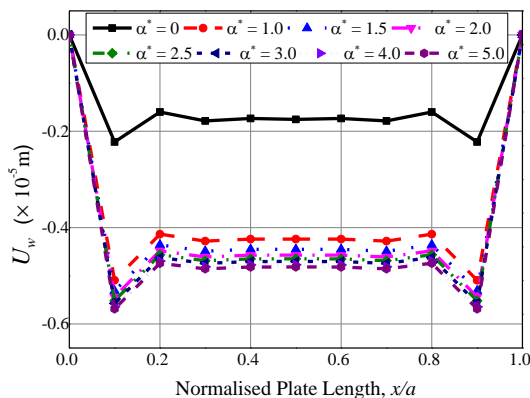
Figure 5.10: Effect of empirical constants on magnetic flux densities (a) B_x (b) B_z of SSSS MEE plate

The dependency of the elastic stiffness coefficients on the temperature rise ΔT and moisture concentration rise Δm is studied by varying the empirical constants α^* and β^* individually. The value of β^* is nullified while evaluating the individual effect of α^* and vice versa. Figures 5.11(a) – (f) and Figs. 5.12(a) - (f) illustrate the influence of α^* and β^* on the displacement component U_w , electric potential ϕ , magnetic potential ψ , normal stress σ_x , magnetic flux density B_z and the electric displacement D_z , respectively. It may be noticed from these figures that the influence of α^* on the displacement U_w is very small as compared to that of the β^* . The electric potential variation is indistinguishable for both the α^* and β^* . Also, it is observed that the increase in the empirical constants α^* and β^* lead to negligible variation in the magnetic potential (ψ) and hence to the magnetic flux density B_z , along the plate

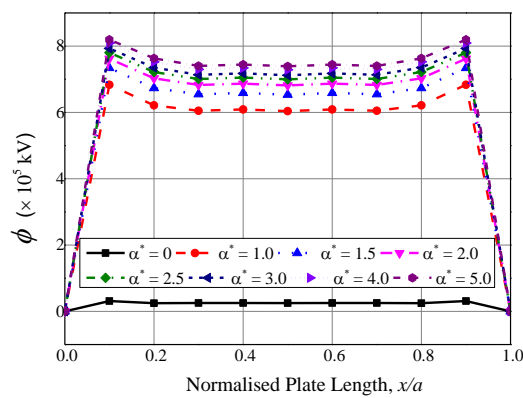
length. Nevertheless, a substantial effect of both the empirical constants α^* and β^* on the variation of normal stress σ_x is observed from Figs. 5.11(d) and 5.12(d), respectively. In contrast to α^* , the predominant effect of β^* is witnessed on the electric displacement D_z .

5.3.5. Clamped MEE plate (CCCC)

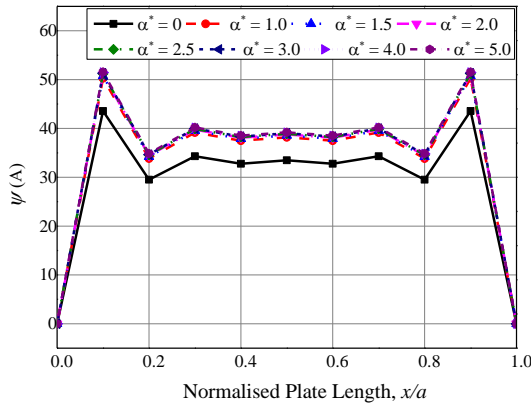
The hygrothermo-magneto-electro-elastic response of MEE plate with all sides clamped (CCCC) as depicted in Fig. 5.2(b) is analysed. Figures 5.13(a) – (c) demonstrate the plots of the displacements U_x , U_y and U_w , respectively. It is noticed that the displacements are symmetric along the plate length. Figures 5.14(a) and (b) illustrate the effect of empirical constants on the variation of the electric and the magnetic potential of the CCCC MEE plate. A higher value of HTMEE coupling (with respect to $\alpha^* = \beta^* = -0.5$) leads to an increased value of the potentials. Further, the empirical constants $\alpha^* = \beta^* = -0.5$ exhibit a significant influence on the direct quantities of the system. When the constants $\alpha^* = \beta^* = 0.0$, the MEE plate experiences the minimum stress, whereas the normal stress σ_x is maximum near the clamped edges, and remains almost constant over the plate length as shown in Fig. 5.15(a). Because of multiphysics interaction, the electric displacement and magnetic flux densities are significantly affected by hygrothermal loading. As seen from Figs. 5.15(b) – (e), the influence of temperature and moisture dependence is pronounced on the z -direction electric displacement (D_z) and the magnetic flux density components (B_z) than the x -direction components (D_x and B_x).



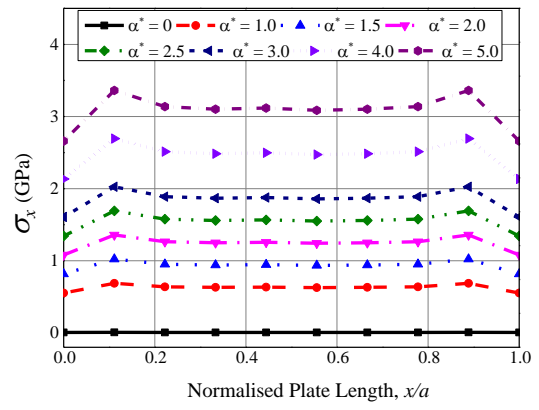
(a)



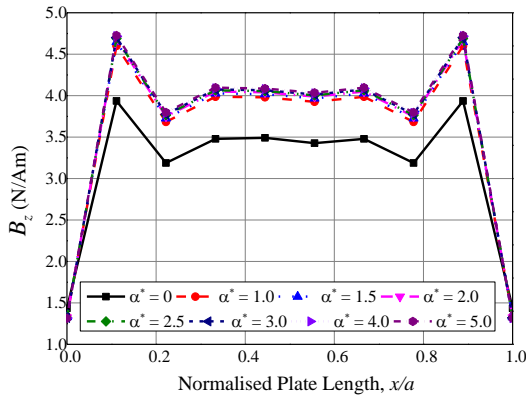
(b)



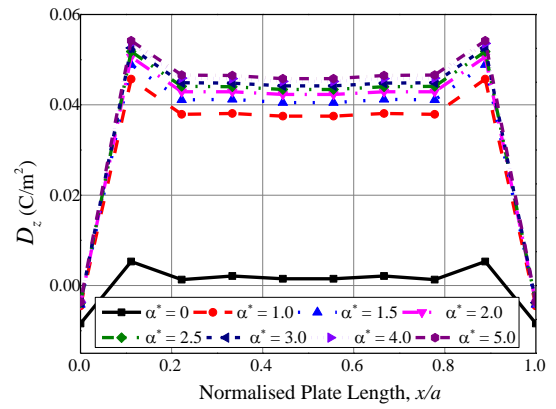
(c)



(d)

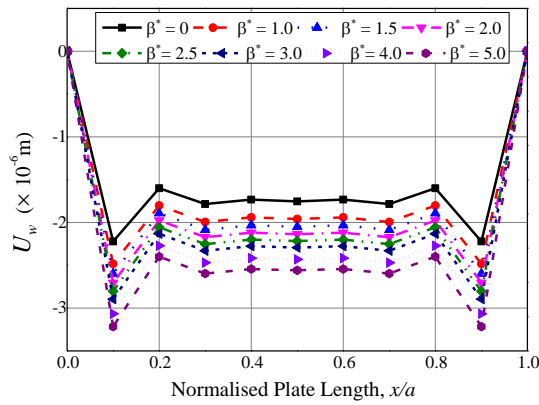


(e)

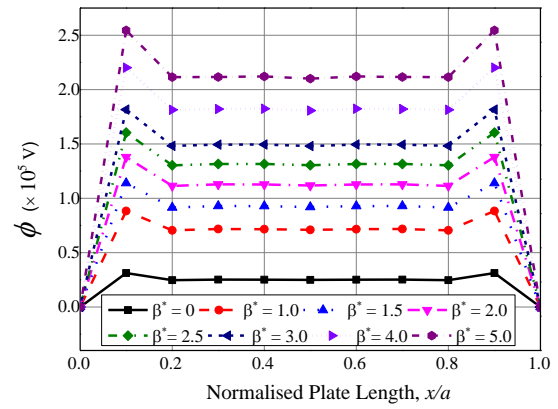


(f)

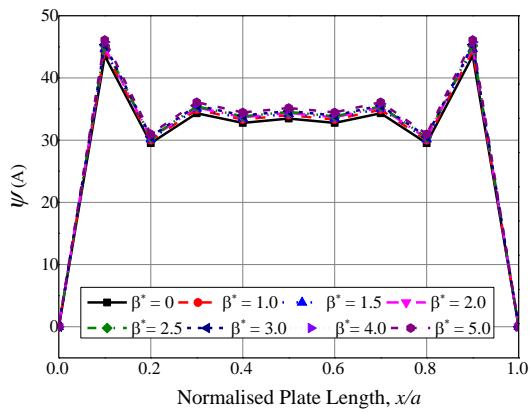
Figure 5.11: Influence of α^* on (a) U_w (b) ϕ (c) ψ (d) σ_x (e) B_z (f) D_z



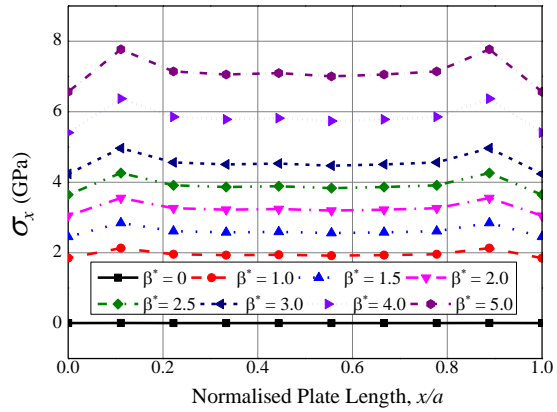
(a)



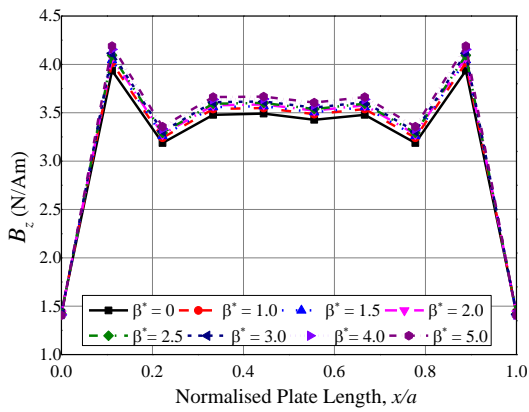
(b)



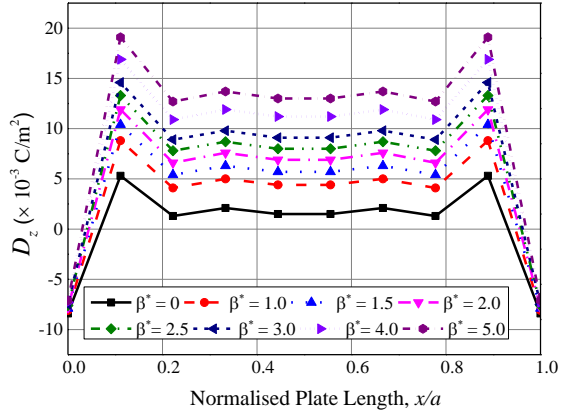
(c)



(d)

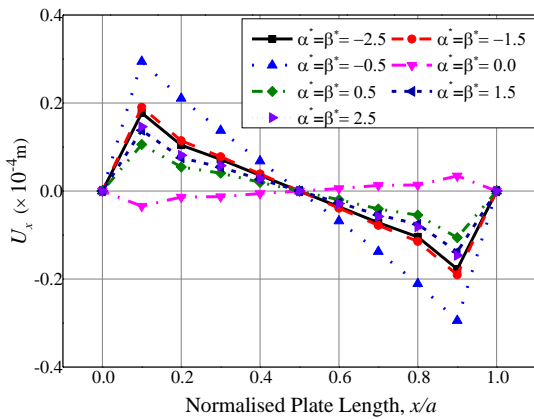


(e)

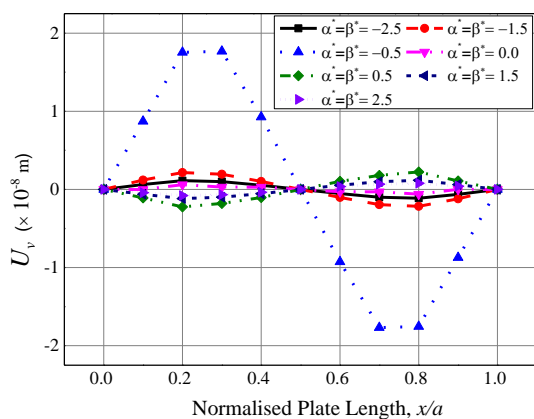


(f)

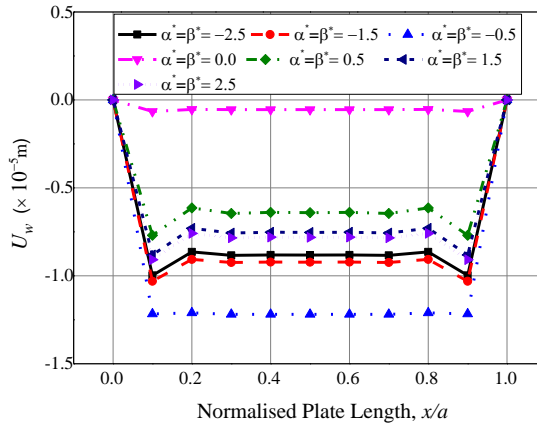
Figure 5.12: Influence of β^* on (a) U_w (b) ϕ (c) ψ (d) σ_x (e) B_z (f) D_z



(a)

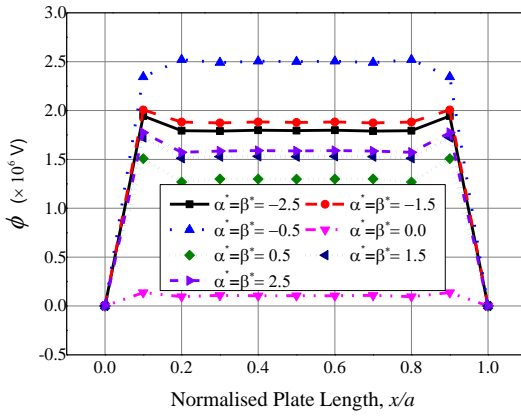


(b)

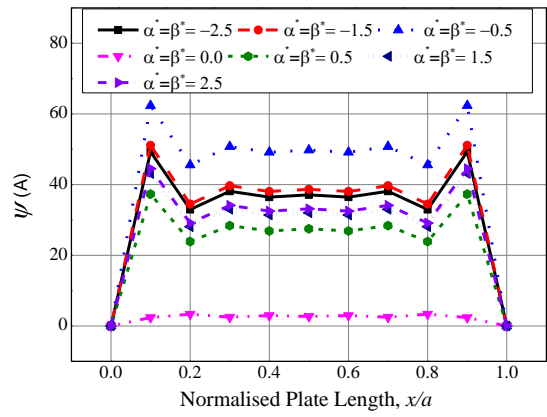


(c)

Figure 5.13: Effect of empirical constants on displacements (a) U_x (b) U_v (c) U_w of CCCC MEE plate

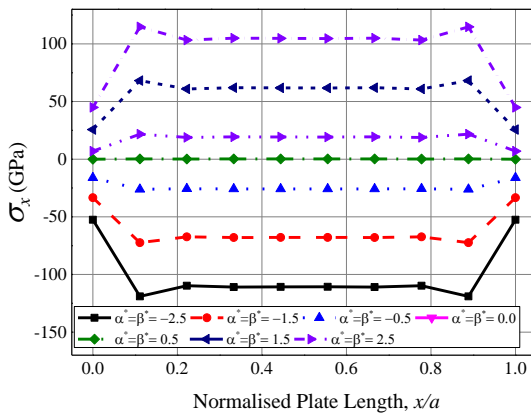


(a)

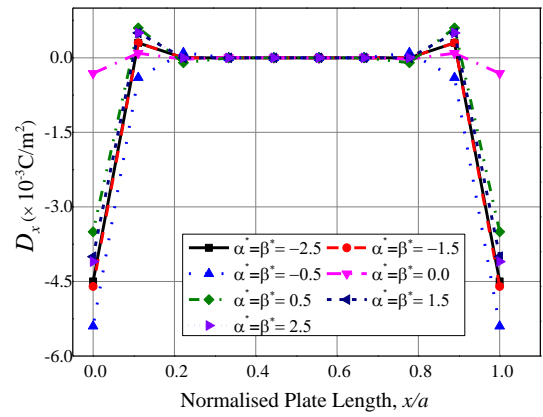


(b)

Figure 5.14: Effect of empirical constants on (a) electric potential ϕ (b) magnetic potential ψ of CCCC MEE plate



(a)



(b)

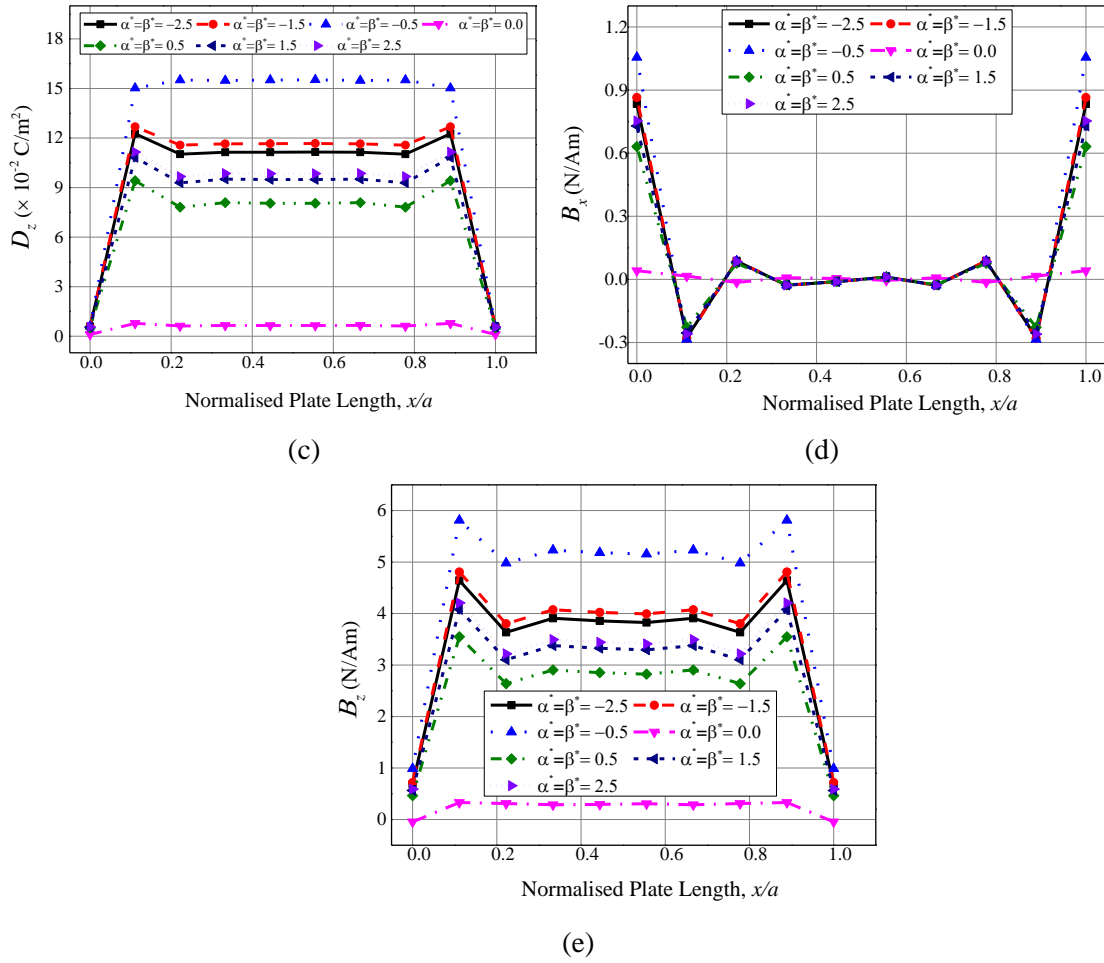


Figure 5.15: Effect of empirical constants on (a) normal stress σ_x (b) electric displacement D_x (c) magnetic flux density B_x of CCCC MEE plate

5.3.6. MEE plate with adjacent side clamped (CFFC)

In this case, a MEE plate with adjacent clamped edges (CFFC) as shown in Fig. 5.2(c) is considered for the analysis. Figure 5.16(a) illustrates the variation of transverse displacement U_w . It may be observed from this figure that the U_w is maximum at the free edge of the plate. This may be attributed to the predominant effect of hygrothermal loads caused due to asymmetric boundary conditions. Figures 5.16(b) and (c) depict the electric potential and magnetic potential distribution, respectively. It may be noticed from these figures that higher positive empirical constants lead to increased electric potential while the electric potential decreases as the negative empirical constants of temperature and moisture increases. Figure 5.16(c)

shows that with the increase in negative empirical constants, the absolute values of the magnetic potential decreases. In addition, as a result of higher HTMEE coupling at the free edge of the MEE plate, the electric potential and magnetic potential display the higher value. The magnitude of normal stress σ_x along the length of the *CFFC* MEE plate increases in response to the increasing empirical constants as displayed in Fig. 5.17(a). Further investigation reveals that the maximum normal stress σ_x is noticed at the clamped end, whereas the maximum shear stress τ_{xz} is observed at the free edge of the MEE plate as shown in Fig. 5.17(b).

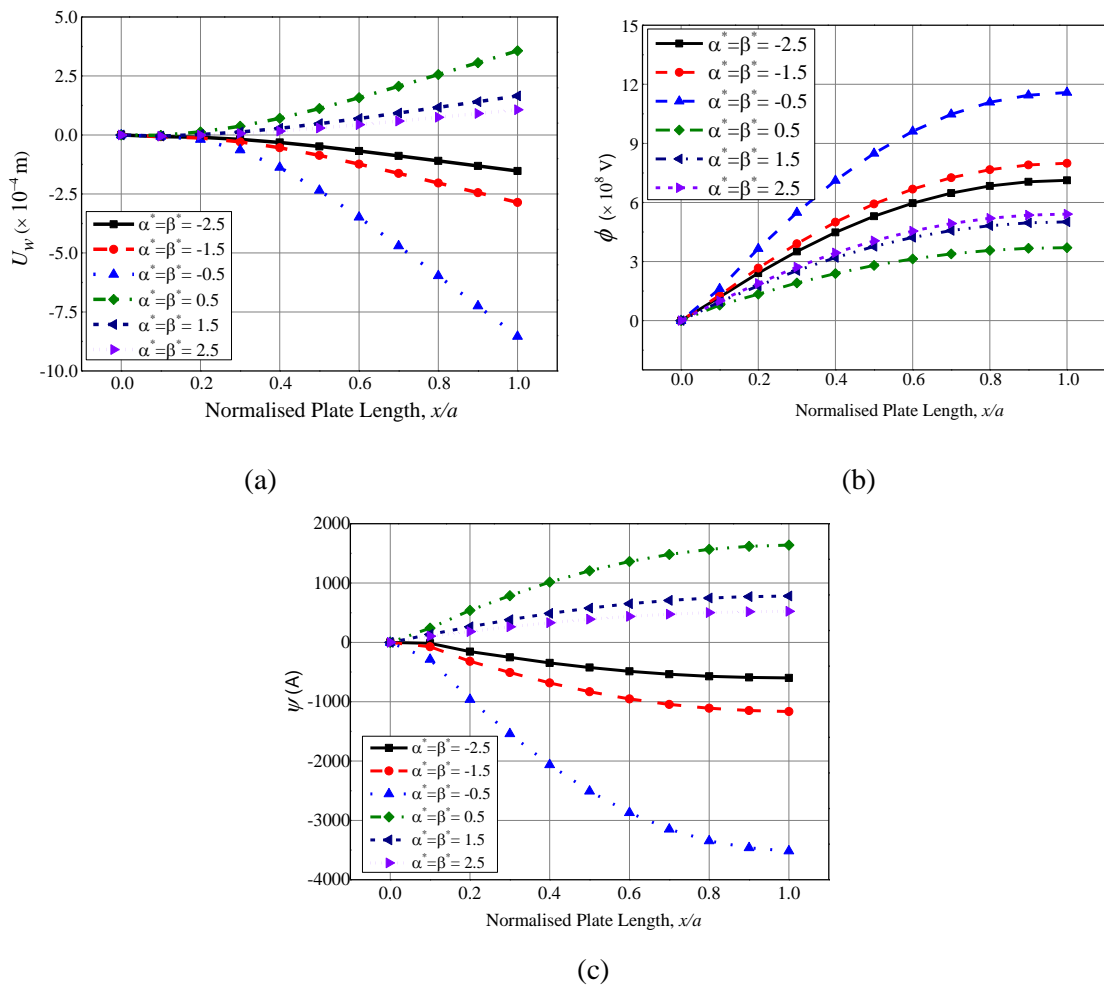


Figure 5.16: Effect of empirical constants on (a) transverse displacement U_w (b) electric potential ϕ (c) magnetic potential ψ of *CFFC* MEE plate

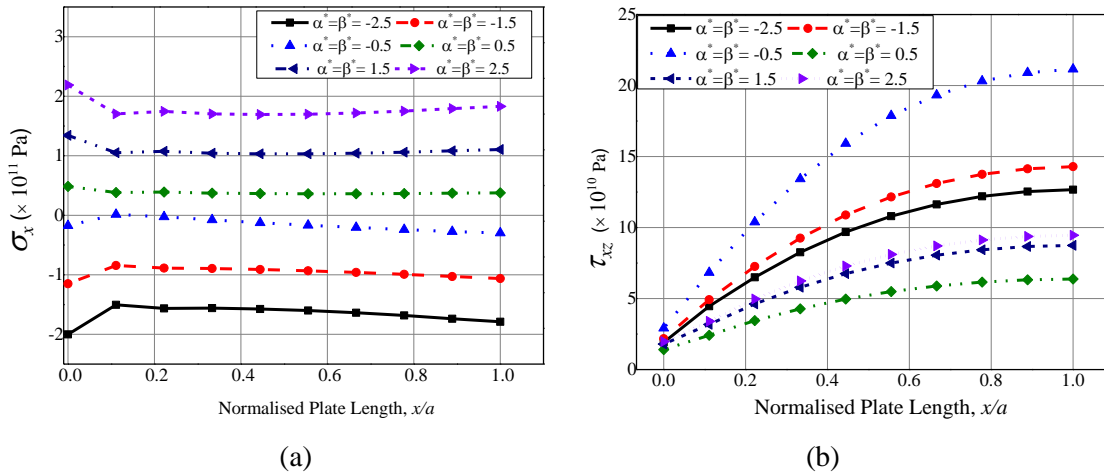


Figure 5.17: Effect of empirical constants on (a) normal stress- σ_x (b) shear stress τ_{xz} of *CFFC* MEE plate

Figures 5.18(a) – (c) show the effect of empirical constants on the electric displacements D_x , D_y and D_z , respectively. Unlike, the symmetric boundary conditions (*SSSS* and *CCCC*) of the MEE plate, a significant influence of empirical constants on the D_x and D_y are observed. This may be attributed to the fact that in comparison with the symmetric boundary condition, the asymmetrical boundary condition magnifies the effect of hygrothermal loads on the coupled responses. Also, it is evident from these figures that a significant influence of empirical constants $\alpha^* = \beta^* = -0.5$ prevails. A linear variation of D_x and D_z along the plate length is witnessed with the maximum values at the clamped end, whereas D_y varies parabolically and reaches the maximum value at the free end. The distribution of magnetic flux densities B_x , B_y and B_z is illustrated in Figs. 5.19(a) – (c), respectively. It can be summarized from Fig. 5.19(a) that in contrast to the MEE plate with positive empirical constants, the negative empirical constants results in an increasing trend of B_x along the plate length. Likewise, for all the empirical constants, the minimal value of B_x is found at the free end, whereas for B_y it is witnessed at the clamped edge.

5.3.7. MEE plate with opposite sides clamped (FCFC)

The hygrothermal analysis of *FCFC* MEE (Fig. 5.2(d)) plate has been carried out for the identical geometry used in the previous section. The displacements U_x , U_y and U_w for the *FCFC* MEE plate are shown in Figs. 5.20(a) – (c), respectively. It is

noticed from Fig. 5.20(a) that a meager influence of empirical constants of $\alpha^* = \beta^* = -0.5$ prevails on U_x . The variation of the electric potential and magnetic potential due to multiphysics interaction of hygrothermal loading is illustrated in Figs. 5.21(a) and (b), respectively. The positive empirical constants are directly proportional to both the potentials (ϕ and ψ), whereas the negative empirical constants have an adverse effect. Further investigation reveals that at the midspan of the MEE plate, the hygrothermal loads generate the maximum and minimum values of the electric potential and magnetic potential, respectively.

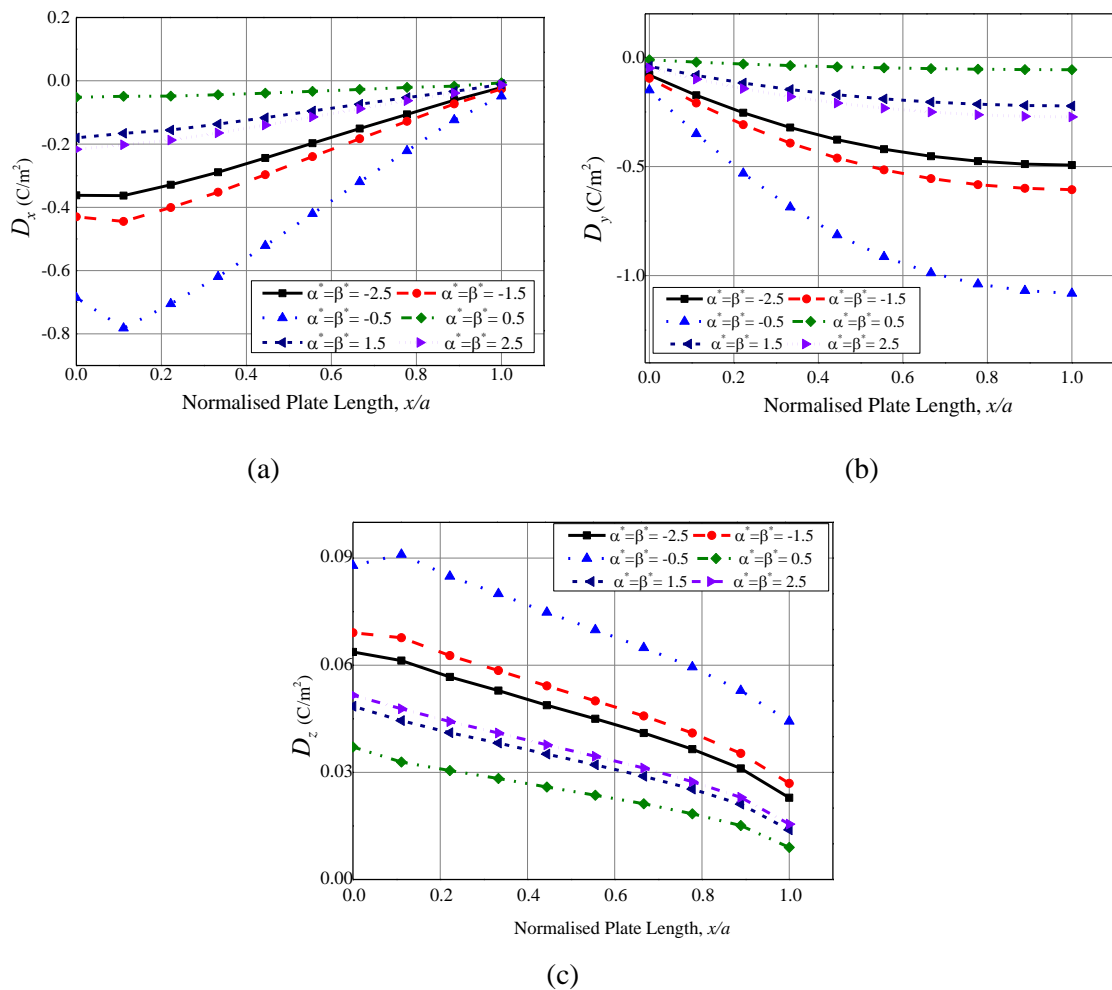
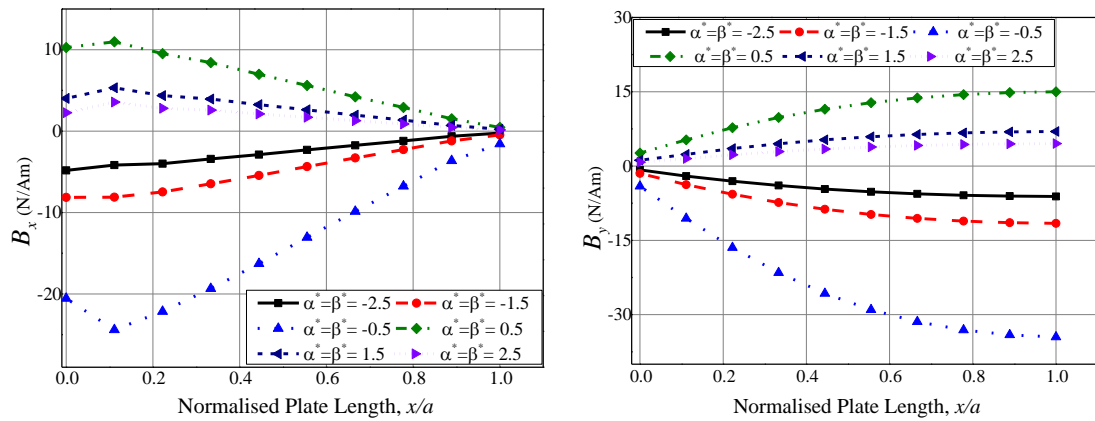
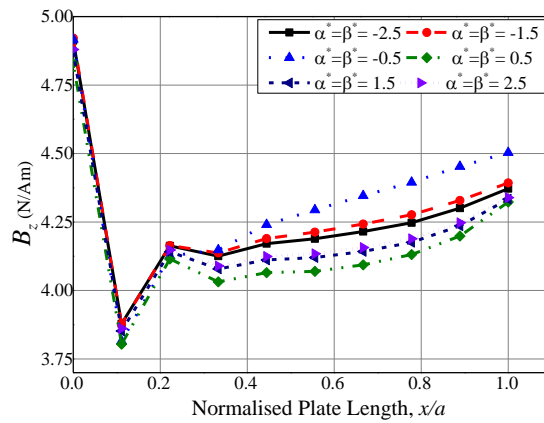


Figure 5.18: Effect of empirical constants on electric displacements (a) D_x (b) D_y (c) D_z of CFFC MEE plate

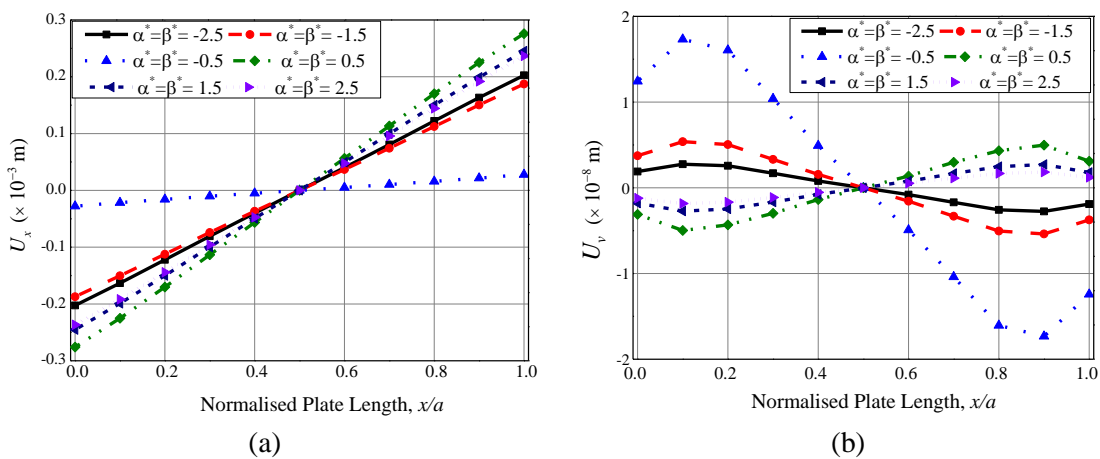


(a) (b)

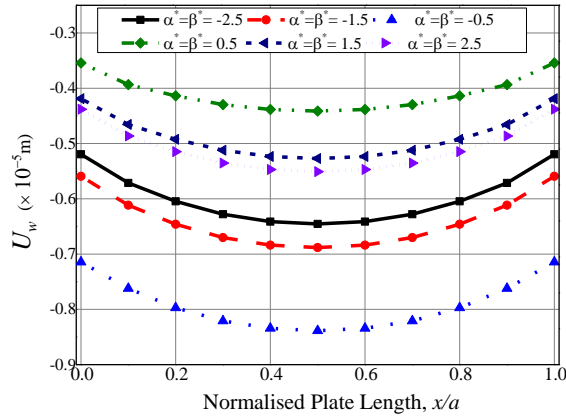


(c)

Figure 5.19: Effect of empirical constants on magnetic flux densities (a) B_x (b) B_y (c) B_z of CFFC MEE plate

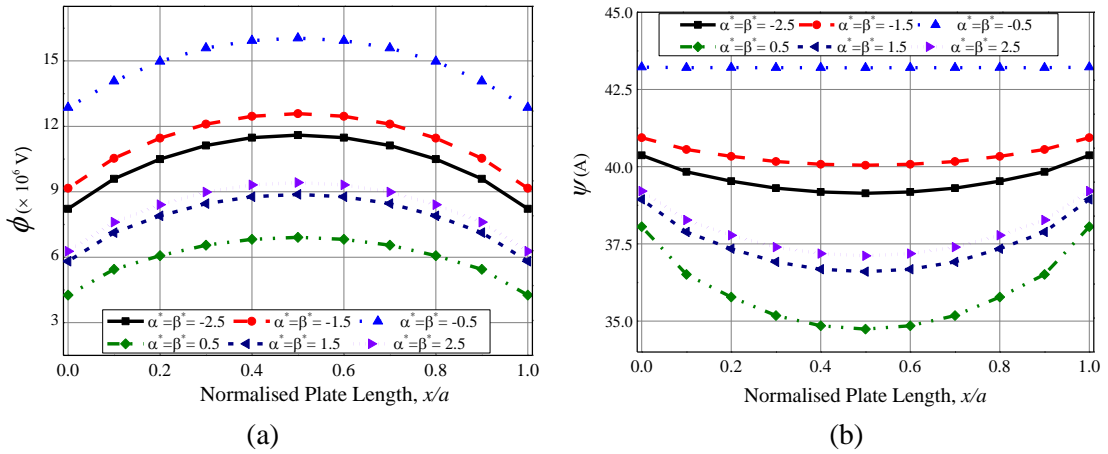


(a) (b)



(c)

Figure 5.20: Effect of empirical constants on displacements (a) U_x (b) U_y (c) U_w of *FCFC* MEE plate



(a)

(b)

Figure 5.21: Effect of empirical constants on (a) electric potential ϕ (b) magnetic potential ψ of *FCFC* MEE plate

The results depicted in Fig. 5.22(a) indicate that the absolute value of the normal stress σ_x along the plate length increases with the increase in both positive and negative empirical constants. For all the empirical constants, the shear stresses τ_{xz} and τ_{xy} vary symmetrically along the plate length as illustrated in Figs. 5.22(b) and (c), respectively. The shear stress component τ_{yz} varies linearly along the plate length (Fig. 5.22(d)). Figures 5.23(a) – (c) demonstrate the effect of empirical constants on the electric displacements D_x , D_y and D_z , respectively. An insignificant effect of the empirical constants may be noticed on the variations of D_x and D_y along the plate length, while a significant effect is witnessed for D_z . Contrary to the *CFFC* MEE

plate, it is noticed from Fig. 5.24(a) that $\alpha^* = \beta^* = -0.5$ has a least influence on the magnetic flux density component B_x . However, for all the empirical constants, the B_x varies linearly along the plate length and reaches the maximum values at the free edges of the *FCFC* MEE plate. Figure 5.24(b) shows the variation of B_y along the plate length of the *FCFC* MEE plate. The distribution of the magnetic flux density component B_z is dominated by the empirical constants $\alpha^* = \beta^* = -0.5$ as illustrated in Fig. 5.24(c).

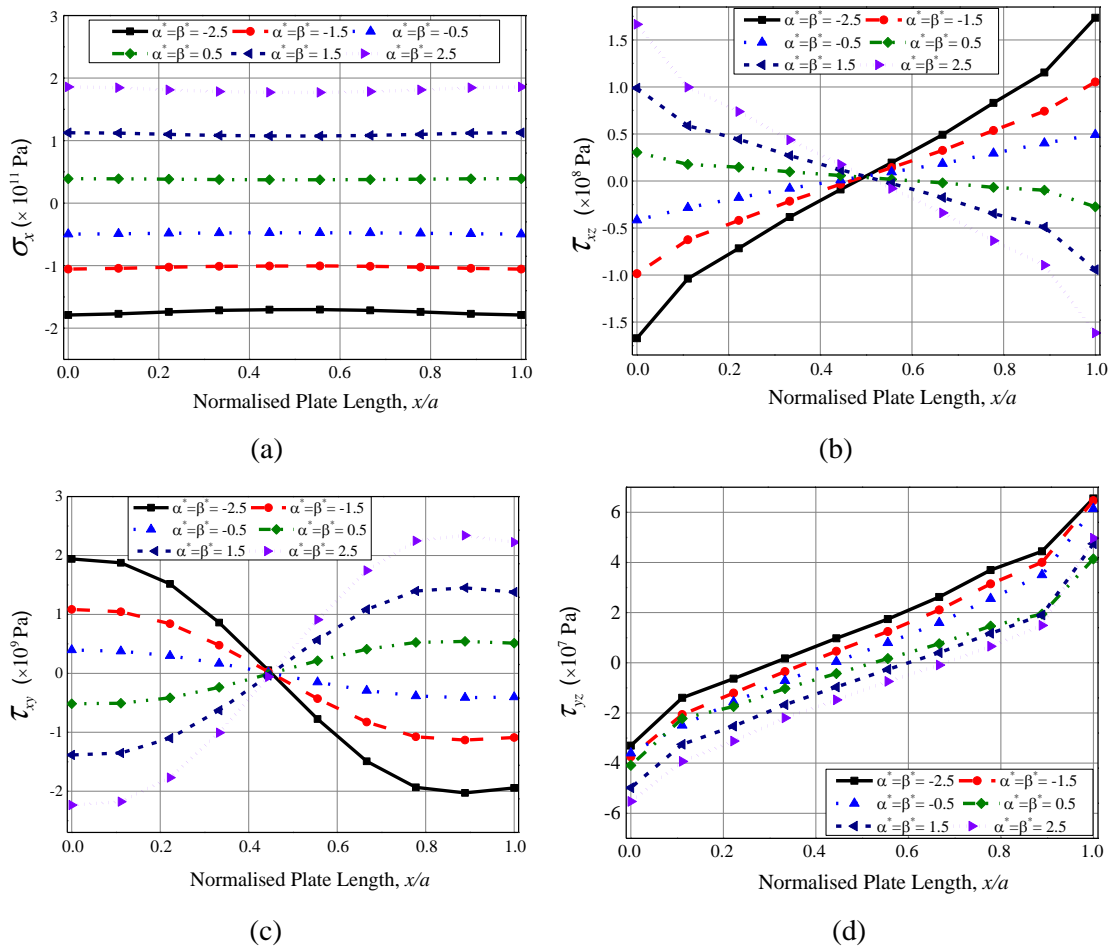
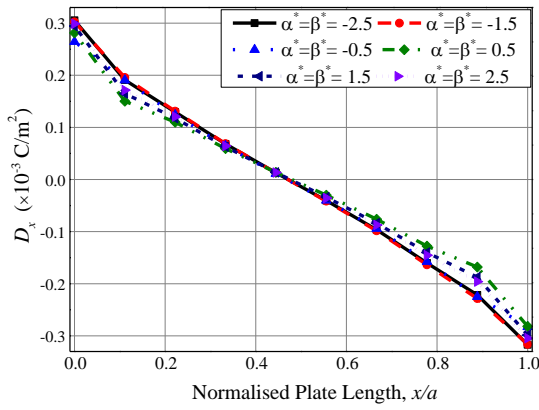
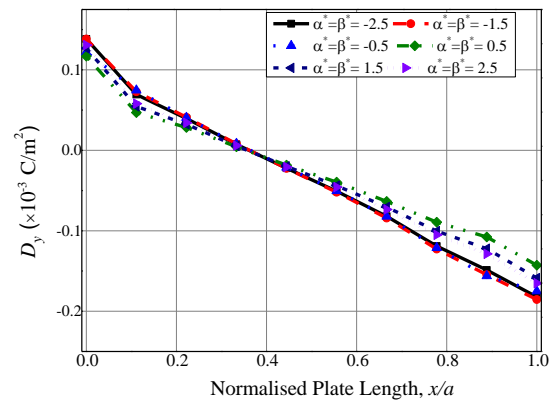


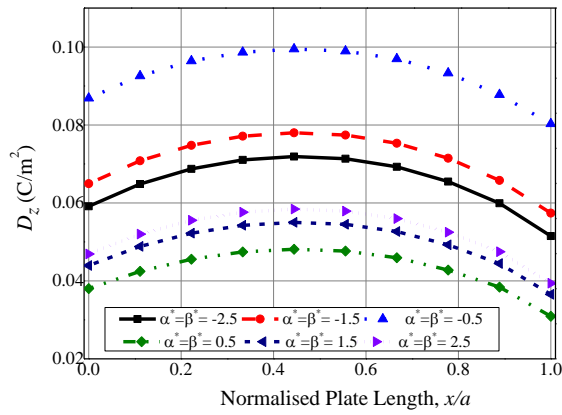
Figure 5.22: Effect of empirical constants on (a) normal stress σ_x (b) shear stress τ_{xz} (c) shear stress τ_{xy} (d) shear stress τ_{yz} of *FCFC* MEE plate



(a)

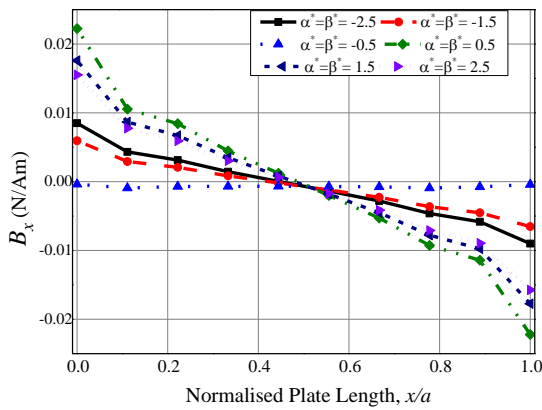


(b)

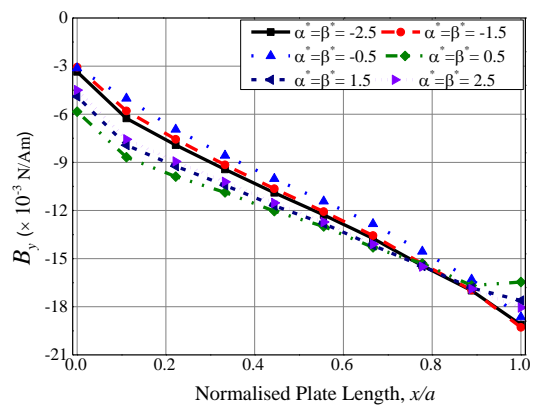


(c)

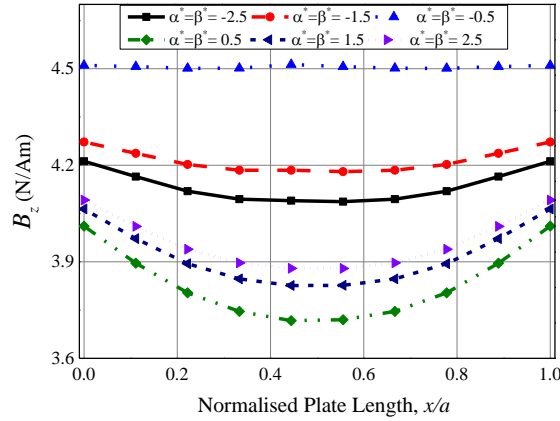
Figure 5.23: Effect of empirical constants on electric displacements (a) D_x (b) D_y (c) D_z of *FCFC* MEE plate



(a)



(b)



(c)

Figure 5.24: Effect of empirical constants on magnetic flux densities (a) B_x (b) B_y (c) B_z of *FCFC* MEE plate

A comparative study of the effect of boundary conditions on the maximum values of the direct quantities is encapsulated in Table 5.2. It can be inferred that the *CFFC* boundary condition of the *HTMEE* plate results in a higher magnitude of displacements and potentials.

Table 5.2: Effect of boundary conditions on the direct quantities of MEE plate

Parameter	<i>CCCC</i>	<i>SSSS</i>	<i>CFFC</i>	<i>FCFC</i>
U_x (m)	0.013792×10^{-3}	-0.15973×10^{-3}	0.2855×10^{-3}	0.245204×10^{-3}
U_v (m)	0.117415×10^{-8}	-0.10567×10^{-9}	0.1927×10^{-3}	0.271777×10^{-8}
U_w (m)	-0.88173×10^{-5}	-0.53245×10^{-5}	6.9×10^{-5}	-0.5271×10^{-5}
ϕ (V)	1.723439×10^6	6.607276×10^5	5.0142×10^8	8.87785×10^5
ψ (A)	43.13319	50.77091	781.2889	38.94086

5.3.8. Effect of a/h ratio

In this section, the effect of aspect ratio (a/h) on some of the parameters of a *FCFC* MEE plate is evaluated. A uniform hygrothermal load of $\Delta T = 100$ K, $\Delta m = 1\%$ moisture concentration change and $\alpha^* = \beta^* = 1.0$ is assumed for the analysis. Figures 5.25(a) – (e) demonstrate the variations of transverse displacement U_w , electric potential ϕ , electric displacement D_x , magnetic flux density B_x , normal stress σ_x and shear stress τ_{xz} , respectively. It may be noticed from these figures that the predominant

effect of the lower aspect ratio ($a/h = 10$) prevails on the HTMEE response of the MEE plates.

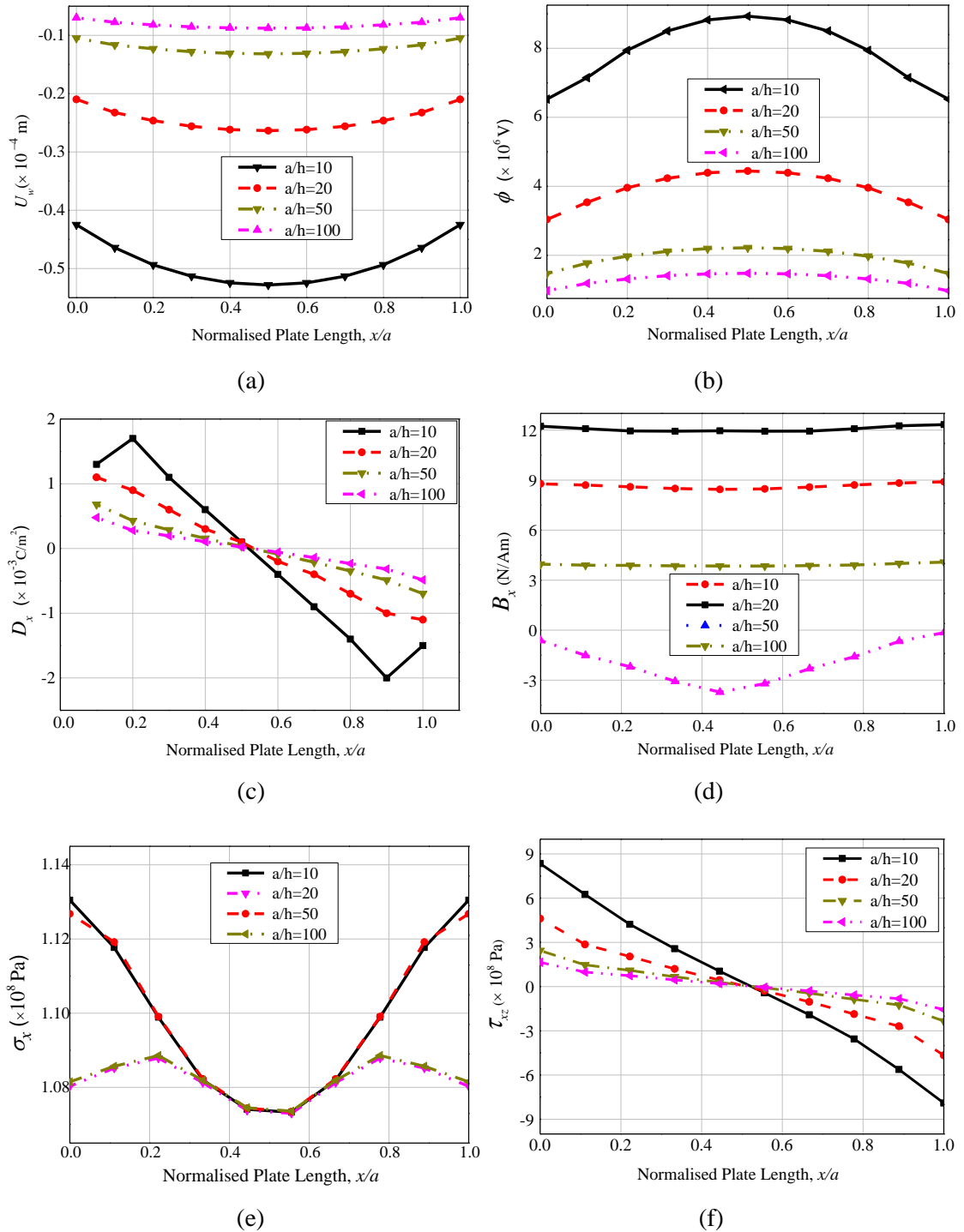


Figure 5.25: Effect of aspect ratio a/h on (a) U_w (b) ϕ (c) D_x (d) B_z (e) σ_x (f) τ_{xz}

5.4. CONCLUSIONS

In this chapter, the effect of hygrothermal loading on the multiphysics response of magneto-electro-elastic (MEE) plate using finite element (FE) method is studied. A FE element formulation is derived using the principle of total potential energy and linear coupled constitutive equations of MEE material. The numerical results suggest that the direct quantities and stresses vary proportionally to the applied hygrothermal loads. However, a negligible influence of hygrothermal loads is observed on the electric displacement components (D_x and D_y) and magnetic flux density components (B_x and B_y). The empirical constants $\alpha^* = \beta^* = -0.5$ has a significant influence on the displacement components and potentials of the MEE plate. The normal stress components vary accordingly with the empirical constants, while the empirical constants have a negligible effect on the shear stresses (τ_{xz} and τ_{yz}), electric displacement (D_x and D_y) and magnetic flux density (B_x and B_y). Among all the boundary conditions considered, a distinguishable effect of empirical constants on the D_x , D_y , B_x and B_y is observed only for *CFFC* MEE plate. In addition, *CFFC* boundary condition has a predominant effect on the direct quantities. The investigation of the effect of aspect ratio reveals that the lower aspect ratio (thick plates) has a significant effect on the static parameters of MEE plate. It is believed that the current results reveal the possible interactions of different physical fields on the structural behaviour of smart systems.

Chapter 6

HYGROTHERMAL ANALYSIS OF MAGNETO-ELECTRO-ELASTIC BEAMS

This chapter presents the analysis of magneto-electro-elastic (MEE) beam subjected to hygrothermal loading. The influence of combined hygrothermal loads and distinct effect of moisture concentration has been investigated. The hygrothermo-magneto-electro-elastic (HTMEE) beam is considered to be made of adaptive wood with properties of piezoelectric and magnetostrictive materials. The influence of temperature and moisture dependent material stiffness coefficients on the static parameters of the MEE beam is also evaluated. The independent effect of temperature and moisture on the coupled responses of the beam is investigated. Significant combination of the empirical constants corresponding to the temperature dependency and moisture dependency is explored, and its effect on the static parameters of HTMEE beam has been studied.

Related article: Vinyas, M., Kattimani, S. C. and Sharnappa, J. (2018), “Hygrothermal coupling analysis of magneto-electroelastic beams using finite element methods”, *Journal of Thermal Stresses*, **41**(8), 1063-1079.

6.1 INTRODUCTION

In Chapter 5, the finite element (FE) formulation of hygrothermo-magneto-electro-elastic (HTMEE) plates has been derived and the effect of hygrothermal fields has been studied in detail. Analogously, in this chapter, the study has been extended for HTMEE beams. For such investigations, an adaptive wood having the properties of piezoelectric (Barium Titanate) and magnetostrictive (Cobalt Ferrite) has been considered. Numerical examples have been solved to investigate the effects of boundary conditions and empirical constants on the static behaviour of HTMEE beam. Further, the most significant value of moisture dependent empirical constant and the

corresponding temperature dependent empirical constant has been determined. In addition, the variations of the primary and secondary quantities are investigated for different hygrothermal loads and boundary conditions. A comparative study on the effect of hygrothermal and temperature loads has also been presented.

6.2 BASIC FORMULATION OF THE PROBLEM

6.2.1. Problem description

Figure 6.1 depicts the schematic representation of hygrothermo-magneto-electro-elastic (HTMEE) beam made up of an adaptive wood possessing the properties of piezoelectric and magnetostrictive (CoFe_2O_4). The co-ordinate system of the HTMEE beam is shown in Fig. 6.1. The length a , width w and the thickness h , runs along the x -, y - and z - coordinates, respectively. It is assumed that the HTMEE beam is exposed to a hygrothermal environment which corresponds to the temperature rise of ΔT and humidity concentration variation of Δm .

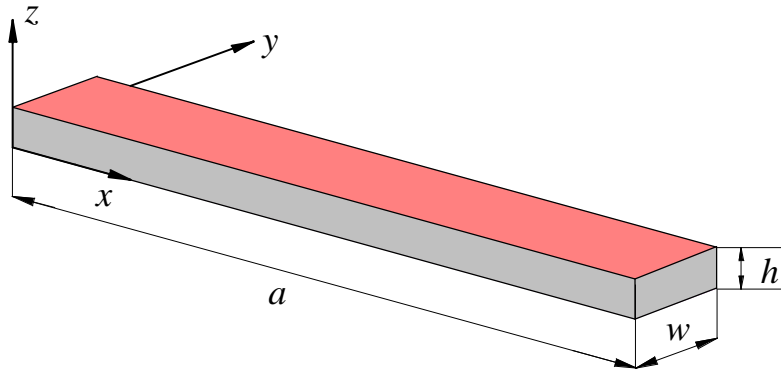


Figure 6.1: Schematic representation of **HTMEE** beam

6.2.2. Finite element formulation and governing equations

In Chapter 5, a 3D FE formulation and the corresponding governing equations of HTMEE structures has been derived. The same FE formulation has been used for the analysis of HTMEE beam also. Consequently, the final global equilibrium equations can be recalled as follows:

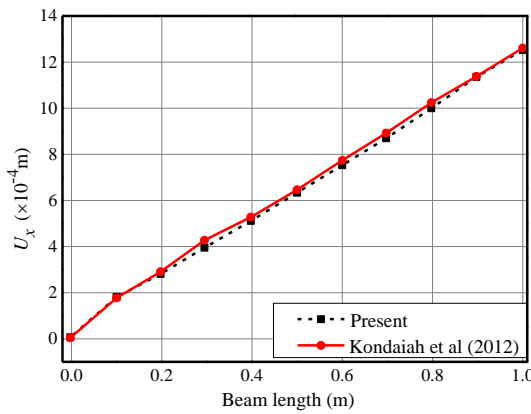
$$\left[K_{tt}^g \right] \{ d_t \} + \left[K_{t\phi}^g \right] \{ \phi \} + \left[K_{t\psi}^g \right] \{ \psi \} = \{ F_{th}^g \} + \{ F_{hy}^g \} \quad (6.1)$$

$$\left[K_{t\phi}^g \right]^T \{d_t\} - \left[K_{\phi\phi}^g \right] \{\phi\} - \left[K_{\phi\psi}^g \right] \{\psi\} = \{F_{p,e}^g\} + \{F_{h,e}^g\} \quad (6.2)$$

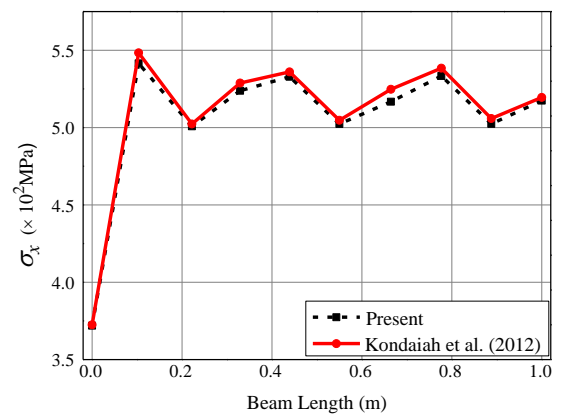
$$\left[K_{t\psi}^g \right]^T \{d_t\} - \left[K_{\phi\psi}^g \right]^T \{\phi\} - \left[K_{\psi\psi}^g \right] \{\psi\} = \{F_{p,m}^g\} + \{F_{h,m}^g\} \quad (6.3)$$

6.3 RESULTS AND DISCUSSIONS

This section addresses the credibility of the proposed FE formulation in predicting the static behaviour of HTMEE beam subjected to moisture and temperature loads. Numerical calculations are performed using the FE formulation derived in the previous chapters. However, to the best of authors' knowledge, no work has been reported on static studies of MEE beams in hygrothermal environment. Therefore, the FE formulation derived here is validated with the results obtained by Kondaiah *et al.* (2012) by neglecting the hygroscopic effect. The results depicted in Figs. 6.2(a) – (d) reveal that the present FE formulation closely agrees with Kondaiah *et al.* (2012). Consequently, in the present study, the independent effect of moisture concentration gradient, different hygrothermal load profiles, temperature and moisture dependent material properties, empirical constants and boundary conditions on the static behaviour of HTMEE beam is demonstrated. The geometrical parameters of the HTMEE beam are: length (a) = 1 m, width (w) = 0.1 m and thickness (h) = 0.1 m. The material properties of adaptive wood made of BaTiO₃ and Cobalt Ferrite CoFe₂O₄ are tabulated in Table 5.1.



(a)



(b)

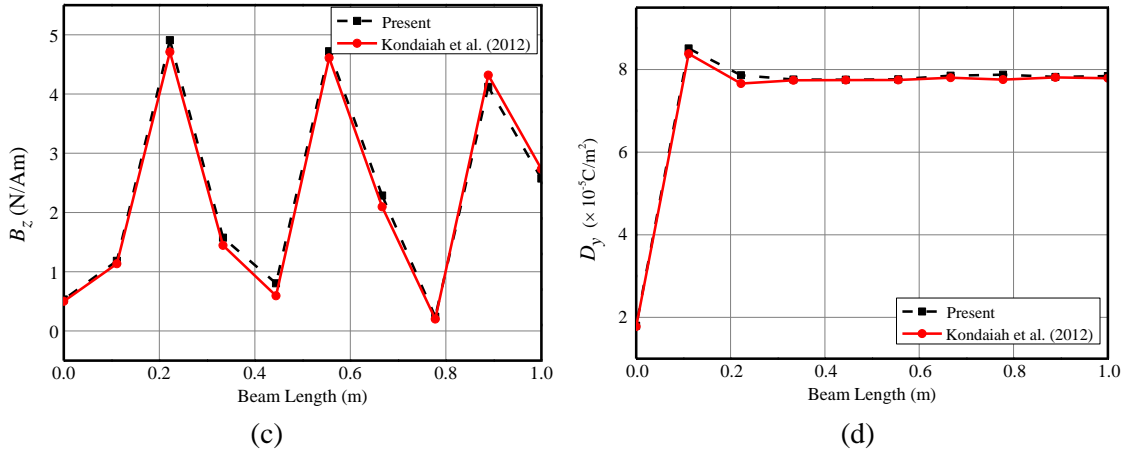


Figure 6.2: Validation plots (a) U_x (b) σ_x (c) B_z (d) D_y of MEE beam

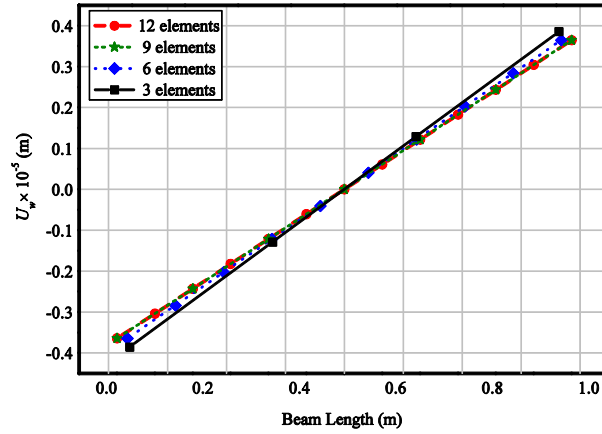


Figure 6.3: Convergence of transverse displacement component U_w

6.3.1. Effect of hygrothermal loads

The influence of uniform hygrothermal loads on the primary (displacements, electric potential and magnetic potential) and secondary quantities (stresses, electric displacements and magnetic flux densities) of clamped-clamped (C-C) HTMEE beam is evaluated. Figures 6.4 and 6.5 illustrate the effect of hygrothermal loads on the primary quantities of C-C HTMEE beam. The primary quantities increase with the increase in hygrothermal loads in accordance with Eq. (5.17). Moreover, at the midspan of the beam, U_x is found to be maximum, while U_v is maximum near the clamped end of the HTMEE beam. It may be witnessed from Fig. 6.4(c) that U_w tends

to vary symmetrically along the beam length while it is zero at the midspan. Due to the predominant influence of pyroeffects, the electric potential and magnetic potential are maximum at the clamped end as plotted in Figs. 6.5(a) and (b), respectively. Figure 6.6(a) illustrates the variation of normal stress σ_x in the HTMEE beam caused due to different hygrothermal loads. The shear stresses τ_{xz} , τ_{xy} and τ_{yz} vary symmetrically along the beam length with maximum value appearing at the clamped end as elucidated in Figs. 6.6(b) – (d), respectively. The electric displacement component D_x is observed to be zero at the midspan of the HTMEE beam as depicted in Fig. 6.7(a). While, Figs. 6.7(b) and (c) display the electric displacements D_y and D_z , respectively. Further, for each case of the hygrothermal loads, the magnetic flux densities B_x , B_y and B_z are depicted in Figs. 6.8(a) – (c), respectively.

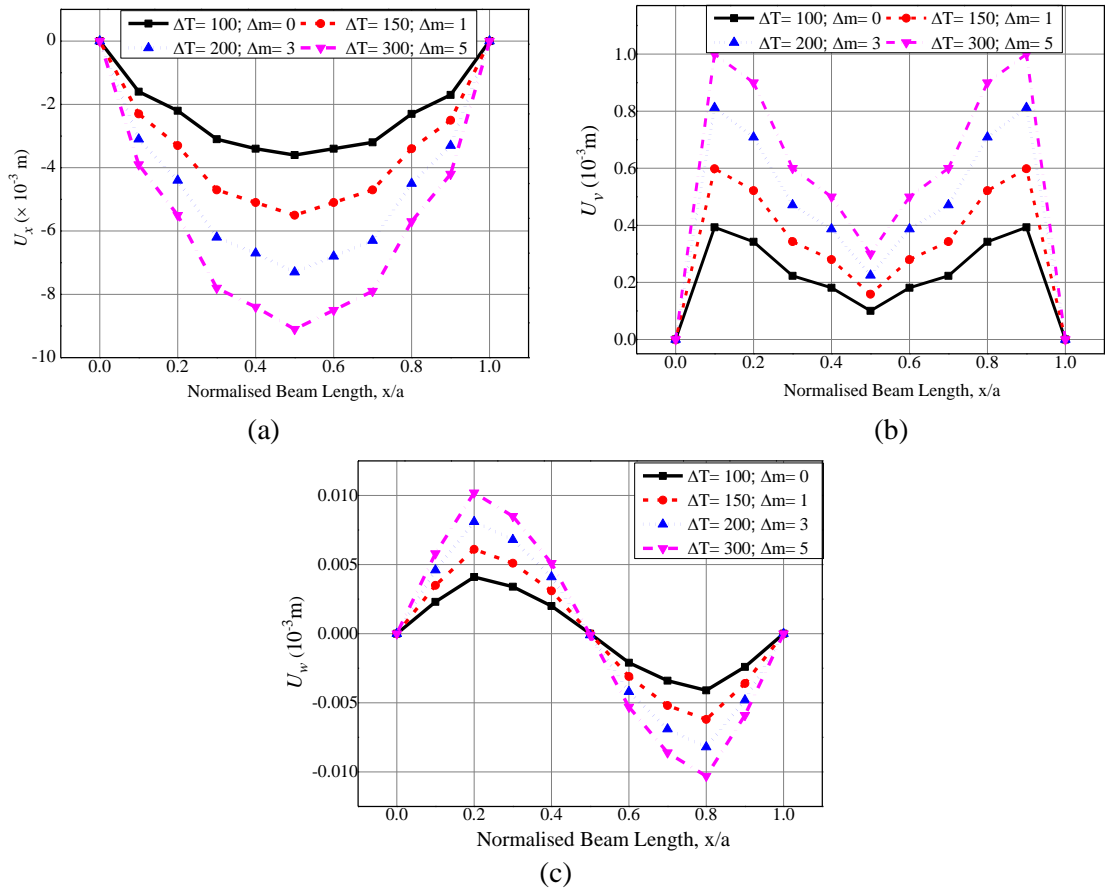


Figure 6.4: Effect of hygrothermal loads on displacement components (a) U_x (b) U_y (c) U_w for C-C HTMEE beam

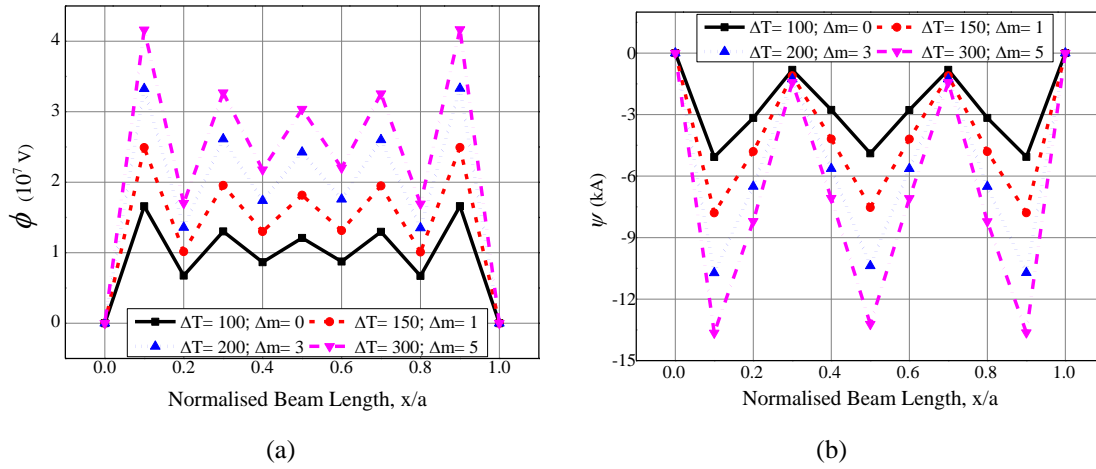


Figure 6.5: Effect of hydrothermal loads on (a) electric potential ϕ (b) magnetic potential ψ for C-C HTMEE beam

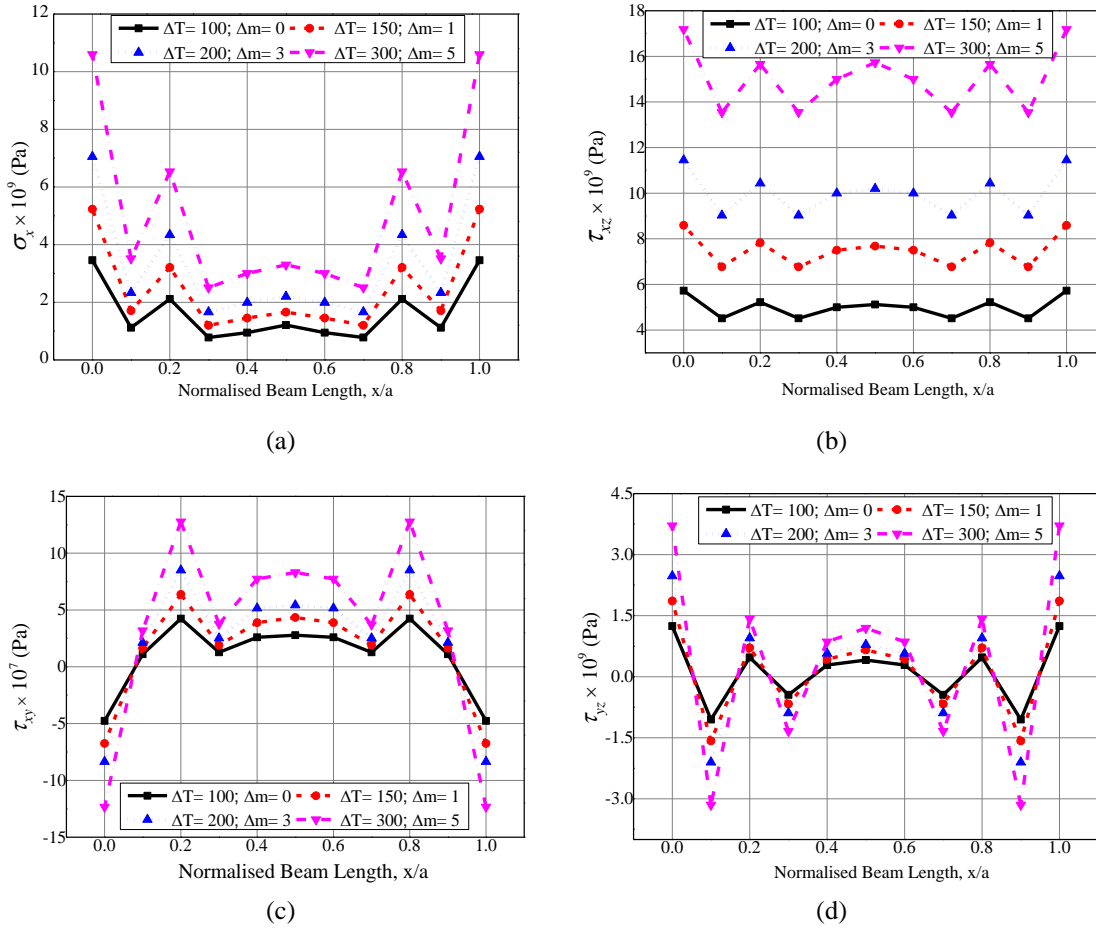
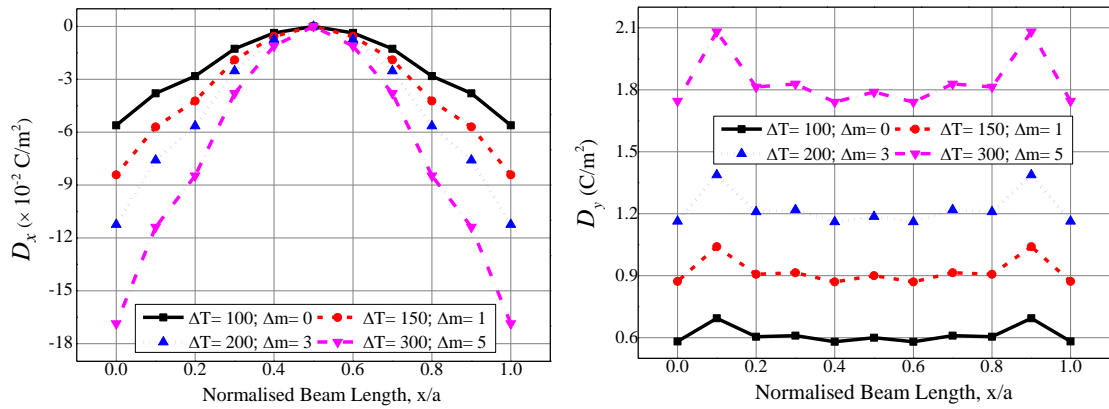
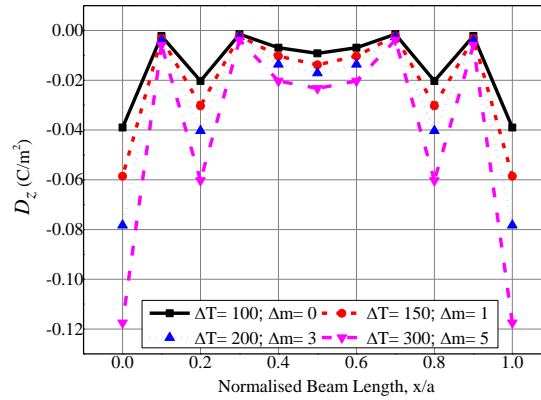


Figure 6.6: Effect of hydrothermal loads on (a) normal stress σ_x (b) shear stress τ_{xz} (c) shear stress τ_{xy} for C-C HTMEE beam



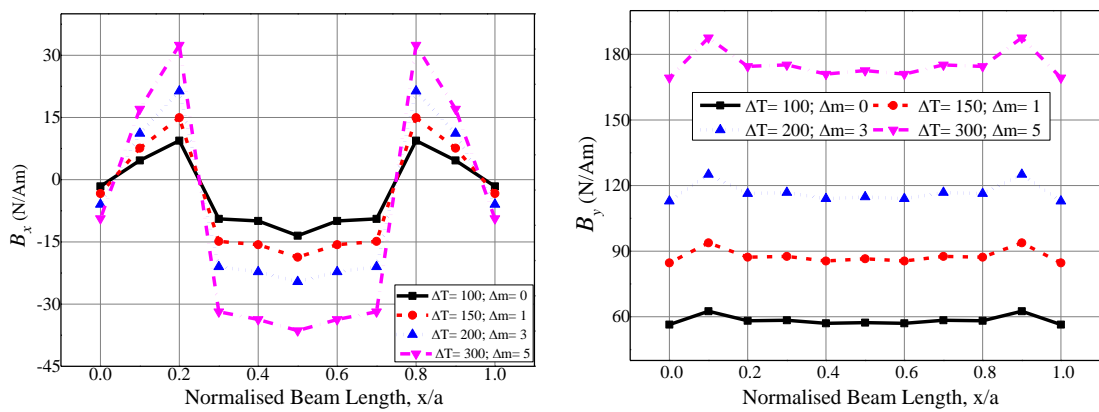
(a)

(b)



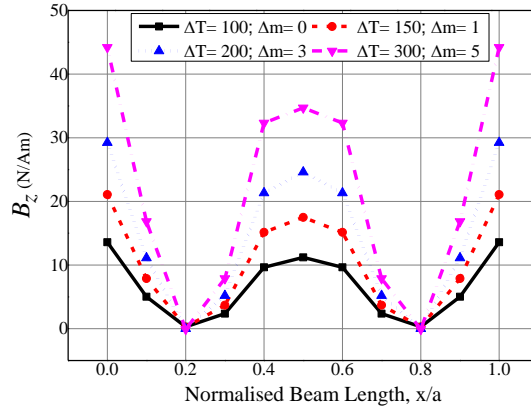
(c)

Figure 6.7: Effect of hygrothermal loads on electric displacements (a) D_x (b) D_y (c) D_z for C-C HTMEE beam



(a)

(b)



(c)

Figure 6.8: Effect of hygrothermal loads on magnetic flux densities (a) B_x (b) B_y (c) B_z for C-C HTMEE beam

Making use of numerical examples, the independent effect of moisture concentration gradient Δm on the static characteristics of HTMEE beam is investigated keeping temperature rise ΔT constant (100 K). The higher the moisture concentration change (Δm) results in greater values of the x -direction displacement U_x and y -direction displacement U_y , whereas a marginal effect prevails on the transverse displacement U_w , as shown in Figs 6.9(a) – (c), respectively. This may be the result of negligible amount of hygroscopic load $\{F_{hy}\}$ developed in the z -direction in comparison with the thermal loads $\{F_{th}\}$ for the considered Δm and ΔT . Investigation on the potentials reveal that meagre influence of Δm exists on the electric potential ϕ (Fig. 6.10(a)), whereas a significant effect on the magnetic potential is seen as shown in Fig. 6.10(b). The normal and shear stresses variations are plotted in Figs. 6.11(a) – (f). It may be observed from these figures that the considerable influence of Δm prevails on all the normal stresses while the effect on the shear stresses is insignificant. Further, the magnified plots of Figs. 6.11(d) – (f) reveal that considerable values of τ_{xz} and τ_{yz} are attained with the increase in hygrothermal load, whereas τ_{xy} reduces with the increase in the Δm . A minimal influence of the Δm on the electric displacements D_x , D_y and D_z is recorded as shown in Figs. 6.12(a) – (c), respectively. It may be due to the

fact that either the electric displacements are affected directly by the electric potential or the hygroscopic effects are very less in comparison with the thermal load. Furthermore, it can be deduced from the further examination that the D_x reduces as the Δm increases. Figures 6.12(a) - (c) display the effect of Δm on D_x , D_y and D_z , respectively. It can be observed from these figures that D_x is zero at the midspan of the HTMEE beam, while D_y is maximum near the clamped end. On the other hand, Figs. 6.13(a) – (c) depict the magnetic flux density distributions B_x , B_y and B_z , respectively, along the beam length. Unlike the electric displacements, a noticeable effect of moisture concentration rise exists on B_x and B_z , while an insignificant influence is observed on B_y . It may also be noticed that the variation profile of the electric displacement and magnetic flux density closely follows the electric potential and magnetic potential, respectively, due to the direct effect.

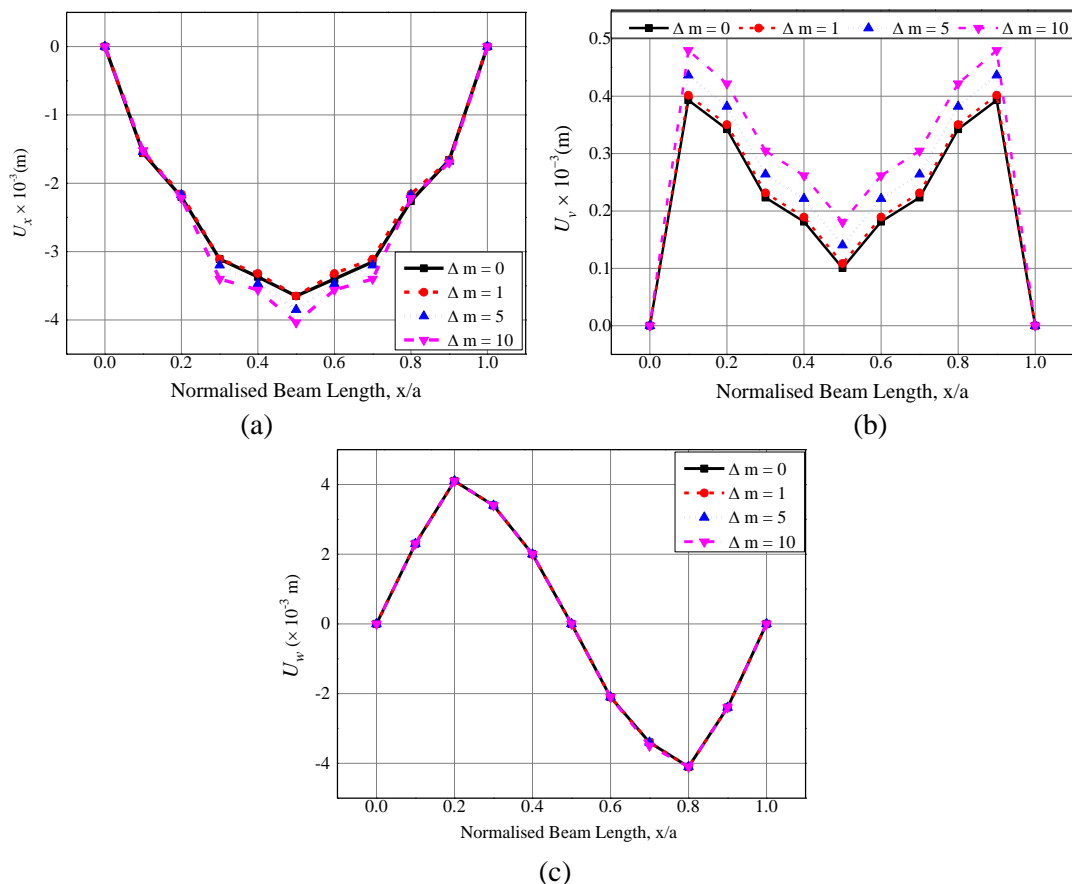
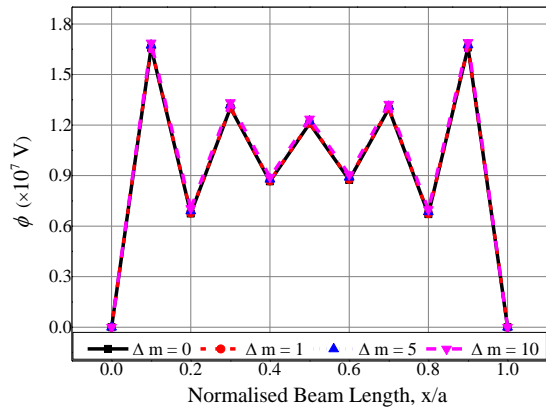
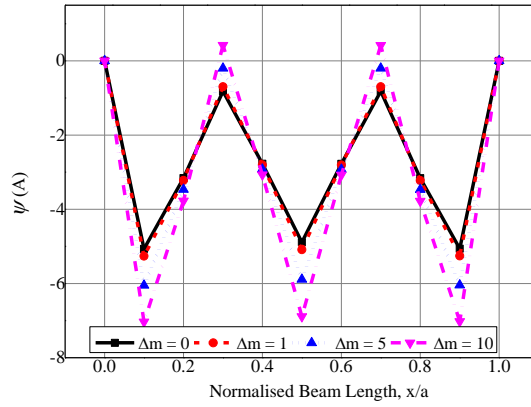


Figure 6.9: Individual effect of moisture concentration gradient Δm on displacement components (a) U_x (b) U_y (c) U_w for C-C HTMEE beam

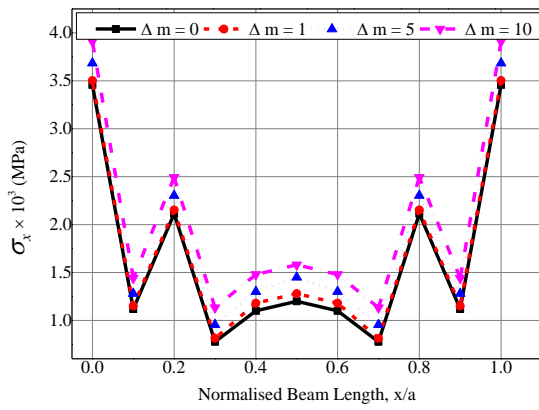


(a)

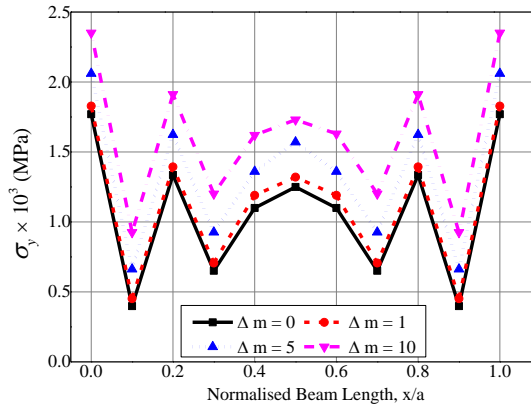


(b)

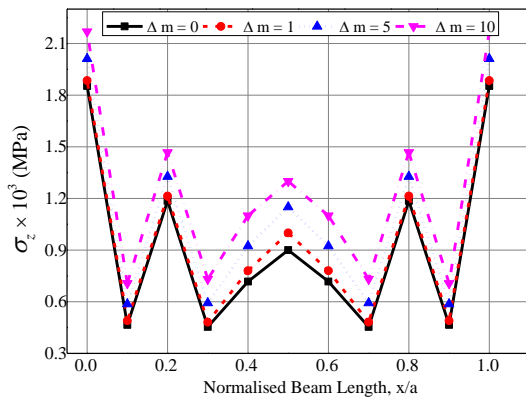
Figure 6.10: Individual effect of moisture concentration gradient Δm on (a) electric potential ϕ (b) magnetic potential ψ for C-C HTMEE beam



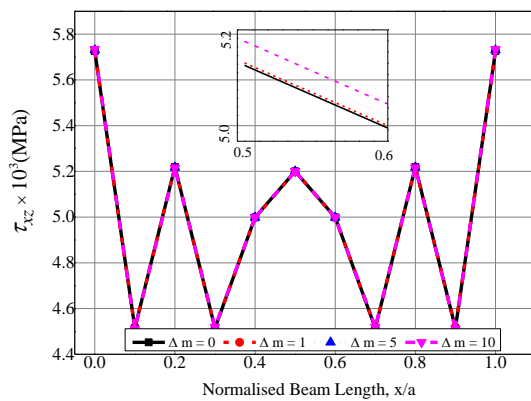
(a)



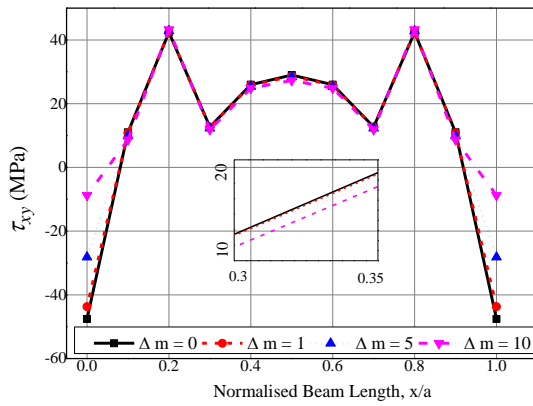
(b)



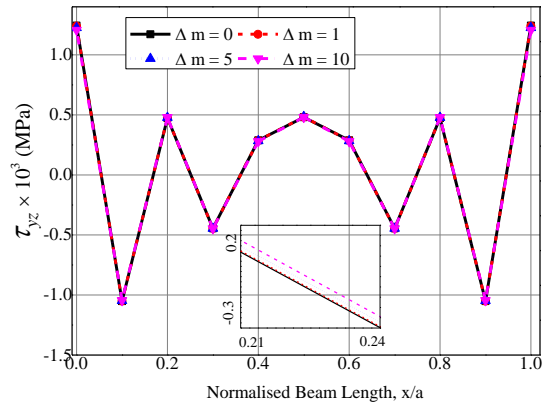
(c)



(d)

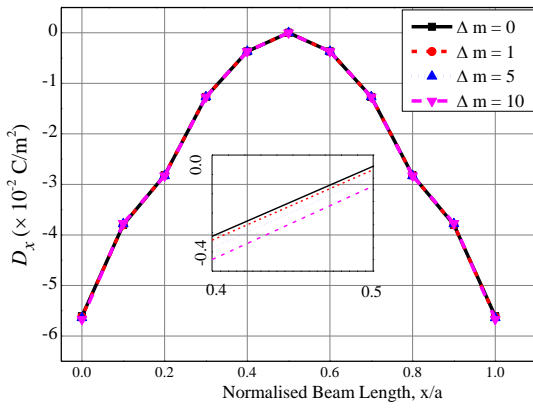


(e)

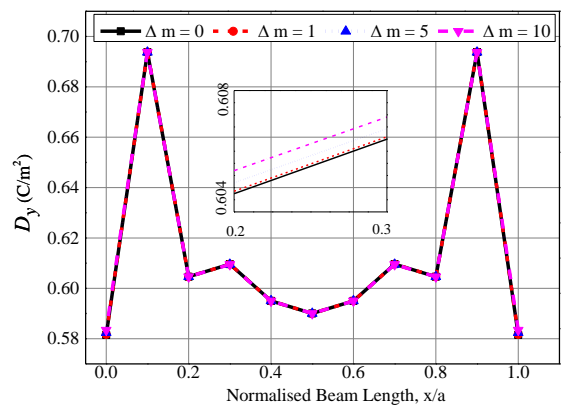


(f)

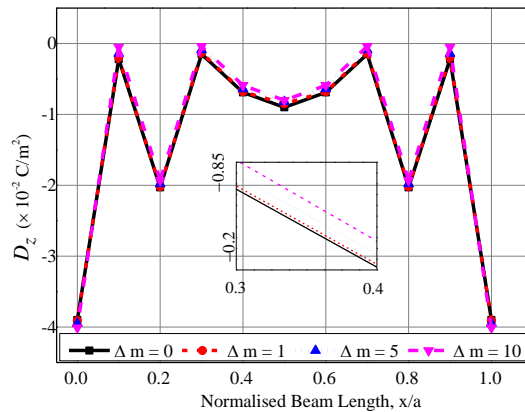
Figure 6.11: Individual effect of moisture concentration gradient Δm on stress components (a) σ_x (b) σ_y (c) σ_z (d) τ_{xz} (e) τ_{xy} (f) τ_{yz} for C-C HTMEE beam



(a)



(b)



(c)

Figure 6.12: Individual effect of moisture concentration gradient Δm on electric displacements

(a) D_x (b) D_y (c) D_z for C-C HTMEE beam

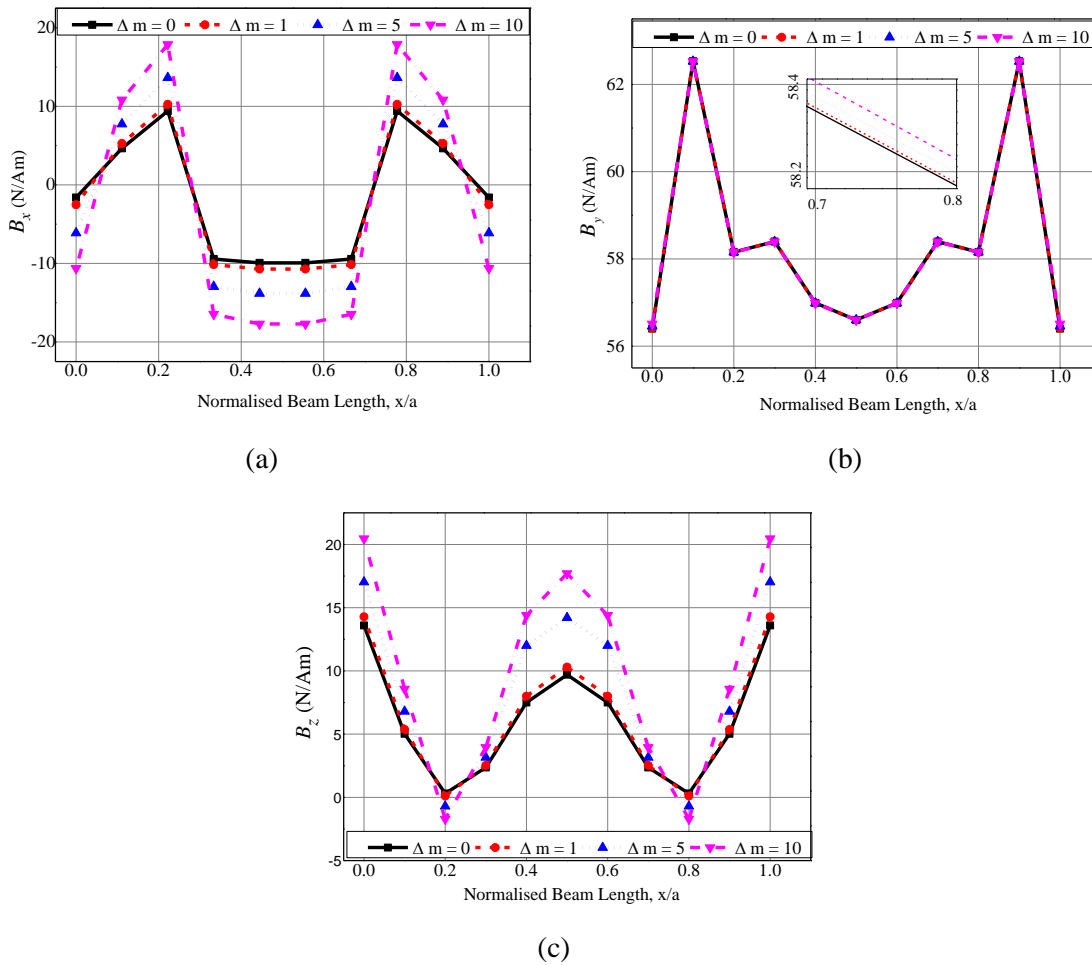


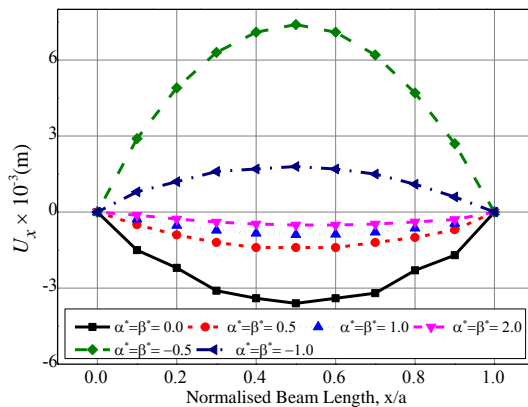
Figure 6.13: Individual effect of moisture concentration gradient Δm on magnetic flux densities (a) B_x (b) B_y (c) B_z for C-C HTMEE beam

6.3.2. Effect of Empirical constants on HTMEE beam

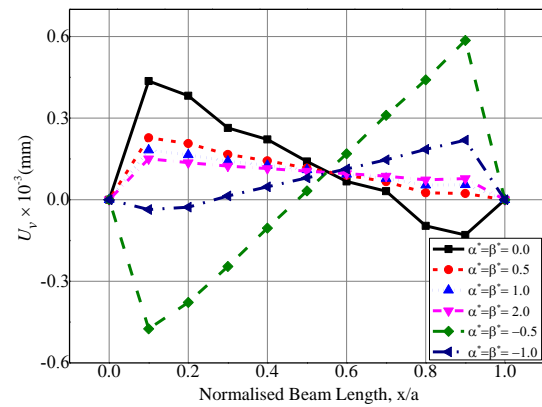
Clamped-Clamped (C-C) HTMEE beam

The effect of temperature and moisture dependent elastic stiffness coefficient (Eq. 5.20) on the static parameters of C-C HTMEE beam is investigated through empirical constants. The thermal load and hygroscopic load considered for the analysis corresponds to a uniform temperature rise of 100 K and 2% moisture rise, respectively. The investigation concerning with the effect of empirical constants α^* and β^* on the primary quantities of HTMEE beam is presented in Figs. 6.14 and 6.15. It can be witnessed from these figures that the empirical constants $\alpha^* = \beta^* = -0.5$ exhibit

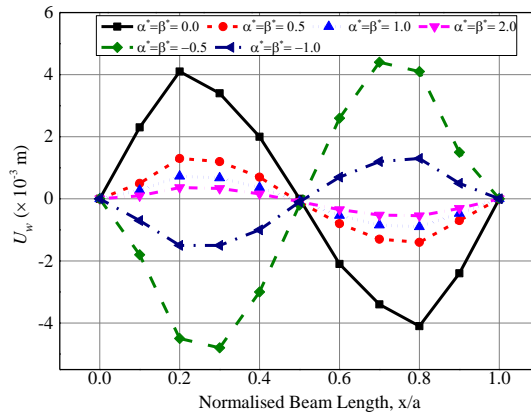
substantial effect on the primary quantities. This may be due to drastic change of the elastic stiffness coefficients for the empirical constants $-0.5 \leq \alpha^* = \beta^* \leq 0$, which leads to the reduction in the stiffness $[K_{eq}]$ making the HTMEE beam more flexible. As a result, the overall $\left([K_{eq}]^{-1}\{F_{eq}\}\right)$ ratio considerably increases. Further increase in absolute value of negative empirical constants ($\alpha^*, \beta^* \geq -0.5$), the elastic stiffness matrix $[K_{eq}]$ improves in such a way that the value $\left([K_{eq}]^{-1}\{F_{eq}\}\right)$ gradually reduces. Also, the predominant effect of negative empirical constants over positive empirical constants is noticed on the electric potential ϕ and magnetic potential ψ . However, from Figs. 6.16(a) - (c), it may be witnessed that with the increase in empirical constants, the normal stresses show an increasing trend, whereas shear stress variation is significantly affected by $\alpha^* = \beta^* = -0.5$. In addition, the negative empirical constants display a substantial effect of the electric displacement and magnetic flux density components as plotted in Figs. 6.17 and 6.18, respectively. The reason may be due to direct effects of the electric potential and magnetic potential on the electric displacements and magnetic flux densities, respectively. It can be further stated that unlike cantilever HTMEE beam, a significant effect of empirical constants on τ_{xy} , τ_{yz} , D_x and B_x is noticed along the length of HTMEE beam.



(a)

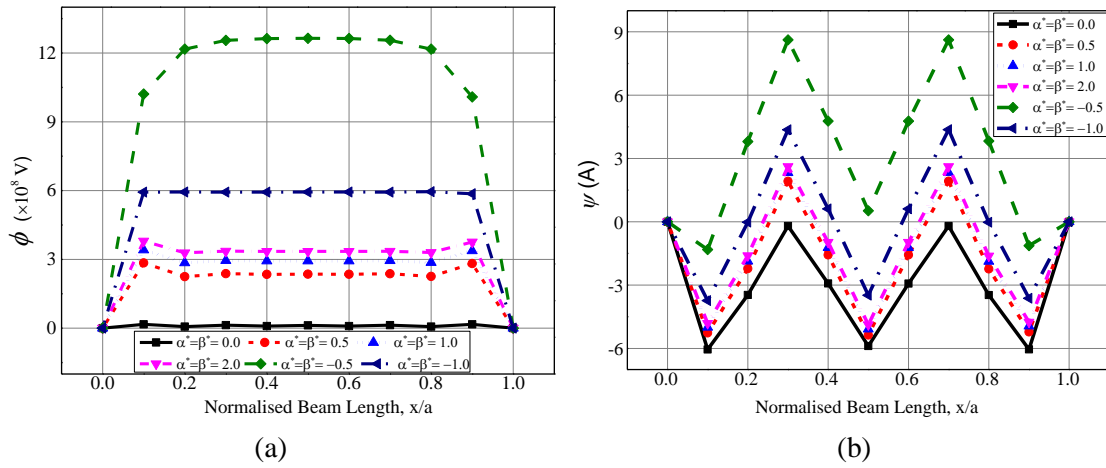


(b)



(c)

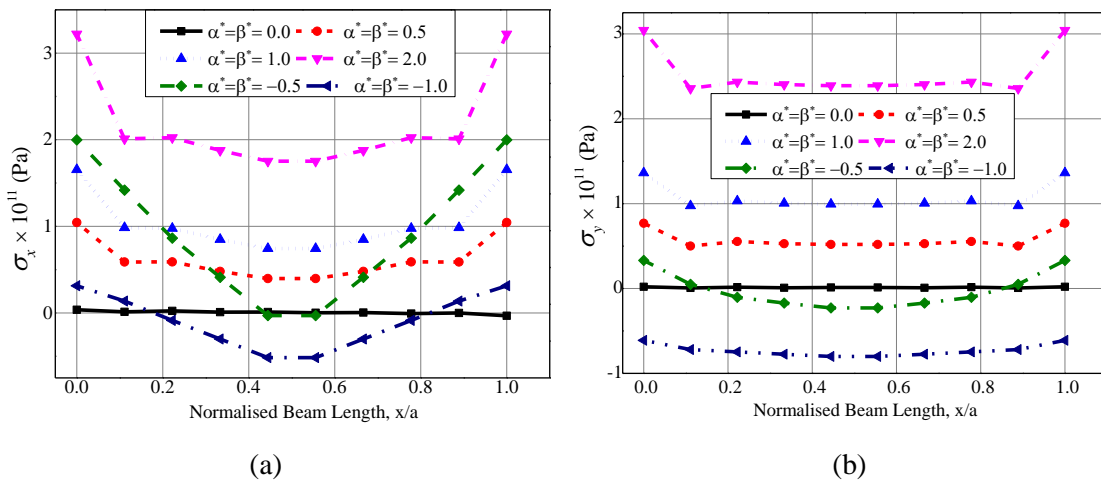
Figure 6.14: Effect of empirical constants on displacements (a) U_x (b) U_v (c) U_w for C-C HTMEE beam



(a)

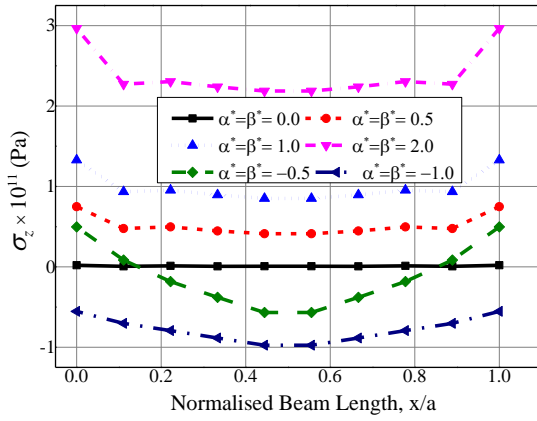
(b)

Figure 6.15: Effect of empirical constants on (a) electric potential ϕ (b) magnetic potential ψ for C-C HTMEE beam

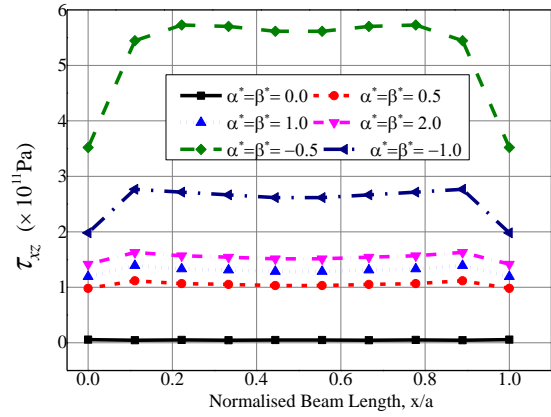


(a)

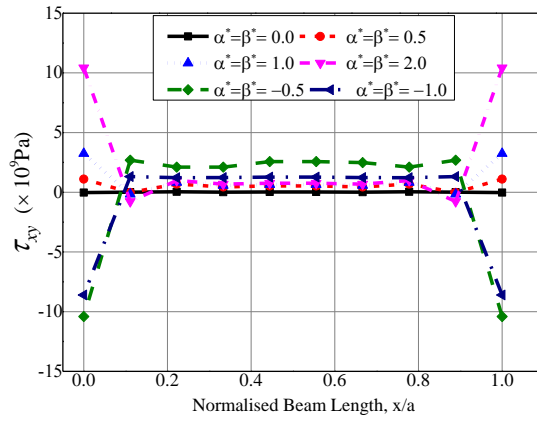
(b)



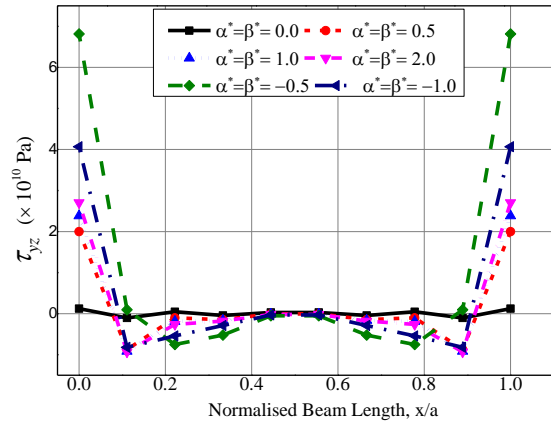
(c)



(d)

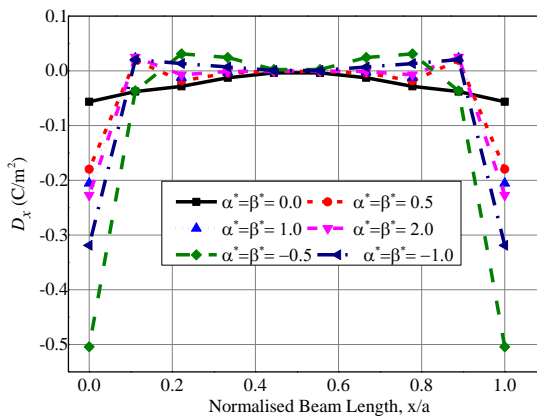


(e)

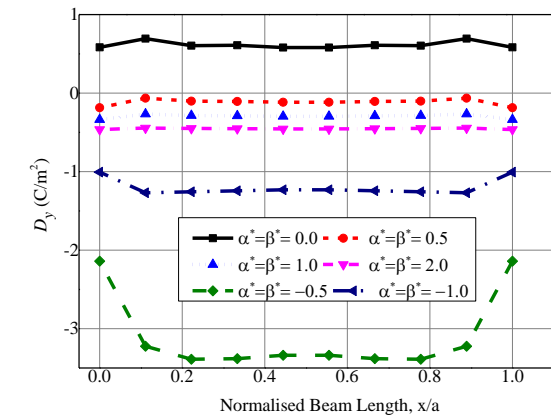


(f)

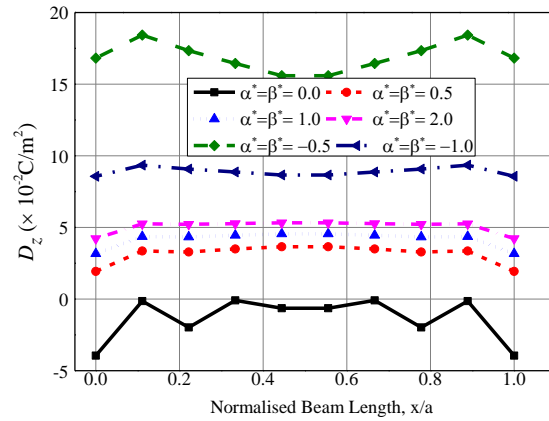
Figure 6.16: Effect of empirical constants on stress components (a) σ_x (b) σ_y (c) σ_z (d) τ_{xz} (e) τ_{xy} (f) τ_{yz} for C-C HTMEE beam



(a)

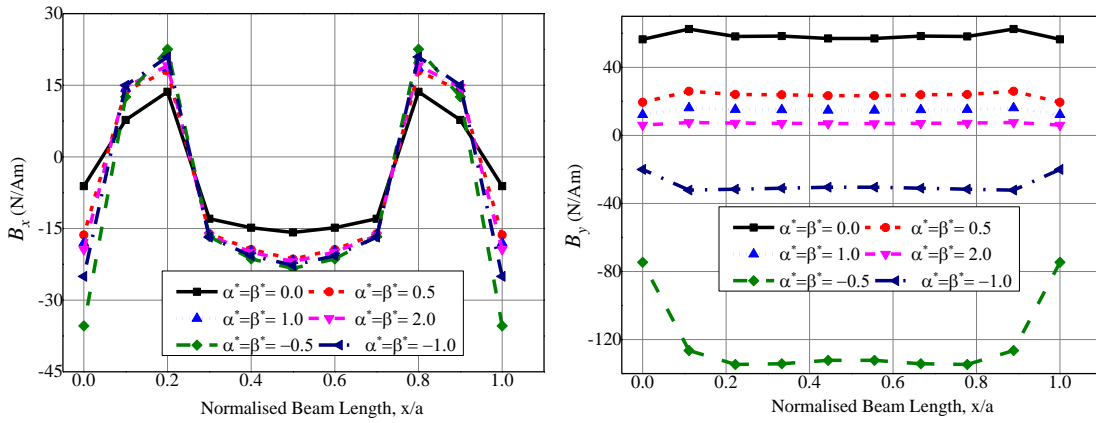


(b)



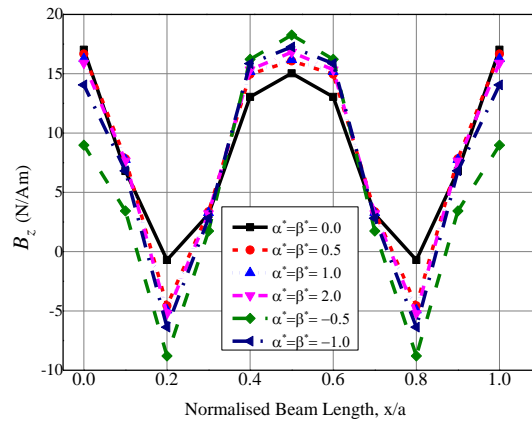
(c)

Figure 6.17: Effect of empirical constants on electric displacements (a) D_x (b) D_y (c) D_z for C-C HTMEE beam



(a)

(b)

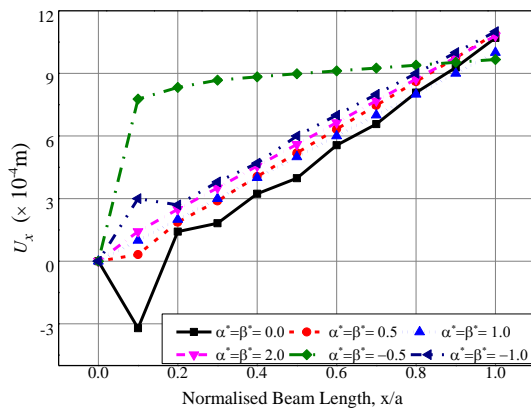


(c)

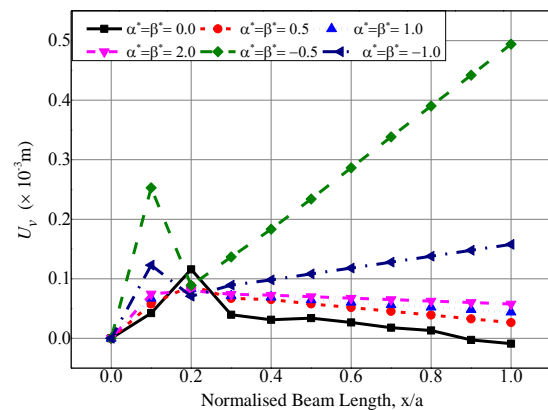
Figure 6.18: Effect of empirical constants on magnetic flux densities (a) B_x (b) B_y (c) B_z for C-C HTMEE beam

Cantilever HTMEE beam

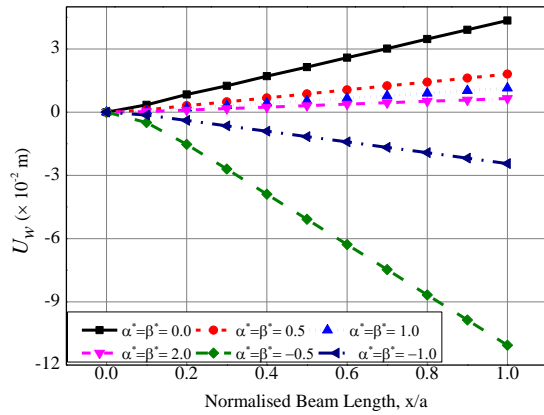
Figures 6.19 and 6.20 illustrate the effect of empirical constants on the displacements and potentials on the cantilever HTMEE beam for the thermal load (uniform rise of 100 K) and hygroscopic load (2% moisture rise), respectively. It can be noticed from these figures (Figs. 6.19 and 6.20) that the displacement components and potentials drastically increases with the decrease in α^* and β^* . This may be attributed to the reduced stiffness coefficients as mentioned for the C-C HTMEE beam. Unlike the primary quantities, the normal stresses increases with the increase in α^* and β^* . It is evident from Figs. 6.21 (a) – (c) that $\alpha^* = \beta^* = 2.0$ has a predominant effect in comparison with the remaining empirical constants. However, the shear stresses are predominantly affected by $\alpha^* = \beta^* = -0.5$ as depicted in Figs. 6.21(d) - (f). Figures 6.22 and 6.23 depict the distribution of the electric displacement components and magnetic flux density components, respectively. As seen from these figures, that a pronounced effect of $\alpha^* = \beta^* = -0.5$ is witnessed. It may also be noticed from these figures that the higher discrepancies are observed near at the clamped end of the beam for D_x and B_x .



(a)

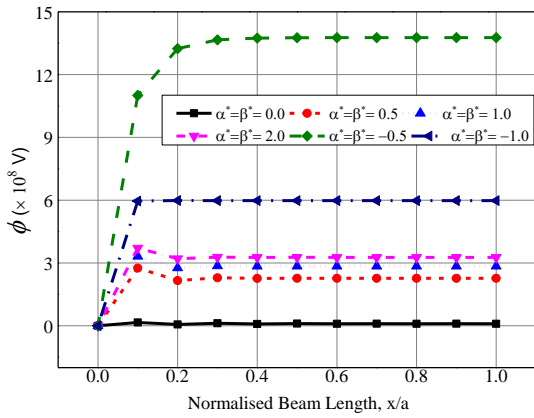


(b)

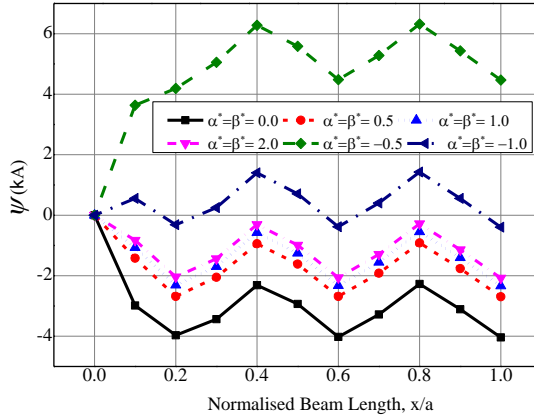


(c)

Figure 6.19: Effect of empirical constants on displacements (a) U_x (b) U_v (c) U_w for cantilever HTMEE beam

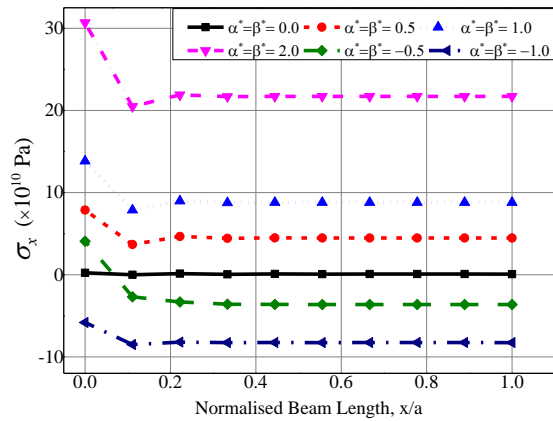


(a)

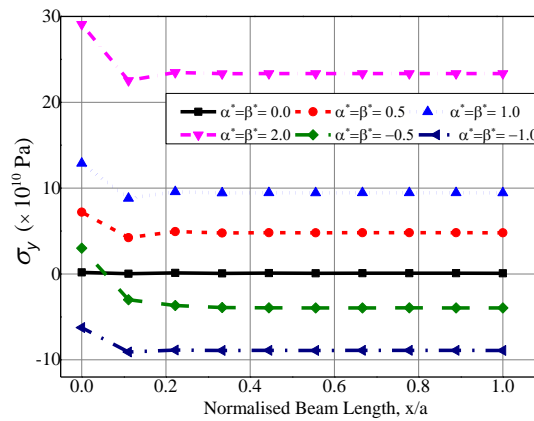


(b)

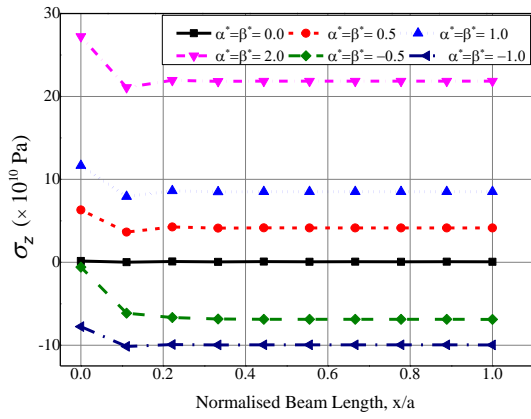
Figure 6.20: Effect of empirical constants on (a) electric potential ϕ (b) magnetic potential ψ for cantilever HTMEE beam



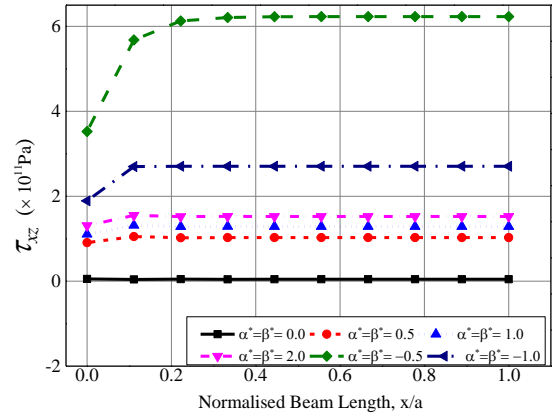
(a)



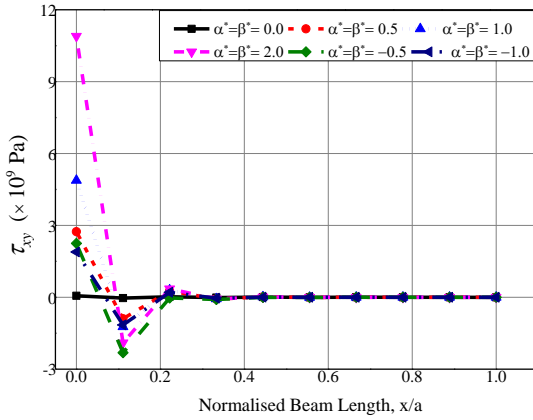
(b)



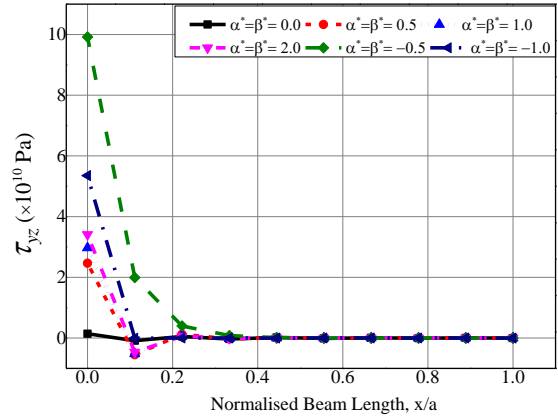
(c)



(d)

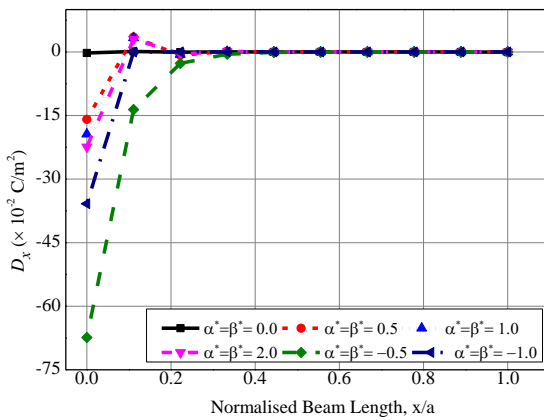


(e)

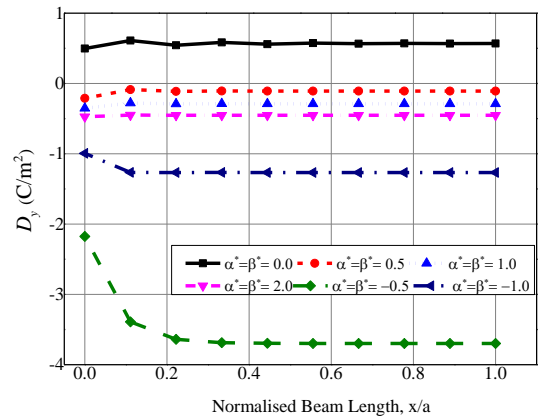


(f)

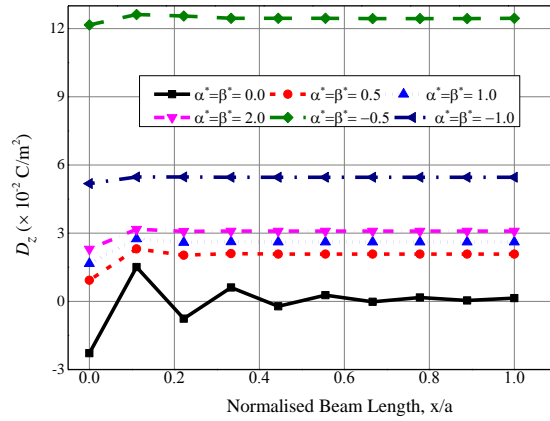
Figure 6.21: Effect of empirical constants on stress components (a) σ_x (b) σ_y (c) σ_z (d) τ_{xz} (e) τ_{xy} (f) τ_{yz} for cantilever HTMEE beam



(a)

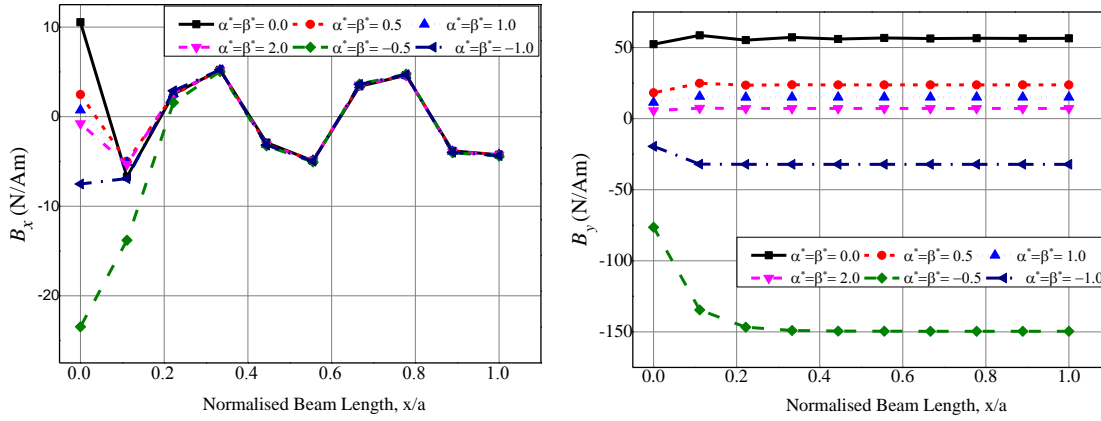


(b)



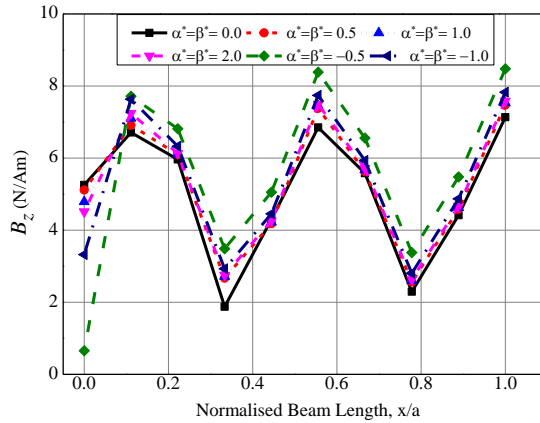
(c)

Figure 6.22: Effect of empirical constants on electric displacements (a) D_x (b) D_y (c) D_z for cantilever HTMEE beam



(a)

(b)



(c)

Figure 6.23: Effect of empirical constants on magnetic flux densities (a) B_x (b) B_y (c) B_z for cantilever HTMEE beam

6.3.3. Significant combination of empirical constant

In this section, an attempt has been made to evaluate the effect of different combination of moisture dependency (β^*) and temperature dependency (α^*) on the behaviour of cantilever HTMEE beam. In this regard, the most significant value of β^* in combination with α^* is evaluated through numerical analysis by keeping $\alpha^* = -0.5$ constant. Analogously, to predict the effect of α^* and to determine the predominant value of α^* , the analysis has been carried out for different value of α^* , while $\beta^* = -0.5$ constant. From Figs. 6.24 – 6.26, it can be noticed that for the constant value of temperature dependency empirical constant ($\alpha^* = -0.5$), a substantial effect of moisture dependency empirical constant $\beta^* = 2.0$ is witnessed on the primary quantities *viz.* transverse displacement component U_w , the electric potential ϕ and the magnetic potential ψ . Moreover, when the moisture dependency empirical constant β^* is set to -0.5, it is deduced that among the different values of α^* considered for the study, $\alpha^* = -0.5$ has a significant influence on the U_w , ϕ and ψ . For both the cases ($\alpha^* = -0.5$ and $\beta^* = -0.5$), the normal stress σ_x displays a maximum value for $\beta^* = 2.0$ and $\alpha^* = 2.0$ as depicted in Fig. 6.27. It is worthy to mention that with respect to both the cases of empirical constants, the shear stress τ_{xz} , electric displacement D_x and magnetic flux density B_x follow the similar trend as that of the primary quantities as elucidated in Figs. 6.28 – 6.30, respectively.

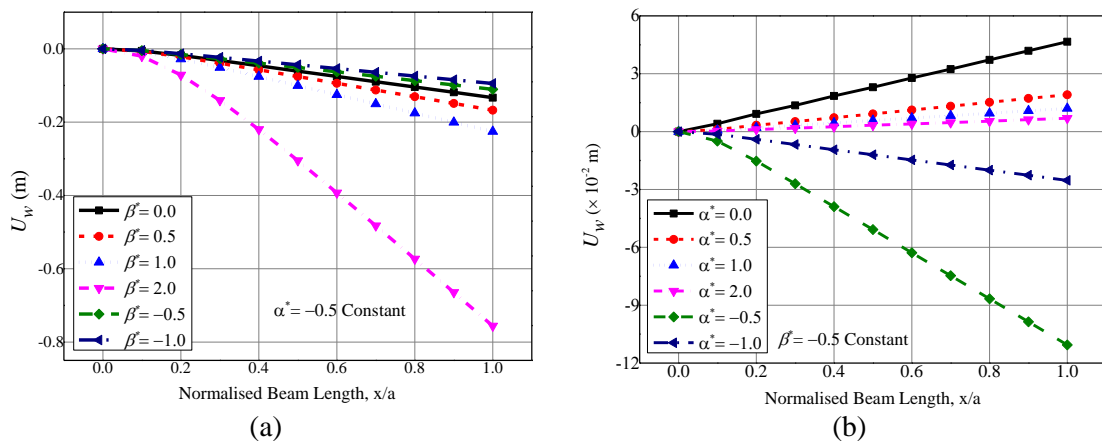


Figure 6.24: Effect of (a) moisture dependency coefficient β^* (b) temperature dependency coefficient α^* on transverse displacement U_w for cantilever HTMEE beam

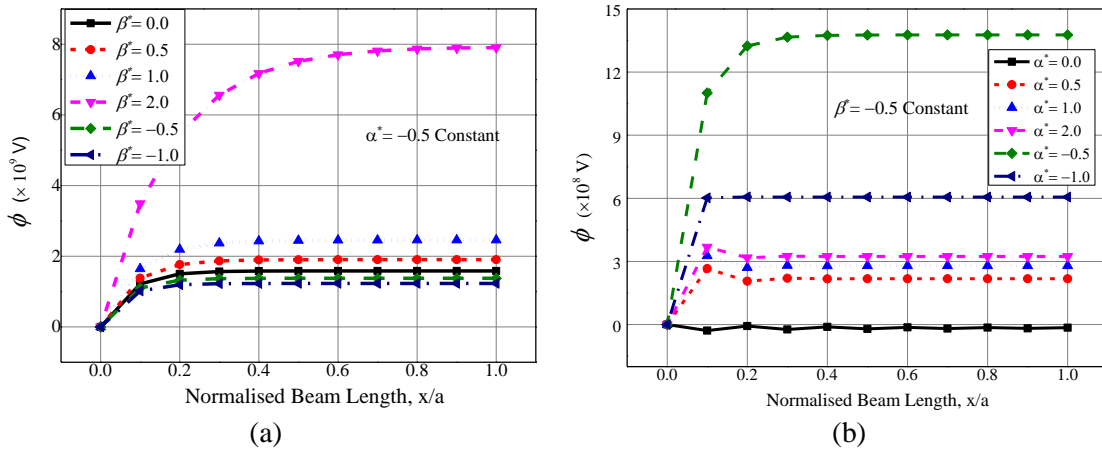


Figure 6.25: Effect of (a) moisture dependency coefficient β^* (b) temperature dependency coefficient α^* on electric potential ϕ for cantilever HTMEE beam

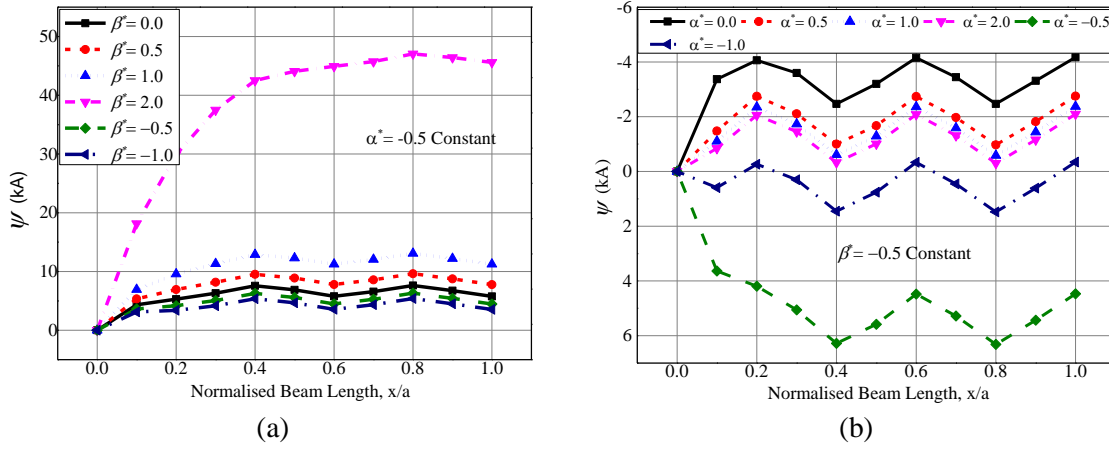


Figure 6.26: Effect of (a) moisture dependency coefficient β^* (b) temperature dependency coefficient α^* on magnetic potential ψ for cantilever HTMEE beam

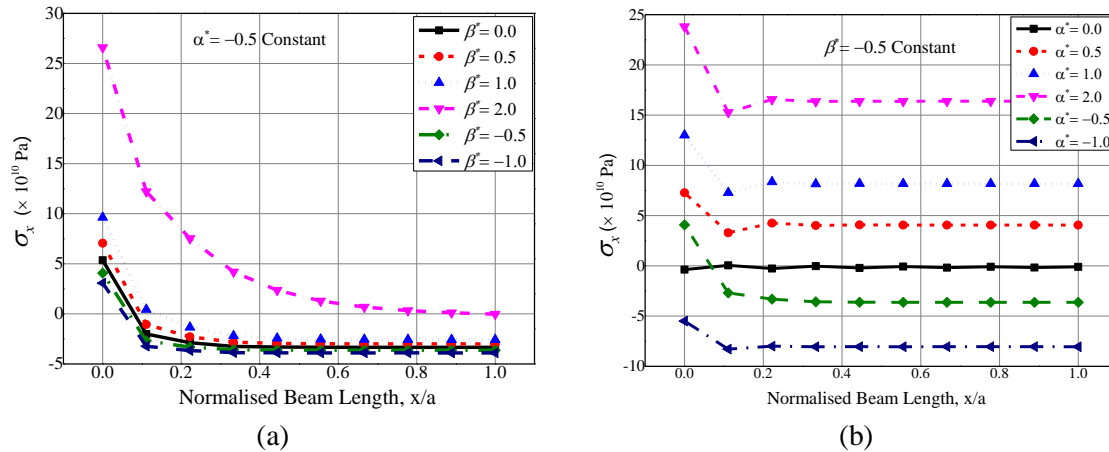


Figure 6.27: Effect of (a) moisture dependency coefficient β^* (b) temperature dependency coefficient α^* on normal stress σ_x for cantilever HTMEE beam

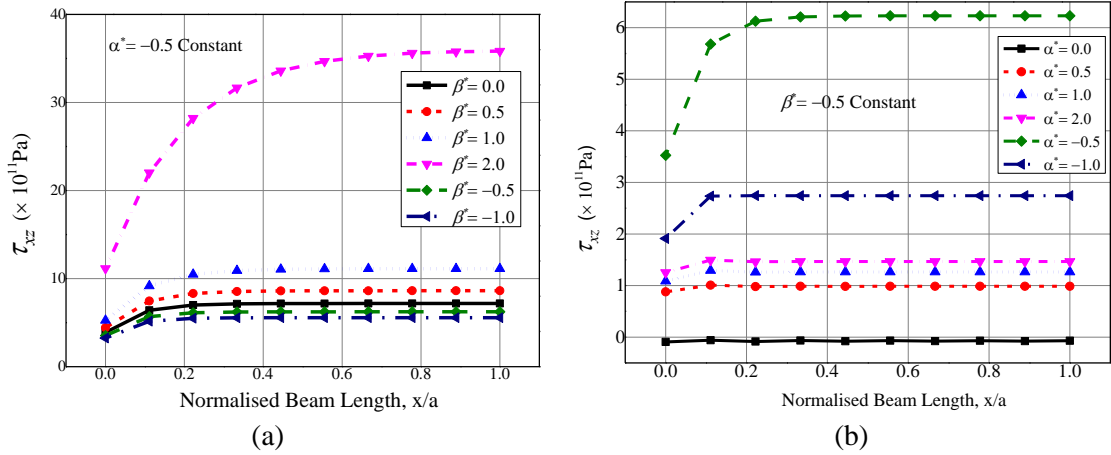


Figure 6.28: Effect of (a) moisture dependency coefficient β^* (b) temperature dependency coefficient α^* on shear stress τ_{xz} for cantilever HTMEE beam

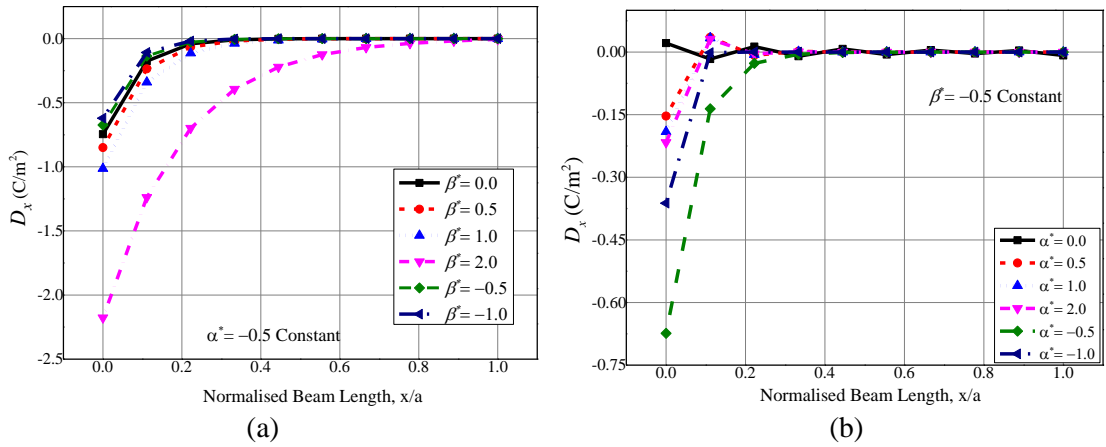


Figure 6.29: Effect of (a) moisture dependency coefficient β^* (b) temperature dependency coefficient α^* on electric displacement D_x for cantilever HTMEE beam

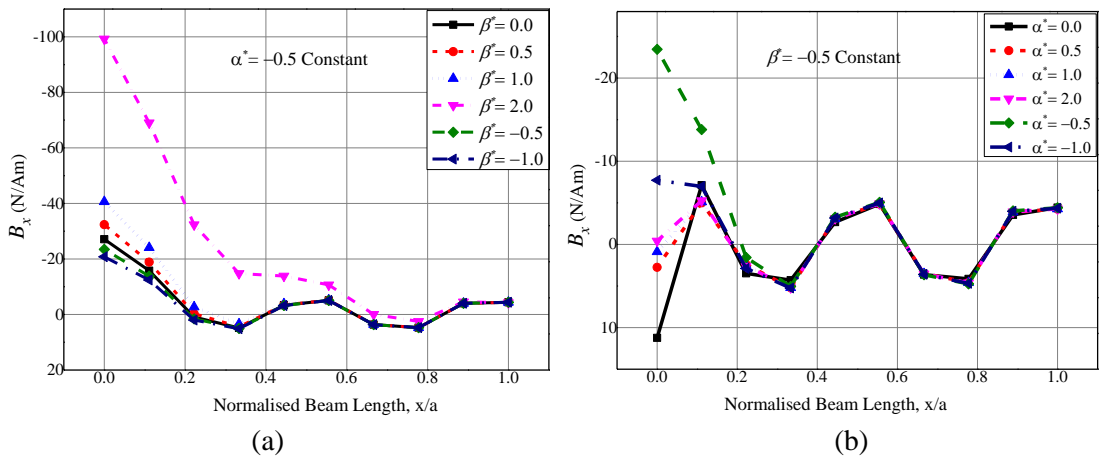


Figure 6.30: Effect of (a) moisture dependency coefficient β^* (b) temperature dependency coefficient α^* on magnetic flux density B_x for cantilever HTMEE beam

6.4. CONCLUSIONS

In this chapter, numerical evaluations are carried out to explore the static behaviour of hygrothermo-magneto-electro-elastic beams using finite element approach. The governing equations of motion accounting for the hygrothermal response of MEE beams are derived using the total potential energy principle and the coupled constitutive equations of HTMEE material. Several numerical examples are considered to evaluate the effect of hygrothermal loads, moisture concentration gradient and boundary conditions on the primary quantities and secondary quantities of HTMEE beams. The results reveal that increase in hygrothermal loads increases the value of static parameters. Making use of empirical constants, the effects of temperature and moisture dependent elastic stiffness coefficients are also examined. It is noticed that the empirical constants $\alpha^* = \beta^* = -0.5$ exhibit a significant influence on all the static parameters except normal stresses. However, for $\alpha^* = \beta^* = 2.0$, the normal stresses have a pronounced effect. In addition, it is also noticed that among different hygrothermal load profiles considered, the uniform hygrothermal load has a predominant effect. Consequently, the present analysis reveals a remarkable impact of hygrothermal loads, empirical constants and boundary conditions on the static performance of HTMEE beams.

Chapter 7

INFLUENCE OF COUPLED FIELDS ON STATIC AND FREE VIBRATION BEHAVIOUR OF STEPPED FUNCTIONALLY GRADED MAGNETO-ELECTRO-THERMO-ELASTIC PLATE

The influence of coupled thermal, elastic, electric and magnetic fields on the free vibrations and static characteristics of stepped functionally graded magneto-electro-thermo-elastic (SFG METE) plate has been investigated. The natural frequencies corresponding to different coupled stiffness matrices are evaluated to analyse the contribution of each phase of SFG METE plate. Particular emphasis has been placed to investigate the effect of different loading forms such as uniform temperature, sinusoidal temperature, magnetic charge and electric charge densities on the static parameters of SFG METE plates.

Related article: Vinyas, M and Kattimani, S.C. (2017). “Influence of coupled fields on free vibration and static behaviour of functionally graded magneto-electro-thermo-elastic plate”, *Journal of Intelligent Material Systems and Structures*.

DOI: 10.1177/1045389X17740739

7.1. INTRODUCTION

The influence of full coupling between the elastic, electric, magnetic and thermal fields on the natural frequency of stepped functionally graded magneto-electro-thermo-elastic (SFG METE) plates has been investigated using the finite element (FE) method. The contribution of overall coupling effect as well as individual elastic, piezoelectric, piezomagnetic and thermal phases towards the stiffness of SFG METE plates is evaluated. A FE formulation is derived using the Hamilton’s principle and coupled constitutive equations of METE material. Based on the first order shear deformation theory (FSDT), kinematics relations are established and the corresponding FE model is developed. Further, the static studies of SFG METE plate

have been carried out by reducing the fully coupled FE formulation to partially coupled state. Particular attention has been paid to investigate the influence of the electric fields, magnetic fields and thermal fields on the behaviour of SFG METE plate. In addition, the effect of pyro coupling on the SFG METE plate has also been studied. Further, the effect of geometrical parameters such as aspect ratio, length-to-thickness ratio, stacking sequence and boundary conditions is also studied in detail.

7.2. PLATE GEOMETRY AND DISPLACEMENT RELATION

The schematic diagram of METE plate comprising of N layers is depicted in Fig 7.1. The METE plate is assumed to have a constant thickness of H . The x , y , and z -axes of Cartesian co-ordinates run along the length a , breadth b and the thickness H of the plate. The first order shear deformation theory (FSDT) is used to model the kinematics of the coupled problem of METE plates. The variation of the in-plane displacements U_x , U_y and U_w are assumed accordingly, as follows:

$$U_x = U_{x0} + z\theta_x \quad (7.1)$$

$$U_y = U_{y0} + z\theta_y \quad (7.2)$$

$$U_w = U_{w0} \quad (7.3)$$

in which, U_{x0} , U_{y0} and U_{w0} are the midplane displacements along the x , y and z axes, respectively. θ_x and θ_y are the rotations of the portions of the normal lying in the xz plane and yz plane, respectively. The reference plane ($z = 0$) is chosen at the midplane of the laminate.

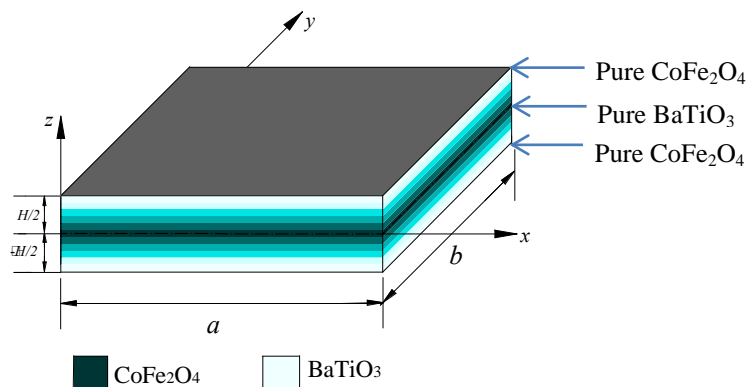


Figure 7.1: Schematic diagram of METE plate

Figures 7.2(a) and (b) depict the stacking arrangement of SFG BFB METE plate and SFG FBF METE plate, respectively. Here, the pure piezoelectric phase is denoted by ‘B’, whereas pure piezomagnetic phase is represented by ‘F’.

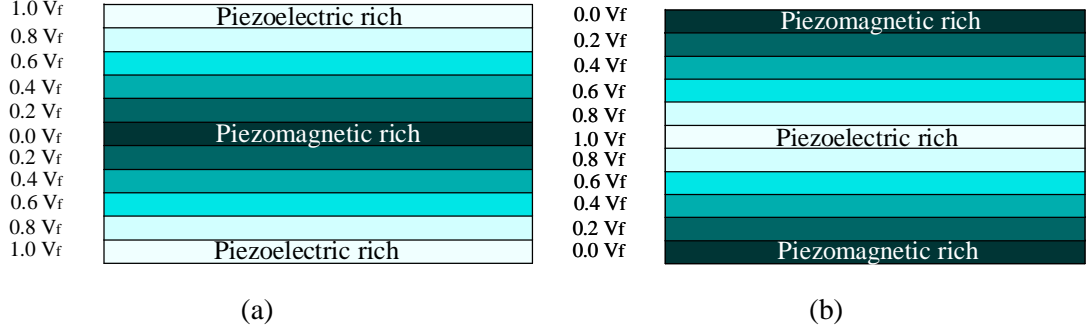


Figure 7.2: Schematic diagram of functionally graded plate showing (a) SFG-BFB and (b) SFG-FBF stacking sequences

7.3. CONSTITUTIVE EQUATIONS

Considering full coupling between elastic, electric, magnetic and thermal fields, the constitutive equations of an anisotropic METE solid can be written as follows:

$$\{\sigma\} = [C]\{\varepsilon\} - [e]\{E\} - [q]\{H\} - [\lambda]\{\theta\} \quad (7.4)$$

$$\{D\} = [e]^T \{\varepsilon\} + [d]\{E\} + [m]\{H\} + [p_e]\{\theta\} \quad (7.5)$$

$$\{B\} = [q]^T \{\varepsilon\} + [m]^T \{E\} + [\mu]\{H\} + [p_m]\{\theta\} \quad (7.6)$$

$$\{\eta\} = [\lambda]^T \{\varepsilon\} + [p_e]^T \{E\} + [p_m]^T \{H\} + C_h \{\theta\} \quad (7.7)$$

where $\{\sigma\}$, $\{D\}$, $\{B\}$ and $\{\eta\}$ represent the stress vector, electric displacement vector, magnetic flux density vector and entropy, respectively. $\{\varepsilon\}$, $\{E\}$, $\{H\}$, and $\{\theta\}$ are strain vector, electric field vector, magnetic field vector and temperature rise, respectively. $[C]$, $[d]$ and $[\mu]$ are the elastic, piezoelectric and magnetostrictive coefficient matrices, respectively. Further, C_h is the heat capacity per unit volume given by $C_h = \rho C_E / T_0$, where C_E is the specific heat of the material. $[e]$, $[q]$, $[\lambda]$, $[m]$, $[p_e]$ and $[p_m]$ are piezoelectric, piezomagnetic, thermal stress moduli, electromagnetic, pyroelectric,

pyromagnetic material coefficient, respectively. The constitutive equations (Eqs. (7.4) - (7.7)) can be described in more generalized global matrix form as follows:

$$\begin{Bmatrix} \sigma_1 \\ \sigma_2 \\ \sigma_3 \\ \sigma_{23} \\ \sigma_{13} \\ \sigma_{12} \\ D_x \\ D_y \\ D_z \\ B_x \\ B_y \\ B_z \\ \eta \end{Bmatrix} = \begin{bmatrix} c11 & c12 & c13 & 0 & 0 & 0 & 0 & 0 & e31 & 0 & 0 & q31 & \lambda1 \\ c12 & c22 & c23 & 0 & 0 & 0 & 0 & 0 & e31 & 0 & 0 & q31 & \lambda2 \\ c13 & c23 & c33 & 0 & 0 & 0 & 0 & 0 & e33 & 0 & 0 & q33 & \lambda3 \\ 0 & 0 & 0 & c44 & c45 & 0 & 0 & e15 & 0 & 0 & q15 & 0 & 0 \\ 0 & 0 & 0 & c45 & c55 & 0 & e15 & 0 & 0 & q15 & 0 & 0 & 0 \\ 0 & 0 & 0 & 0 & 0 & c66 & 0 & 0 & 0 & 0 & 0 & 0 & 0 \\ 0 & 0 & 0 & 0 & e15 & 0 & d11 & 0 & 0 & m11 & 0 & 0 & 0 \\ 0 & 0 & 0 & e15 & 0 & 0 & 0 & d22 & 0 & 0 & m22 & 0 & p_e \\ e31 & e31 & e33 & 0 & 0 & 0 & 0 & 0 & d33 & 0 & 0 & m33 & 0 \\ 0 & 0 & 0 & 0 & q15 & 0 & m11 & 0 & 0 & \mu11 & 0 & 0 & 0 \\ 0 & 0 & 0 & q15 & 0 & 0 & 0 & m22 & 0 & 0 & \mu22 & 0 & p_m \\ q31 & q31 & q33 & 0 & 0 & 0 & 0 & 0 & m33 & 0 & 0 & \mu33 & 0 \\ \lambda1 & \lambda2 & \lambda3 & 0 & 0 & 0 & 0 & p_e & 0 & 0 & p_m & 0 & C_h \end{bmatrix} \begin{Bmatrix} \varepsilon_x \\ \varepsilon_y \\ \varepsilon_z \\ \gamma_{xz} \\ \gamma_{yz} \\ \gamma_{xy} \\ E_x \\ E_y \\ E_z \\ H_x \\ H_y \\ H_z \\ \theta \end{Bmatrix} \quad (7.8)$$

7.4. FINITE ELEMENT FORMULATION

The FE model of the METE plate is generated using eight noded quadrilateral element with each node having eight degrees of freedom *viz.* three translational (U_x, U_y and U_w), two rotational (θ_x and θ_y) and one for each electric potential (ϕ), magnetic potential (ψ) and temperature rise (θ). The generalized translational displacement vector and rotational vector associated with the i^{th} ($i=1, 2, 3 \dots 8$) node of the element can be represented as

$$\{d_{ti}\} = [U_{xi} \ U_{yi} \ U_{wi}]^T, \quad \{d_{ri}\} = [\theta_x \ \theta_y]^T \quad (7.9)$$

The generalized translational vectors $\{d_t\}$, rotational vectors $\{d_r\}$, electric potential vectors $\{\phi\}$, magnetic potential vector $\{\psi\}$ and temperature $\{\theta\}$ at any point within the element can be represented in terms of the nodal displacement vector, nodal electric potential, nodal magnetic potential vector and nodal temperature rise, respectively, as follows:

$$\{d_t\} = [N_t] \{d_t^e\}; \quad \{d_r\} = [N_r] \{d_r^e\}; \quad \{\phi\} = [N_\phi] \{\phi^e\};$$

$$\{\psi\} = [N_\psi] \{\psi^e\}; \{\theta\} = [N_\theta] \{\theta^e\} \quad (7.10)$$

in which,

$$\begin{aligned} \{d_t^e\} &= \left[\{d_{t1}\}^T \{d_{t2}\}^T \dots \{d_{t8}\}^T \right]^T, \{d_r^e\} = \left[\{d_{r1}\}^T \{d_{r2}\}^T \dots \{d_{r8}\}^T \right]^T, \\ \{\phi^e\} &= [\phi_1 \phi_2 \dots \phi_8]^T, \{\psi^e\} = [\psi_1 \psi_2 \dots \psi_8]^T, \{\theta^e\} = [\theta_1 \theta_2 \dots \theta_8]^T, \\ [N_t] &= [N_{t1} \ N_{t2} \ \dots \ N_{t8}], \ N_{ti} = N_i I_t, \ [N_r] = [N_{r1} \ N_{r2} \ \dots \ N_{r8}], \ N_{ri} = N_i I_r, \\ [N_\psi] &= [N_\theta] = [N_\phi] = [N_1 \ N_2 \ \dots \ N_8] \end{aligned} \quad (7.11)$$

where, N_i is the natural coordinate shape function associated with the i^{th} node of the quadrilateral element. I_t and I_r are (3 x 3) and (2 x 2) identity matrices, respectively.

By using the FSDT for plates, strains can be related to the nodal degree of freedom as follows:

$$\begin{aligned} \{\varepsilon_b\} &= [B_{tb}] \{d_t^e\} + z [B_{rb}] \{d_r^e\} \\ \{\varepsilon_s\} &= [B_{ts}] \{d_t^e\} + [B_{rs}] \{d_r^e\} \end{aligned} \quad (7.12)$$

where the derivative of shape function matrices $[B_{tb}]$, $[B_{rb}]$, $[B_{ts}]$ and $[B_{rs}]$ can be expressed as,

$$[B_{tb}] = \begin{bmatrix} \frac{\partial N_i}{\partial x} & 0 & 0 \\ 0 & \frac{\partial N_i}{\partial y} & 0 \\ \frac{\partial N_i}{\partial y} & \frac{\partial N_i}{\partial x} & 0 \end{bmatrix}, [B_{rb}] = \begin{bmatrix} \frac{\partial N_i}{\partial x} & 0 \\ 0 & \frac{\partial N_i}{\partial y} \\ \frac{\partial N_i}{\partial y} & \frac{\partial N_i}{\partial x} \end{bmatrix}, [B_{ts}] = \begin{bmatrix} 0 & 0 & \frac{\partial N_i}{\partial x} \\ 0 & 0 & \frac{\partial N_i}{\partial y} \end{bmatrix}, [B_{rs}] = \begin{bmatrix} 1 & 0 \\ 0 & 0 \end{bmatrix} \quad (7.13)$$

The electric field and the magnetic field vectors are a negative gradient of electric and magnetic potentials, respectively. Using derivative of shape function matrices, the electric field and the magnetic field can be related to the nodal electric potential and nodal magnetic potential, respectively, as follows:

$$\{E\} = \{E_x, E_y, E_z\} = \left\{ -\frac{\partial \phi}{\partial x}, -\frac{\partial \phi}{\partial y}, -\frac{\partial \phi}{\partial z} \right\} = -[B_\phi] \{\phi^e\} \quad (7.14)$$

$$\{H\} = \{H_x, H_y, H_z\} = \left\{ -\frac{\partial \psi}{\partial x}, -\frac{\partial \psi}{\partial y}, -\frac{\partial \psi}{\partial z} \right\} = -[B_\psi] \{\psi^e\} \quad (7.15)$$

in which, the derivative of shape function matrices $[B_\phi]$ and $[B_\psi]$ can be expressed as

$$[B_{\phi_i}] = [B_{\psi_i}] = \begin{bmatrix} \frac{\partial Ni}{\partial x} & \frac{\partial Ni}{\partial y} & \frac{\partial Ni}{\partial z} \end{bmatrix}^T \quad (7.16)$$

7.5. EQUATIONS OF MOTION

The Hamilton's principle in association with the first variations of total potential energy T_p and kinetic energy T_k is invoked to derive the governing equations of motion corresponding to SFG METE plate

$$\begin{aligned} \delta T_p = & \frac{1}{2} \sum_{k=1}^N \int_{\Omega^k} \delta \{\varepsilon_b\}^T \{\sigma_b\} d\Omega^k - \frac{1}{2} \sum_{k=1}^N \int_{\Omega^k} \delta \{\varepsilon_s\}^T \{\sigma_s\} d\Omega^k - \frac{1}{2} \sum_{k=1}^N \int_{\Omega^k} \delta \{E\}^T \{D\} d\Omega^k \\ & - \frac{1}{2} \sum_{k=1}^N \int_{\Omega^k} \delta \{H\}^T \{B\} d\Omega^k - \frac{1}{2} \sum_{k=1}^N \int_{\Omega^k} \delta \{\theta\}^T \{\eta\} d\Omega^k - \int_A \delta \{d_t\}^T \{f\} dA \\ & - \int_A \delta \{\phi\} Q^\phi dA - \int_A \delta \{\psi\} Q^\psi dA - \int_A \delta \{\theta\} \bar{q} dA \end{aligned} \quad (7.17)$$

$$\delta T_k = \int_{\Omega^k} \delta \{d_t\} \rho \{\ddot{d}_t\} d\Omega^k \quad (7.18)$$

Since, the METE plate thickness considered for the analysis is very thin, the rotary inertia may be neglected (Panda and Ray 2008, 2009; Ray and Shivakumar 2009). Substituting the constitutive equations (Eqs. (7.4) – (7.7)) into Eqs. (7.17) and (7.18), the equilibrium equations of motion can be obtained as follows:

$$\begin{aligned} & \frac{1}{2} \sum_{k=1}^N \left(\int_{\Omega^k} \{\varepsilon_b\}^T [C_b^k] \{\varepsilon_b\} d\Omega^k - \int_{\Omega^k} \{\varepsilon_b\}^T [e^k] \{E\} d\Omega^k - \int_{\Omega^k} \{\varepsilon_s\}^T [C_s^k] \{\varepsilon_s\} d\Omega^k - \right. \\ & \int_{\Omega^k} \{\varepsilon_b\}^T [q^k] \{H\} d\Omega^k - \int_{\Omega^k} \{\varepsilon_b\}^T [\lambda^k] \{\theta\} d\Omega^k - \int_{\Omega^k} \{E\}^T [e^k]^T \{\varepsilon_b\} d\Omega^k - \\ & \left. \int_{\Omega^k} \{E\}^T [\eta^k] \{E\} d\Omega^k - \int_{\Omega^k} \{E\}^T [m^k] \{H\} d\Omega^k - \int_{\Omega^k} \{E\}^T [p_e^k] \{\theta\} d\Omega^k - \right) \end{aligned}$$

$$\begin{aligned}
& \int_{\Omega^k} \{H\}^T [q^k]^T \{\varepsilon_b\} d\Omega^k - \int_{\Omega^k} \{H\}^T [m^k] \{E\} d\Omega^k - \int_{\Omega^k} \{H\}^T [\mu^k] \{H\} d\Omega^k - \\
& \int_{\Omega^k} \{H\}^T [p_m^k] \{\theta\} d\Omega^k - \int_{\Omega^k} \{\theta\}^T [\lambda^k]^T \{\varepsilon_b\} d\Omega^k - \int_{\Omega^k} \{\theta\}^T [p_e^k] \{E\} d\Omega^k - \\
& \int_{\Omega^k} \{\theta\}^T [p_m^k] \{H\} d\Omega^k - \int_{\Omega^k} \{\theta\}^T [a] \{\theta\} d\Omega^k - \int_A \delta \{d_t\}^T \{f\} dA - \int_A \delta \{\phi\} Q^\phi dA - \\
& \left. \int_A \delta \{\psi\} Q^\psi dA - \int_A \delta \{\theta\} \bar{q} dA + \int_{\Omega^k} \delta \{d_t\} \rho \{\ddot{d}_t\} d\Omega^k = 0 \right) \quad (7.19)
\end{aligned}$$

Substituting Eqs. (7.9) – (7.16) in Eq. (7.19), we obtain

$$\begin{aligned}
& \frac{1}{2} \sum_{k=1}^N \delta \left(\int_{\Omega^k} \left([B_{tb}] \{d_t^e\} + z [B_{rb}] \{d_r^e\} \right)^T [C_b^k] \left([B_{tb}] \{d_t^e\} + z [B_{rb}] \{d_r^e\} \right) d\Omega^k - \right. \\
& \int_{\Omega^k} \left[\left([B_{tb}] \{d_t^e\} + z [B_{rb}] \{d_r^e\} \right)^T [e^k] [B_\phi] \{\phi\}^e \right] d\Omega^k - \\
& \int_{\Omega^k} \left([B_{tb}] \{d_t^e\} + z [B_{rb}] \{d_r^e\} \right)^T [q^k] [B_\psi] \{\psi\}^e d\Omega^k - \\
& \int_{\Omega^k} \left([B_{tb}] \{d_t^e\} + z [B_{rb}] \{d_r^e\} \right)^T [\lambda^k] [N_\phi] \{\theta\}^e d\Omega^k - \\
& \int_{\Omega^k} \left([B_{ts}] \{d_t^e\} + [B_{rs}] \{d_r^e\} \right)^T [C_s^k] \left([B_{ts}] \{d_t^e\} + [B_{rs}] \{d_r^e\} \right) d\Omega^k - \\
& \int_{\Omega^k} \left([B_\phi] \{\phi^e\} \right)^T [e^k]^T [B_{tb}] \{d_t^e\} d\Omega^k - \int_{\Omega^k} \left([B_\phi] \{\phi^e\} \right)^T [e^k]^T [B_{rb}] \{d_r^e\} d\Omega^k - \\
& \int_{\Omega^k} \left([B_\phi] \{\phi^e\} \right)^T [d^k] [B_\phi] \{\phi^e\} d\Omega^k - \int_{\Omega^k} \left([B_\phi] \{\phi^e\} \right)^T [m^k] [B_\psi] \{\psi^e\} d\Omega^k - \\
& \int_{\Omega^k} \left([B_\phi] \{\phi^e\} \right)^T [p_e^k] [N_\theta] \{\theta^e\} d\Omega^k - \int_{\Omega^k} \left([B_\psi] \{\psi^e\} \right)^T [q^k]^T [B_{tb}] \{d_t^e\} d\Omega^k - \\
& \int_{\Omega^k} \left([B_\psi] \{\psi^e\} \right)^T [q^k]^T z [B_{rb}] \{d_r^e\} d\Omega^k - \int_{\Omega^k} \left([B_\psi] \{\psi^e\} \right)^T [m^k] [B_\phi] \{\phi^e\} d\Omega^k - \\
& \left. \int_{\Omega^k} \left([B_\psi] \{\psi^e\} \right)^T [\mu^k] [B_\psi] \{\psi^e\} d\Omega^k - \int_{\Omega^k} \left([B_\psi] \{\psi^e\} \right)^T [p_m^k] [N_\theta] \{\theta^e\} d\Omega^k - \right.
\end{aligned}$$

$$\begin{aligned}
& \int_{\Omega^k} \left([N_\theta] \{ \theta^e \} \right)^T [C_b^k] \{ \alpha^k \} [B_{ib}] \{ d_t^e \} d\Omega^k - \int_{\Omega^k} \left([N_\theta] \{ \theta^e \} \right)^T [C_b^k] \{ \alpha^k \} z [B_{rb}] \{ d_r^e \} d\Omega^k - \\
& \int_{\Omega^k} \left([N_\theta] \{ \theta^e \} \right)^T [p_e^k]^T [B_\phi] \{ \phi^e \} d\Omega^k - \int_{\Omega^k} \left([N_\theta] \{ \theta^e \} \right)^T [p_m^k]^T [B_\psi] \{ \psi^e \} d\Omega^k - \\
& \int_{\Omega^k} \left([N_\theta] \{ \theta^e \} \right)^T C_h [N_\theta] \{ \theta^e \} d\Omega^k \Bigg) - \int_A \delta \{ d_t^e \}^T \{ F_m^e \} - \int_A \delta \{ \phi^e \}^T \{ F_\phi^e \} - \\
& \int_A \delta \{ \psi^e \}^T \{ F_\psi^e \} - \int_A \delta \{ \theta^e \}^T \{ F_q^e \} + [M_{tt}^e] \{ \ddot{d}_t^e \} = 0 \tag{7.20}
\end{aligned}$$

Upon simplification and rearranging of Eq. (7.20), the governing equations for the fully coupled SFG METE plate in the global form can be written as follows:

$$\begin{aligned}
& [M_{tt}^g] \{ \ddot{d}_t \} + [K_{tt}^g] \{ d_t \} + [K_{tr}^g] \{ d_r \} + [K_{t\phi}^g] \{ \phi \} + [K_{t\psi}^g] \{ \psi \} + [K_{t\theta}^g] \{ \theta \} = \{ F_{t-m} \} \\
& [K_{tr}^g]^T \{ d_t \} + [K_{rr}^g] \{ d_r \} + [K_{r\phi}^g] \{ \phi \} + [K_{r\psi}^g] \{ \psi \} + [K_{r\theta}^g] \{ \theta \} = \{ F_{r-m}^g \} \\
& [K_{t\phi}^g]^T \{ d_t \} + [K_{r\phi}^g]^T \{ d_r \} - [K_{\phi\phi}^g] \{ \phi \} - [K_{\phi\psi}^g] \{ \psi \} - [K_{\phi\theta}^g] \{ \theta \} = \{ F_\phi^g \} \\
& [K_{t\psi}^g]^T \{ d_t \} + [K_{r\psi}^g]^T \{ d_r \} - [K_{\psi\psi}^g] \{ \psi \} - [K_{\psi\theta}^g] \{ \theta \} = \{ F_\psi^g \} \\
& [K_{t\theta}^g]^T \{ d_t \} + [K_{r\theta}^g]^T \{ d_r \} - [K_{\theta\theta}^g] \{ \theta \} = \{ F_q^g \} \tag{7.21}
\end{aligned}$$

The various global stiffness matrices and force vectors appearing in Eq. (7.21) are described in **Appendix A**. The mathematical expressions for the force vectors, global stiffness matrices and the corresponding rigidity matrices are explicitly given in **Appendix B**. The global equations of motion can be condensed (**Appendix C**) to represent in a simple form as follows:

$$[M_{tt}^g] \{ \ddot{d}_t \} + [K_{eq}^g] \{ d_t \} = \{ F_{eq} \} \tag{7.22}$$

In case of free vibration analysis, Eq. (7.22) can be expressed as follows:

$$[M_{tt}^g] \{ \ddot{d}_t \} + [K_{eq}^g] \{ d_t \} = 0 \tag{7.23}$$

Eq. (7.23) can be represented in the matrix form as follows:

$$\left(\begin{bmatrix} K_{tt}^g & K_{tr}^g & K_{t\phi}^g & K_{t\psi}^g & K_{t\theta}^g \\ K_{rt}^g & K_{rr}^g & K_{r\phi}^g & K_{r\psi}^g & K_{r\theta}^g \\ K_{\phi t}^g & K_{\phi r}^g & K_{\phi\phi}^g & K_{\phi\psi}^g & K_{\phi\theta}^g \\ K_{\psi t}^g & K_{\psi r}^g & K_{\psi\phi}^g & K_{\psi\psi}^g & K_{\psi\theta}^g \\ K_{\theta t}^g & K_{\theta r}^g & K_{\theta\phi}^g & K_{\theta\psi}^g & K_{\theta\theta}^g \end{bmatrix} - \omega^2 \begin{bmatrix} M_{tt} & 0 & 0 & 0 & 0 \\ 0 & 0 & 0 & 0 & 0 \\ 0 & 0 & 0 & 0 & 0 \\ 0 & 0 & 0 & 0 & 0 \\ 0 & 0 & 0 & 0 & 0 \end{bmatrix} \right) \begin{Bmatrix} d_t \\ d_r \\ \phi \\ \psi \\ \theta \end{Bmatrix} = \begin{Bmatrix} 0 \\ 0 \\ 0 \\ 0 \\ 0 \end{Bmatrix} \quad (7.24)$$

Further, following assumptions have been made to reduce the fully coupled equilibrium equations for SFG METE plate to account for the static analysis,

1. Thermal fields are partially coupled with magneto-electro-elastic fields. Hence, the thermal effects can be treated as external loads.
2. The effect of externally applied electric charge and magnetic current is not zero.

Considering the above assumptions, the equations of motion for METE plates accounting the different loading conditions can be rewritten as follows:

$$\begin{aligned} & \left[K_{tt}^g \right] \{d_t\} + \left[K_{tr}^g \right] \{d_r\} + \left[K_{t\phi}^g \right] \{\phi\} + \left[K_{t\psi}^g \right] \{\psi\} = \{F_{t_m}^g\} + \{F_{t\theta}^g\} \\ & \left[K_{tr}^g \right]^T \{d_t\} + \left[K_{rr}^g \right] \{d_r\} + \left[K_{r\phi}^g \right] \{\phi\} + \left[K_{r\psi}^g \right] \{\psi\} = \{F_{r_m}^g\} + \{F_{r\theta}^g\} \\ & \left[K_{t\phi}^g \right]^T \{d_t\} + \left[K_{r\phi}^g \right]^T \{d_r\} - \left[K_{\phi\phi}^g \right] \{\phi\} - \left[K_{\phi\psi}^g \right] \{\psi\} = \{F_{\phi^s}\} - \{F_{\phi\theta}^g\} \\ & \left[K_{t\psi}^g \right]^T \{d_t\} + \left[K_{r\psi}^g \right]^T \{d_r\} - \left[K_{\phi\psi}^g \right]^T \{\phi\} - \left[K_{\psi\psi}^g \right] \{\psi\} = \{F_{\psi^s}\} - \{F_{\psi\theta}^g\} \end{aligned} \quad (7.25)$$

7.6. RESULTS AND DISCUSSION

This section addresses the static and free vibration behaviour of SFG METE plates in the thermal environment. The effect of different forms of external field loads such as uniform temperature rise, non-uniform temperature rise, electric field force and magnetic field force is analysed. To this end, the partially coupled governing equations derived in the previous section are used. Numerical examples are solved and analysed in order to evaluate the variation of static parameters of METE plates with respect to different boundary conditions, aspect ratio and length-to-thickness ratio. A comparative study of the conventional three layered METE (BFB and FBF)

and SFG METE (BFB and FBF) plates is presented. Also, a special attention has been given for evaluating the effect of pyroelectric and pyromagnetic coupling.

In case of free vibration study, fully coupled FE formulation derived in the previous section is used to investigate the influence of various coupled stiffness matrices on the natural frequency of SFG METE plate. Further, the effect of boundary conditions and stacking sequences on the natural frequency of SFG METE plate is thoroughly evaluated.

7.6.1. Validation of the FE formulation

The correctness of the proposed FE formulation to evaluate the static response of SFG METE plate is justified by comparing the results obtained with that of the results reported by Moita *et al.* (2009) for the case of mechanical loading. It can be noticed from Figs. 7.4(a)-(c) that the results from the present numerical formulation closely agree with that of Moita *et al.* (2009). Thus, the present FE formulation can be extended to other forms of loading which are discussed in the subsequent sections. The material properties corresponding to various volume fractions of BaTiO₃ and CoFe₂O₄ are tabulated in Table 2.1. In order to validate the present FE model for natural frequencies, a simply supported BFFB METE square plate ($a = 1$ m, $H = 0.04$ m) studied by Moita *et al.*(2009) and Lage *et al.* (2005) is considered for the comparison. The results obtained from the present FE formulation are analogous to the results reported by Moita *et al.*(2009) and Lage *et al.* (2005) as tabulated in Table 7.1. In addition, the normalized frequencies of a simply supported BFB MEE plate ($a = 1$ m and $H = 0.3$ m) is also validated. Table 7.2 compares the result ($\omega_n = \omega (a^2/H\sqrt{\rho/C_{11}})$, $\rho = 1600$ kg/m³) obtained using the present numerical code and the results reported by Moita *et al.* (2009). It can be observed from this table (Table 7.2) that the results are in very good agreement with Moita *et al.* (2009). Further, the convergence of the natural frequency results with mesh refinement has been explicitly depicted in Table 7.3. Hence, it is expected that the present FE formulation can dependably produce results for various conditions of METE plate.

7.6.2. Effect of uniform temperature rise

The static analysis of SSSS METE plate subjected to uniform temperature rise ($T = T_0$) is carried out. From Fig. 7.4(a), it can be observed that SFG METE plate results in a lesser stress than the conventional three layered METE plate. The through thickness variation of magnetic flux density and electric displacement are plotted in Figs. 7.4(b) and (c), respectively. From these figures, it can be noticed that magnetic flux density (B_z) and electric displacement (D_z) are zero at the pure piezomagnetic and pure piezoelectric phases of the corresponding stacking sequence, respectively.

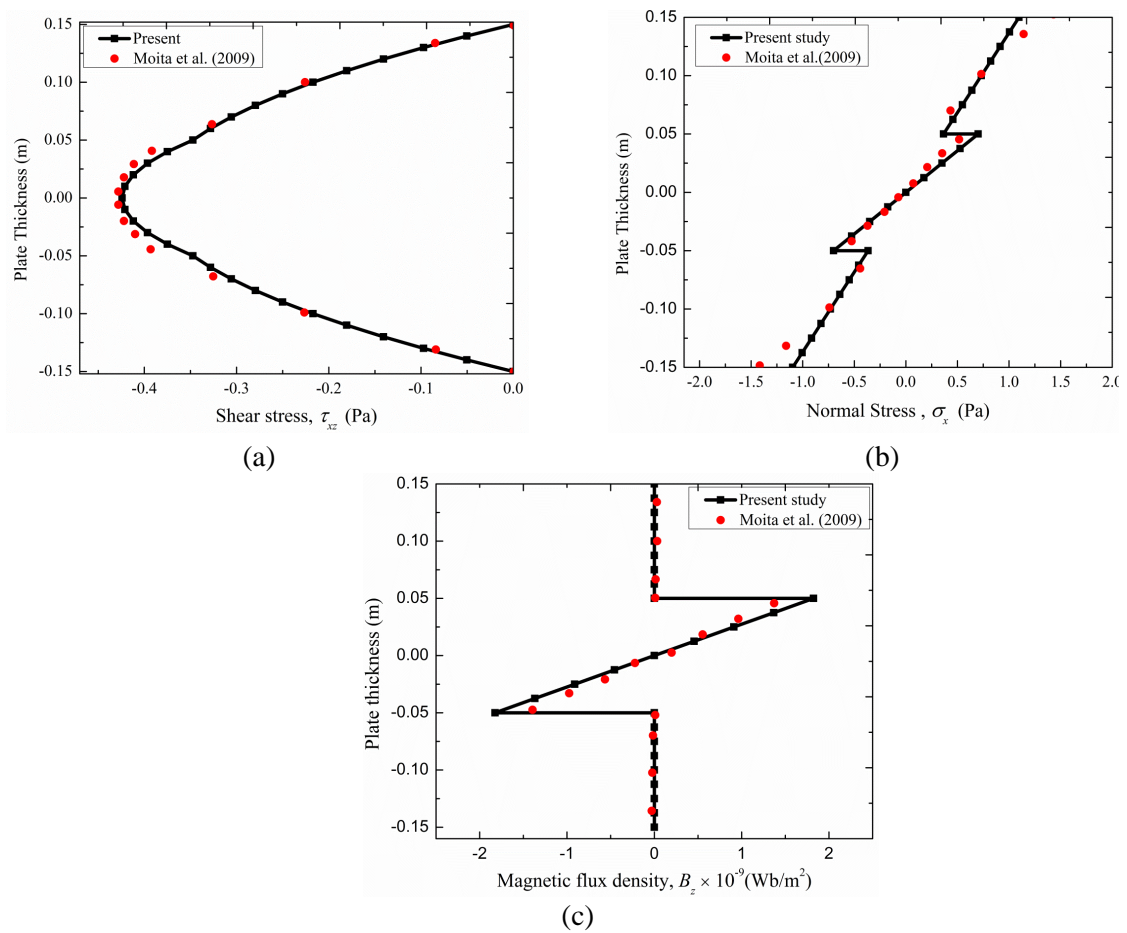


Figure 7.3: Validation plots of (a) shear stress τ_{xz} (b) normal stress σ_x (c) magnetic flux density, B_z

Table 7.1: Natural frequency for BFFB stacked MEE plate

Mode	Lage <i>et al.</i> (2005)	Moita <i>et al.</i> (2009)	Present
1	2542.9	2449.7	2432.2
2	6391	6280.6	6268.4
3	6391	6280.6	6268.4
4	10192	10461.5	10316.1

Table 7.2: Normalized Frequencies ($\omega_n = \omega (a^2/H\sqrt{\rho/C_{11}})$), for simply supported three layered BFB plate; $a = 1$ m; $H = 0.3$ m

Mode	Moita <i>et al.</i> (2009)	Present
1	4.262	4.342
2	8.312	8.211
3	8.592	8.689
4	11.521	11.463
5	11.521	11.463
6	12.655	12.726

Table 7.3: Convergence of the natural frequency of MEE plate with mesh size

Mode No.	Mesh size				Moita <i>et al.</i> (2009)
	4×4	6×6	8×8	10×10	
1	2422.14	2428.60	2432.14	2432.21	2449.7
2	6255.74	6264.67	6268.31	6268.40	6280.6
3	6255.74	6264.67	6268.31	6268.40	6280.6
4	10306.52	10313.28	10316.01	10316.1	10461.5

In addition, the variation of longitudinal displacement component U_x , transverse displacement component U_w , electric potential ϕ and magnetic potential ψ along the plate length ($y = 0.5 a$ and $x = 0$ to a) are shown in Figs. 7.5(a) – (d), respectively. A negligible variation in the distribution of U_x is noticed for all the stacking sequences. It may be observed from this figure (Fig. 7.5(a)) that U_x is zero at the midspan, whereas the transverse deflection U_w is maximum at the midspan as illustrated in Fig. 7.5(b). In comparison with conventional three layered METE plate, SFG METE plate exhibit a higher central deflection. Figure 7.5(c) illustrates that SFG-FBF METE plate results in a higher magnetic potential while the SFG-FBF METE plate exhibits a higher electric potential (Fig. 7.5(d)). Also, the magnetic potential and

the electric potential are zero at both the edges and become constant along the length of the plate.

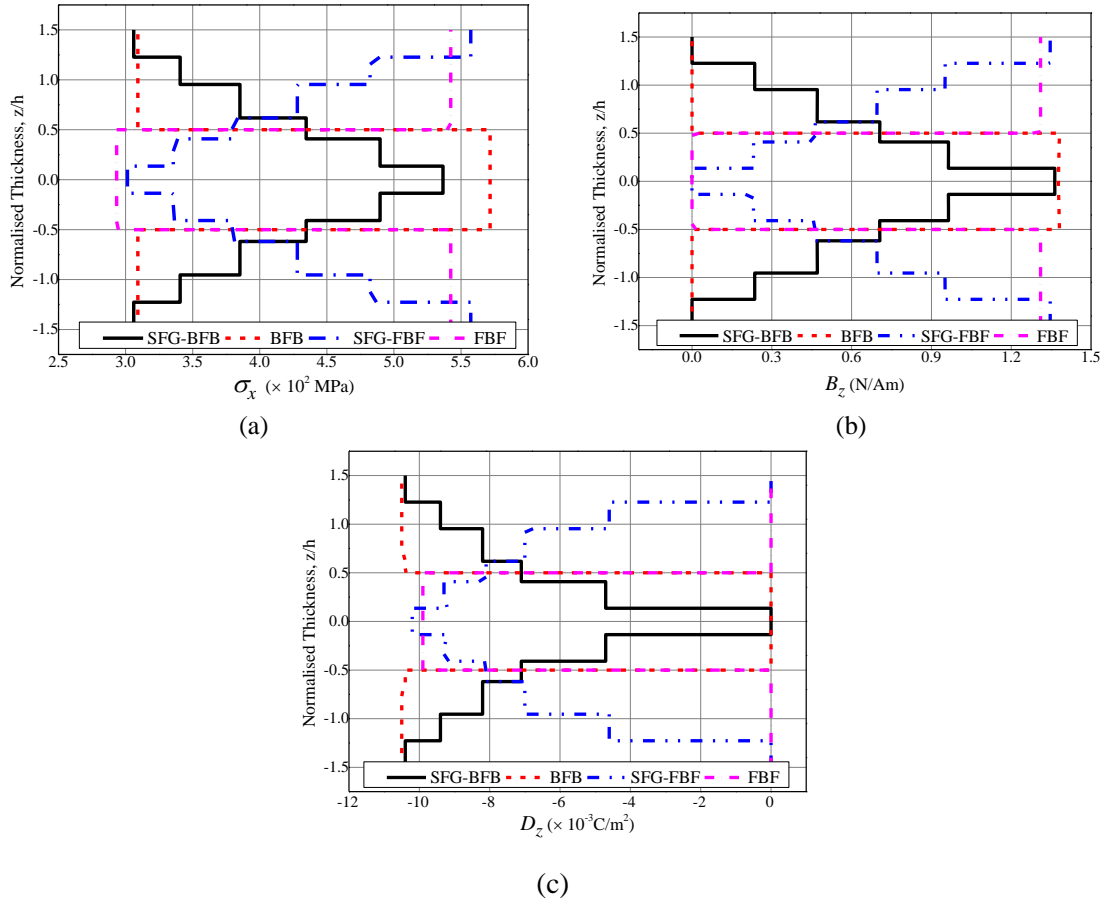
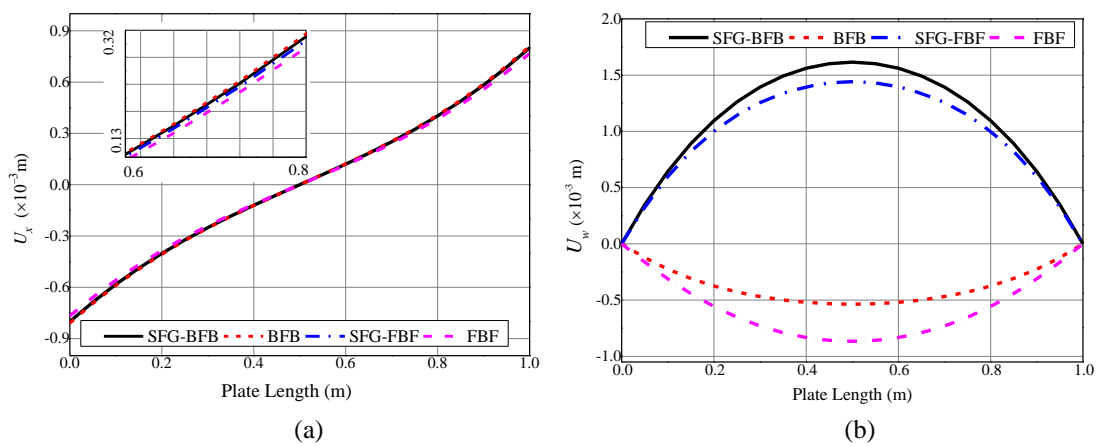


Figure 7.4: Variation of the (a) normal stress σ_x (b) magnetic flux density B_z and (c) electric displacement D_z , across the plate thickness of METE plate subject to uniform temperature rise



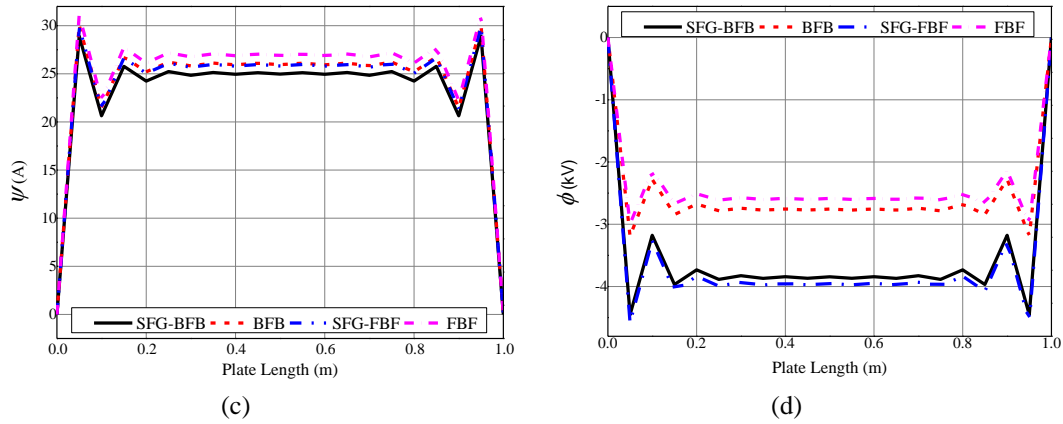


Figure 7.5: Variation of (a) displacement U_x (b) centre deflection U_w (c) magnetic potential, ψ (d) electric potential, ϕ along plate length of the simply supported METE plate subject to uniform temperature rise

7.6.3. Effect of non-uniform temperature rise

The static response of METE plate exposed to the sinusoidal temperature field is evaluated. The expressions for the temperature distribution can be represented as follows:

$$T(x, y, z) = f(z)\bar{T}(x, y) \quad (7.26)$$

where,

$$f(z) = T_0 \text{ and } \bar{T}(x, y) = \text{Sin} \frac{\pi x}{a} \text{Sin} \frac{\pi y}{b} \quad (7.27)$$

It may be observed from Fig. 7.6(a) that the stress developed is lesser compared to the uniform temperature loading for the same magnitude of T_0 (Fig. 7.4(a)). The variation of B_z and D_z across the thickness of the plate is depicted in Figs. 7.6(b) and (c), respectively. It may be noticed from Fig. 7.7(a) that the displacement component U_x is marginally higher for BFB METE plate than the other stacking sequence. As illustrated in Fig. 7.7(b), the central deflection U_w of METE plate subjected to sinusoidal temperature loading follows the similar variation trend as that of the uniform temperature rise (Fig.7.5(a)). The magnetic and electric potential is observed to be maximum at the midlength of the plate while it is zero at the edges, as shown in Figs. 7.7(c) and (d), respectively. It may be attributed to the temperature distribution considered for the analysis. From Figs.

7.7(a) and (b), it can also be noticed that the magnitude of the displacement (U_x) and centre deflection (U_w) are lower than the uniform temperature profile. In addition, SFG-FBF METE plate has a predominant effect on both the magnetic and electric potential as depicted in Figs. 7.7(c) and (d), respectively.

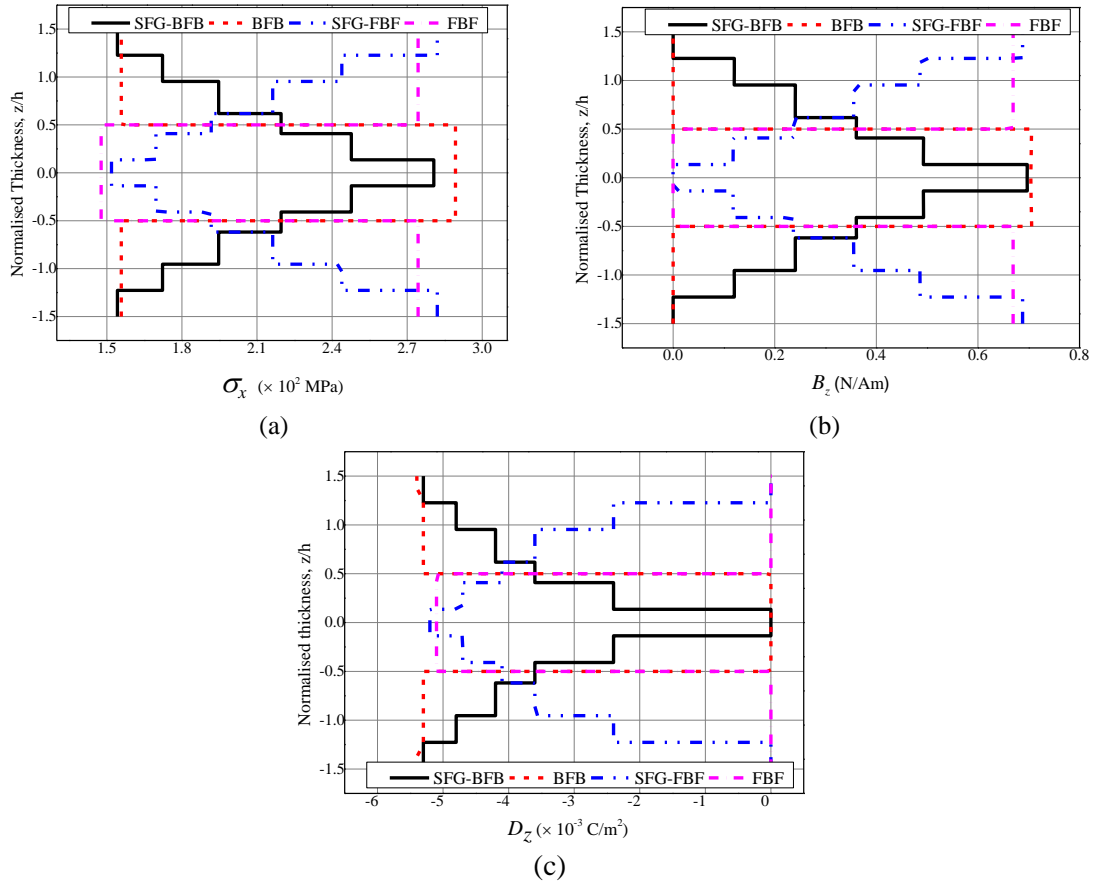
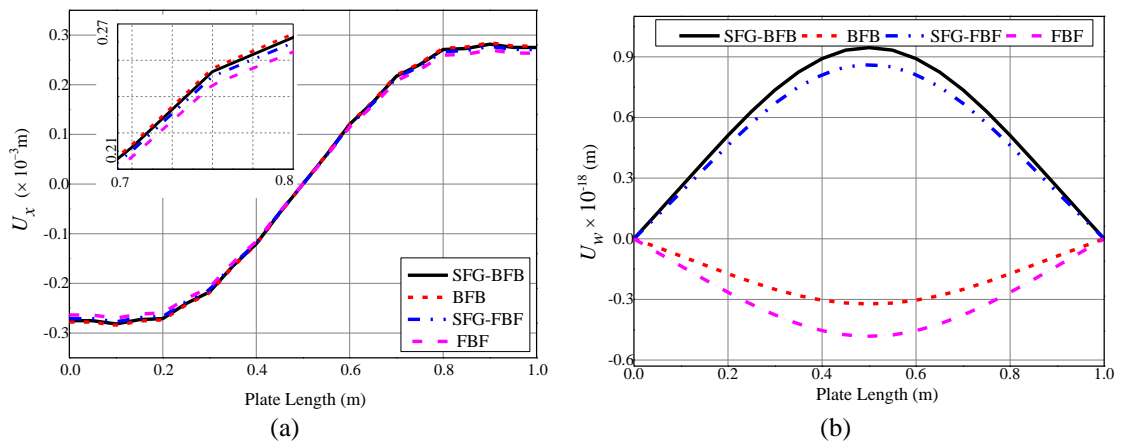


Figure 7.6: Variation of the (a) σ_x (b) B_z and (c) D_z , across the plate thickness for METE plate subject to non-uniform temperature rise



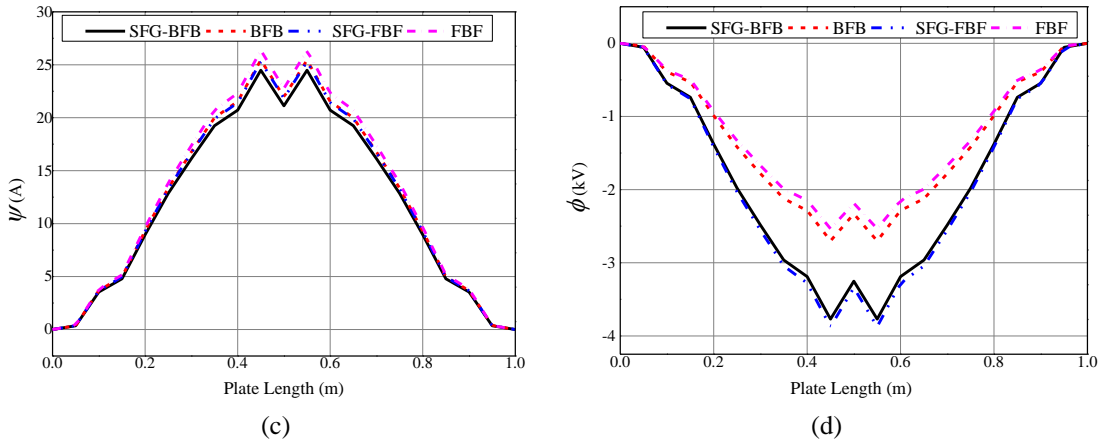


Figure 7.7: Variations of (a) displacement U_x (b) centre deflection U_w (c) magnetic potential, ψ and (d) electric potential, ϕ , along plate length of METE plate subject to non-uniform temperature rise

7.6.4. Effect of electric field force

The variation of the static parameters of SFG METE plate and conventional three layered METE plate under the influence of electric field force F_e is studied in this section. It may be noted that the electric field force is applied along the thickness direction alone. Figures 7.8(a) and (b) illustrate the distribution of normal stress and magnetic flux density across the plate thickness. The negative in-plane stress (σ_x) in Fig. 7.8(a) indicates that the plate is under compression at a particular location of interest. From Fig. 7.8(b), it is observed that the magnitude of magnetic flux density B_z is insignificant in the top and the bottom layer of the SFG-BFB METE plate. It may be accounted to the presence of pure piezoelectric phase at the top and the bottom layers. Further, B_z rises to the maximum at the middle layer composed of pure piezomagnetic phase. This explanation holds good for conventional METE plate also. It may be noticed from Fig. 7.8(c) that the D_z varies linearly in each pure piezoelectric phase. In addition, the electric displacement D_z has a negligible value at the top and the bottom layers and then gradually increases till the middle layer where it drastically falls to zero due to the presence piezomagnetic phase. The maximum D_z is noticed for SFG-FBF stacking sequence at the middle layer composed of pure piezoelectric phase. Unlike the temperature loading, a noticeable discrepancy exists with respect to

displacement U_x along the plate length as shown in Fig. 7.9(a). It can also be observed that the displacement U_x is the maximum at the clamped end and varies almost linearly along the plate length. The central deflection U_w is the minimum for FBF METE plate, while it is the maximum for SFG-FBF METE plate as shown in Fig. 7.9(b). The magnetic potential (ψ) and electric potential (ϕ) are the maximum near clamped end and attain constant values over the plate length as depicted in Figs. 7.9(c) and (d), respectively.

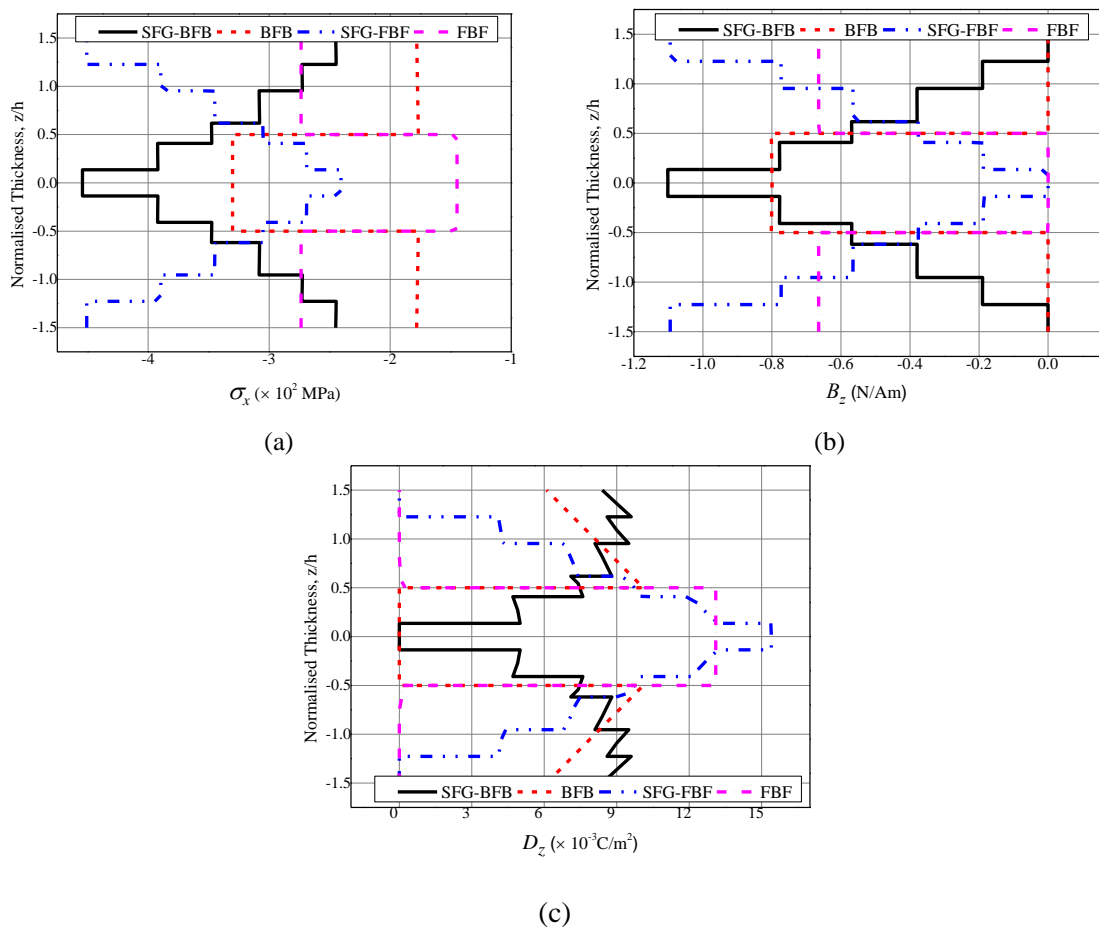


Figure 7.8: Variation of the (a) normal stress σ_x (b) magnetic flux density B_z and (c) electric displacement D_z , across the plate thickness for METE plate subject to electric field force

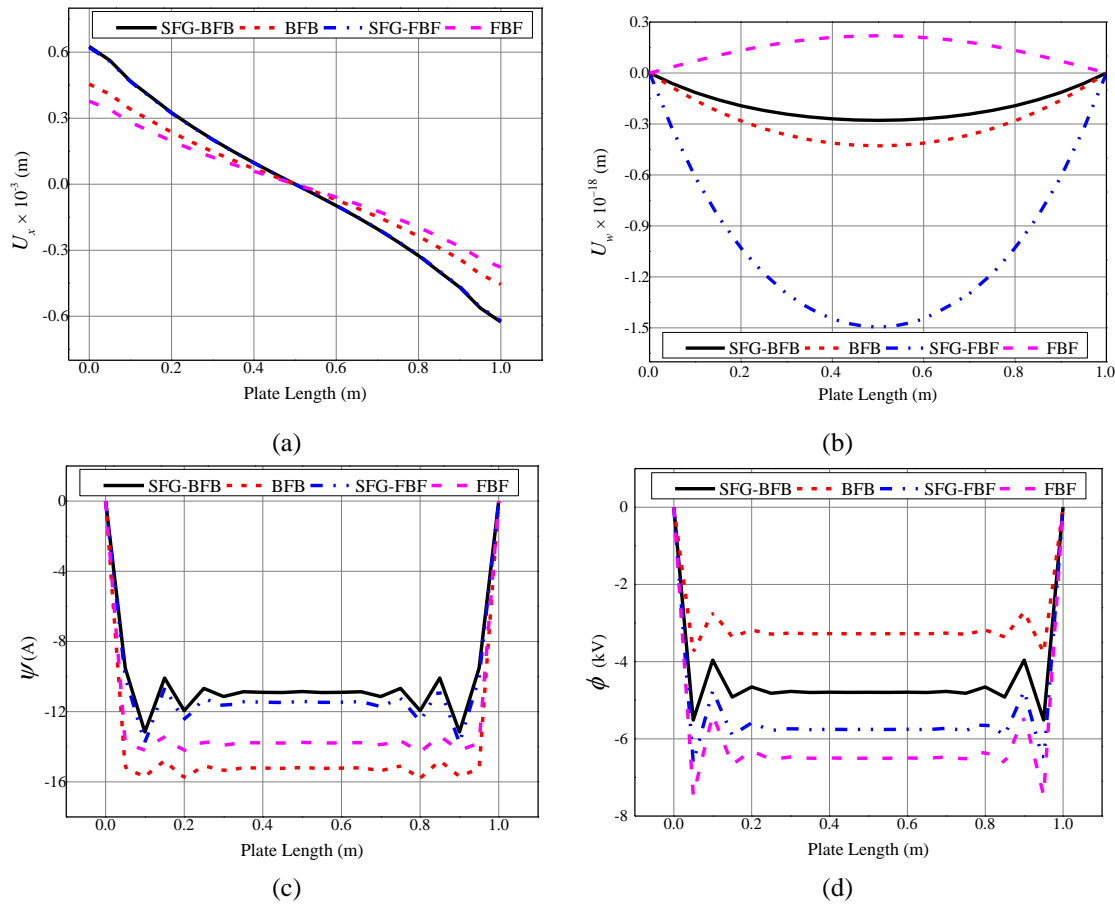


Figure 7.9: Variations of (a) displacement U_x (b) centre deflection U_w (c) magnetic potential, ψ and (d) electric potential, ϕ along plate length of the METE plate subject to electric field force

7.6.5. Effect of magnetic field force

In this study, analogous to the electric field, the magnetic field force has been considered for the analysis. From Fig. 7.10(a), it may be observed that the stress variation follows a similar trend as that of the electric loading (Fig. 7.8(a)). The magnetic flux density B_z varies almost linearly across the thickness of each layer except at the pure piezoelectric phase as illustrated in Fig. 7.10(b). The SFG-BFB plate shows an increasing trend with the maximum values appearing at the midplane while SFG-FBF plate exhibits a decreasing trend. Further, the maximum B_z is attained by three-layered BFB METE plate. Figure 7.10(c) depicts the variation of electric displacement component D_z across the thickness of the plates. A negligible variation

with respect to U_x along the plate length is noticed for all the stacking sequences as shown in Fig. 7.11(a). Similarly, from Fig. 7.11(b), it is observed that SFG-FBF plate experiences more central deflection U_w while it is the minimum in three-layered FBF METE plate. The variation of electric potential is depicted in Fig. 7.11(c). It can be noticed from this figure that the maximum value is obtained at the edges and it remains almost constant along the plate length. In addition, from Fig. 7.11(d), it can be seen that BFB stacking sequence has a prominent effect on the magnetic potential while FBF METE plate results in a comparatively lesser magnetic potential.

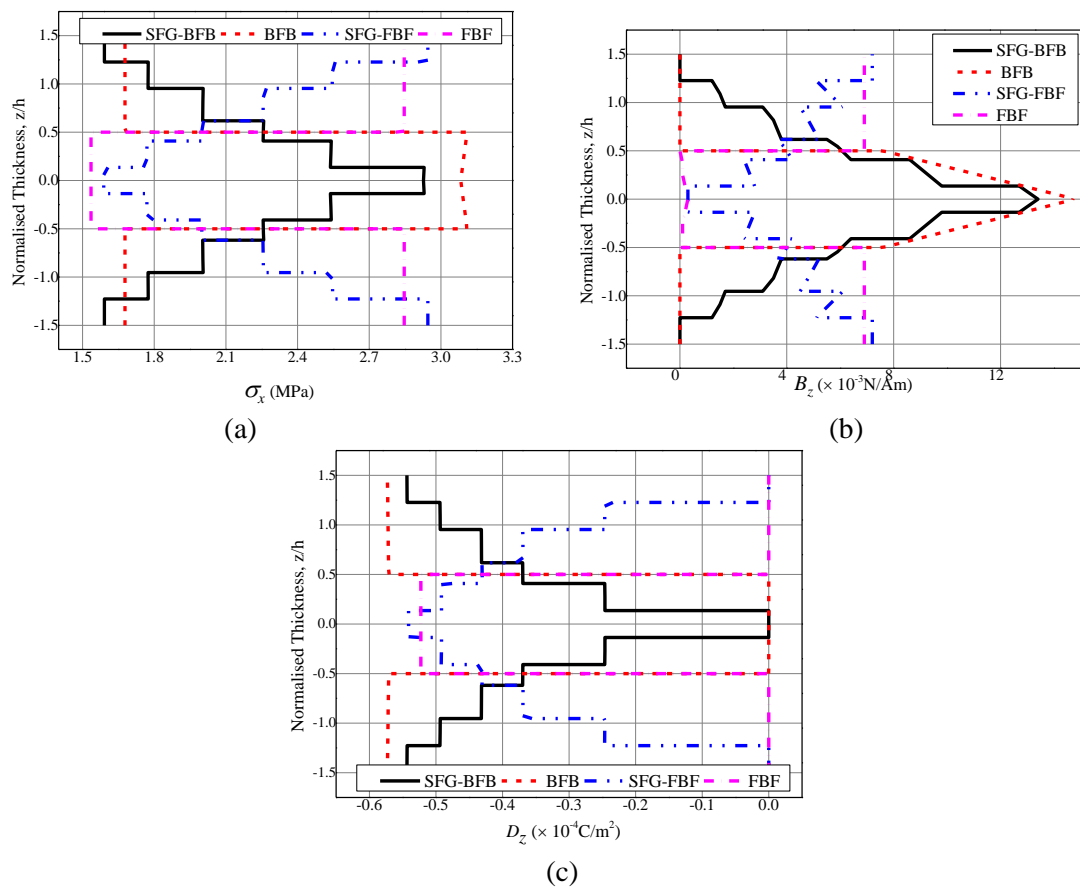


Figure 7.10: Variation of the (a) normal stress σ_x (b) magnetic flux density B_z (c) electric displacement D_z across the plate thickness for METE plate subject to magnetic field force

7.6.6. Effect of combined loading

The combined effects of thermal, electric and magnetic field forces on the behaviour of METE plates are evaluated. The uniform temperature rise of 100 K,

electric force of 10 C/m^2 and the magnetic force of 10 T (Tesla) are considered for the analysis. Figures 7.12(a)-(c) illustrate the distribution of normal stress σ_x , magnetic flux density B_z and electric displacement component D_z , respectively. It may be witnessed from these figures that the thermo-magnetic load exhibit a substantial effect followed by electro-magnetic loading. Further, a marginal discrepancy exists between thermo-electric and thermo-electro-magnetic loads. The variation of displacements U_x , U_w , electric potential and magnetic potential along the plate length is depicted in Figs. 7.13(a)-(d), respectively. It can be observed that the thermo-magnetic load has a predominant influence on the displacement components. Further, a significant effect of the thermo-electric and electro-magnetic loads are seen on the electric potential and magnetic potential, respectively.

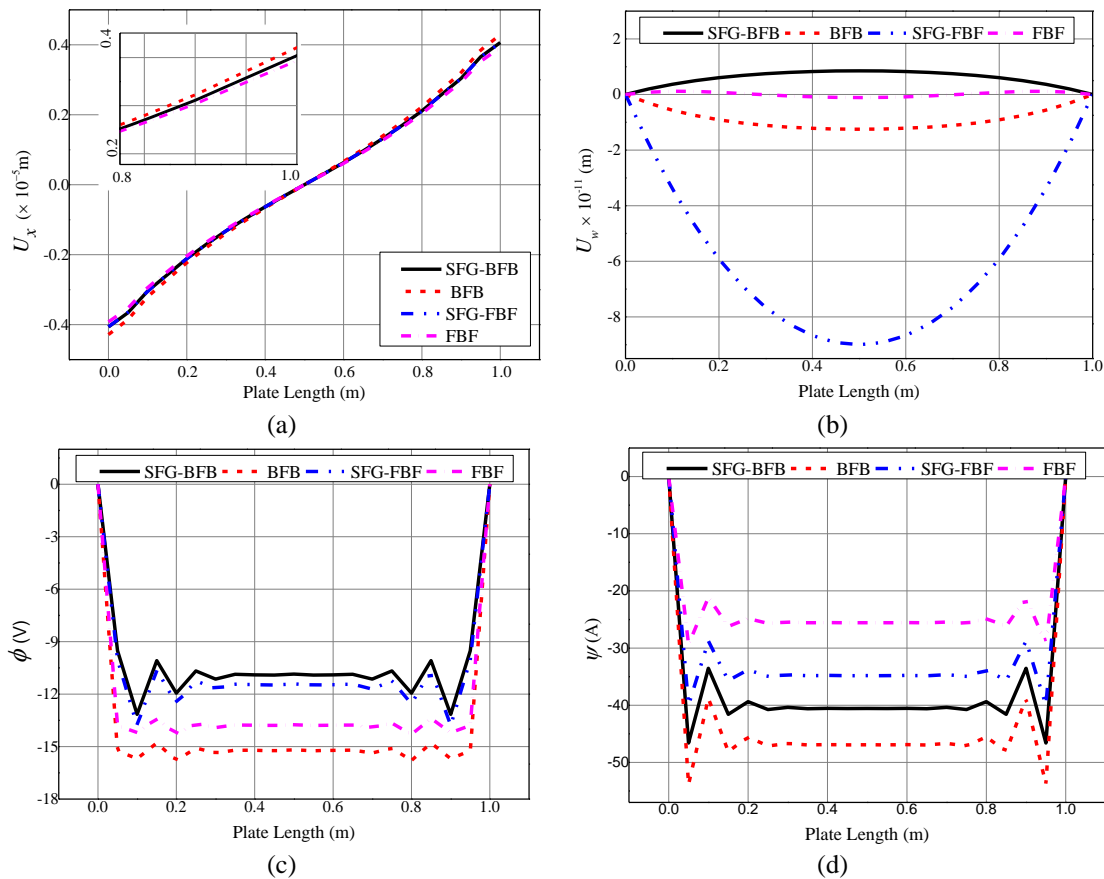


Figure 7.11: Variation of (a) displacement U_x (b) centre deflection U_w (c) electric potential, ϕ and (d) magnetic potential, ψ , along plate length of the METE plate subject to magnetic field force

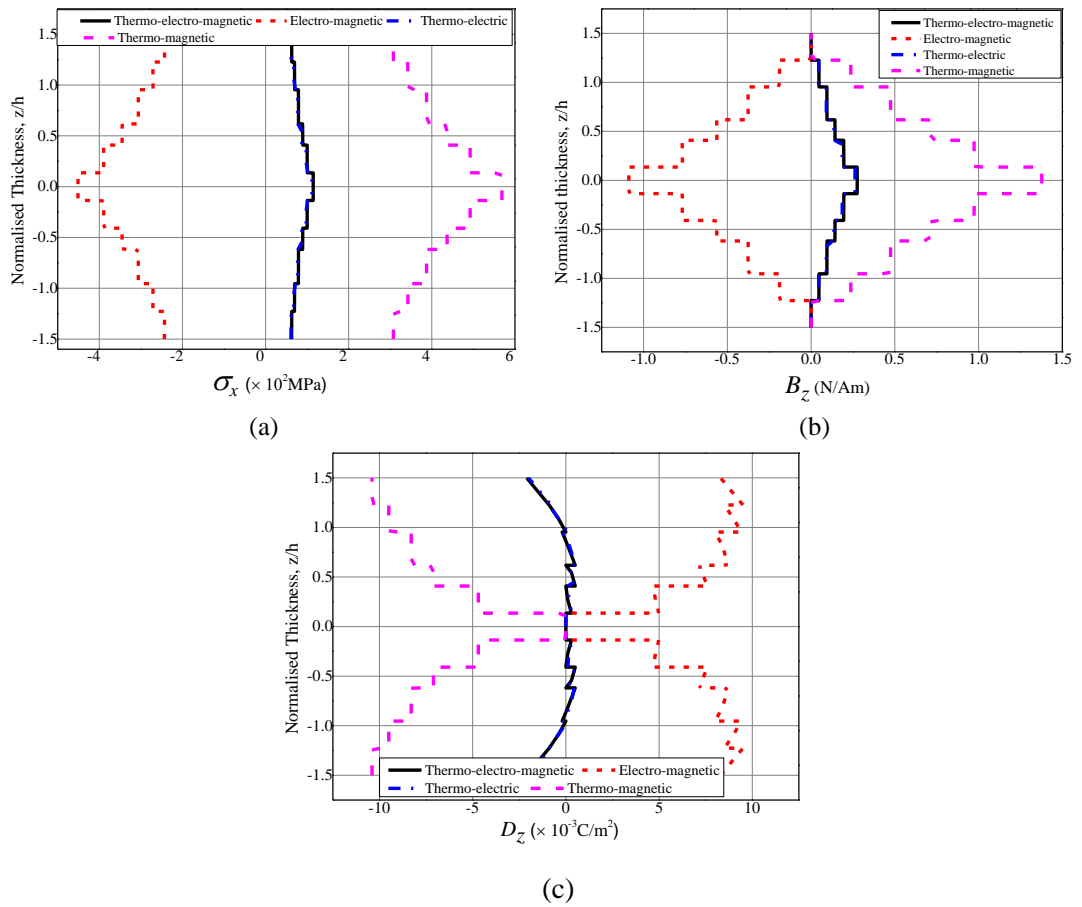
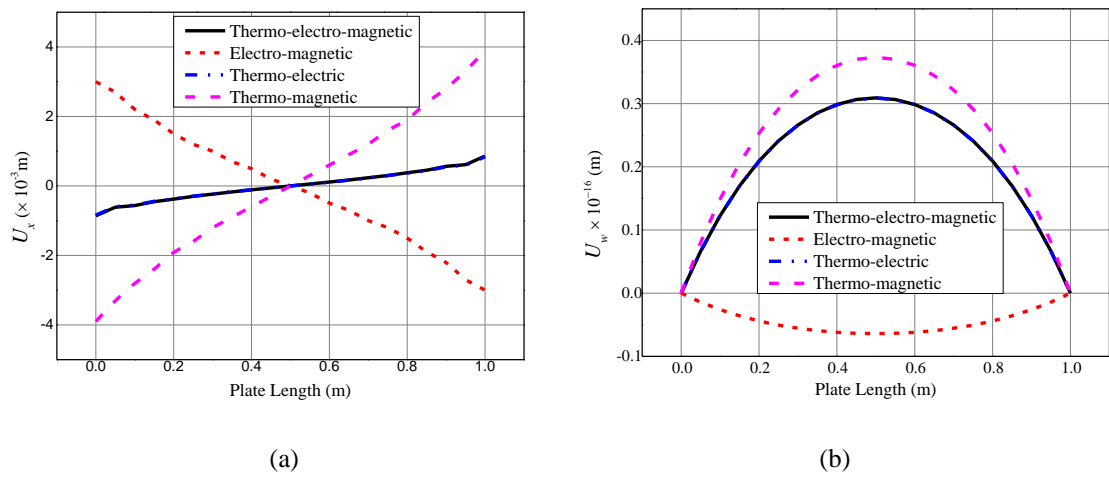


Figure 7.12: Influence of combined loads on (a) normal stress σ_x (b) magnetic flux density B_z (c) electric displacement D_z



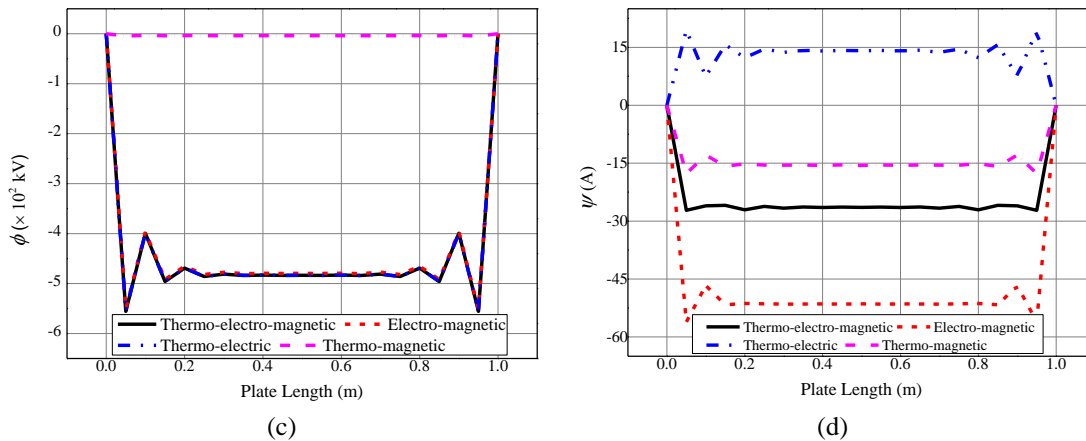


Figure 7.13: Influence of combined loads on (a) displacement component U_x (b) centre deflection U_w (c) electric potential ϕ (d) magnetic potential ψ

7.6.7. Influence of pyroeffects

The numerical investigation is carried out to evaluate the influence of pyroeffects on METE plates subjected to uniform and sinusoidal temperature loads. It is noticed that only the electric potential of the METE plate experiences a direct pyro coupling effect. For both the stacking sequences, Figs. 7.14(a) and (b) show the influence of pyroeffects on the electric potential of SFG-METE plate under uniform and sinusoidal temperature loads, respectively. It can be deduced from these figures that the pyroeffects tends to improve the electric potential of the METE plate for both forms of temperature loads.

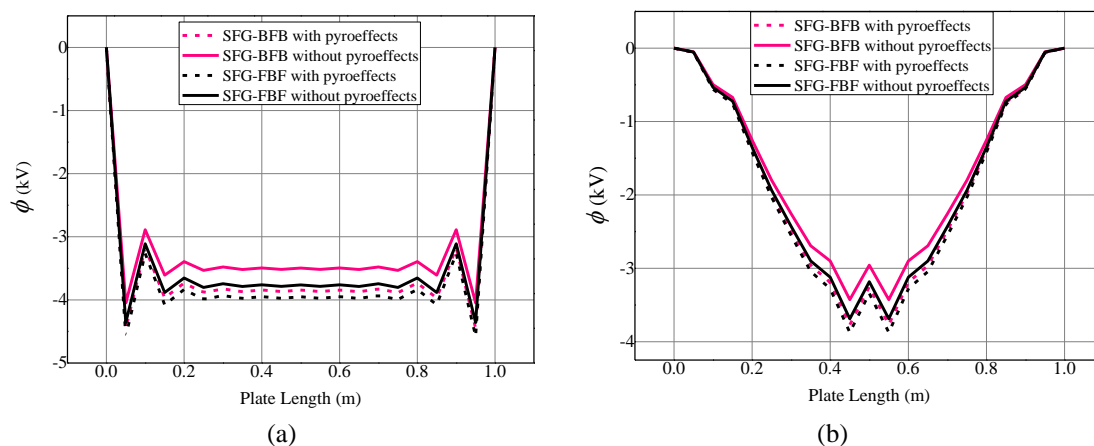


Figure 7.14: Influence of pyroeffects (a) uniform temperature loads (b) sinusoidal temperature loads

7.6.8. Effect of boundary conditions

The distribution of direct and derived quantities for the various boundary conditions of the plate is investigated. The boundary conditions employed in the present analysis are given as follows:

$$\text{Clamped edge (C):} \quad U_x = U_v = U_w = \theta_x = \theta_y = 0$$

$$\text{Free edge (F):} \quad U_x = U_v = U_w = \theta_x = \theta_y \neq 0$$

$$\text{Simply supported edge (S):} \quad U_x \neq 0; U_v = U_w = \phi = \psi = 0 \text{ at } x = 0, a$$

$$U_x \neq 0; U_v = U_w = \phi = \psi = 0 \text{ at } y = 0, b \quad (7.28)$$

Figures 7.15(a)-(c) illustrate the comparison of the variation of magnetic flux density, normal stress (σ_x), and electric displacement, respectively, for different boundary conditions. It can be seen from these figures that the *CFFF* boundary condition has a predominant effect due to more number of free edges while the *CCCC* boundary condition has a negligible effect. In addition, for the *CCFF* and *CFFF* boundary conditions, the maximum value of direct quantities is noticed at the free end as shown in Figs. 7.16(a)-(d). This may be due to asymmetric boundary conditions. For the symmetric boundary conditions (*viz.* *CCCC*, *SSSS*, and *CSCS*), the maximum central deflection U_w is noticed at the midspan of the plate. The longitudinal displacement component U_x varies symmetrically along the plate length for the *CSCS* and *CFCF* METE plates. The electric potential and the magnetic potential are plotted in Figs. 7.16(c) and (d), respectively. It may be observed from these figures that for the *SSSS* METE plate, the electric potential ϕ and magnetic potential ψ remain constant along the plate length with the maximum values appearing at the edges. Further, for the *CFCF* and *CSCS* METE plate, the maximum ϕ and ψ are observed at the mid length of the plate. However, for the *CCSS* METE plate ϕ and ψ gradually increases from the clamped end to simply supported end.

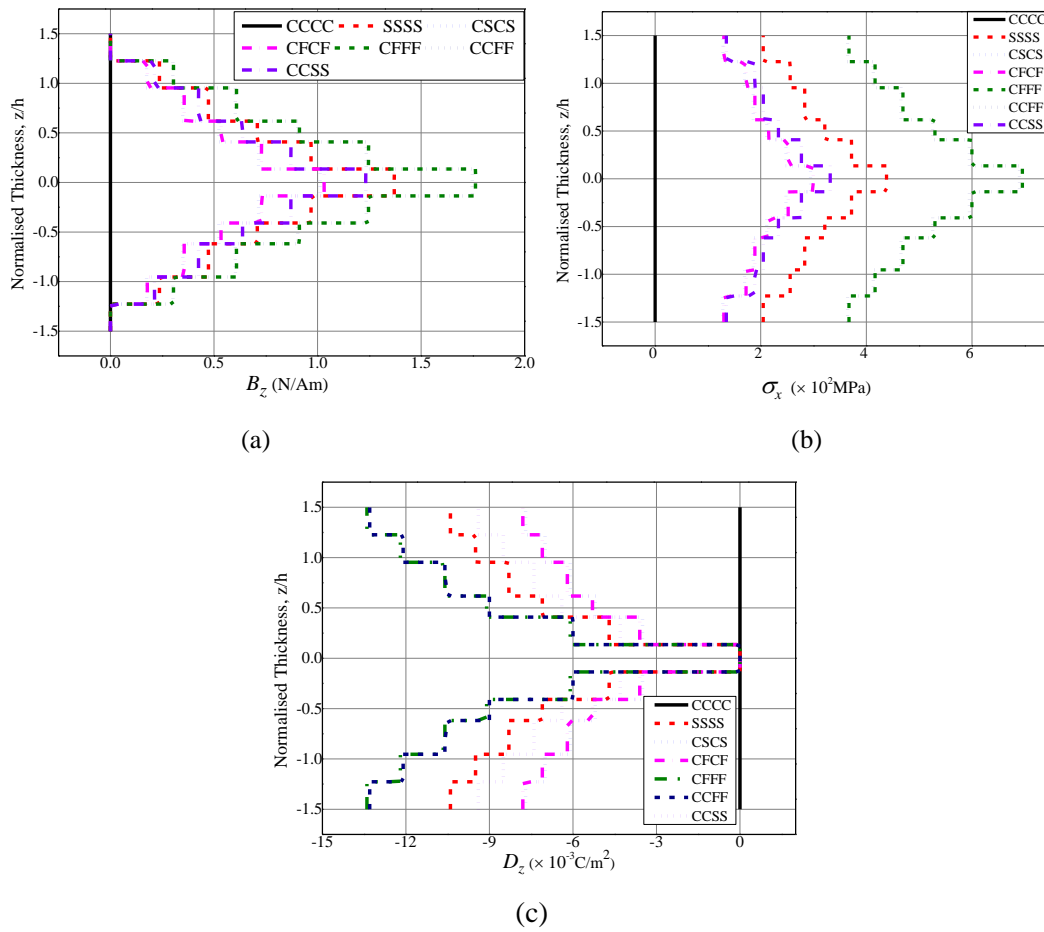
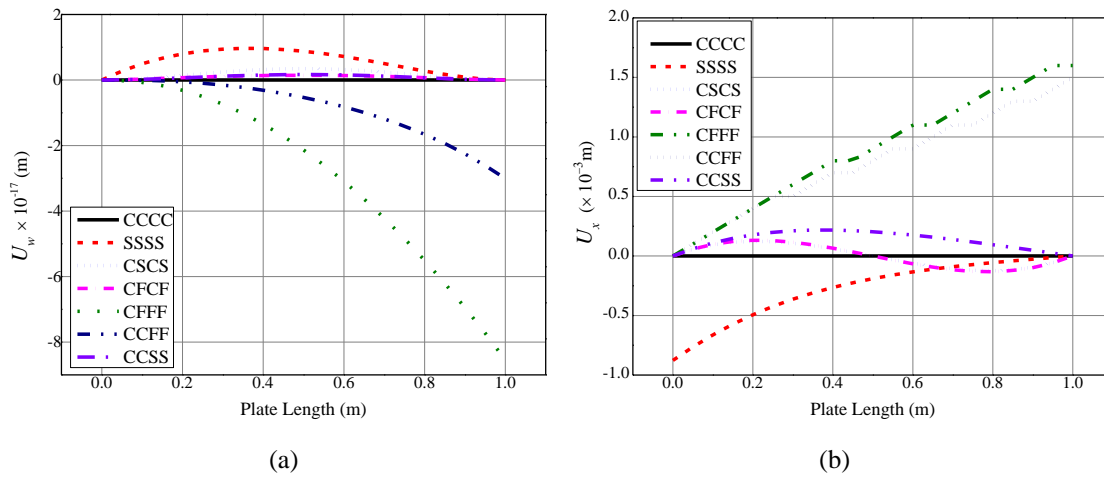


Figure 7.15: Effect of boundary condition on (a) magnetic field density (b) normal stress - σ_x (c) electric displacement



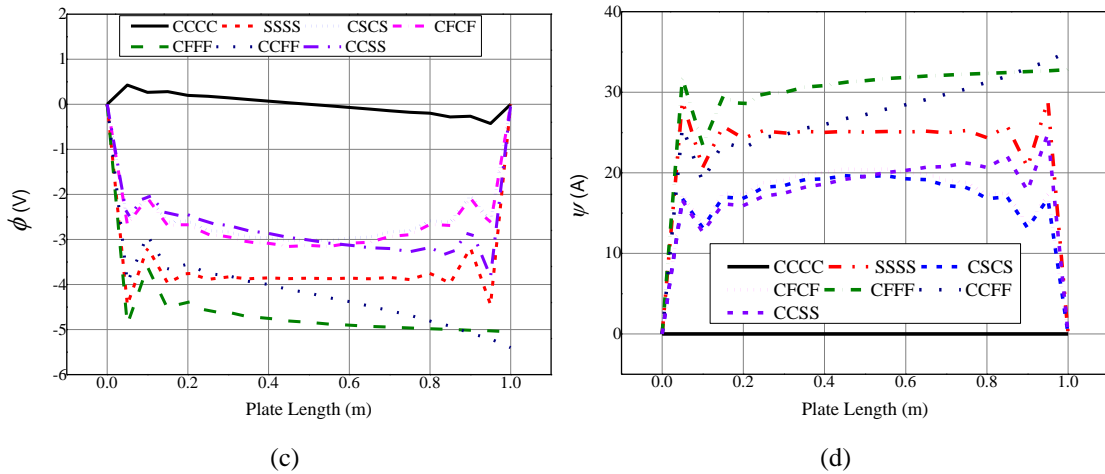


Figure 7.16: Effect of boundary condition on (a) centre deflection U_w (b) longitudinal displacement component U_x (c) electric potential (d) magnetic potential

7.6.9. Effect of aspect ratio (a/b) and length-to-thickness ratio (a/H)

The effect of aspect ratio (a/b) and the length-to-thickness ratio (a/H) on the displacement components of SSSS METE plate is investigated by considering uniform temperature load. The displacement components directly affect all the static parameters. Hence, in the present study the effect of a/H and a/b ratio is limited to displacement components only. From Figs. 7.17(a) and (b), it can be noticed that with the increase in aspect ratio, the displacement components increases. Similarly, the variation in the displacement components is proportional to the length-to-thickness ratio (a/H) as illustrated in Figs. 7.18(a) and (b).

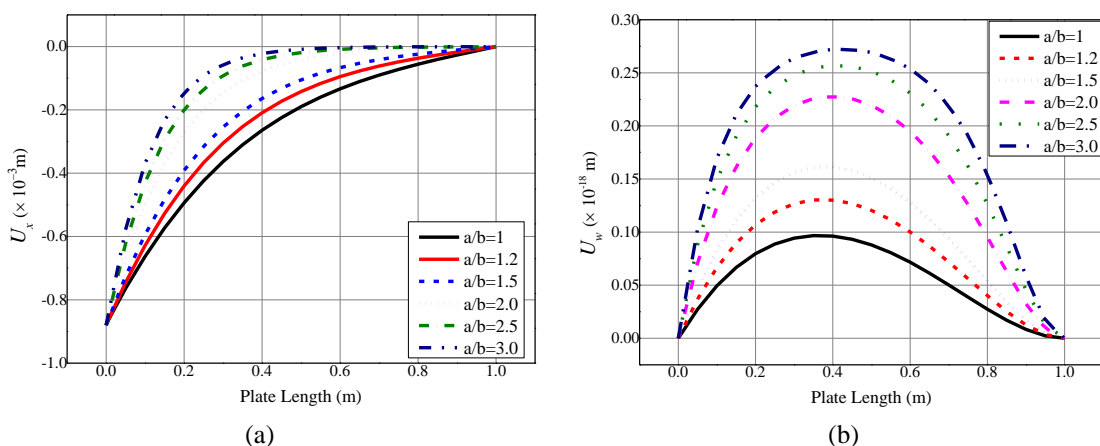


Figure 7.17: Effect of a/b ratio on (a) U_x (b) U_w of METE plate subjected to uniform temperature load

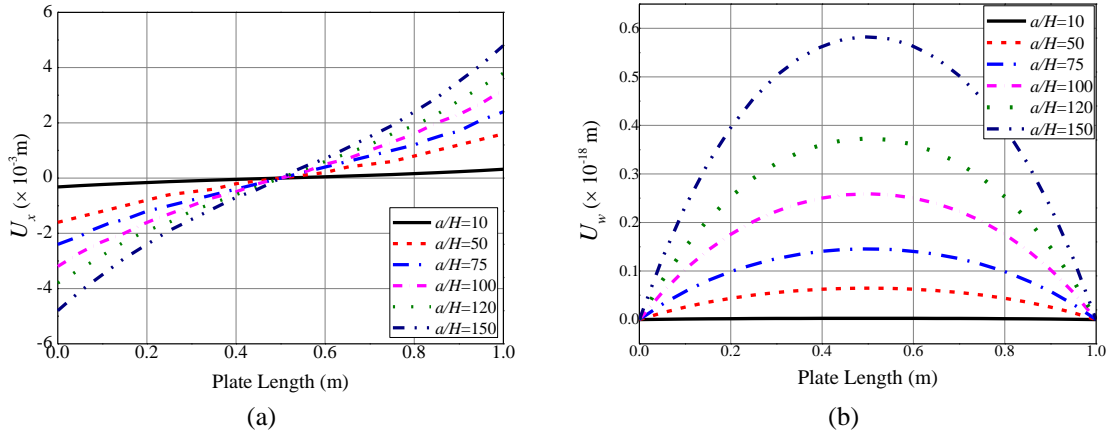


Figure 7.18: Effect of a/H ratio on (a) U_x (b) U_w of METE plate subjected to uniform temperature load

7.6.10. Free vibration analysis of SFG METE plate: Evaluation of effect of coupling factors

Free vibration analysis of SFG METE plate is carried out by considering full coupling of the thermal field with magnetic, electric and elastic fields. The effect of METE coupling, the electric effect of piezoelectric (PE) phase, magnetic effect of piezo magnetic (PM) phase and effect of thermal constants on the natural frequencies is investigated. In this regard, the equivalent stiffness matrices $[K_{eq}]$, $[K_{eq_elastic}]$, $[K_{eq_\phi\phi}]$, $[K_{eq_psi\psi}]$ and $[K_{eq_theta\theta}]$ for each case is derived as illustrated in *Appendix D*. Table 7.4 encapsulates the description and significance of the different frequencies computed along with the corresponding stiffness matrices. Further, the effect of stacking sequence and boundary conditions on the natural frequency is also studied.

The following cases of boundary conditions have been considered for the free vibration analysis of SFG METE plate.

Case 1: Simply supported on all edges (SSSS)

$$U_x(x, y, 0) \text{ and } \theta_x = 0 \text{ at } y = 0 \text{ and } y = a;$$

$$U_v(x, y, 0) = 0 \text{ and } \theta_y = 0 \text{ at } x = 0 \text{ and } x = a;$$

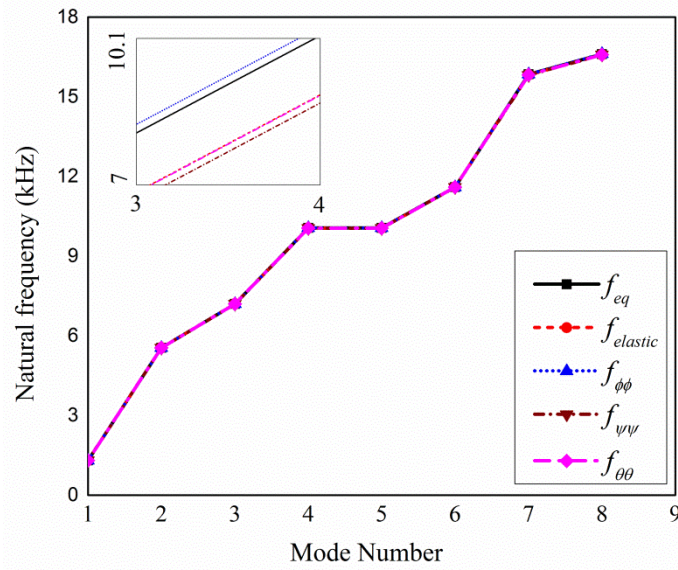
$$U_w(x, y, 0) = 0 \text{ at } x = 0, x = a, y = 0 \text{ and } y = a;$$

$$\phi(x, y, 0) = \psi(x, y, 0) = T(x, y, 0) = 0 \text{ at } x = 0, x = a, y = 0 \text{ and } y = a; \quad (7.29)$$

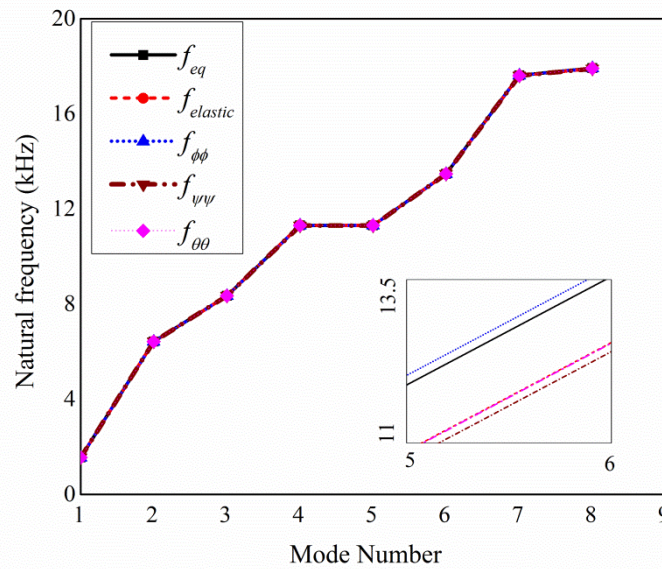
The effect of coupled fields on the natural frequency is presented in Table 7.5. It is evident from Table 7.5 that the effect of coupling parameters on the natural frequency is significant for higher modes for both the SFG-BFB and SFG-FBF stacking sequences. In comparison with $f_{elastic}$, the fully coupled effects (f_{eq}) tend to increase the frequency of the system. Also, it can be noticed from Table 7.5 that $f_{\psi\psi}$ and $f_{\theta\theta}$ are less than f_{eq} while $f_{\phi\phi}$ is higher than f_{eq} . This suggests that a marginal dominance of $f_{\phi\phi}$ prevails for both the stacking sequences. The electric effect of PE phase increases the frequency of the system. But, the magnetic effect of PM phase along with thermal properties tends to deteriorate the system frequency. The same is graphically illustrated in Figs. 7.19(a) and (b) for SFG-BFB and SFG-FBF stacking sequences, respectively.

Table 7.4: Different stiffness matrices

Stiffness matrix symbol	Related Frequency	Description	Significance
$[K_{eq}]$	f_{eq}	Stiffness matrix for fully coupled magneto-thermo-electro-elastic material	Effect of coupled fields
$[K_{elastic}]$	$f_{elastic}$	Stiffness matrix neglecting coupling effects	Effect of elastic constants only
$[K_{eq_{\phi\phi}}]$	$f_{\phi\phi}$	Stiffness matrix considering piezoelectric effect	Effect of piezoelectric phase
$[K_{eq_{\psi\psi}}]$	$f_{\psi\psi}$	Stiffness matrix considering piezomagnetic effect	Effect of piezomagnetic phase
$[K_{eq_{\theta\theta}}]$	$f_{\theta\theta}$	Stiffness matrix considering thermal effect	Effect of thermal constants



(a)

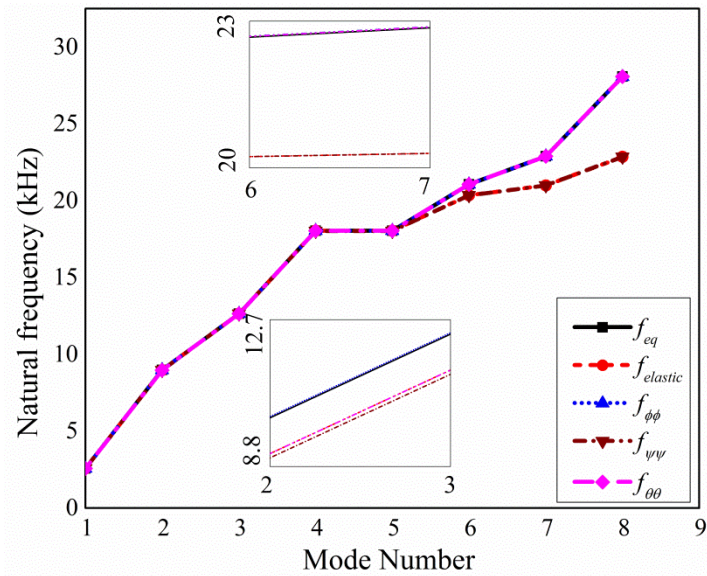


(b)

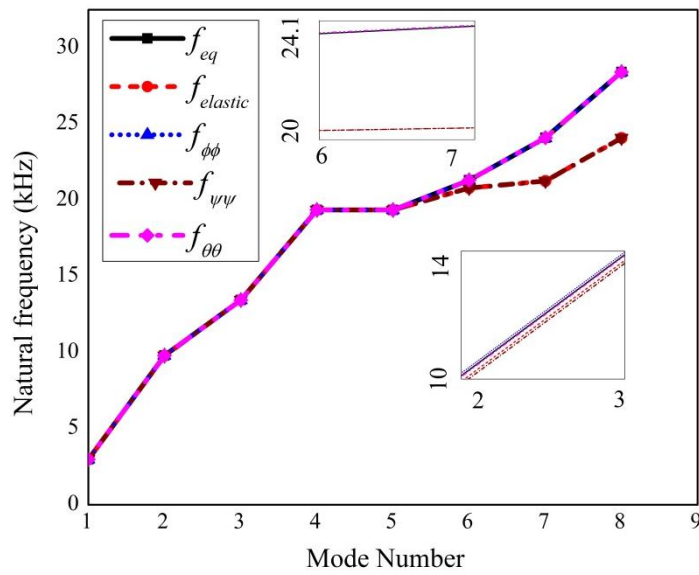
Figure 7.19: Comparison of natural frequency (a) SFG-BFB (b) SFG-FBF SSSS METE plate
Case 2: Clamped on all edges (CCCC)

In this case, all the degrees of freedom of the nodes lying at the edges are fully-constrained. As illustrated in Table 7.6, for the higher modes (mode no 6 and above), $f_{\theta\theta}$ is almost equal to f_{eq} . This is accounted to the predominant influence of thermal properties over the PE and PM effect in clamped boundary condition. Hence, for both

the stacking sequences (BFB and FBF), the inclusion of thermal properties increases the frequency of the plate at the higher modes as shown in Fig. 7.20(a) and (b), respectively.



(a)



(b)

Figure 7.20: Comparison of natural frequency (a) SFG-BFB (b) SFG-FBF CCCC METE plate

The effect of different boundary conditions on the natural frequency of METE plates is tabulated in Table 7.7. It can be noticed from this table that for both the stacking sequences, the *CCCC* boundary condition results in a higher natural frequency. Further, the SFG-FBF METE plate has a predominant effect on the natural frequency than the SFG-BFB METE plate. This may be attributed to the higher values of elastic constants of the magnetostrictive layer.

7.7. CONCLUSIONS

This chapter makes an attempt to evaluate the effect of fully coupled fields on the static and free vibration behaviour of magneto-electro-thermo-elastic plates. A finite element formulation is derived using the Hamilton's principle and constitutive equations of METE solids taking into account the full coupling between elastic, electric, magnetic and thermal fields. The numerical results suggest that the pyroeffects tend to improve the electric potential of the system. The uniform temperature loads exhibit a predominant influence on the direct and derived quantities. This is attributed to the constant pyroloads generated due to pyroelectric and pyromagnetic coupling effects. A comparative study of the influence of different boundary conditions reveals that asymmetric boundary condition (*CFFF*) has a prominent influence on the direct quantities. Further, increase in the aspect ratio (a/b) and length-thickness (a/H) ratio increases the displacement components. It is believed that the present study can be helpful for understanding the structural response of SFG METE plate subjected to various loading condition.

Further examination revealed that the pure piezoelectric phase has a predominant effect on the natural frequency of METE plate. In addition, for the *SSSS* boundary condition, the magnetostrictive phase and the thermal properties inclusion has a negligible effect on the frequency of SFG METE plates whereas, for the *CCCC* boundary condition, a significant effect of thermal properties on the natural frequency is noticed.

Table 7.5: Natural frequencies (rad/s) for SSSS SFG METE plate; $a = 1 \text{ m}$; $H = 0.04 \text{ m}$

Mode number	Simply supported condition									
	SFG-BFB					SFG-FBF				
	f_{eq}	$f_{elastic}$	$f_{\varphi\varphi}$	$f_{\psi\psi}$	$f_{\theta\theta}$	f_{eq}	$f_{elastic}$	$f_{\varphi\varphi}$	$f_{\psi\psi}$	$f_{\theta\theta}$
1	1303.87	1303.72	1303.91	1303.72	1303.64	1550.22	1550.20	1550.25	1550.21	1550.16
2	5546.78	5544.76	5547.07	5544.48	5544.74	6428.41	6427.36	6428.89	6426.81	6427.37
3	7204.42	7202.89	7204.59	7202.81	7202.91	8350.74	8349.98	8351.09	8349.81	8350.01
4	10059.04	10052.52	10059.76	10051.67	10052.51	11309.98	11307.04	11311.35	11305.5	11307.03
5	10059.04	10052.52	10059.76	10051.67	10052.51	11309.98	11307.04	11311.35	11305.5	11307.03
6	11598.45	11595.51	11599.01	11595.14	11595.51	13479.73	13478.41	13480.39	13477.71	13478.39
7	15846.27	15821.91	15848.99	15818.79	15821.89	17617.66	17608.23	17622.09	17603.31	17608.23
8	16606.86	16585.27	16609.09	16582.49	16585.26	17919.05	17910.18	17923.07	17905.64	17910.17

Table 7.6: Natural frequencies for CCCC SFG METE plate; $a=1\text{ m}$; $H=0.04\text{ m}$

Mode number	Clamped condition									
	SFG-BFB					SFG-FBF				
	f_{eq}	$f_{elastic}$	$f_{\varphi\varphi}$	$f_{\psi\psi}$	$f_{\theta\theta}$	f_{eq}	$f_{elastic}$	$f_{\varphi\varphi}$	$f_{\psi\psi}$	$f_{\theta\theta}$
1	2572.91	2571.88	2572.94	2571.76	2571.88	2975.81	2975.35	2976.01	2975.11	2975.74
2	8989.57	8974.86	8991.17	8973.01	8974.84	9795.74	9790.44	9798.26	9787.71	9795.43
3	12651.33	12648.94	12651.56	12648.63	12648.96	13451.57	13450.46	13452.07	13449.91	13451.4
4	18040.12	18035.24	18040.69	18034.62	18035.23	19359.84	19357.83	19360.78	19356.82	19359.83
5	18040.12	18035.24	18040.69	18034.62	18035.23	19359.84	19357.83	19360.78	19356.82	19359.83
6	21065.42	20361.18	21058.74	20361.05	21063.87	21312.58	20790.54	21302.81	20790.4	21312.41
7	22898.11	21000.39	22890.38	21000.39	22897.38	24098.89	21262.26	24084.48	21258.95	24098.71
8	28079.23	22861.37	28067.19	22856.73	28078.78	28419.88	24086.48	28411.94	24080.15	28419.72

Table 7.7: Effect of boundary conditions on natural frequencies for SFG METE plate ($a = 1\text{ m}$; $H = 0.04\text{ m}$)

Mode number	Simply supported		Clamped-Clamped		Clamped-Free	
	SFG-BFB	SFG-FBF	SFG-BFB	SFG-FBF	SFG-BFB	SFG-FBF
1	1303.87	1550.22	2572.91	2975.81	1541.32	1786.85
2	5546.78	6428.41	8989.57	9795.74	4712.77	5337.23
3	7204.42	8350.74	12651.33	13451.57	5524.01	6355.67
4	10059.04	11309.98	18040.12	19359.84	9178.37	10147.13
5	10059.04	11309.98	18040.12	19359.84	10869.01	12338.07
6	11598.45	13479.73	21065.42	21312.58	12124.55	12776.81
7	15846.27	17617.66	22898.11	24098.89	14383.36	15819.56
8	16606.86	17919.05	28079.23	28419.88	15642.39	17142.28

Chapter 8

EFFECT OF PARTICLE ARRANGEMENT ON COUPLED RESPONSE OF MAGNETO-ELECTRO-THERMO-ELASTIC PLATES

In this chapter, the influence of Barium Titanate ($BaTiO_3$) and Cobalt Ferrite ($CoFe_2O_4$) particle arrangement on the static response of magneto-electro-thermo-elastic (METE) plate is studied. The three prominent particle arrangements such as body centered cubic (BCC), face centered cubic (FCC) and simple cubic (SC) structures are considered. The investigation on the influence of pyroeffects associated with the different forms of particle arrangements is given special consideration. In addition, the influence of geometrical parameters which includes boundary conditions and aspect ratios are also studied.

Related article: Vinyas, M. and Kattimani, S.C. (2018). “Investigation of the effect of $BaTiO_3/CoFe_2O_4$ particle arrangement on the static response of magneto-electro-thermo-elastic plates”, *Composite Structures*, **185(1), 51-64.**

8.1. INTRODUCTION

The material composition plays an important role in deciding the overall behaviour of structures. In case of magneto-electro-thermo-elastic (METE) materials, the multiple coupled fields distributes differently based upon the heterogeneous composition (Koutsawa 2015). The fluctuations in the effective constituent properties of the METE materials and hence the fields associated with it directly influences the static parameters. Therefore, in this chapter, the METE plates consisting the most prominent microstructure arrangements of the $BaTiO_3/CoFe_2O_4$ particulate composite such as body centered cube (BCC), face centered cube (FCC) and simple cubic (SC) are considered. The variations in the effective properties with respect to different spatial distribution or particle arrangement of $BaTiO_3/CoFe_2O_4$ are extracted from Koutsawa (2015). Using the finite element (FE) formulation derived in Chapter 2, the static coupled response of METE plates with different particle arrangement is

analysed. Furthermore, the analysis is extended to evaluate the effect of boundary conditions and aspect ratio.

8.2. PROBLEM DESCRIPTION AND FINITE ELEMENT GOVERNING EQUATIONS

The schematic representation of magneto-electro-thermo-elastic (METE) plates is shown in Fig. 8.1. The length, breadth and thickness of METE plate are denoted by a , b and h , respectively. The various spatial distribution forms of particulate BaTiO₃/CoFe₂O₄ composites are illustrated in Fig. 8.2. The material properties of the volume fraction ($0.45 V_f$) of two phase particle reinforced BaTiO₃/CoFe₂O₄ METE material are tabulated in Table 8.1.

The FE governing equations of METE plates considering the effect of various particle arrangements can be expressed analogous to Eqs. (2.21) – (2.23).

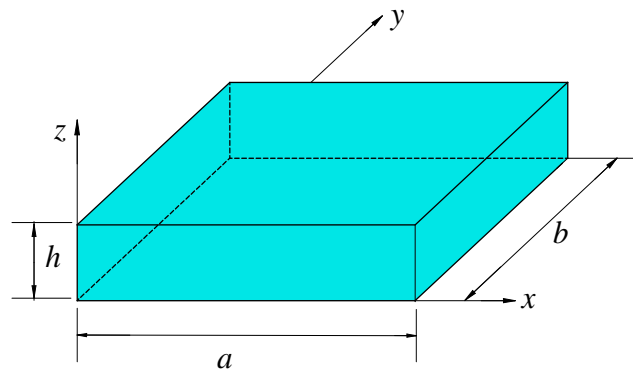


Figure 8.1: Multiphase METE plate geometry

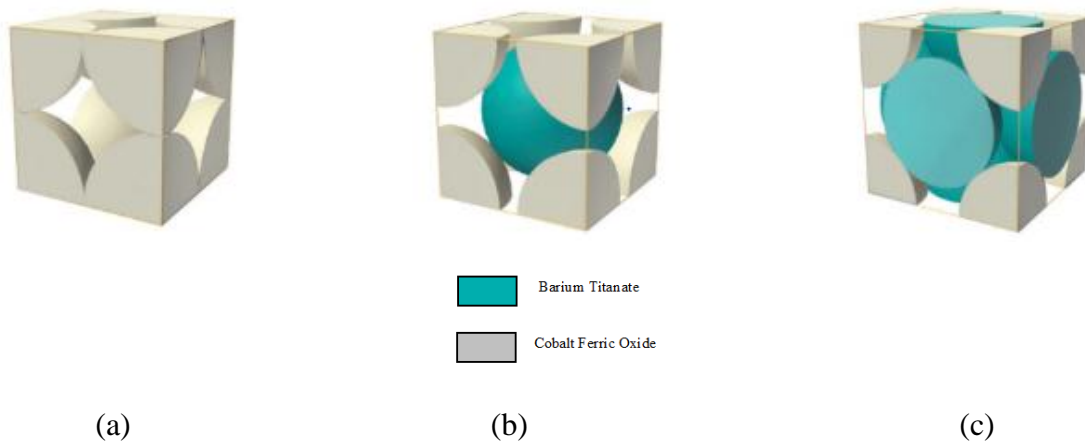


Figure 8.2: Packing arrangement of particulate BaTiO₃/CoFe₂O₄ composites (a) simple cubic (SC) (b) body centered cube (BCC) (c) face centered cube (FCC)

Table 8.1: Material properties of BaTiO₃/CoFe₂O₄ particles with different spatial distribution (BCC, FCC & SC) (Aboudi 2001; Koutsawa 2015).

Material Property	Notation	0.45 V_f of BaTiO ₃ /CoFe ₂ O ₄		
		<i>BCC</i>	<i>FCC</i>	<i>SC</i>
Co-efficient of thermal expansion, ($\times 10^{-6}$, 1/K)	α_{33}	8.361	8.309	8.28
	$\alpha_{11} = \alpha_{22}$	12.31	12.33	12.36
	$\varepsilon_{11} = \varepsilon_{22}$	31.31	30.94	30.56
Dielectric constants ($\times \varepsilon_0$ C/Vm)	ε_{33}	33.48	34.09	34.88
	$e_{15} = e_{24}$	0.199	0.192	0.187
Piezoelectric constants (C/m ²)	$e_{31} = e_{32}$	-0.0615	-0.061	-0.063
	e_{33}	0.307	0.317	0.332
	$q_{15} = q_{24}$	80.52	225.917	252.77
Piezomagnetic constants (N/Am)	$q_{31} = q_{32}$	277.93	235.29	215.44
	q_{33}	373.63	310.90	280.91
	$\mu_{11} = \mu_{22}$	-71.00	-184.78	-203.62
Magnetic permeability constants ($\times \mu_0$)	μ_{33}	86.81	70.58	63.77
	p_{33}	8.264	7.056	5.49
Pyroelectric constants ($\times 10^{-7}$ C/m ² K)				
Pyromagnetic constants ($\times 10^{-3}$ N/AmK)	τ_{33}	-2.48	-1.64	-1.22

$$\mu_0 = 1.2566 \times 10^{-6} \text{ N/A}^2.$$

$$\varepsilon_0 = 8.85418782 \times 10^{-12} \text{ C/Vm}.$$

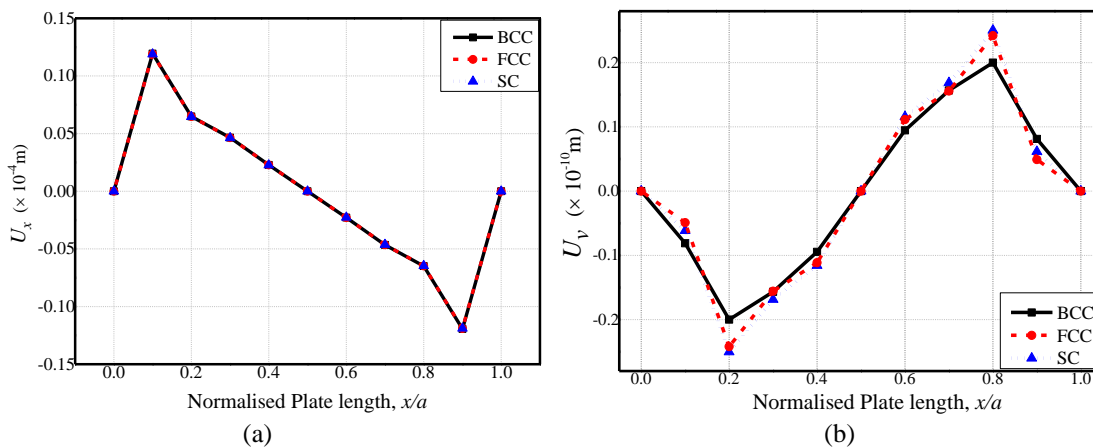
8.3. RESULTS AND DISCUSSIONS

Numerical examination of the multiphysics coupled response of METE plates with arbitrary arranged BaTiO₃/CoFe₂O₄ particulate composite is studied. The FE formulation proposed in Chapter 2 is utilized in this regard. Further, a various illustrations are examined to assess the importance of pyro coupling, boundary conditions and aspect ratio on the static response of METE plates.

8.3.1. Effect of particle arrangement

The influence of various arbitrary positioned BaTiO₃/CoFe₂O₄ particulate composite on the direct and derived quantities of METE plate has been investigated.

To this end, METE plate clamped on all edges (CCCC) and subjected to uniform temperature gradient of 100 K is considered for the analysis. The numerical evaluation demonstrates that only the direct quantities U_v , ϕ and ψ are sensitive to particle arrangement (Figs. 8.3(a) – (e)). It is worthy to note that the influence of SC particulate arrangement is significant on the U_v and ϕ , whereas a marginally higher value of ψ is observed for BCC particle arrangement. This can be attributed to the higher magnitude of piezoelectric and piezomagnetic constants for SC and BCC particle structures, respectively. Figures 8.4(a) and (b) display the variation of normal stress σ_x and shear stress τ_{xz} along the length of METE plate. It is also observed that the particle arrangement has a negligible influence on the stress distribution along the METE plate length. Figures 8.5 and 8.6 depict the electric displacements and magnetic flux densities, respectively. It may be observed from these figures that due to significant difference in the piezoelectric and piezomagnetic constants along the z -direction of various forms of particulate composites, a predominant discrepancy can be observed with respect to D_z and B_z . It may be noted that the METE plates with other boundary conditions (*SSSS*, *CFFC* and *FCFC*) also follow the same trend of the static quantity variation with respect to particle arrangement. Hence, for the sake of brevity, they are discussed in the subsequent section along with the influence of pyroeffects.



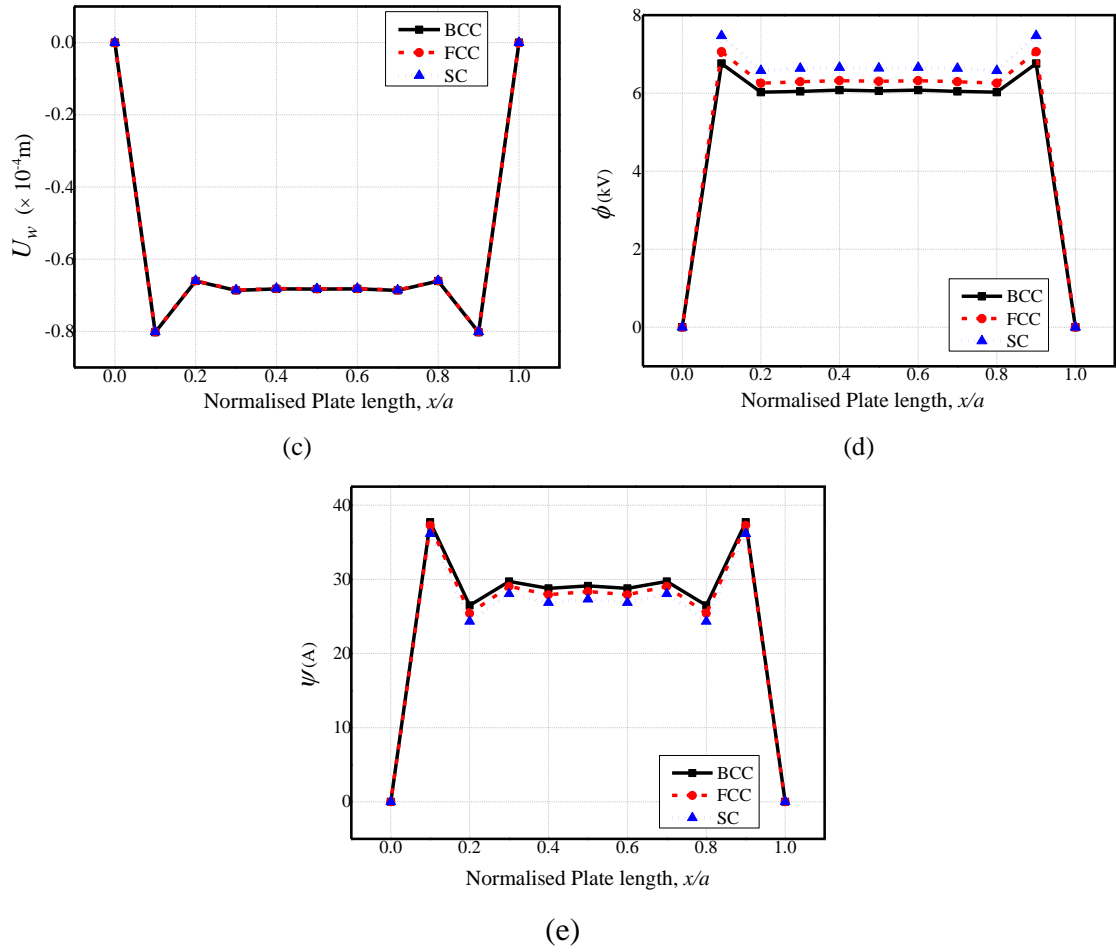


Figure 8.3: Effect of particle arrangement on (a) U_x (b) U_v (c) U_w (d) electric potential ϕ (e) magnetic potential ψ of CCCC METE plate

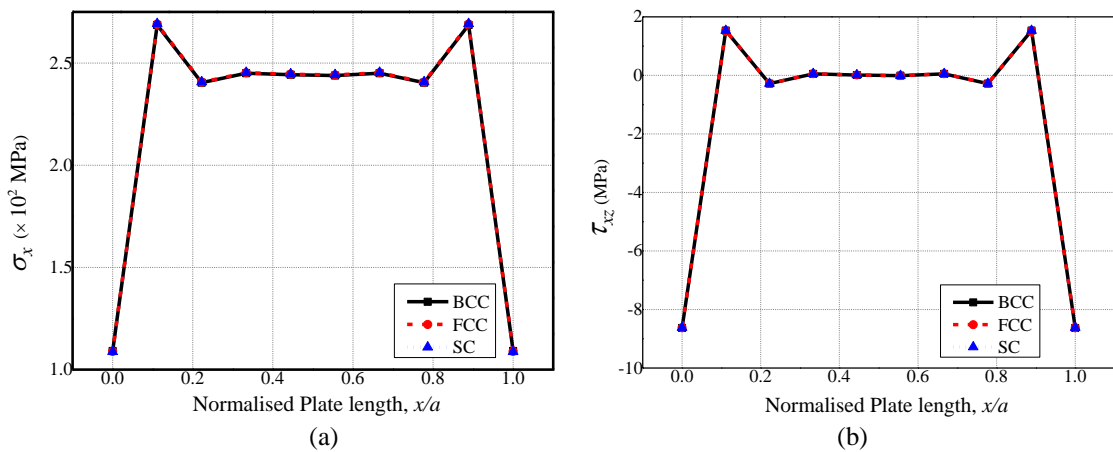


Figure 8.4: Effect of particle arrangement on (a) normal stress σ_x (b) shear stress τ_{xz} of CCCC METE plate

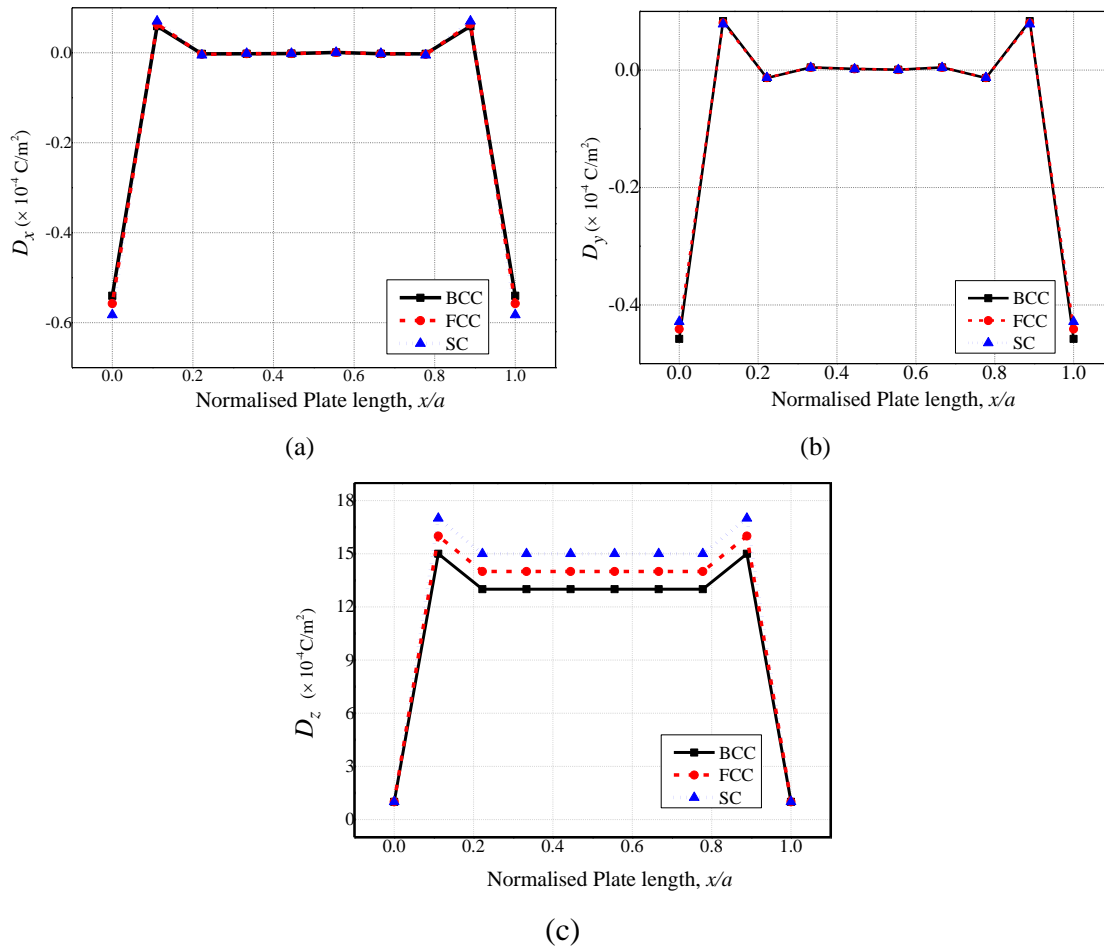
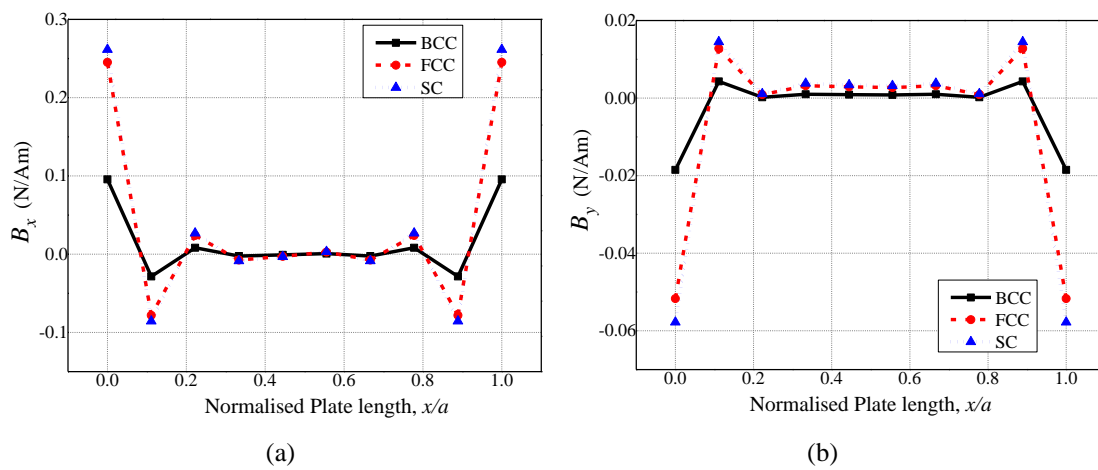
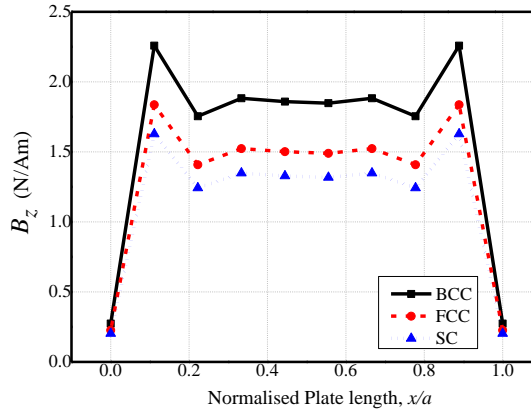


Figure 8.5: Effect of particle arrangement on electric displacements (a) D_x (b) D_y (c)

D_z of CCCC METE plate





(c)

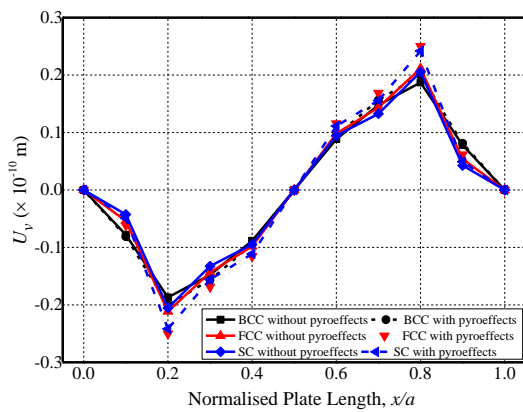
Figure 8.6: Effect of particle arrangement on magnetic flux densities (a) B_x (b) B_y (c) B_z of CCCC METE plate

8.3.2. Influence of pyroeffects and particle arrangement

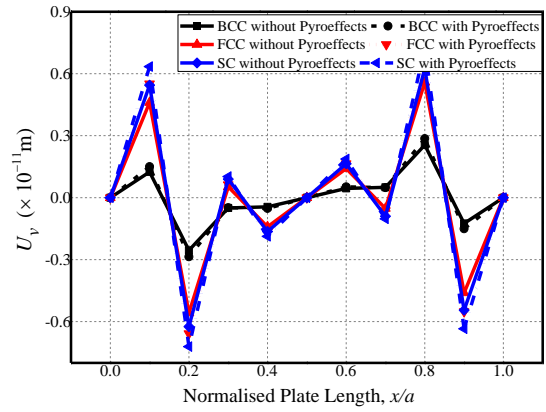
In this section, the pyroelectric and pyromagnetic effects are considered in the analysis through the pyroloads. A uniform temperature gradient of 100 K is applied on the METE plate with different boundary conditions. However, it is learnt from the analysis that the static components such as longitudinal x -direction displacement components U_x , transverse z -direction displacement component U_w , electric displacement components D_x and D_y , magnetic flux density components B_x and B_y experience a meagre influence of pyroelectric and pyromagnetic couplings. Therefore, a comparative study is presented for the variation of the other static parameters with and without pyroeffects. The influence of pyroeffects on the static parameters of METE plates with different particle arrangement and boundary conditions (CCCC, SSSS, CFFC and FCFC) is studied. From Figs. 8.7(a) – (c), it can be noticed that a minute influence of pyroeffects prevails on U_v . Unlike other boundary conditions, CFFC METE plates display a negligible pyroeffect on U_v . In addition, it is found that the SC particle arrangement displays a higher influence. It can also be noted that the U_v has the maximum magnitude near the constrained edge and free edge for the CCCC, SSSS METE plate and CFFC, FCFC METE plates, respectively. Figures 8.8 and 8.9 illustrate the influence of pyroeffects on the electric potential and the magnetic potential, respectively. It is observed from these figures that irrespective of boundary conditions, the pyroeffects tends to increase the electric potential and magnetic potential of the plate due to the direct effect. The values of electric potential and

magnetic potential considering the pyroeffects are compared with the conventional approach (neglecting pyroeffects). Further, it is observed that a higher discrepancy is witnessed for BCC particle arrangement. The reason may be due to the higher magnitude of pyroelectric and pyromagnetic coefficients for the BCC in contrast to the FCC and SC particle arrangement.

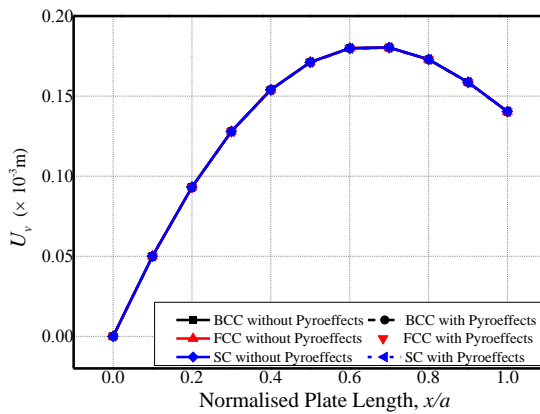
It can be noticed from Figs. 8.8(a) and (b) that for the *CCCC* and *SSSS* METE plate, the electric potential is maximum near the constrained edge and remains almost constant along the plate length, while ϕ drastically reduces at the free end of the *CFFC* METE plate. A symmetric distribution of electric potential is observed for the *FCFC* plate with maximum electric potential appearing at the midspan as shown in Fig. 8.8(d). A similar variation trend is noticed for the *CCCC* and *SSSS* METE plates for the magnetic potential. Analogous to the electric potential, the minimum value of magnetic potential is observed at the midspan of *FCFC* plate. Furthermore, Figs. 8.10 and 8.11 depict the influence of pyro coupling on the variation of D_z and B_z , respectively. These parameters experience the direct effect of electric and magnetic potential, respectively. Therefore, the variation trend remains almost same as that of the electric and magnetic potential. According to Figs. 8.12(a) - (d), it is seen that irrespective of the boundary conditions, the pyroeffects has a negligible impact on the normal stress. It may be due to the fact that the pyroeffects have a negligible indirect effect on the stress components. Table 8.2 elucidates the influence of pyroeffects, boundary conditions and particle arrangement in terms of the maximum values of electric potential, magnetic potential, electric displacement and magnetic flux density. It can be deduced from this table that the pyroeffects are prominent on the BCC particle arrangement followed by FCC and SC arrangement. This may be attributed to the fact that the pyroelectric and pyromagnetic coefficients considered in the present analysis are higher for BCC BaTiO₃/CoFe₂O₄ particulate composite. It can also be noticed that *SSSS* plates display a higher percentage change (Δ) of ϕ and D_z when the pyrocoupling are neglected, whereas for ψ and B_z , *CCCC* METE plates show a predominant influence.



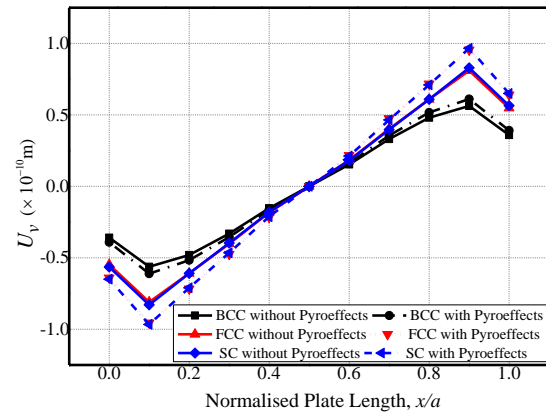
(a) CCCC



(b) SSSS

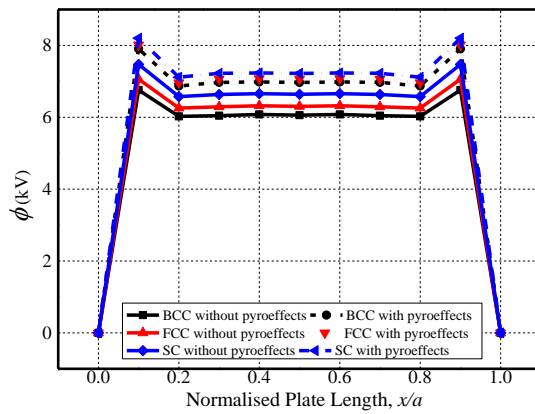


(c) CFFC

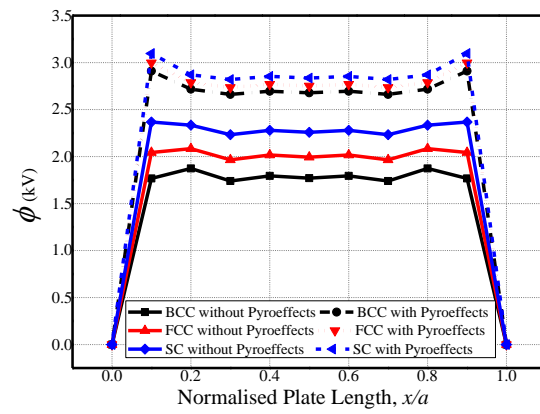


(d) FCFC

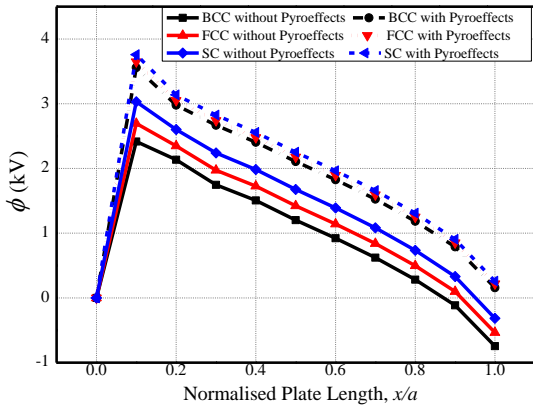
Fig. 8.7: Influence of pyroeffects on displacement component U_v of METE plates



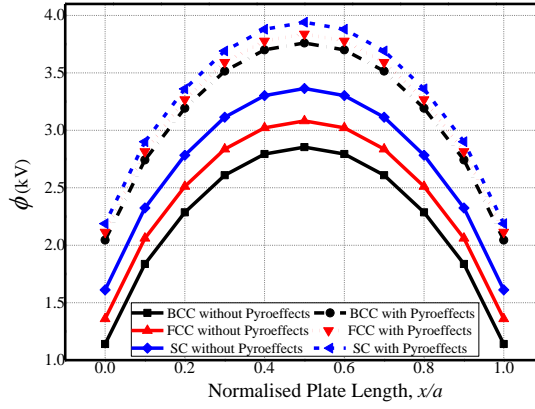
(a) CCCC



(b) SSSS

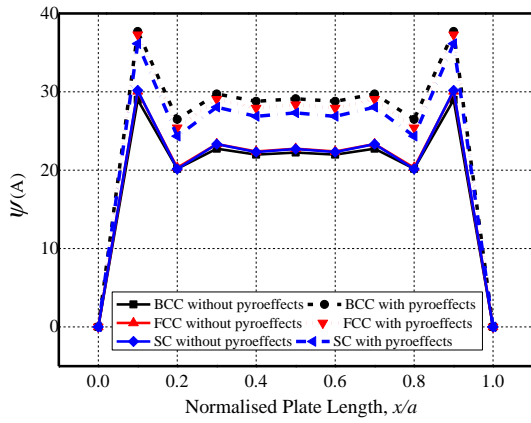


(c) CFCC

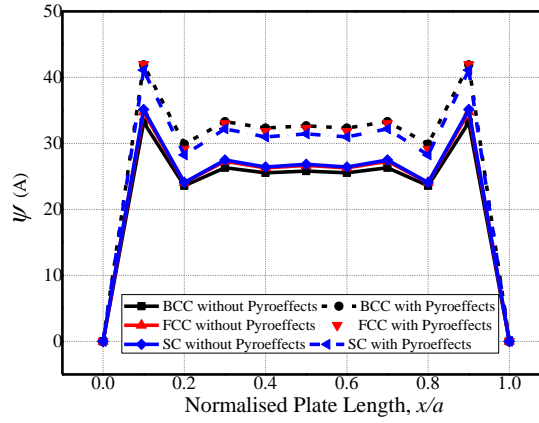


(d) FCFC

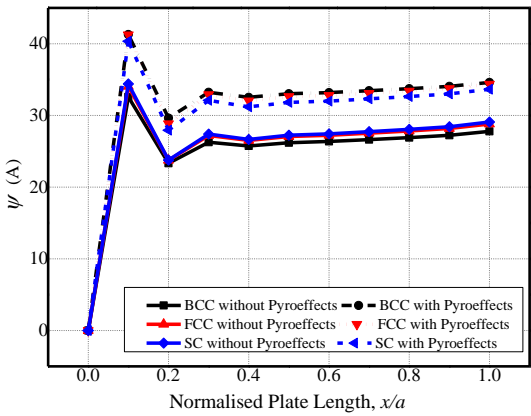
Figure 8.8: Influence of pyroeffects on electric potential of METE plates



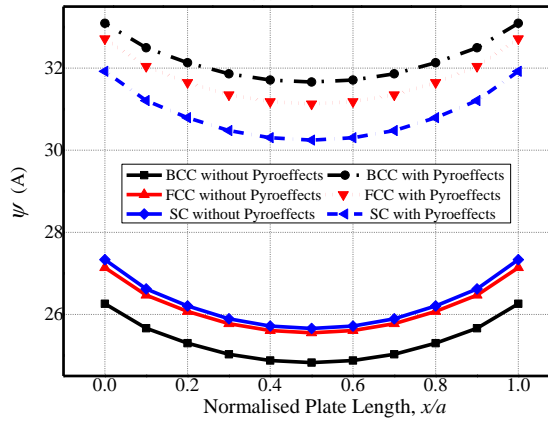
(a) CCCC



(b) SSSS

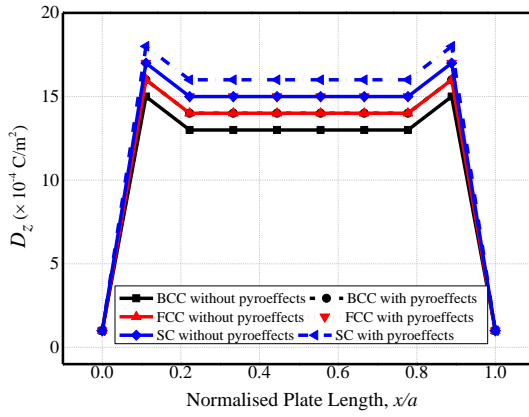


(c) CFCC

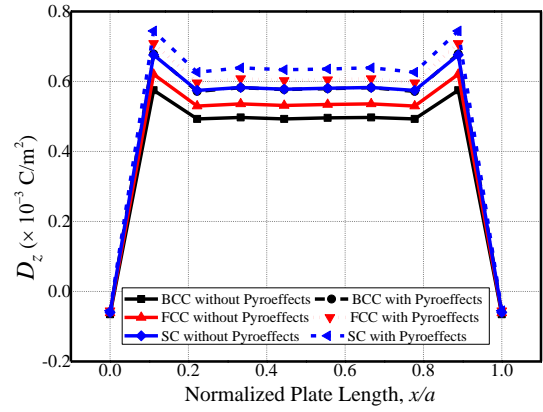


(d) FCFC

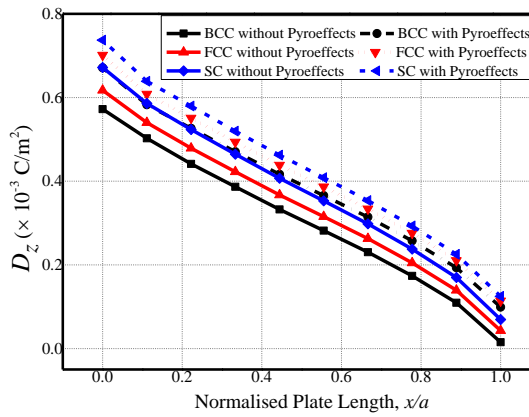
Figure 8.9: Influence of pyroeffects on magnetic potential of METE plates



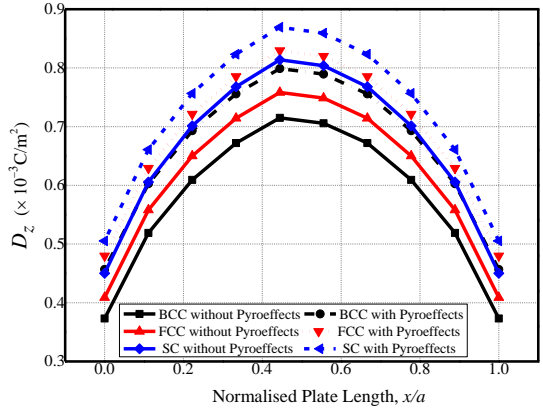
(a) CCCC



(b) SSSS

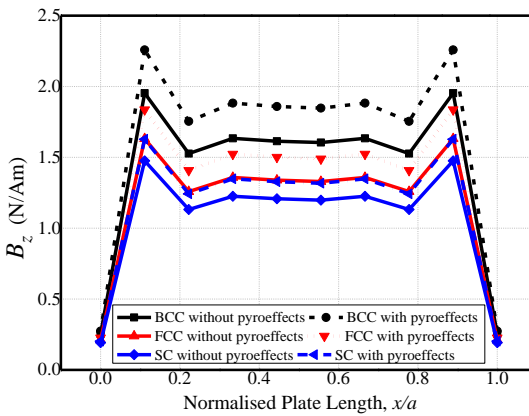


(c) CFFC

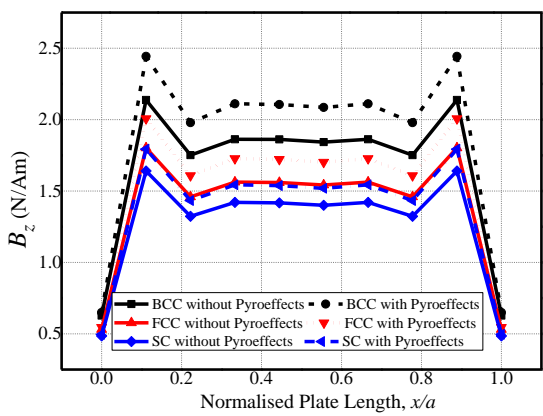


(d) FCFC

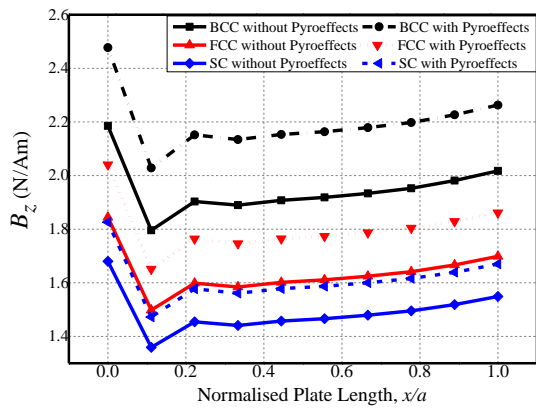
Figure 8.10: Influence of pyroeffects on electric displacement D_z of METE plates



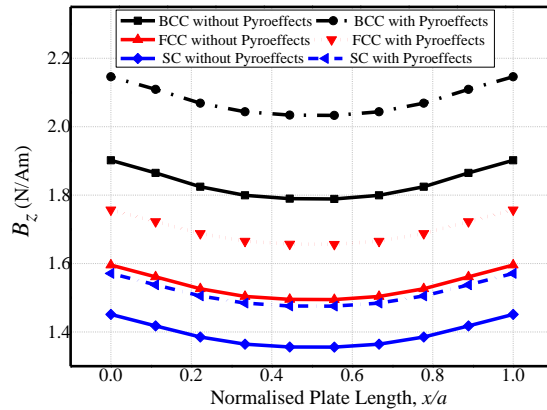
(a) CCCC



(b) SSSS

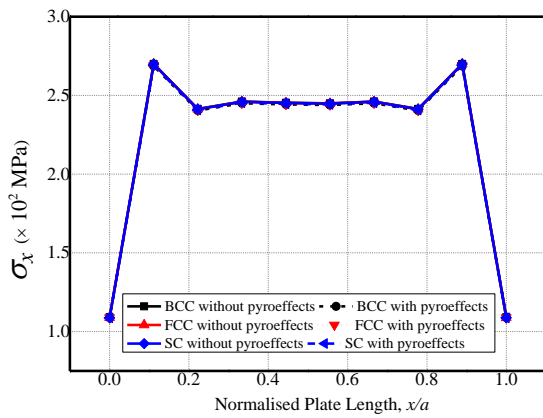


(c) CFCC

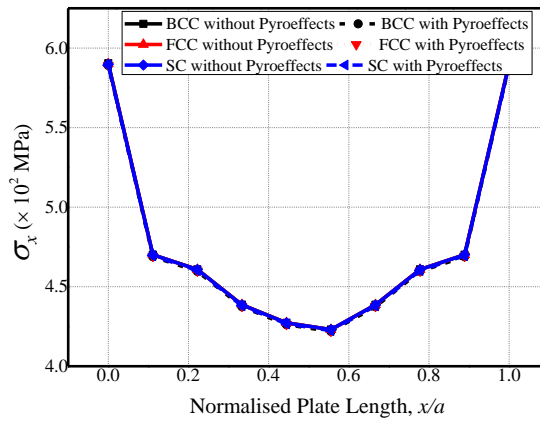


(d) FCFC

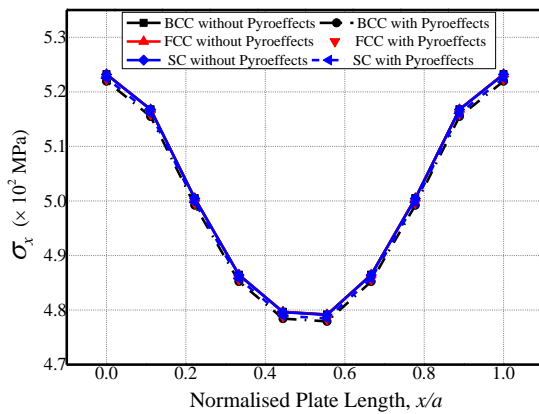
Figure 8.11: Influence of pyroeffects on magnetic flux density B_z of METE plates



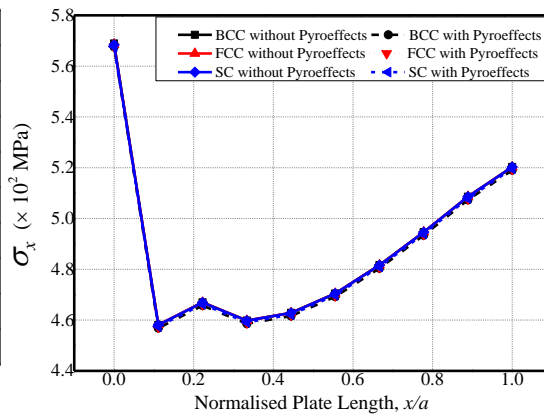
(a) CCCC



(b) SSSS



(c) CFCC



(d) FCFC

Figure 8.12: Influence of pyroeffects on normal stress σ_x of METE plates

Table 8.2: Effect of pyro coupling on electric potential, magnetic potential, electric displacement and magnetic flux density for different boundary conditions and spatial particle arrangement ($a/h = 50$; $a/b = 1$).

Boundary Condition	Particle Arrangement	ϕ_{max} (kV)			ψ_{max} (A)			D_z (10^{-3} C/m ²)			B_z (N/Am)		
		W.P	WoP	Δ	W.P	WoP	Δ	W.P	WoP	Δ	W.P	WoP	Δ
CCCC	BCC	7.90	6.75	14.5	37.7	28.98	23.12	1.6	1.5	6.25	2.29	2.0	12.66
	FCC	8.02	7.06	11.9	37.3	30.06	19.36	1.7	1.6	5.88	1.87	1.67	10.69
	SC	8.20	7.47	8.90	36.1	30.18	16.49	1.8	1.7	5.55	1.66	1.51	9.06
SSSS	BCC	2.91	1.87	35.6	41.90	33.185	20.8	0.68	0.57	15.28	2.49	2.2	11.5
	FCC	3.00	2.08	30.5	41.96	34.75	17.18	0.71	0.62	12.4	2.05	1.86	9.46
	SC	3.10	2.37	23.5	41.10	35.14	14.51	0.74	0.68	9.3	1.84	1.7	7.9
CFFC	BCC	3.56	2.41	32.1	41.29	32.58	21.1	0.67	0.57	14.7	2.48	2.18	11.76
	FCC	3.65	2.70	26.1	41.25	34.05	17.44	0.70	0.61	8.4	2.04	1.84	9.6
	SC	3.76	3.03	19.4	40.35	34.4	14.72	0.74	0.67	8.8	1.82	1.68	8.01
FCFC	BCC	3.76	2.85	24.1	33.09	26.26	20.65	0.8	0.71	10.51	2.15	1.91	11.37
	FCC	3.83	3.08	19.5	32.71	27.14	17.04	0.83	0.76	7.12	1.75	1.59	9.19
	SC	3.94	3.36	14.6	31.9	27.33	14.36	0.87	0.81	6.38	1.57	1.45	7.63

W.P= with pyroeffects; WoP= without pyroeffects; Δ = % change = (W.P-Wo.P)/W.P

8.3.3. Effect of aspect ratio (a/h)

The influence of aspect ratio on the electric and magnetic potential of METE plate under thermal gradient is evaluated for different boundary conditions. The results tabulated in Tables 8.3 and 8.4 represent the maximum electric and the magnetic potential, respectively. These tables reveal that thick METE plates exhibit a predominant influence on the maximum electric potential and magnetic potential. The discrepancies of these parameters reduce as the aspect ratio increases (thin plates).

Table 8.3: Variation of maximum electric potential for different a/h ratio, particle arrangement and boundary conditions

Particle Arrangement	SSSS				CCCC			
	$a/h=5$	$a/h=25$	$a/h=50$	$a/h=100$	$a/h=5$	$a/h=25$	$a/h=50$	$a/h=100$
BCC	22.01	3.77	2.91	0.94	65.1	13.2	7.91	3.4
FCC	25.52	4.23	3.00	1.04	69.3	13.8	8.01	3.55
SC	51.18	4.77	3.01	1.19	90.7	14.5	8.20	3.76
	CFFC				FCFC			
BCC	21.4	4.70	3.55	1.22	26.7	5.71	3.76	1.43
FCC	23.1	5.21	3.64	1.36	36.4	6.16	3.83	1.54
SC	41.0	5.79	3.75	1.53	54.5	6.67	3.94	1.68
	CSCS				CCSS			
BCC	36.01	8.26	4.24	2.46	37.5	7.95	4.08	2.05
FCC	42.06	8.78	4.52	2.28	43.3	8.47	4.36	2.20
SC	62.3	9.46	4.89	2.46	61.5	9.15	4.73	2.38

Table 8.4: Variation of maximum magnetic potential for different a/h ratio, particle arrangement and boundary conditions

Particle arrangement	SSSS				CCCC			
	$a/h=5$	$a/h=25$	$a/h=50$	$a/h=100$	$a/h=5$	$a/h=25$	$a/h=50$	$a/h=100$
BCC	3962	95.78	42.05	20.85	3408.5	84.22	37.71	18.77
FCC	3567	91.86	41.96	20.62	3034.2	81.60	37.28	18.34
SC	2960	85.49	41.9	20.14	2505.4	76.84	36.15	17.71
	CFFC				FCFC			
BCC	5341.2	110.30	41.29	20.55	1071.9	70.50	33.09	16.54
FCC	1182.3	89.34	41.25	20.31	413.30	66.33	32.71	16.33
SC	1180.8	84.129	40.34	19.78	777.80	66.07	31.92	15.96
	CSCS				CCSS			
BCC	3812.2	90.11	39.82	19.50	3809.2	95.09	41.72	20.74
FCC	3417.6	86.75	39.63	18.93	3427.1	91.33	41.46	20.52
SC	2842.7	81.18	38.64	18.43	2824.3	85.04	40.85	20.01

8.4. CONCLUSIONS

In this chapter, the influence of spatial arrangement of BaTiO₃/CoFe₂O₄ particulate composite on static behaviour of METE plates is evaluated. It is evident from the results that the spatial arrangement has a significant effect on the static parameters of METE plates. The electric potential and magnetic potential are predominantly affected by SC and BCC particle arrangement due to higher piezoelectric and piezomagnetic constants, respectively. Also, it is revealed from the study that the pyro coupling tends to improve the electric potential ϕ , magnetic potential ψ , electric displacement D_z and magnetic flux density B_z . Moreover, it is found that among the various particle arrangement considered, BCC displays a higher magnitude of pyroelectric and pyromagnetic coefficients. The influence of pyroeffect on electric potential and electric displacement D_z is found to be greatest for SSSS boundary condition, whereas for magnetic potential and magnetic flux density B_z , it is noticed for CCCC METE plate. Further, it is deduced that the lower aspect ratio shows a predominant effect on the METE plate.

Chapter 9

CONCLUSIONS AND FUTURE SCOPE

This chapter encapsulates the major outcomes of the present research work and the future possible improvements on the analysis of magneto-electro-elastic (MEE) structures in thermal and hygrothermal environment.

9.1. MAJOR FINDINGS

This dissertation imparts the investigation on the effect of external thermal and hygrothermal fields on the coupled response of MEE beams and plates composed of stepped functionally graded stacking sequence and multiphase layers. A three-dimensional finite element formulation has been derived with the aid of total potential energy principle and constitutive equations of MEE solid accounting the coupling between elastic, electric, magnetic, thermal and moisture fields. The in-plane and through thickness temperature distributions are considered. The numerical evaluation suggests that the thermal and hygrothermal fields have a significant influence on the multiphysics response of MEE plates and beams. A special attention has been devoted to evaluate the influence of pyroeffects on the static behaviour of MEE structures.

The numerical investigation on the coupled response of the SFGMEE plates and beams has been carried out. It is observed that the static behaviour of the SFGMEE beams and plates are significantly influenced by the variations of thermal loads across the thickness, and along the length of the beams/plates. The stacking arrangements play the prominent role in deciding the variations of direct and derived quantities. Further, the pyroeffects associated with various load profiles and stacking sequences exhibit considerable influence on the behaviour of the SFGMEE plates and beams. The pronounced effect of aspect ratio, length-to-width ratio and boundary conditions on the displacements, potentials, stresses, electric displacements and magnetic flux density components of the SFGMEE plates has been noticed. It is also observed that the different regions of the SFGMEE beam exhibit different magnitude of static parameters.

The research has also been devoted to evaluate the static response of homogeneous multiphase magneto-electro-elastic beam under various in-plane temperature loading. The MEE beam with the different volume fraction of Barium Titanate and Cobalt Ferrite is taken into consideration. It is found from the parametric study that the remarkable influence of boundary conditions, beam depth ratio, pyroeffects on the direct and derived quantities of the MEE beam.

Further, the multiphysics response of hygrothermo-magneto-electro-elastic (HTMEE) beams and plates are evaluated. The finite element formulation of the HTMEE beams/plates is derived by considering the effect of moisture field in the coupled constitutive equations. The comprehensive analysis reveals that the moisture and temperature dependent elastic stiffness coefficients exhibit a predominant effect on the direct and derived quantities of HTMEE beams and plates. In addition, the HTMEE plates with lower aspect ratio exhibit a higher magnitude of static parameters.

The contribution of various constitutive coupled phases of magneto-electro-thermo-elastic (METE) material towards the stiffness of the METE plates has been investigated. In order to accomplish this, the Hamilton's principle is used by incorporating the first order shear deformation theory. The numerical evaluation revealed that the stiffness of the METE plate for different coupled fields display a considerable discrepancies, and the discrepancies increases for the higher modes. Further investigation reveals that in addition to thermal loads, the other forms of loads such as magnetic and electric loads exhibit a significant effect on the static performance of METE plates. The investigation on the effect of particle arrangement of two phase $\text{BaTiO}_3/\text{CoFe}_2\text{O}_4$ composites is also carried out. The variation of direct and derived quantities along the METE length has been assessed by considering the prominent forms of particle arrangements like body centered cubic (BCC), face centered cubic (FCC) and simple cubic (SC). It is evident from the results that a predominant influence of $\text{BaTiO}_3/\text{CoFe}_2\text{O}_4$ particle arrangement exists on the static behaviour of METE plates.

The major outcomes drawn from the present research work are outlined as follows:

1. Among the various temperature distribution profiles, the uniform temperature distribution exhibits a prominent influence on the SFGMEE beams/plates.
2. The MEE beams/plates with SFG-BFB stacking sequence has a predominant influence on the electric potential and electric displacement, whereas SFG-FBF stacking sequence exhibit a pronounced effect on magnetic potential and magnetic flux densities.
3. The SFGMEE plates with a lower aspect ratio (a/h) results in a higher value of static parameters across the plate thickness.
4. Irrespective of the temperature profiles, the pyroeffects tends to improve the electric potential of the system.
5. In the absence of pyroeffects, bi-triangular temperature profile has a significant reduction in the electric potential of the SFGMEE plates.
6. The influence of pyroeffects decreases with the decrease in aspect ratio of the SFGMEE plate.
7. The displacement components of MEE beam are higher for SFG-BFB stacking sequence than SFG-FBF sequence.
8. The pyroeffects increases the electric potential for Clamped-free and Clamped-simply supported multiphase MEE beam while decreases for Clamped-clamped (C-C) MEE beam.
9. The maximum electric potential exists for the volume fraction of 0.2.
10. The moisture and temperature dependent material stiffness coefficients have a significant influence on the direct and derived quantities of HTMEE beams/plates. Most of the static parameters of HTMEE beams/plates are highest for $\alpha^* = \beta^* = -0.5$, while for $\alpha^* = \beta^* = 2.0$ the normal stresses shows a pronounced effect.
11. Asymmetric boundary condition (CFFC) of HTMEE plate results in the maximum value of the direct quantities.
12. The stiffness matrix corresponding to the thermal phase has a noticeable influence on the natural frequencies of METE plates.

13. Piezoelectric phase tends to improve the stiffness of the METE plate while piezomagnetic phase deteriorates the natural frequency. Further, the coupling coefficients exhibit a predominant effect on the natural frequencies at the higher modes.
14. The electric potential and magnetic potential are predominantly affected by SC and BCC particle arrangement, respectively. Among the various particle arrangement considered, BCC displays a higher magnitude of pyroelectric and pyromagnetic effects.

9.2. SCOPE FOR FUTURE RESEARCH

The basic purpose of this Thesis has been fulfilled by the contributions presented in the preceding chapters of this dissertation. However, there is still scope for further research which facilitates the enhancement of the performance of MEE structures. Among them, few possible future research topics have been outlined as follows:

1. An experimental verification of the proposed coupled finite element model will be handy for future applications of MEE structures in hygrothermal environment.
2. Analysis of magneto-electro-elastic nano structures in thermal environment using Eringen's non-local theory is still an overlooked area.

APPENDIX- A: LIST OF NOTATIONS

B_x, B_y, B_z	Electric displacement components along x, y and z directions
D_x, D_y, D_z	Magnetic flux density components along x, y and z directions
K	Kelvin
L_t, L_ϕ, L_ψ	Differential operators
N	Total number of layers
k	Layer number under consideration
Q^ϕ	Electric charge density
Q^ψ	Magnetic charge density
T_p	Total potential energy of the overall <i>SFGMEE</i> plate
U_x, U_y, U_z	Displacement components along x, y and z directions
V_f	Volume fraction of Barium Titanate (BaTiO_3) and Cobalt Ferrite (CoFe_2O_4)
z	Position of the point of interest from the bottom layer
<i>Matrices and Vectors</i>	
$\{B^k\}$	Magnetic flux density vector
$[B_t], [B_\phi], [B_\psi]$	Derivative of shape function matrices
$[C^k]$	Elastic stiffness matrix
$\{d_t^e\}$	The nodal displacement vector
$\{D^k\}$	Electric displacement vector
$[e^k]$	Piezoelectric coefficient matrix
$\{E^k\}$	Electric field vector
$\{F_{body}\}$	Body force
$\{F_{conc}\}$	Point force
$\{F_{eq}\}$	Equivalent force vector
$\{F_{hy}^g\}$	Global hygrothermal load vector
$\{F_{h.e}^g\}$	Global hygroelectric load vector
$\{F_{h.m}^g\}$	Global hygromagnetic load vector

$\{F_m^e\}, \{F_{t,m}^g\}, \{F_{r,m}^e\}$	Elemental mechanical load vector
$\{F_{p,e}^g\}$	Global pyroelectric load vector
$\{F_{p,m}^g\}$	Global pyromagnetic load vector
$\{F_{surface}\}$	Surface force
$\{F_{th}^g\}$	Global thermal load vector
$\{F_q^g\}$	Global heat flux load vector
$\{F_\phi^g\}$	Elemental electric load vector
$\{F_\psi^g\}$	Elemental magnetic load vector
$\{H^n\}$	Magnetic field vector
$[K_{eq}]$	Equivalent stiffness matrix
$[K_{tt}^g], [K_{rr}^g]$	Global elastic stiffness matrix
$[K_{t\phi}^g], [K_{r\phi}^g]$	Global electro-elastic coupling stiffness matrix
$[K_{t\psi}^g], [K_{r\psi}^g]$	Global magneto-elastic coupling stiffness matrix
$[K_{\phi\phi}^g]$	Global electric stiffness matrix
$[K_{\psi\psi}^g]$	Global magnetic stiffness matrix
$[K_{\phi\psi}^g]$	Global electro-magnetic stiffness matrix
$[m^k]$	Electromagnetic coefficient matrix
$[M_{tt}^g]$	Global mass matrix
$[K_{t\theta}^g], [K_{r\theta}^g]$	Global thermo-elastic stiffness matrix
$[K_{\theta\theta}^g]$	Global thermal stiffness matrix
$[N_t], [N_\phi], [N_\psi]$	Nodal shape function matrices
$\{p^k\}$	Pyroelectric coefficient vector
$[q^k]$	Magnetostrictive coefficient matrix
<i>Greek Symbols</i>	
ϕ	Electric potential
ψ	Magnetic potential

ΔT	Temperature rise
ΔC	Moisture concentration rise
T_{max}	The maximum temperature
T_0	Stress free temperature
T_i	Initial temperature at the bottom layer of SFGMEE plate/beam
$\{\sigma^k\}$	Stress tensor
$\{\lambda^k\}$	Thermal stress tensor
$\{\alpha^k\}$	Thermal expansion coefficient vector
$\{\xi^k\}$	Moisture expansion coefficient vector
$\{\gamma^k\}$	Hygroscopic stress tensor
$\{\chi^k\}$	Hygroelectric coefficient vector
$\{v^k\}$	Hygromagnetic coefficient vector
$\{\varepsilon^k\}$	Strain tensor of the k^{th} layer
$[\eta^k]$	Dielectric constant matrix
$\{\tau^k\}$	Pyromagnetic coefficient vector
$[\mu^k]$	Magnetic permeability constant matrix
$\{\phi^e\}$	The nodal electric potential vector
$\{\psi^e\}$	The nodal magnetic potential vector

APPENDIX-B

The various elemental stiffness matrices associated in attaining the global FE governing equations of fully coupled SFG METE plate (Eq. 7.21) are explicitly presented as follows:

$$\begin{aligned}
\left[K_{tb}^e \right] &= \int_0^{a_e} \int_0^{b_e} [B_{tb}]^T [D_{tb}] [B_{tb}] dx dy, \quad \left[K_{trb}^e \right] = \int_0^{a_e} \int_0^{b_e} [B_{tb}]^T [D_{trb}] [B_{rb}] dx dy, \\
\left[K_{rrb}^e \right] &= \int_0^{a_e} \int_0^{b_e} [B_{rb}]^T [D_{rrb}] [B_{rb}] dx dy, \quad \left[K_{t\phi}^e \right] = \int_0^{a_e} \int_0^{b_e} [B_t]^T [D_{t\phi}] [B_\phi] dx dy \\
\left[K_{t\psi}^e \right] &= \int_0^{a_e} \int_0^{b_e} [B_t]^T [D_{t\psi}] [B_\psi] dx dy, \quad \left[K_{t\theta}^e \right] = \int_0^{a_e} \int_0^{b_e} [B_t]^T [D_{t\theta}] [N_\theta] dx dy, \\
\left[K_{r\phi}^e \right] &= \int_0^{a_e} \int_0^{b_e} [B_r]^T [D_{r\phi}] [B_\phi] dx dy, \quad \left[K_{r\psi}^e \right] = \int_0^{a_e} \int_0^{b_e} [B_r]^T [D_{r\psi}] [B_\psi] dx dy, \\
\left[K_{r\theta}^e \right] &= \int_0^{a_e} \int_0^{b_e} [B_r]^T [D_{r\theta}] [N_\theta] dx dy, \quad \left[K_{\phi\phi}^e \right] = \int_0^{a_e} \int_0^{b_e} [B_\phi]^T [D_{\phi\phi}] [B_\phi] dx dy \\
\left[K_{\phi\psi}^e \right] &= \int_0^{a_e} \int_0^{b_e} [B_\phi]^T [D_{\phi\psi}] [B_\psi] dx dy, \quad \left[K_{\phi\theta}^e \right] = \int_0^{a_e} \int_0^{b_e} [B_\phi]^T [D_{\phi\theta}] [N_\theta] dx dy, \\
\left[K_{\psi\psi}^e \right] &= \int_0^{a_e} \int_0^{b_e} [B_\psi]^T [D_{\psi\psi}] [B_\psi] dx dy, \quad \left[K_{\psi\theta}^e \right] = \int_0^{a_e} \int_0^{b_e} [B_\psi]^T [D_{\psi\theta}] [N_\theta] dx dy, \\
\left[K_{tt}^e \right] &= \left[K_{tb}^e \right] + \left[K_{ts}^e \right], \quad \left[K_{trb}^e \right] = \left[K_{trs}^e \right] + \left[K_{tr}^e \right], \quad \left[K_{rrb}^e \right] = \left[K_{rrs}^e \right] + \left[K_{rr}^e \right] \\
\left[K_{\theta\theta}^e \right] &= \int_0^{a_e} \int_0^{b_e} [N_\theta]^T [D_{\theta\theta}] [N_\theta] dx dy, \quad \left\{ F_{t_m} \right\} = \int_0^{a_e} \int_0^{b_e} [N_t]^T [0 \ 0 \ P_z] dx dy \\
\left\{ F_{r_m} \right\} &= \int_0^{a_e} \int_0^{b_e} [N_r]^T [0 \ 0 \ M_z] dx dy \quad \left\{ F_\phi \right\} = \int_0^{a_e} \int_0^{b_e} [N_\phi]^T [F_e] dx dy \\
\left\{ F_\psi \right\} &= \int_0^{a_e} \int_0^{b_e} [N_\psi]^T [F_m] dx dy, \quad \left\{ F_{\bar{q}} \right\} = \int_0^{a_e} \int_0^{b_e} [N_\theta]^T \bar{q} dx dy
\end{aligned} \tag{B-1}$$

where, the rigidity matrices and vectors are given as follow,

$$\begin{aligned}
[D_{tb}] &= \sum_{k=1}^N \int_{h_k}^{h_{k+1}} [C_b^k] dz, \quad [D_{trb}] = \sum_{k=1}^N \int_{h_k}^{h_{k+1}} z [C_b^k] dz, \quad [D_{t\phi}] = \sum_{k=1}^N \int_{h_k}^{h_{k+1}} [e^k] dz, \\
[D_{t\theta}] &= \sum_{k=1}^N \int_{h_k}^{h_{k+1}} [C_b^k] \{\alpha^k\} dz, \quad [D_{r\theta}] = \sum_{k=1}^N \int_{h_k}^{h_{k+1}} z [C_b^k] \{\alpha^k\} dz, \\
[D_{trs}] &= \sum_{k=1}^N \int_{h_k}^{h_{k+1}} [C_s^k] dz, \quad [D_{t\psi}] = \sum_{k=1}^N \int_{h_k}^{h_{k+1}} [q^k] dz, \\
[D_{rrb}] &= \sum_{k=1}^N \int_{h_k}^{h_{k+1}} z^2 [C_b^k] dz, \quad [D_{r\phi}] = \sum_{k=1}^N \int_{h_k}^{h_{k+1}} z [e^k] dz, \\
[D_{r\psi}] &= \sum_{k=1}^N \int_{h_k}^{h_{k+1}} z [q^k] dz, \quad [D_{\phi\phi}] = \sum_{k=1}^N \int_{h_k}^{h_{k+1}} [d^k] dz, \\
[D_{\phi\psi}] &= \sum_{k=1}^N \int_{h_k}^{h_{k+1}} [m^k] dz, \quad [D_{\phi\theta}] = \sum_{k=1}^N \int_{h_k}^{h_{k+1}} [p_e^k] dz, \\
[D_{\psi\psi}] &= \sum_{k=1}^N \int_{h_k}^{h_{k+1}} [\mu^k] dz, \quad [D_{\psi\theta}] = \sum_{k=1}^N \int_{h_k}^{h_{k+1}} [p_m^k] dz, \\
[D_{\theta\theta}] &= \sum_{k=1}^N \int_{h_k}^{h_{k+1}} C_h dz, \tag{B-2}
\end{aligned}$$

APPENDIX - C

The condensation technique used for solving Eq. (7.21) is as follow,

$$\begin{aligned}
[K_1] &= [K_{t\psi}^g]^T - [K_{\psi\theta}^g] [K_{\theta\theta}^g]^{-1} [K_{t\theta}^g]^T, \\
[K_2] &= [K_{r\psi}^g]^T - [K_{\psi\theta}^g] [K_{\theta\theta}^g]^{-1} [K_{r\theta}^g]^T, \\
[K_3] &= [K_{\phi\psi}^g]^T - [K_{\psi\theta}^g] [K_{\theta\theta}^g]^{-1} [K_{\phi\theta}^g]^T, \\
[K_4] &= [K_{\psi\psi}^g]^T - [K_{\psi\theta}^g] [K_{\theta\theta}^g]^{-1} [K_{\psi\theta}^g]^T, \\
[K_5] &= [K_4]^{-1} [K_1], \quad [K_6] = [K_4]^{-1} [K_2], \quad [K_7] = [K_4]^{-1} [K_3], \\
[K_0] &= [K_4]^{-1} [K_{\psi\theta}^g] [K_{\theta\theta}^g], \quad [K_8] = [K_{t\phi}^g]^T - [K_{\phi\theta}^g] [K_{\theta\theta}^g]^{-1} [K_{t\theta}^g]^T,
\end{aligned}$$

$$\begin{aligned}
[K_9] &= [K_{r\phi}^g]^T - [K_{\phi\theta}^g][K_{\theta\theta}^g]^{-1}[K_{r\theta}^g]^T, \\
[K_{10}] &= [K_{\phi\phi}^g]^T - [K_{\phi\theta}^g][K_{\theta\theta}^g]^{-1}[K_{\phi\theta}^g]^T, \\
[K_{11}] &= [K_{\phi\psi}^g]^T - [K_{\phi\theta}^g][K_{\theta\theta}^g]^{-1}[K_{\psi\theta}^g]^T, [K_{12}] = [K_8] - [K_{11}][K_5], \\
[K_{13}] &= [K_9] - [K_{11}][K_6], [K_{14}] = [K_{10}] + [K_{11}][K_7], \\
[K_{15}] &= [K_{14}]^{-1}[K_{12}], \\
[K_{16}] &= [K_{14}]^{-1}[K_{13}], [K_{17}] = [K_{14}]^{-1}[K_{11}][K_4]^{-1}, \\
[K_{18}] &= [K_{14}]^{-1}[K_{\phi\theta}^g][K_{\theta\theta}^g]^{-1} - [K_{14}]^{-1}[K_{11}][K_0], \\
[K_{19}] &= [K_{tr}^g]^T + [K_{r\theta}^g][K_{\theta\theta}^g]^{-1}[K_{t\theta}^g]^T, \\
[K_{20}] &= [K_{rr}^g]^T + [K_{r\theta}^g][K_{\theta\theta}^g]^{-1}[K_{r\theta}^g]^T, \\
[K_{21}] &= [K_{r\phi}^g]^T - [K_{r\theta}^g][K_{\theta\theta}^g]^{-1}[K_{\phi\theta}^g]^T, \\
[K_{22}] &= [K_{r\psi}^g]^T - [K_{r\theta}^g][K_{\theta\theta}^g]^{-1}[K_{\psi\theta}^g]^T, [K_{23}] = [K_{19}] + [K_{22}][K_5], \\
[K_{24}] &= [K_{20}] + [K_{22}][K_6], [K_{25}] = [K_{21}] + [K_{22}][K_7], \\
[K_{26}] &= [K_{22}][K_4]^{-1}, [K_{27}] = [K_{r\theta}][K_{\theta\theta}]^{-1} - [K_{22}][K_0], \\
[K_{28}] &= [K_{23}] + [K_{25}][K_{15}], [K_{29}] = [K_{24}] + [K_{25}][K_{16}], \\
[K_{30}] &= -[K_{29}]^{-1}[K_{28}], \\
[K_{31}] &= [K_{29}]^{-1}([K_{26}] - [K_{25}][K_{17}]), [K_{32}] = [K_{29}]^{-1}[K_{25}][K_{14}]^{-1}, \\
[K_{33}] &= [K_{29}]^{-1}([K_{27}] - [K_{25}][K_{18}]), \\
[K_{34}] &= [K_{tt}^g]^T + [K_{t\theta}^g][K_{\theta\theta}^g]^{-1}[K_{t\theta}^g]^T, \\
[K_{35}] &= [K_{tr}^g]^T + [K_{t\theta}^g][K_{\theta\theta}^g]^{-1}[K_{r\theta}^g]^T, \\
[K_{36}] &= [K_{t\phi}^g]^T - [K_{t\theta}^g][K_{\theta\theta}^g]^{-1}[K_{\phi\theta}^g]^T, \\
[K_{37}] &= [K_{t\psi}^g]^T - [K_{t\theta}^g][K_{\theta\theta}^g]^{-1}[K_{\psi\theta}^g]^T, [K_{38}] = [K_{34}] + [K_{37}][K_5], \\
[K_{39}] &= [K_{35}] + [K_{37}][K_6],
\end{aligned}$$

$$\begin{aligned}
[K_{40}] &= [K_{36}] + [K_{37}][K_7], [K_{41}] = [K_{t\theta}^g][K_{\theta\theta}^g]^{-1} - [K_{37}][K_0], \\
[K_{42}] &= [K_{37}][K_4]^{-1} \\
[K_{43}] &= [K_{38}] + [K_{40}][K_{15}], [K_{44}] = [K_{39}] + [K_{40}][K_{16}], \\
[K_{45}] &= [K_{42}] - [K_{40}][K_{17}], \\
[K_{46}] &= [K_{41}] - [K_{40}][K_{18}], [K_{47}] = [K_{40}][K_{14}]^{-1}, \\
[K_{48}] &= [K_{43}] + [K_{44}][K_{30}], \\
[K_{49}] &= [K_{45}] - [K_{44}][K_{31}], [K_{50}] = [K_{46}] - [K_{44}][K_{33}], \\
[K_{51}] &= [K_{47}] - [K_{44}][K_{32}], [K_{52}] = -[K_{44}][K_{29}]^{-1}, \\
[K_{eq}] &= [K_{48}], \\
\{F_{eq}^g\} &= [K_{49}]\{F_{\psi}^g\} + [K_{50}]\{F_{\theta}^g\} + [K_{51}]\{F_{\phi}^g\} - [K_{52}]\{F_{r_m}^g\} + \{F_{t_m}^g\}
\end{aligned} \tag{C-1}$$

APPENDIX - D

The effect of ϕ can be deduced as follows:

$$\begin{aligned}
[K_{tt}^e]\{dt^e\} + [K_{tr}^e]\{dr^e\} + [K_{t\phi}^e]\{\phi^e\} &= 0 \\
[K_{tr}^e]^T\{dt^e\} + [K_{rr}^e]\{dr^e\} + [K_{r\phi}^e]\{\phi^e\} &= 0 \\
[K_{t\phi}^e]^T\{dt^e\} + [K_{r\phi}^e]^T\{dr^e\} - [K_{\phi\phi}^e]\{\phi^e\} &= 0 \\
\{\phi^e\} &= [K_{\phi\phi}^e]^{-1}[K_{t\phi}^e]\{dt^e\} + [K_{\phi\phi}^e]^{-1}[K_{r\phi}^e]\{dr^e\} \\
[K_{tr}^e]\{dt^e\} + [K_{rr}^e]\{dr^e\} + [K_{r\phi}^e][K_{\phi\phi}^e]^{-1}[K_{t\phi}^e]\{dt^e\} + \\
[K_{r\phi}^e][K_{\phi\phi}^e]^{-1}[K_{r\phi}^e]\{dr^e\} & \\
\{dt^e\}\left[[K_{tr}^e] + [K_{r\phi}^e][K_{\phi\phi}^e]^{-1}[K_{t\phi}^e]\right] + \{dr^e\}[K_{rr}^e] + \\
\{dr^e\}[K_{r\phi}^e][K_{\phi\phi}^e]^{-1}[K_{r\phi}^e] & \\
[K_{\phi\phi_1}^e]\{dt^e\} + [K_{\phi\phi_2}^e]\{dr^e\} &= 0 \\
\{dr^e\} &= -[K_{\phi\phi_2}^e]^{-1}[K_{\phi\phi_1}^e]\{dt^e\}
\end{aligned}$$

$$\begin{aligned}
& \left[K_{tt}^e \right] \left\{ dt^e \right\} + \left[K_{tr}^e \right] \left\{ dr^e \right\} + \left[K_{t\phi}^e \right] \left[K_{\phi\phi} \right]^{-1} \left[K_{t\phi}^e \right] \left\{ dt^e \right\} + \\
& \left[K_{t\phi}^e \right] \left[K_{\phi\phi} \right]^{-1} \left[K_{r\phi}^e \right] \left\{ dr^e \right\} = 0 \\
& \left\{ dt^e \right\} \left[\left[K_{tt}^e \right] + \left[K_{t\phi}^e \right] \left[K_{\phi\phi} \right]^{-1} \left[K_{t\phi}^e \right] \right] + \left\{ dr^e \right\} \left[K_{tr}^e \right] \\
& + \left\{ dr^e \right\} \left[K_{t\phi}^e \right] \left[K_{\phi\phi} \right]^{-1} \left[K_{r\phi}^e \right] = 0 \\
& \left[K_{\phi\phi-3} \right] \left\{ dt^e \right\} + \left[K_{\phi\phi-4} \right] \left\{ dr^e \right\} = 0 \\
& \left[K_{\phi\phi-3} \right] \left\{ dt^e \right\} - \left[K_{\phi\phi-4} \right] \left[K_{\phi\phi-2} \right]^{-1} \left[K_{\phi\phi-1} \right] \left\{ dt^e \right\} = 0 \\
& \left[K_{\phi\phi-eq} \right] = \left[K_{\phi\phi-3} \right] - \left[K_{\phi\phi-4} \right] \left[K_{\phi\phi-2} \right]^{-1} \left[K_{\phi\phi-1} \right] \\
& \left[K_{\phi\phi-1} \right] = \left[K_{tr}^e \right] + \left[K_{r\phi}^e \right] \left[K_{\phi\phi} \right]^{-1} \left[K_{t\phi}^e \right] \\
& \left[K_{\phi\phi-2} \right] = \left[K_{rr}^e \right] + \left[K_{r\phi}^e \right] \left[K_{\phi\phi} \right]^{-1} \left[K_{r\phi}^e \right] \\
& \left[K_{\phi\phi-3} \right] = \left[K_{tt}^e \right] + \left[K_{t\phi}^e \right] \left[K_{\phi\phi} \right]^{-1} \left[K_{t\phi}^e \right] \\
& \left[K_{\phi\phi-4} \right] = \left[K_{tr}^e \right] + \left[K_{t\phi}^e \right] \left[K_{\phi\phi} \right]^{-1} \left[K_{r\phi}^e \right]
\end{aligned} \tag{D-1}$$

The effect of ψ can be deduced as follows:

$$\begin{aligned}
& \left[K_{tt}^e \right] \left\{ dt^e \right\} + \left[K_{tr}^e \right] \left\{ dr^e \right\} + \left[K_{t\psi}^e \right] \left\{ \psi^e \right\} = 0 \\
& \left[K_{tr}^e \right]^T \left\{ dt^e \right\} + \left[K_{rr}^e \right] \left\{ dr^e \right\} + \left[K_{r\psi}^e \right] \left\{ \psi^e \right\} = 0 \\
& \left[K_{t\psi}^e \right]^T \left\{ dt^e \right\} + \left[K_{r\phi}^e \right]^T \left\{ dr^e \right\} - \left[K_{\psi\psi}^e \right] \left\{ \psi^e \right\} = 0 \\
& \left[K_{eq-\psi\psi} \right] = \left[K_{\psi\psi-3} \right] - \left[K_{\psi\psi-4} \right] \left[K_{\psi\psi-2} \right]^{-1} \left[K_{\psi\psi-1} \right] \\
& \left[K_{\psi\psi-1} \right] = \left[K_{tr}^e \right] + \left[K_{r\psi}^e \right] \left[K_{\psi\psi} \right]^{-1} \left[K_{t\psi}^e \right] \\
& \left[K_{\psi\psi-2} \right] = \left[K_{rr}^e \right] + \left[K_{r\psi}^e \right] \left[K_{\psi\psi} \right]^{-1} \left[K_{r\psi}^e \right] \\
& \left[K_{\psi\psi-3} \right] = \left[K_{tt}^e \right] + \left[K_{t\psi}^e \right] \left[K_{\psi\psi} \right]^{-1} \left[K_{t\psi}^e \right] \\
& \left[K_{\psi\psi-4} \right] = \left[K_{tr}^e \right] + \left[K_{t\psi}^e \right] \left[K_{\psi\psi} \right]^{-1} \left[K_{r\psi}^e \right]
\end{aligned}$$

$$\begin{aligned}
\{\psi^e\} &= [K_{\psi\psi}]^{-1} [K_{t\psi}^e] \{dt^e\} + [K_{\psi\psi}]^{-1} [K_{r\psi}^e] \{dr^e\} \\
\{dr^e\} &= -[K_{\psi\psi_{-2}}]^{-1} [K_{\psi\psi_{-1}}] \{dt^e\}
\end{aligned} \tag{D-2}$$

The effect of θ can be deduced as follows:

$$\begin{aligned}
[K_{tt}^e] \{dt^e\} + [K_{tr}^e] \{dr^e\} + [K_{t\theta}^e] \{\theta^e\} &= 0 \\
[K_{tr}^e]^T \{dt^e\} + [K_{rr}^e] \{dr^e\} + [K_{r\theta}^e] \{\theta^e\} &= 0 \\
[K_{t\theta}^e]^T \{dt^e\} + [K_{r\theta}^e]^T \{dr^e\} - [K_{\theta\theta}^e] \{\theta^e\} &= 0 \\
[K_{eq_{-\theta\theta}}] &= [K_{\theta\theta_{-3}}] - [K_{\theta\theta_{-4}}] [K_{\theta\theta_{-2}}]^{-1} [K_{\theta\theta_{-1}}] \\
[K_{\theta\theta_{-1}}] &= [K_{tr}^e] + [K_{r\theta}^e] [K_{\theta\theta}]^{-1} [K_{t\theta}^e] \\
[K_{\theta\theta_{-2}}] &= [K_{rr}^e] + [K_{r\theta}^e] [K_{\theta\theta}]^{-1} [K_{r\theta}^e] \\
[K_{\theta\theta_{-3}}] &= [K_{tt}^e] + [K_{t\theta}^e] [K_{\theta\theta}]^{-1} [K_{t\theta}^e] \\
[K_{\theta\theta_{-4}}] &= [K_{tr}^e] + [K_{t\theta}^e] [K_{\theta\theta}]^{-1} [K_{r\theta}^e] \\
\{\theta^e\} &= [K_{\theta\theta}]^{-1} [K_{t\theta}^e] \{dt^e\} + [K_{\theta\theta}]^{-1} [K_{r\theta}^e] \{dr^e\} \\
\{dr^e\} &= -[K_{\theta\theta_{-2}}]^{-1} [K_{\theta\theta_{-1}}] \{dt^e\}
\end{aligned} \tag{D-3}$$

REFERENCES

- Aboudi, J. (2001). "Micromechanical analysis of fully coupled electro-magneto-thermo-elastic multiphase composites". *Smart materials and Structures*, **10**(5), 867.
- Ahmad, S.N., Upadhyay, C.S. and Venkatesan, C. (2006). "Electro-thermo-elastic formulation for the analysis of smart structures". *Smart Materials and Structures*, **15**(2), 401.
- Akbarzadeh, A.H and Chen, Z.T. (2012). "Magneto-electroelastic behaviour of rotating cylinders resting on an elastic foundation under hygrothermal loading". *Smart Materials and Structures*, **2**, 125013.
- Akbarzadeh, A.H. and Chen, Z.T. (2013). "Hygrothermal stresses in one dimensional functionally graded piezoelectric media in constant magnetic field". *Composite Structures*, **97**, 317-31.
- Akbarzadeh, A.H. and Pasini, D. (2014). "Multiphysics of multilayered and functionally graded cylinders under prescribed hygrothermo magneto electromechanical loading". *Journal of Applied Mechanics*, **81**, 041018.
- Alashti, R.A. and Khorsand, M. (2011). "Three-dimensional thermo-elastic analysis of a functionally graded cylindrical shell with piezoelectric layers by differential quadrature method". *International Journal of Pressure Vessels and Piping*, **88**(5), 167-180.
- Alibeigloo, A. (2011). "Thermoelastic solution for static deformations of functionally graded cylindrical shell bonded to thin piezoelectric layers". *Composite Structures*, **93**(2), 961-972.
- Allam, M.N.M., Zenkour, A.M. and Tantawy, R. (2014). "Analysis of functionally graded piezoelectric cylinders in a hygrothermal environment". *Advances in Applied Mathematics and Mechanics*, **6**(2), 233-246.
- Allam, M.N.M., Tantawy, R. and Zenkour, A.M. (2016). "Semi-empirical and efficient solutions for FGPM hollow spheres in hygrothermal environment". *KSCE Journal of Civil Engineering*, **20**(5), 1958-1965.
- Altay, G. A. and Dokmeci, M. C. (2000). "Some Hamiltonian-type variational principles for motions of a hygrothermoelastic medium", *Journal of Thermal Stresses*. **23**, 273–284.
- Altay, G. and Dokmeci, M. C. (2007). "Variational principles for piezoelectric, thermopiezoelectric, and hygrothermopiezoelectric continua revisited", *Mechanics of Advanced Materials and Structures*. **14**, 549–562.

Altay, G. A. and Dokmeci, M. C. (2008). "Certain Hygrothermopiezoelectric Multi-Field Variational Principles for Smart Elastic Laminae". *Mechanics of Advanced Materials and Structures*, **15**(1), 21-32.

Annigeri, A.R., Ganesan, N. and Swarnamani, S. (2006a). "Free vibrations of clamped-clamped magneto-electro-elastic cylindrical shells". *Journal of Sound and Vibration*, **292**(1), 300-314.

Annigeri, A.R., Ganesan, N. and Swarnamani, S. (2006b). "Free vibrations of simply supported layered and multiphase magneto-electro-elastic cylindrical shells. *Smart Materials and Structures*, **15**(2), 459.

Annigeri, A.R., Ganesan, N. and Swarnamani, S. (2007). "Free vibration behaviour of multiphase and layered magneto-electro-elastic beam". *Journal of Sound and Vibration*, **299**(1), 44-63.

Ansari, R., Hasrati, E., Gholami, R. and Sadeghi, F. (2015a). "Nonlinear analysis of forced vibration of nonlocal third-order shear deformable beam model of magneto-electro-thermo elastic nanobeams". *Composites Part B: Engineering*, **83**, 226-241.

Ansari, R., Gholami, R. and Rouhi, H. (2015b). "Size-dependent nonlinear forced vibration analysis of magneto-electro-thermo-elastic Timoshenko nanobeams based upon the nonlocal elasticity theory". *Composite Structures*, **126**, 216-226.

Ansari, R. and Gholami, R. (2016a). Nonlocal free vibration in the pre-and post-buckled states of magneto-electro-thermo elastic rectangular nanoplates with various edge conditions. *Smart Materials and Structures*, **25**(9), 095033.

Ansari, R. and Gholami, R., (2016b). "Nonlocal nonlinear first-order shear deformable beam model for post-buckling analysis of magneto-electro-thermo-elastic nanobeams". *Scientia Iranica. Transaction F, Nanotechnology*, **23**(6), 3099.

Ansari, R. and Gholami, R. (2016c). "Size-dependent nonlinear vibrations of first-order shear deformable magneto-electro-thermo elastic nanoplates based on the nonlocal elasticity theory". *International Journal of Applied Mechanics*, **8**(4), 1650053.

Ansari, R. and Gholami, R. (2017). "Size-dependent buckling and postbuckling analyses of first-order shear deformable magneto-electro-thermo elastic nanoplates based on the nonlocal elasticity theory". *International Journal of Structural Stability and Dynamics*, **17**(01), 1750014.

Arani, A.G., Maraghi, Z.K., Mozdianfard, M.R. and Shajari, A.R. (2010). "Thermo-piezo-magneto-mechanical stresses analysis of FGPM hollow rotating thin disk". *International Journal of Mechanics and Materials in Design*, **6**(4), 341-349.

Arefi, M. and Zenkour, A.M. (2016). “Employing sinusoidal shear deformation plate theory for transient analysis of three layers sandwich nanoplate integrated with piezo-magnetic face-sheets”. *Smart Materials and Structures*, **25**(11), 115040.

Arefi, M. and Zenkour, A.M. (2017a). “Thermo-electro-magneto-mechanical bending behaviour of size-dependent sandwich piezomagnetic nanoplates”. *Mechanics Research Communications*. **84**, 27-42.

Arefi, M. and Zenkour, A.M. (2017b). “Size-dependent free vibration and dynamic analyses of piezo-electro-magnetic sandwich nanoplates resting on viscoelastic foundation”. *Physica B: Condensed Matter*, **521**, 188-197.

Babaei, M.H. and Chen, Z.T. (2008). “Analytical solution for the electromechanical behaviour of a rotating functionally graded piezoelectric hollow shaft”. *Archive of Applied Mechanics*, **78**(7), 489-500.

Bacigalupo, A., Morini, L. and Piccolroaz, A. (2016). “Multiscale asymptotic homogenization analysis of thermo-diffusive composite materials”. *International Journal of Solids and Structures*, **85**, 15-33.

Badri, T.M. and Al-Kayiem, H.H. (2013). “Analytical solution for simply supported and multilayered Magneto-Electro-Elastic Plates”. *Asian journal of scientific research*, **6**, 236-244.

Bakkali, A., Azrar, L. and Aljinaidi, A.A. (2016). “Viscomagnetoelastic effective properties’ modeling for multi-phase and multi-coated magnetoelastic composites”. *Journal of Intelligent Material Systems and Structures*, **27**(16), 2261-2286.

Barati, M.R., Zenkour, A.M. and Shahverdi, H. (2016). “Thermo-mechanical buckling analysis of embedded nanosize FG plates in thermal environments via an inverse cotangential theory”. *Composite Structures*, **141**, 203-212.

Barati, A.R. and Jabbari, M. (2015). “Two-dimensional piezothermoelastic analysis of a smart FGM hollow sphere”. *Acta Mechanica*, **226**(7), 2195.

Bhangale, R.K. and Ganesan, N. (2005). “Free vibration studies of simply supported non-homogeneous functionally graded magneto-electro-elastic finite cylindrical shells”. *Journal of Sound and Vibration*, **288**(1), 412-422.

Bhangale, R.K. and Ganesan, N. (2006). “Static analysis of simply supported functionally graded and layered magneto-electro-elastic plates”. *International Journal of Solids and Structures*, **43**(10), 3230-3253.

Biju, B., Ganesan, N. and Shankar, K. (2009). “Finite element formulation using magnetic vector potential approach: effects of displacement current in magneto-electro-elastic cylindrical shells”. *Smart Materials and Structures*, **19**(1), 015009.

Biju, B., Ganesan, N. and Shankar, K. (2010). "Harmonic Response of Magneto-electro-elastic Sensors Bonded to Cylindrical Shells". *Sensors & Transducers*, **116**(5), 89.

Biju, B., Ganesan, N., Shankar, K. and Hyde, T.H. (2010). "The transient dynamic response of multiphase magneto-electroelastic sensors bonded to a shell structure". *Proceedings of the Institution of Mechanical Engineers, Part L: Journal of Materials: Design and Applications*, **224**(3), 123-132.

Biju, B., Ganesan, N. and Shankar, K. (2011). "Dynamic response of multiphase magneto-electroelastic sensors using 3D magnetic vector potential approach". *IEEE Sensors Journal*, **11**(9), 2169-2176.

Biju, B., Ganesan, N. and Shankar, K. (2012). "Dynamic analysis of magneto-electro-elastic cylindrical shells by quasi-static and fully dynamic electromagnetic theories". *Multidiscipline Modeling in Materials and Structures*, **8**(3), 403-416.

Boonphennimit, P., Rungamornrat, J. and Senjuntichai, T. (2013). "Thermo-Electro-Mechanical Behaviour of Finite Piezocomposites Cylinder". *Advanced Materials Research*, **740**, 368-373.

Bravo-Castillero, J., Rodríguez-Ramos, R., Mechkour, H., Otero, J.A., Cabanas, J.H., Sixto, L., Guinovart-Díaz, R. and Sabina, F.J. (2009). "Homogenization and effective properties of periodic thermomagneto-electroelastic composites". *Journal of Mechanics of Materials and Structures*, **4**(5), 819-836.

Brischetto, S. (2013). "Hygrothermoelastic analysis of multilayered composite and sandwich shells". *Journal of Sandwich Structures and Materials*. **15**(2), 168–202.

Carman, G.P., Cheung, K.S. and Wang, D. (1995). "Micro-mechanical model of a composite containing a conservative nonlinear electro-magneto-thermo-mechanical material". *Journal of Intelligent Material Systems and Structures*, **6**(5), 691-699.

Challagulla, K.S. and Georgiades, A.V. (2011). "Micromechanical analysis of magneto-electro-thermo-elastic composite materials with applications to multilayered structures". *International Journal of Engineering Science*, **49**(1), 85-104.

Chen, J.Y., Heyliger, P.R. and Pan, E. (2014). "Free vibration of three-dimensional multilayered magneto-electro-elastic plates under combined clamped/free boundary conditions". *Journal of Sound and Vibration*, **333**(17), 4017-4029.

Chen, W.Q., Lee, K.Y. and Ding, H.J. (2005). "On free vibration of non-homogeneous transversely isotropic magneto-electro-elastic plates". *Journal of Sound and Vibration*, **279** (1), 237-251.

Chen, J., Chen, H., Pan, E. and Heyliger, P.R. (2007). "Modal analysis of magneto-electro-elastic plates using the state-vector approach". *Journal of Sound and Vibration*, **304**(3), 722-734.

Cook, A.C. and Vel, S.S. (2013). "Multiscale thermopiezoelectric analysis of laminated plates with integrated piezoelectric fiber composites". *European Journal of Mechanics-A/Solids*, **40**, 11-33.

Daga, A., Ganesan, N. and Shankar, K. (2008). "Transient response of magneto-electro-elastic simply supported cylinder using finite element". *Journal of Mechanics of Materials and Structures*, **3**(2), 375-389.

Daga, A., Ganesan, N. and Shankar, K. (2009a). "Behaviour of magneto-electro-elastic sensors under transient mechanical loading". *Sensors and Actuators A: Physical*, **150**(1), 46-55.

Daga, A., Ganesan, N. and Shankar, K. (2009b). "Transient dynamic response of cantilever magneto-electro-elastic beam using finite elements". *International Journal for Computational Methods in Engineering Science and Mechanics*, **10**(3), 173-185.

Dai, H.L. and Wang, X. (2006). "Magneto-thermo-electro-elastic transient response in a piezoelectric hollow cylinder subjected to complex loadings". *International Journal of Solids and Structures*, **43**(18), 5628-5646.

Dai, H.L., Hong, L., Fu, Y.M. and Xiao, X. (2010). "Analytical solution for electromagnetothermoelastic behaviours of a functionally graded piezoelectric hollow cylinder". *Applied Mathematical Modelling*, **34**(2), 343-357.

Davi, G. and Milazzo, A. (2011). "A regular variational boundary model for free vibrations of magneto-electro-elastic structures". *Engineering Analysis with Boundary Elements*, **35**(3), 303-312.

Dini, A. and Abolbashari, M.H. (2016). "Hygro-thermo-electro-elastic response of a functionally graded piezoelectric cylinder resting on an elastic foundation subjected to non-axisymmetric loads". *International Journal of Pressure Vessels and Piping*, **147**, 21-40.

Dong, C.Y. (2008). "Vibration of electro-elastic versus magneto-elastic circular/annular plates using the Chebyshev-Ritz method". *Journal of Sound and Vibration*, **317**(1), 219-235.

Dunn, M.L. (1993). "Micromechanics of coupled electroelastic composites: effective thermal expansion and pyroelectric coefficients". *Journal of Applied Physics*, **73**(10), pp.5131-5140.

Ebrahimi, F., Barati, M.R. and Dabbagh, A. (2016). "A nonlocal strain gradient theory for wave propagation analysis in temperature-dependent inhomogeneous nanoplates". *International Journal of Engineering Science*, **107**, 169-182.

- Ebrahimi, F. and Barati, M.R., (2016a). “An exact solution for buckling analysis of embedded piezoelectro-magnetically actuated nanoscale beams”. *Adv. Nano Res*, **4**(2), 65-84.
- Ebrahimi, F. and Barati, M.R. (2016b). “Temperature distribution effects on buckling behaviour of smart heterogeneous nanosize plates based on nonlocal four-variable refined plate theory”. *International Journal of Smart and Nano Materials*, **7**(3), 119-143.
- Ebrahimi, F. and Barati, M.R. (2016c). “Buckling analysis of smart size-dependent higher order magneto-electro-thermo-elastic functionally graded nanosize beams”. *Journal of Mechanics*, **33**(1), 23-33.
- Ebrahimi, F. and Barati, M.R. (2016d). “Electromechanical buckling behaviour of smart piezoelectrically actuated higher-order size-dependent graded nanoscale beams in thermal environment”. *International Journal of Smart and Nano Materials*, **7**(2), 69-90.
- Ebrahimi, F. and Barati, M.R. (2016e). “A unified formulation for dynamic analysis of nonlocal heterogeneous nanobeams in hygro-thermal environment”. *Applied Physics A*, **122**(9), 792.
- Ebrahimi, F. and Barati, M.R. (2016f). “Dynamic modeling of a thermo–piezo-electrically actuated nanosize beam subjected to a magnetic field”. *Applied Physics A*, **122**(4), 451.
- Ebrahimi, F. and Barati, M.R. (2016g). “Vibration analysis of smart piezoelectrically actuated nanobeams subjected to magneto-electrical field in thermal environment”. *Journal of Vibration and Control*, 1077546316646239.
- Ebrahimi, F. and Barati, M.R. (2016h). “Vibration analysis of nonlocal beams made of functionally graded material in thermal environment”. *The European Physical Journal Plus*, **131**(8), 279.
- Ebrahimi, F., Jafari, A. and Barati, M.R. (2016i). “Free vibration analysis of smart porous plates subjected to various physical fields considering neutral surface position”. *Arabian Journal for Science and Engineering*, **42**(5), 1865-1881.
- Ebrahimi, F. and Barati, M.R. (2017a). “Buckling analysis of piezoelectrically actuated smart nanoscale plates subjected to magnetic field”. *Journal of Intelligent Material Systems and Structures*, 1045389X16672569.
- Ebrahimi, F. and Barati, M.R. (2017b). “Small-scale effects on hygro-thermo-mechanical vibration of temperature-dependent nonhomogeneous nanoscale beams”. *Mechanics of Advanced Materials and Structures*, **24**(11), 924-936.

Ebrahimi, F. and Barati, M.R. (2017c). “Magnetic field effects on dynamic behaviour of inhomogeneous thermo-piezo-electrically actuated nanoplates”. *Journal of the Brazilian Society of Mechanical Sciences and Engineering*, **39**(6), 2203-2223.

Ebrahimi, F., Jafari, A. and Barati, M.R. (2017d). “Vibration analysis of magneto-electro-elastic heterogeneous porous material plates resting on elastic foundations”. *Thin-Walled Structures*, **119**, 33-46.

Ebrahimi, F. and Barati, M.R. (2017e). “Porosity-dependent vibration analysis of piezo-magnetically actuated heterogeneous nanobeams”. *Mechanical Systems and Signal Processing*, **93**, 445-459.

Ebrahimi, F. and Barati, M.R. (2017f). “Electro-magnetic effects on nonlocal dynamic behaviour of embedded piezoelectric nanoscale beams”. *Journal of Intelligent Material Systems and Structures*, **28**(15), 2007 – 2022.

Eringen, A.C. (1972a). “Theory of micromorphic materials with memory”. *International Journal of Engineering Science*, **10**(7), 623-641.

Eringen, A.C. (1972b). “Nonlocal polar elastic continua”. *International journal of engineering science*, **10**(1), 1-16.

Eringen, A.C. (1983). “On differential equations of nonlocal elasticity and solutions of screw dislocation and surface waves”. *Journal of applied physics*, **54**(9), 4703-4710.

Espinosa-Almeyda, Y., Camacho-Montes, H., Rodríguez-Ramos, R., Guinovart-Díaz, R., López-Realpozo, J.C., Bravo-Castillero, J. and Sabina, F.J. (2017). “Influence of imperfect interface and fiber distribution on the antiplane effective magneto-electro-elastic properties for fiber reinforced composites”. *International Journal of Solids and Structures*, **112**, 155-168.

Farajpour, A., Yazdi, M.H., Rastgoo, A., Loghmani, M. and Mohammadi, M. (2016). “Nonlocal nonlinear plate model for large amplitude vibration of magneto-electro-elastic nanoplates”. *Composite Structures*, **140**, 323-336.

Ganesan, N., Kumaravel, A. and Sethuraman, R. (2007). “Finite element modeling of a layered, multiphase magneto-electro-elastic cylinder subjected to an axisymmetric temperature distribution”. *Journal of Mechanics of Materials and Structures*, **2**, 655–74.

Gholami, R., Ansari, R. and Gholami, Y. (2017). “Size-dependent bending, buckling and vibration of higher-order shear deformable magneto-electro-thermo-elastic rectangular nanoplates”. *Materials Research Express*, **4**, 065702.

Grossinger, R., Giap, V.D and Sato-Turtelli, R. (2008). “The physics of magneto-electro-elastic composites.” *Journal of Magnetism and Magnetic Materials*, **320**, 1972-1977.

- H**adjiloizi, D.A., Georgiades, A.V., Kalamkarov, A.L. and Jothi, S. (2013a). “Micromechanical modeling of piezo-magneto-thermo-elastic composite structures: Part I–Theory”. *European Journal of Mechanics-A/Solids*, **39**, 298-312.
- Hadjiloizi, D.A., Georgiades, A.V., Kalamkarov, A.L. and Jothi, S. (2013b). “Micromechanical modeling of piezo-magneto-thermo-elastic composite structures: Part II–Applications”. *European Journal of Mechanics-A/Solids*, **39**, 313-327.
- Haitao, D., Wei, C. and Mingzhi, L. (2008). “Static/dynamic analysis of functionally graded and layered magneto-electro-elastic plate/pipe under Hamiltonian system”. *Chinese Journal of Aeronautics*, **21**(1), 35-42.
- Harshe, G., Dougherty, J.P. and Newnham, R.E. (1993). "Magnetolectric effect in composite materials." *Mathematics in Smart Structures* 1919, 224.
- Hashemi, R. (2016). “Magneto-electro-elastic properties of multiferroic composites containing periodic distribution of general multi-coated inhomogeneities”. *International Journal of Engineering Science*, **103**, 59-76.
- Hashemi, M. and Kargarnovin, M.H. (2016). “Analysis of stress and electric fields in a piezoelectric long solid cylinder under axisymmetric thermo-electro-mechanical loadings”. *Mathematics and Mechanics of Solids*, **21**(5), 578-594.
- Heyliger, P.R. and Pan, E. (2004). “Static fields in magnetoelastoelectric laminates”. *AIAA Journal*, **42**(7), 1435 – 1443.
- Hou, P.F., Ding, H.J. and Leung, A.Y.T. (2006). “The transient responses of a special non-homogeneous magneto-electro-elastic hollow cylinder for axisymmetric plane strain problem”. *Journal of Sound and Vibration*, **291**(1), 19-47.
- Hu, J., Chen, L.Q. and Nan, C.W. (2016). "Multiferroic heterostructures integrating ferroelectric and magnetic materials." *Advanced Materials*, **28**(1), 15-39.
- Huang, J.H., Liu, H.K. and Dai, W.L. (2000). “The optimized fiber volume fraction for magnetolectric coupling effect in piezoelectric–piezomagnetic continuous fiber reinforced composites”. *International Journal of Engineering Science*, **38**(11), 1207-1217.
- Huang, D.J., Ding, H.J. and Chen, W.Q. (2007). “Analytical solution for functionally graded magneto-electro-elastic plane beams”. *International Journal of Engineering Science*, **45**(2), 467-485.
- Huang, D.J., Ding, H.J. and Chen, W.Q. (2010). “Static analysis of anisotropic functionally graded magneto-electro-elastic beams subjected to arbitrary loading”. *European Journal of Mechanics-A/Solids*, **29**(3), 356-369.

- J**abbari, M. and Barati, A.R. (2015). “Analytical Solution for the Thermopiezoelectric Behaviour of a Smart Functionally Graded Material Hollow Sphere Under Radially Symmetric Loadings”. *Journal of Pressure Vessel Technology*, **137**(6), 061204.
- Jandaghian, A.A. and Rahmani, O. (2016). “Free vibration analysis of magneto-electro-thermo-elastic nanobeams resting on a Pasternak foundation”. *Smart Materials and Structures*, **25**(3), 035023.
- Jian, A. and Ding, H. (2007). “Analytical solutions for density functionally gradient magneto-electro-elastic cantilever beams”. *Smart Structures and Systems*, **3**(2), 173-188.
- Jiang, J.P. and Li, D.X. (2007). “A new finite element model for piezothermoelastic composite beam”. *Journal of Sound and Vibration*, **306**(3), 849-864.
- Jiangyi, C., Hualing, C. and Ernian, P. (2006). “Free vibration of functionally graded, magneto-electro-elastic, and multilayered plates”. *Acta Mechanica Sinica*, **19**(2), 160-166.
- K**apuria, S. and Achary, G.G.S. (2008). “Benchmark 3D solution and assessment of a zigzag theory for free vibration of hybrid plates under initial electrothermomechanical stresses”. *Composites Science and Technology*, **68**(1), 297-311.
- Kattimani, S.C. and Ray, M.C. (2014a). “Smart damping of geometrically nonlinear vibrations of magneto-electro-elastic plates.” *Composite Structures*, **114**(1), 51–63.
- Kattimani, S.C. and Ray, M.C. (2014b). “Active control of large amplitude vibrations of smart magneto – electro – elastic doubly curved shells.” *International Journal of Mechanics and Materials in Design*, **10**(4), 351–378.
- Kattimani, S.C. and Ray, M.C. (2015). “Control of geometrically nonlinear vibrations of functionally graded magneto-electro-elastic plates.” *International Journal of Mechanical Sciences*, **99**, 154–167.
- Kattimani, S.C. (2017a). “Geometrically nonlinear vibration analysis of multiferroic composite plates and shells.” *Composite Structures*, **163**, 185-194.
- Kattimani, S.C. (2017b). “Active damping of multiferroic composite plates using 1-3 Piezoelectric composites”. *Smart Materials and Structures*, **26**(12), 125021.
- Ke, L.L., Wang, Y.S., Yang, J. and Kitipornchai, S. (2014). “Free vibration of size-dependent magneto-electro-elastic nanoplates based on the nonlocal theory”. *Acta Mechanica Sinica*, **30**(4), 516-525.

- Ke, L.L. and Wang, Y.S. (2014). “Free vibration of size-dependent magneto-electro-elastic nanobeams based on the nonlocal theory”. *Physica E: Low-dimensional Systems and Nanostructures*, **63**, 52-61.
- Khoshgoftar, M.J., Arani, A.G. and Arefi, M. (2009). “Thermoelastic analysis of a thick walled cylinder made of functionally graded piezoelectric material”. *Smart Materials and Structures*, **18**(11), 115007.
- Kim, J.Y. (2011). “Micromechanical analysis of effective properties of magneto-electro-thermo-elastic multilayer composites”. *International Journal of Engineering Science*, **49**(9), 1001-1018.
- Koutsawa, Y. (2015). “Overall thermo-magneto-electro-elastic properties of multiferroics composite materials with arbitrary heterogeneities spatial distributions”. *Composite Structures*, **133**, 764-773.
- Kondaiah, P., Shankar K., Ganesan N. (2012). “Studies on magneto-electro-elastic cantilever beam under thermal environment”. *Coupled Systems Mechanics*, **1**(2), 205-217
- Kondaiah, P., Shankar K., Ganesan N. (2013a). “Pyroelectric and pyromagnetic effects on behaviour of magneto-electro-elastic plate”. *Coupled Systems Mechanics*, **2**, 1-22.
- Kondaiah, P., Shankar, K. and Ganesan, N. (2013b). “Pyroelectric and pyromagnetic effects on multiphase magneto–electro–elastic cylindrical shells for axisymmetric temperature”. *Smart Materials and Structures*, **22**(2), 025007.
- Kondaiah, P., Shankar, K. and Ganesan, N. (2014). “Pyroeffects on multiphase magneto-electroelastic sensor patch bonded on mild steel plate”. *International Journal on Smart Sensing & Intelligent Systems*, **7**(3), 1134-1155.
- Kondaiah, P. and Shankar, K. (2017). “Pyroeffects on Magneto – Electro – Elastic sensor patch subjected to thermal load”, *Smart Structures and Systems*, **19**(3), 299-307.
- Kulikov, G.M. and Plotnikova, S.V. (2017). “An analytical approach to three-dimensional coupled thermoelectroelastic analysis of functionally graded piezoelectric plates”. *Journal of Intelligent Material Systems and Structures*, **28**(4), 435-450.
- Kumar, A.M.S., Panda, S. and Chakraborty, D. (2016). “Piezo-viscoelastically damped nonlinear frequency response of functionally graded plates with a heated plate-surface”. *Journal of Vibration and Control*, **22**(2), 320-343.
- Kumar, R.S. and Ray, M.C. (2013). “Active control of geometrically nonlinear vibrations of doubly curved smart sandwich shells using 1–3 piezoelectric composites”. *Composite Structures*, **105**, 173-187.

- Kumaravel, A., Ganesan N and Sethuraman, R. (2007). "Steady-state analysis of a three-layered electro-magneto-elastic strip in a thermal environment. *Smart Materials and Structures*, **16**(2), 282–295.
- Kundalwal, S.I., Kumar, R.S. and Ray, M.C. (2013). "Smart damping of laminated fuzzy fiber reinforced composite shells using 1–3 piezoelectric composites". *Smart Materials and Structures*, **22**(10), 105001.
- Kuo, H.Y. and Wang, Y.L. (2012). "Optimization of magnetoelectricity in multiferroic fibrous composites". *Mechanics of Materials*, **50**, 88-99.
- Lage, R.G., Soares, C.M., Soares, C.M. and Reddy, J.N. (2004). "Layerwise partial mixed finite element analysis of magneto-electro-elastic plates". *Computers & Structures*, **82**(17), 1293-1301.
- Li, X.Y., Ding, H.J. and Chen, W.Q. (2008). "Three-dimensional analytical solution for functionally graded magneto–electro-elastic circular plates subjected to uniform load". *Composite Structures*, **83**(4), 381-390.
- Li, Y.S., Cai, Z.Y. and Shi, S.Y. (2014). "Buckling and free vibration of magneto-electro-elastic nanoplate based on nonlocal theory". *Composite Structures*, **111**, 522-529.
- Liew, K.M., He, X.Q., Ng, T.Y. and Sivashanker, S. (2001). "Active control of FGM plates subjected to a temperature gradient: modelling via finite element method based on FSDT". *International Journal for Numerical Methods in Engineering*, **52**(11), 1253-1271.
- Liew, K.M., He, X.Q., Ng, T.Y. and Kitipornchai, S. (2003). "Finite element piezothermoelasticity analysis and the active control of FGM plates with integrated piezoelectric sensors and actuators". *Computational Mechanics*, **31**(3), 350-358.
- Liu, C.B., Bian, Z.G., Chen, W.Q. and Lü, C.F. (2012). "Three-dimensional pyroelectric analysis of a functionally graded piezoelectric hollow sphere". *Journal of Thermal Stresses*, **35**(6), 499-516.
- Liu, M.F. (2011). "An exact deformation analysis for the magneto-electro-elastic fiber-reinforced thin plate". *Applied Mathematical Modelling*, **35**(5), 2443-2461.
- Loja, M.A.R., Soares, C.M. and Barbosa, J.I. (2014). "Optimization of magneto-electro-elastic composite structures using differential evolution". *Composite Structures*, **107**, 276-287.
- Lopatin, S., Lopatina, I. and Lisnecsckaya, I. (1994). "Magnetoelectric PZT/ferrite composite material." *Ferroelectrics*, **162**(1), 63-68.
- Lv, J., Yang, K., Zhang, H., Yang, D. and Huang, Y. (2014). "A hierarchical multiscale approach for predicting thermo-electro-mechanical behaviour of

heterogeneous piezoelectric smart materials". *Computational Materials Science*, **87**, 88-99.

Miara, B. and Sejje Suárez, J. (2013). "Asymptotic pyroelectricity and pyroelasticity in thermopiezoelectric plates". *Asymptotic Analysis*, **81**(3-4), 211-250.

Milazzo, A. Orlando, C. and Alaimo, A. (2009). "An analytical solution for the magneto-electro-elastic bimorph beam forced vibrations problem." *Smart Materials and Structures*, **18**(8), 08501296.

Milazzo, A. (2012). "An equivalent single-layer model for magneto-electroelastic multilayered plate dynamics". *Composite Structures*, **94**(6), 2078-2086.

Milazzo, A. (2013). "A one-dimensional model for dynamic analysis of generally layered magneto-electro-elastic beams". *Journal of Sound and Vibration*, **332**(2), 465-483.

Milazzo, A. and Orlando, C. (2012). "A beam finite element for magneto-electro-elastic multilayered composite structures". *Composite Structures*, **94**(12), 3710-3721.

Mohammadimehr, M., B. Roustá Navi, and A. Ghorbanpour Arani. (2017). "Dynamic stability of modified strain gradient theory sinusoidal viscoelastic piezoelectric polymeric functionally graded single-walled carbon nanotubes reinforced nanocomposite plate considering surface stress and agglomeration effects under hydro-thermo-electro-magneto-mechanical loadings." *Mechanics of Advanced Materials and Structures*. **24**(16), 1325-1342.

Moita, J.M.S., Soares, C.M.M. and Soares, C.A.M. (2009). "Analyses of magneto-electro-elastic plates using a higher order finite element model". *Composite Structures*, **91**(4), 421-426.

Nan, C.W. and Jin, F.S. (1993). "Multiple-scattering approach to effective properties of piezoelectric composites." *Physical Review B*, **48**(12), 8578.

Nan, C.W. (1994). "Magneto-electric effect in composites of piezoelectric and piezomagnetic phases". *Physical Review B*, **50**(9), 6082.

Oh, J. and Cho, M. (2004). "A finite element based on cubic zig-zag plate theory for the prediction of thermo-electric-mechanical behaviours". *International Journal of Solids and Structures*, **41**(5), 1357-1375.

Ootao, Y. and Tanigawa, Y. (2005). "Transient analysis of multilayered magneto-electro-thermoelastic strip due to nonuniform heat supply". *Composite Structures*, **68**(4), 471-480.

Pan, E. (2001). "Exact solution for simply supported and multilayered magneto-electro-elastic plates". *Journal of Applied Mechanics*, **68**(4), 608-618.

- Pan, E. and P. R. Heyliger. (2002), "Free vibrations of simply supported and multilayered magneto-electro-elastic plates." *Journal of Sound and Vibration*, **252**(3), 429-442.
- Pan, E. and Heyliger, P.R. (2003). "Exact solutions for magneto-electro-elastic laminates in cylindrical bending". *International Journal of Solids and Structures*, **40**(24), 6859-6876.
- Pan, E. and Han, F. (2005). "Exact solution for functionally graded and layered magneto-electro-elastic plates". *International Journal of Engineering Science*, **43**(3), 321-339.
- Panda , S. and Ray, M.C . (2008). "Active constrained layer damping of geometrically nonlinear vibrations of functionally graded plates using piezoelectric fiber-reinforced composites". *Smart Materials and Structures*, **17**(2), 025012.
- Panda , S. and Ray, M.C . (2009). "Active control of geometrically nonlinear vibrations of functionally graded laminated composite plates using piezoelectric fiber reinforced composites". *Journal of Sound and Vibration*, **325**(1), 186-205.
- Pérez-Fernández, L.D., Bravo-Castillero, J., Rodri, R and Sabina, F.J. (2009). "On the constitutive relations and energy potentials of linear thermo-magneto-electro-elasticity". *Mechanics Research Communication*, **36**(3), 343-350.
- R**aja, S., Sinha, P. K., Raja, S., Dwarakanathan, D., Sinha, P.K., Prathap, G. (2004a). "Bending behaviour of piezo-hygrothermo-elastic smart laminated composite flat and curved plates with active control", *Journal of Reinforced Plastic and Composites*. **23**, 265–290.
- Raja, S., Sinha, P. K., Prathap, G., Dwarakanathan, D. (2004b). "Influence of active stiffening on dynamic behaviour of piezo-hygro-thermo-elastic composite plates and shells", *Journal of Sound and Vibrations*, **278**, 257–283.
- Ramirez, F., Heyliger, P.R. and Pan, E. (2006a). "Free vibration response of two-dimensional magneto-electro-elastic laminated plates". *Journal of Sound and Vibration*, **292**(3), 626-644.
- Ramirez, F., Heyliger, P.R. and Pan, E. (2006b). "Discrete layer solution to free vibrations of functionally graded magneto-electro-elastic plates". *Mechanics of Advanced Materials and Structures*, **13**(3), 249-266.
- Ray, M.C. and Pradhan, A.K. (2008). "Performance of vertically and obliquely reinforced 1–3 piezoelectric composites for active damping of laminated composite shells". *Journal of Sound and Vibration*, **315**(4), 816-835.
- Ray, M.C. and Shivakumar, J. (2009). "Active constrained layer damping of geometrically nonlinear transient vibrations of composite plates using piezoelectric fiber-reinforced composite". *Thin-Walled Structures*, **47**(2), 178-189.

Razavi, S. and Shooshtari, A. (2014). "Free vibration analysis of a magneto-electro-elastic doubly-curved shell resting on a Pasternak-type elastic foundation". *Smart Materials and Structures*, **23**(10), 105003.

Razavi, S. and Shooshtari, A. (2015). "Nonlinear free vibration of magneto-electro-elastic rectangular plates". *Composite Structures*, **119**, 377-384.

Roy, T., Manikandan, P. and Chakraborty, D. (2010). "Improved shell finite element for piezothermoelastic analysis of smart fiber reinforced composite structures". *Finite elements in analysis and design*, **46**(9), 710-720.

Ryu, J., Priya, S., Uchino, K. and Kim, H.E. (2002). "Magnetoelectric effect in composites of magnetostrictive and piezoelectric materials." *Journal of Electroceramics*, **8**(2), 107-119.

Saadatfar, M., Khafri, A.M. (2014). "Hygrothermomagnetoelastic analysis of a functionally graded magnetoelastic hollow sphere resting on an elastic foundation". *Smart Materials and Structures*, **23**, 035004.

Shahverdi, H. and Barati, M.R. (2017). "Vibration analysis of porous functionally graded nanoplates". *International Journal of Engineering Science*, **120**, 82-99.

Sharma, J.N., Pal, M. and Chand, D. (2004). "Three-dimensional vibration analysis of a piezothermoelastic cylindrical panel". *International journal of engineering science*, **42**(15), 1655-1673.

She, G.L., Shu, X. and Ren, Y.R. (2017). "Thermal buckling and postbuckling analysis of piezoelectric FGM beams based on high-order shear deformation theory". *Journal of Thermal Stresses*, **40**(6), 783-797.

Shegokar, N.L. and Lal, A. (2014). "Stochastic finite element nonlinear free vibration analysis of piezoelectric functionally graded materials beam subjected to thermo-piezoelectric loadings with material uncertainties". *Meccanica*, **49**(5), 1039-1068.

Shooshtari, A. and Razavi, S. (2015). "Nonlinear vibration analysis of rectangular magneto-electro-elastic thin plates". *IJE transactions A: Basics*, **28**(1), 139-147.

Shooshtari, A. and Razavi, S. (2017). "Vibration of a multiphase magneto-electro-elastic simply supported rectangular plate subjected to harmonic forces". *Journal of Intelligent Material Systems and Structures*, **28**(4), 451-467.

Shi, S., Li, P. and Jin, F. (2017). "The establishment of coupled magneto-electro-thermo-elastic theory with the consideration of surface and non-local effects and its application in laminated nano-devices". *Composite Structures*, **179**, 541-551.

Sixto-Camacho, L.M., Bravo-Castillero, J., Brenner, R., Guinovart-Díaz, R., Mechkour, H., Rodríguez-Ramos, R. and Sabina, F.J. (2013). "Asymptotic

homogenization of periodic thermo-magneto-electro-elastic heterogeneous media”. *Computers & Mathematics with Applications*, **66**(10), 2056-2074.

Sladek, J., Sladek, V., Repka, M., Kasala, J. and Bishay, P. (2017). “Evaluation of effective material properties in magneto-electro-elastic composite materials”. *Composite Structures*, **174**, 176-186.

Smittakorn, W. and Heyliger, P. R. (2000). “A discrete-layer model of laminated hygrothermopiezoelectric plates”, *Mechanics of Composite Materials and Structures*, **7**, 79–104.

Smittakorn, W. and Heyliger, P. R. (2001). “An adaptive wood composite: Theory”. *Wood and Fiber Science*, **33**(4), 595–608.

Smittakorn, W. and Heyliger, P. R. (2003). “Adaptive wood composite: experiment”. *Journal of Structural Engineering*, **129**, 699–702.

Soh, A.K. and Liu, A.J. (2005). “On the constitutive equations of magneto-electro-elastic solids”. *Journal of Intelligent Material Systems and Structures*, **16** (7-8), 597-602.

Sun, K.H. and Kim, Y.Y. (2010). “Layout design optimization for magneto-electro-elastic laminate composites for maximized energy conversion under mechanical loading”. *Smart Materials and Structures*, **19**(5), 055008.

Sunar M, Ahmed Z Al-Garni, Ali MH and Kahraman R. (2002). “Finite Element Modeling of Thermopiezomagnetic Smart Structures”. *AIAA Journal*, **40**, 1845-1851.

Sunar, M., Al-Athel, K., Yilbas, B.S., Al-Qahtani, H. and Ayar, T. (2012). “Modeling and Placement of Thermopiezoelectro-Magnetic Materials”. *Advanced Materials Research*, **445**, 520-525.

Tauchert, T.R. (1996). “Cylindrical bending of hybrid laminates under thermo-electro-mechanical loading”. *Journal of Thermal Stresses*, **19**, 287-296.

Tian, X., Zhang, J., Shen, Y. and Lu, T.J. (2007). “Finite element method for generalized piezothermoelastic problems”. *International journal of solids and structures*, **44**(18), 6330-6339.

Tsai, Y.H. and Wu, C.P. (2008). “Dynamic responses of functionally graded magneto-electro-elastic shells with open-circuit surface conditions”. *International Journal of Engineering Science*, **46**(9), 843-857.

Vaezi, M., Shirbani, M.M. and Hajnayeb, A. (2016). “Free vibration analysis of magneto-electro-elastic microbeams subjected to magneto-electric loads”. *Physica E: Low-dimensional Systems and Nanostructures*, **75**, 280-286.

- Wang, J., Chen, L. and Fang, S. (2003). "State vector approach to analysis of multilayered magneto-electro-elastic plates". *International Journal of Solids and Structures*, **40**(7), 1669-1680.
- Wang, X., Lee, J.S. and Zheng, X. (2003). "Magneto-thermo-elastic instability of ferromagnetic plates in thermal and magnetic fields". *International Journal of Solids and Structures*, **40**(22), 6125-6142.
- Wang, H.M. and Ding, H.J. (2006a). "Transient responses of a magneto-electro-elastic hollow sphere for fully coupled spherically symmetric problem". *European Journal of Mechanics-A/Solids*, **25**(6), 965-980.
- Wang, H.M. and Ding, H.J. (2006b). "Transient responses of a special non-homogeneous magneto-electro-elastic hollow cylinder for a fully coupled axisymmetric plane strain problem". *Acta mechanica*, **184**(1), 137-157.
- Wang, H.M. and Ding, H.J. (2006c). "Spherically symmetric transient responses of functionally graded magneto-electro-elastic hollow sphere". *Structural Engineering and Mechanics*, **23**(5), 525-542.
- Wang, Y., Xu, R., Ding, H. and Chen, J. (2010). "Three-dimensional exact solutions for free vibrations of simply supported magneto-electro-elastic cylindrical panels." *International Journal of Engineering Science*, **48**(12), 1778-17.
- Wang, J., Qu, L. and Qian, F. (2010). "State vector approach of free-vibration analysis of magneto-electro-elastic hybrid laminated plates". *Composite structures*, **92**(6), 1318-1324.
- Wang, R., Han, Q. and Pan, E. (2010). "An analytical solution for a multilayered magneto-electro-elastic circular plate under simply supported lateral boundary conditions". *Smart materials and Structures*, **19**(6), 065025.
- Wu, X.H., Shen, Y.P. and Chen, C. (2003). "An exact solution for functionally graded piezothermoelastic cylindrical shell as sensors or actuators". *Materials Letters*, **57**(22), 3532-3542.
- Wu, C.P. and Tsai, Y.H. (2007). "Static behaviour of functionally graded magneto-electro-elastic shells under electric displacement and magnetic flux". *International Journal of Engineering Science*, **45**(9), 744-769.
- Wu, C.P. and Lu, Y.C. (2009). "A modified Pagano method for the 3D dynamic responses of functionally graded magneto-electro-elastic plates". *Composite Structures*, **90**(3), 363-372.
- Wu, C.P. and Tsai, Y.H. (2010). "Dynamic responses of functionally graded magneto-electro-elastic shells with closed-circuit surface conditions using the method of multiple scales". *European Journal of Mechanics-A/Solids*, **29**(2), 166-181.

- X**in, L. and Hu, Z. (2015). “Free vibration of simply supported and multilayered magneto-electro-elastic plates”. *Composite structures*, **121**, 344-350.
- Y**ing, C. and Zhifei, S. (2005). “Exact solutions of functionally gradient piezothermoelastic cantilevers and parameter identification”. *Journal of intelligent material systems and structures*, **16**(6), 531-539.
- Z**enkour, A.M. (2012). “Piezoelectric behaviour of an inhomogeneous hollow cylinder with thermal gradient”. *International Journal of Thermophysics*, **33**(7), 1288-1301.
- Zenkour, A.M. (2014a). “Hygro-thermoelastic responses of inhomogeneous piezoelectric and exponentially graded cylinders”. *International Journal of Pressure Vessels and Piping*, **119**, 8-18.
- Zenkour, A.M. (2014b). “Exact solution of thermal stress problem of an inhomogeneous hygrothermal piezoelectric hollow cylinder”. *Applied Mathematical Modelling*, **38**(24), 6133-6143.
- Zenkour, A.M. (2016a). “Bending analysis of piezoelectric exponentially graded fiber-reinforced composite cylinders in hygrothermal environment”. *International Journal of Mechanics and Materials in Design*, 1-15.
- Zenkour, A.M. (2016b). “Hygrothermal analysis of heterogeneous piezoelectric elastic cylinders”. *Journal of Mathematical Models in Engineering*, **2**(1), 1-18.
- Zhao, X., Li, X.Y. and Li, Y.H. (2017). “Axisymmetric analytical solutions for a heterogeneous multi-ferroic circular plate subjected to electric loading”. *Mechanics of Advanced Materials and Structures*, 1-10.
- Zheng, S.J., Dai, F. and Song, Z. (2009). “Active control of piezothermoelastic FGM shells using integrated piezoelectric sensor/actuator layers”. *International Journal of Applied Electromagnetics and Mechanics*, **30**, 107-124.
- Zhong, Z. and Shang, E.T. (2005). “Exact analysis of simply supported functionally graded piezothermoelastic plates”. *Journal of Intelligent Material Systems and Structures*, **16**(7-8), 643-651.
- Zhou, K., Li, Y.D. and Liu, S.L. (2017). “Effects of the volume fraction of piezoelectric particles in the magneto-electro-elastic interfacial region on the fracture behaviour of a laminate multiferroic plate”. *Acta Mechanica*, **228**(4), 1229-1248.

List of Publications based on PhD Research Work

Sl. No	Title of the Paper	Authors (In the same order as in the paper, underline the Research Scholar's name)	Name of the Journal / Conference /Symposium, Vol., No., Pages	Month & Year of Publication	Category *
1.	Static studies of stepped functionally graded magneto-electro-elastic beam subjected to different thermal loads	<u>Vinvas M.</u> , S.C. Kattimani	Composite Structures, 2017 Vol. 163, pages 216-237.	December, 2016	1
2.	A finite element based assessment of static behaviour of multiphase magneto-electro-elastic beams under different thermal loading	<u>Vinvas M.</u> , S.C. Kattimani	Structural Engineering and Mechanics, 2017, Vol. 62(5), pages 519 - 535	March, 2017	1
3.	Multiphysics response of magneto-electro-elastic beams in thermo-mechanical environment	<u>Vinvas M.</u> , S.C. Kattimani	Coupled System Mechanics, 2017 Vol. 6(3), pages 351 - 368	May, 2017	1
4.	Static behaviour of thermally loaded multilayered Magneto-Electro-Elastic beam	<u>Vinvas M.</u> , S.C. Kattimani	Structural Engineering and Mechanics, 2017, Vol. 63(4), pages 481 - 495	June, 2017	1
5.	Static analysis of stepped functionally graded magneto-electric-elastic plates in thermal environment: A finite element study	<u>Vinvas M.</u> , S.C. Kattimani	Composite Structures, 2017 Vol. 178, pages 63-86.	July, 2017	1
6.	Hygrothermal analysis of magneto-electro-elastic plate using 3D finite element analysis	<u>Vinvas M.</u> , S.C. Kattimani	Composite Structures, 2017 Vol. 180, pages 617-637	August, 2017	1
7.	Influence of coupled fields on free vibration and static behaviour of functionally graded magneto-electro-thermo-elastic plate	<u>Vinvas M.</u> , Piyush J Sagar, S.C. Kattimani	Journal of Intelligent Material Systems and Structures DOI: 10.1177/1045389X17740739	September, 2017	1

BIO-DATA

1	Name	VINYAS M.
2	Father's Name	Mahesh T.G.
3	Date of Birth	December 5, 1991
4	Nationality	Indian
5	Permanent Address	#128, "Samarpane", Behind Kailasashram, Saptagiri Extension, Shettyhalli Road, Tumkur- 572102, Karnataka, India
6	Mobile Number	+91-9535364640
7	Email Id	Vinyas.mahesh@gmail.com

Educational Qualification:

Sl. No.	Qualification	University	College	Period	Performance
1.	Ph.D	National Institute of Technology Karnataka	National Institute of Technology Karnataka	2015-2017	8.77
2	M.Tech, Machine Design	Visvesvariah Technological University	UBDT, Davangere	2013-2015	84.91% (University 3 rd Rank)
3	B.E, Mechanical	Visvesvariah Technological University	Siddaganga Institute of Technology, Tumkur	2009-2013	9.67

I declare that above information is true and correct to best of my knowledge.

(VINYAS M)